



The
University
Of
Sheffield.

Novel 6-phase Fractional-slot Permanent Magnet Machine for Electric Vehicle Applications

by

Vipulkumar I. Patel

A thesis submitted for the degree of PhD in
Department of Electronic & Electrical Engineering,
The University of Sheffield, UK

March 2014

raja-vidya raja-guhyam pavitram idam uttamam
pratyakshavagamam dharmyam su-sukham kartum avyayam¹

raja-vidya—the king of all wisdom; *raja-guhyam*—the king of all that is confidential;
pavitram—purifying; *idam*—this knowledge; *uttamam*—the topmost; *pratyaksha*—
direct realization; *avagamam*—able to be perceived by; *dharmyam*—in righteousness;
su-sukham—very joyous; *kartum*—to perform; *avyayam*—everlasting.

This knowledge is the king of all wisdom; the king of all that's confidential, the
topmost in righteousness, purifying, able to be perceived by direct realization,
very joyous to perform and everlasting.

¹ Shree Bhagavad Gita, Chapter 9, Verse 2

Abstract

To tackle the issues concerning the global warming and the international energy security, the only way forward is the wide spread adoption of plug-in electric vehicles (EV) in the transportation industry. High power dense and highly efficient electrical machines pave the way for the swift realization of EV.

The research underpinned in this thesis describes the new winding configurations and associated slot-pole combinations for permanent magnet (PM) brushless machines that lead to improved performance and facilitate cost reduction. The current state-of-the-art machine technologies and their topologies are weighed against one another qualitatively through a comprehensive literature survey, and quantitatively by a preliminary design study of the most competitive machine technologies for a micro-sized EV application. Compared to the current state-of-the-art, the salient feature of the proposed winding designs is elimination and/or reduction of undesirable space harmonics which result from the existing fractional-slot per pole per phase PM machines with concentrated windings. This brings the benefits of significant reduction of the eddy current loss in the rotor permanent magnets, shorter end-windings and hence reduced copper loss and copper usage, increased power/torque density, reduction in manufacturing cost, and improved energy efficiency. In order to improve power drivetrain availability for EV applications, the thesis proposes the design of 6-phase PM machine as two independent 3-phase systems using the proposed winding configuration. A number of possible phase shifts between two sets of 3-phase windings due to their slot-pole combination and winding configuration are investigated and the optimum phase shift is selected by analysing the harmonic distributions and their effect on machine performance including the eddy current loss in the magnets. The proposed 6-phase winding configuration is applied to the design of an interior permanent magnet (IPM) machine for segment-A EV, under the electrical, thermal, and volumetric constraints, and demonstrated by a series of preliminary functional tests on the prototype machines. The design study and the measurement results show that the proposed winding configuration results into high torque/power dense PM machine with high efficiency over wide operating range. The important design aspects of the new machine topologies for EV application are investigated in detail, which include effect of phase shifts on magnet eddy current loss and unbalanced magnetic pull of the machine, demagnetization assessment of the new machine topology under various fault conditions, and thermal analyses over the driving cycles.

THE DEDICATION OF THIS THESIS

IS SPLIT SEVEN WAYS

TO NISHA,

TO HITENBHAI,

TO KALPANABHABHI,

TO ARNAV,

TO HARIT,

& TO MY PARENTS AND MY PARENT-IN-LAWS.

Acknowledgments

“Gratitude is the hardest of emotion, one cannot find adequate words to convey all what one feels!”

Let me express my sincere gratitude to Prof. Jiabin Wang for guiding and sailing me through this long and enduring journey, called PhD. I feel extremely fortunate to have him as my supervisor who helped me gain the technical expertise and the interpersonal skills during the course of my research degree. I wish to thank my other supervisors, Prof. Zi-Qiang Zhu and Prof. Kais Atallah for their continuous motivation. I would also like to express my indebtedness to European Commission for funding the research work and to CASTOR project partners for helping me expand the breadth in other relevant research areas of Electric Vehicles.

My sincere thanks to Dr. Weiya Wang for helping me build the prototype machines, and to Mr. Xiao Chen for his support in the mechanical design of the rotor. My deep thanks to Dr. Khoa Hoang, Mr. Dian Nugraha, and Mr. Radovan Vuletic for their support during testing of the prototype machines.

I am thankful to Mr. John Wilkinson, Mr. Andy Race, Mr. Richard Garraway, Mr. Lawrence Obodo, and Mr. Clive Thompson for their technical support in the lab during prototyping and testing. I am also thankful to Panagiotis Lazari, Xiao Chen, Liang Chen, and Bhaskar Sen for the fruitful technical discussion during weekly meetings and tea breaks.

Special thanks to Amit, Anjudidi, Hrishikesh, Narayanswamy, Parag, Rageshree and Satish for their everlasting support. Thanks to my other friends in UK for making my stay memorable.

With all my sincerity, I would like to thank my mentors, Dr. R. Anbarasu, Dr. Rajen Bhatt, and Prof. K. R. Rajagopal, to motivate and encourage me for pursuing PhD.

Last but not the least, without the support, help and motivation of my entire family, this journey would not have come to an end. Indeed, special thanks to my wife, Nisha, for her unconditional love towards me and personal sacrifices owing to my involvement with the research degree.

Table of Contents

Abstract	IV
Acknowledgements.....	VI
Table of Contents.....	VII
1 Introduction to Electric Vehicles	1
1.1 Electric Vehicles – promising pathway to increased energy security ...	1
1.1.1 History of Electric Vehicles	3
1.1.2 Types of electric vehicles.....	6
1.1.3 Merits and challenges of electric vehicles	6
1.2 Architectures of electric vehicles	8
1.2.1 Architectures of hybrid electric vehicles	8
1.2.2 Architectures of battery electric vehicles	10
1.2.3 Classification of EVs based on the car size.....	12
1.3 Recent commercial electric vehicles	13
1.4 Target goals for traction drive in future EVs.....	16
1.5 History of permanent magnet motors.....	17
1.6 Motivation for the doctoral research work.....	18
1.7 Main contributions of the thesis.....	20
1.8 Outline of the thesis	21
1.9 List of publications	23
2 Electrical Machine Technologies and Topologies for EV	25
2.1 Basic requirements for an electrical machine for EV	25
2.2 Conventional machine technologies	27
2.2.1 DC machines (DCM).....	27
2.2.2 Induction machines (IM).....	28
2.2.3 Switched reluctance machines (SRM)	29
2.2.4 Permanent magnet (PM) machines	29

2.2.5	Synchronous wound field machines (SM)	30
2.2.6	Comparison of conventional machine technologies.....	30
2.3	State-of-the-art technologies for EV	33
2.3.1	Multi-phase induction machines	33
2.3.2	Switched reluctance machines	35
2.3.3	Synchronous reluctance machines	35
2.3.4	Permanent magnet machines	37
2.4	Selection of advanced machine technologies for a micro-sized EV.....	50
3	Preliminary Design Study on Advanced Machine Technologies for a Micro-sized EV	52
3.1	Most promising machine technologies for EV	52
3.1.1	Fractional-slot SPM – 12 slot, 14-pole	52
3.1.2	Fractional-slot IPM – 24 slot, 14-pole	54
3.1.3	Hybrid excited flux switching machines	56
3.2	Power drivetrain of a micro-sized EV	59
3.3	Design specifications and constraints	59
3.4	Design process and optimization	61
3.4.1	Design optimization of FSCW SPM with 12-slot, 14-pole	61
3.4.2	Design optimization of FSCW IPM with 24-slot, 14-pole	61
3.4.3	Design optimization of HE-PMFSM with 12-slot, 14-pole.....	65
3.5	Performance evaluation of the promising machine technologies	69
3.6	Assessment of the promising machine technologies for a micro-sized EV application.....	73
3.6.1	Peak torque capability	74
3.6.2	Torque ripple	74
3.6.3	Efficiency at the rated and the peak torque operation and over the NEDC	75
3.6.4	Power electronics converter	76
3.6.5	Mechanical structure	77
3.7	Summary.....	77
4	Novel Fractional-slot per Pole per Phase Winding Configuration with Low Space Harmonics Content	79

4.1	Characteristic features of fractional-slot per pole per phase PM machines.....	79
4.1.1	Mitigation of the demerits of FSCW configuration	81
4.2	Novel 3-phase fractional-slot per pole per phase winding configurations with low space harmonics	83
4.2.1	Proposed 3-phase, 18-slot, 8-pole winding configuration.....	85
4.2.2	Proposed 3-phase, 18-slot, 10-pole winding configuration.....	90
4.2.3	Proposed 3-phase, 36-slot, 10-pole winding configuration	92
4.2.4	Applicability of novel fractional-slot per pole per phase winding configurations.....	94
4.3	Configuration of the proposed winding as multiple 3-phase winding systems.....	96
4.3.1	Development of 6-phase, 18-slot, 8-pole winding	97
4.3.2	Stator MMF profile of 6-phase, 18-slot, 8-pole winding configuration.....	99
4.3.3	Optimal phase shift between two sets of 3-phase windings in the proposed 6-phase, 18-slot, 8-pole winding configuration	99
5	Design and Analysis of 6-phase, 18-slot, 8-pole IPM Machine for Segment-A Electric Vehicle	105
5.1	Drivetrain configuration.....	105
5.2	Vehicle data and target performance	106
5.3	Motor design specifications	107
5.3.1	Required wheel torque and power over the NEDC	109
5.3.2	Determining design specifications of the drive motor	109
5.3.3	Summary of motor design specifications	115
5.4	Distribution of energy consumption over the NEDC and equivalent energy distribution	116
5.5	Design constraints for EV traction machine.....	119
5.5.1	Constraints on d -axis inductance for efficient field-weakening operations of an IPM machine	120
5.5.2	Volumetric, electrical, mechanical and thermal constraints	123
5.6	Design and analysis of 6-phase, 18-slot, 8-pole IPM machine for segment-A EV.....	124

5.6.1	Design optimization process.....	125
5.6.2	Design optimization trends.....	127
5.6.3	Mechanical design.....	130
5.6.4	Cooling system design.....	134
5.6.5	Thermal analyses of the optimized machine.....	137
5.6.6	Sensitivity studies on the machine temperatures.....	142
5.7	Performance of the optimized design of 6-phase, 18-slot, 8-pole IPM machine.....	148
5.7.1	Performance at the rated and the peak torque operation.....	149
5.7.2	Performance over the NEDC.....	150
5.7.3	Torque ripple, flux lines and flux density plots.....	150
5.7.4	Efficiency map of the optimized machine.....	153
5.8	<i>d-q</i> axis model and parameters of 6-phase, 18-slot, 8-pole IPM machine.....	155
5.8.1	<i>d-q</i> axis model of the machine.....	155
5.8.2	Parameters of the machine.....	156
6	Prototyping and Experimental Validation of 6-phase, 18-slot, 8-pole IPM Machine.....	160
6.1	Prototype of 6-phase, 18-slot, 8-pole IPM machine.....	160
6.1.1	Components and assembly of the prototype machine.....	160
6.1.2	Instrumentation and feedback device.....	164
6.2	Instruments, test set-up and data acquisition.....	165
6.2.1	Instruments for the test set-up.....	165
6.2.2	Test set-up.....	166
6.2.3	Data acquisition.....	168
6.3	List of preliminary tests.....	170
6.4	No-load tests on the prototype motor.....	171
6.4.1	Insulation testing.....	171
6.4.2	Resistance measurement.....	172
6.4.3	Back EMF measurement.....	175
6.4.4	Check on mechanical integrity.....	178
6.4.5	No-load loss measurement.....	178
6.5	Load tests on the prototype motor.....	182

6.5.1	Validation of control modes.....	182
6.5.2	Measurement of motor parameters (parameter characterization) ..	185
6.5.3	Efficiency measurement.....	193
6.5.4	Peak torque capability	197
6.5.5	Thermal test at the rated torque operation	198
6.6	Investigation of partial demagnetization of the prototype motor during high speed testing	200
6.6.1	Sequence of events	202
6.6.2	Investigation of root causes	202
6.6.3	Summary of investigation.....	208
6.6.4	Preventive measures undertaken	209
6.7	Comparison of two prototypes.....	209
6.8	Preliminary tests on 2 nd prototype motor.....	213
6.8.1	Back EMF measurement.....	213
6.8.2	No-load loss measurement.....	213
6.8.3	Measurement of efficiency map	215
6.8.4	Thermal test.....	220
7	Design Aspects of Novel Fractional-slot per Pole per Phase (18- slot, 8-pole) Winding Configuration for EV Applications.....	223
7.1	Effect of phase shifts on PM eddy current loss and unbalanced magnetic pull.....	223
7.1.1	2-D transient finite element model and operating conditions under consideration	225
7.1.2	Effect of phase shifts on magnet eddy current loss	226
7.1.3	Effect of phase shifts on unbalanced magnetic pull.....	231
7.1.4	Summary.....	236
7.2	Demagnetization assessment of 6-phase fractional-slot PM machines under various fault conditions.....	237
7.2.1	Demagnetization analysis of 6-phase, 18-slot, 8-pole IPM machine	239
7.2.2	Investigation for vulnerability of first pole magnets to demagnetization than other poles	250
7.2.3	Comparison of distributed winding and fractional-slot winding with respect to demagnetization during faults	253
7.2.4	Summary.....	261

7.3	Thermal analyses over the driving cycles	262
7.3.1	Thermal analyses over the driving cycles	263
7.3.2	Summary.....	267
8	Conclusions and Future Scope of Work	268
8.1	Conclusions	268
8.2	Future scope of work.....	272
	References.....	274
	Table of Figures.....	287
	List of Tables	296
	List of Symbols and Acronyms	301
	Appendices.....	311
Appendix A	Winding functions for 3-phase, 9-slot, 8-pole, and 3-phase, 18-slot, 8-/10-pole machine	311
Appendix B	Winding configurations for each of the phase shifts between A-B-C and D-E-F windings of 6-phase, 18-slot, 8-pole Machine	315
Appendix C	Inductance and flux-linkage map of the designed 6-phase, 18-slot, 8-pole IPM machine (or 1 st prototype machine).....	321
Appendix D	Procedures for various preliminary functional tests on the prototype machine.....	324
Appendix E	Comparison of predicted and measured d - and q -axis inductances.....	329
Appendix F	Inductance and flux-linkage map of the 2 nd prototype of 6-phase, 18-slot, 8-pole IPM machine.....	331
Appendix G	Demagnetization characteristics of a typical NdFeB magnet of grade N35EH.....	334

Chapter 1

Introduction to Electric Vehicles

This chapter introduces the global drive towards electric vehicles and their adoption in the transportation sector as the answer to the issue of ever increasing CO₂ and harmful pollutant emissions, and the global warming. The electric vehicles are first classified with respect to architecture of the power drivetrain, and later with respect to size of the car. The recent commercial electric vehicles are listed, which gives an overall idea of the various design requirements and performance expectations by the automotive industries. In the later part, the history of permanent magnet machines is described, followed by the motivation for the thesis and main contributions. The outline of the thesis is presented. Finally, a list of publications by the author during the course of PhD study is reported.

1.1 Electric Vehicles – promising pathway to increased energy security

According to the most recent United Nations estimates, the human population of 7.2 billion in mid-2013 is expected to reach 8.1 billion by 2025, and 9.6 billion by 2050 [1], major part of this growth in the developing countries of Asia and Africa. With ever increasing population in the developing countries, a hunger for better social life will demand for more energy in form of food, coal, oil, etc. The increasing global population translates to increased global energy consumption making energy security a biggest challenge ever faced by mankind in its history.

Over the past two decades, the global energy consumption has increased by 52%. Over the last 10 years, global energy consumption has increased by 30%, almost all of which is outside OECD (Organisation for Economic Co-operation and Development) countries [2], as shown in Figure 1.1. In addition to rapid economic growth in developing countries, rising ownership of vehicles for personal mobility is a key supporting factor for a sharp increase in oil consumption of non-OECD

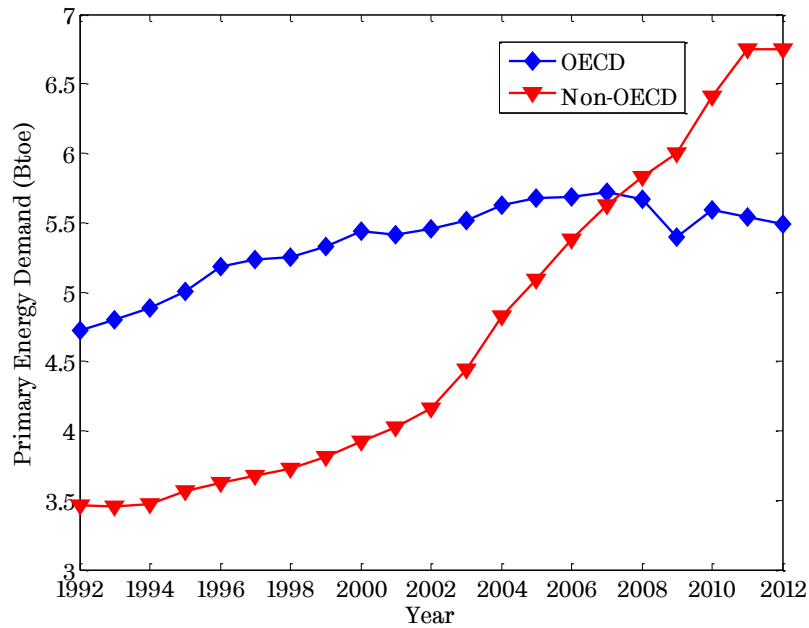


Figure 1.1. Primary energy demand of the world in past two decades²

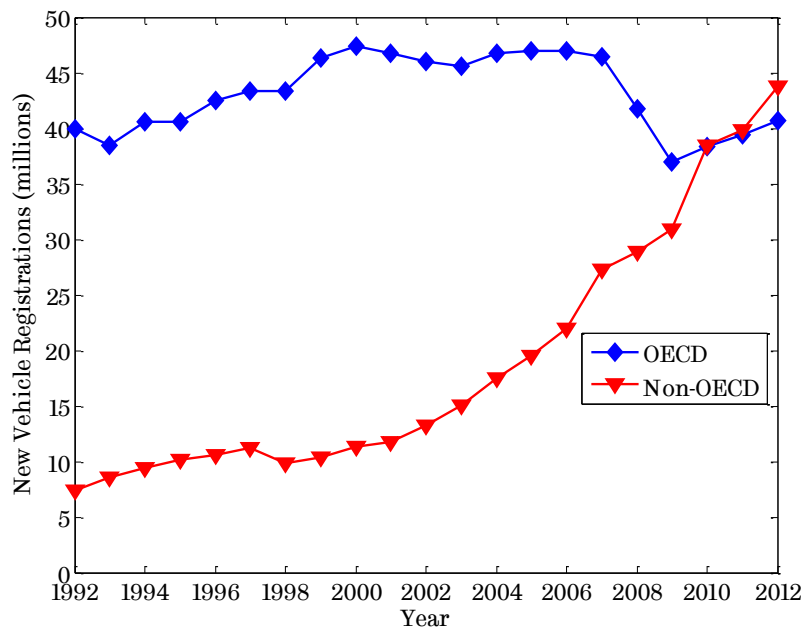


Figure 1.2. New registrations of vehicles in the world²

countries. As seen from Figure 1.2, the emerging economies purchased 16% of the world’s new vehicles in 1992, whereas their share has sharply increased to 52% by

² BP statistical review 2013, <http://www.bp.com/en/global/corporate/about-bp/statistical-review-of-world-energy-2013.html>

2012. The growing demand of internal combustion engine (ICE) based vehicles for personal mobility has posed a serious concern on energy security.

With ever increasing use of ICE for personal mobility, the CO₂ and pollutant emissions impose another serious concern on global warming and environment. As per International Energy Agency (IEA), the global greenhouse-gas emissions are increasing rapidly, and in May 2013, CO₂ levels in the atmosphere exceeded 400 ppm for the first time in several hundred millennia [3].

As countries seek to address future energy requirements in a rapidly growing and changing world, achieving sustainable transportation has emerged as a vital mission. As per IEA's "2DS" scenario (2°C scenario), which aims to develop future energy system that would limit average global temperature increase to 2°C by 2050, the transport industry's potential share of overall CO₂ reduction would be 21%. In order to meet this goal, three-fourths of all vehicles sales by 2050 would need to be plug-in electric vehicles [4]. Electric vehicles (or EVs herein referred) represent one of the most promising pathways to increased energy security and reduced emissions of greenhouse gases and other pollutants, if they can be powered from renewable energy sources.

1.1.1 History of Electric Vehicles

Across all continents of the world, the history of electric vehicles demonstrates the persistent ingenuity of the mankind to adopt the transportation sector for personal mobility to the changing resources, which is distinctively visible from Figure 1.3. The history of the EVs can be seen as the evolution of electric mobility over the time. *The Beginning* of EVs started as early as 1801-1850 by Scottish and American inventors. During *The First Age* (1850-1900), EVs entered the marketplace and found a broad appeal across the world. The EVs reach historical peaks in 1912, later to be replaced by petrol-powered cars, making it *The Boom & the Bust* period from 1901-1950. *The Second Age* of EVs commenced between 1950 and 2000, during which the high oil prices and air pollution renewed the interest in EVs. From 2001, public and private sectors recommitted themselves to research and development in electric mobility, making it *The Third Age* of EVs.

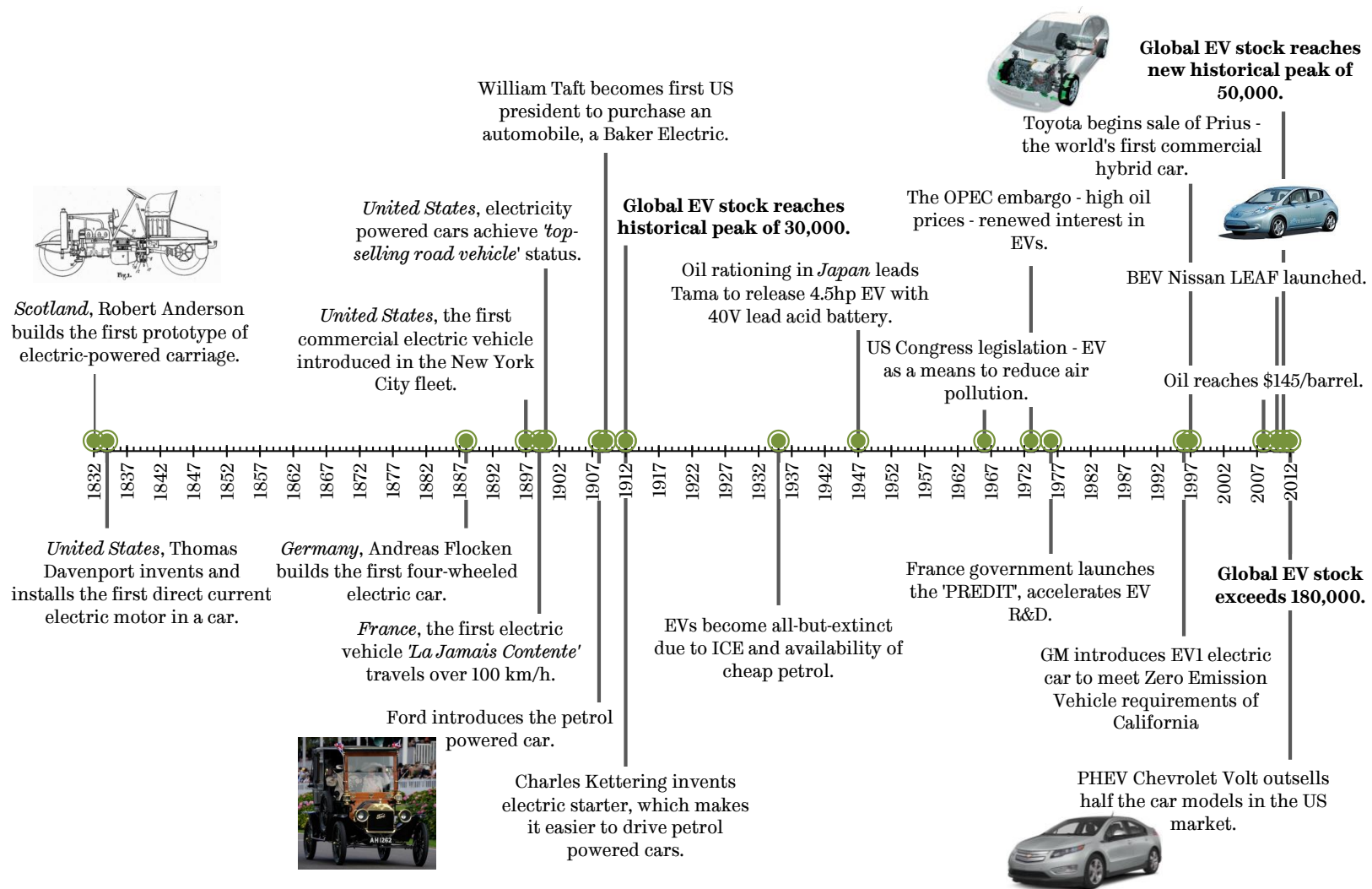


Figure 1.3. Timeline of Electric Vehicles [4-6]

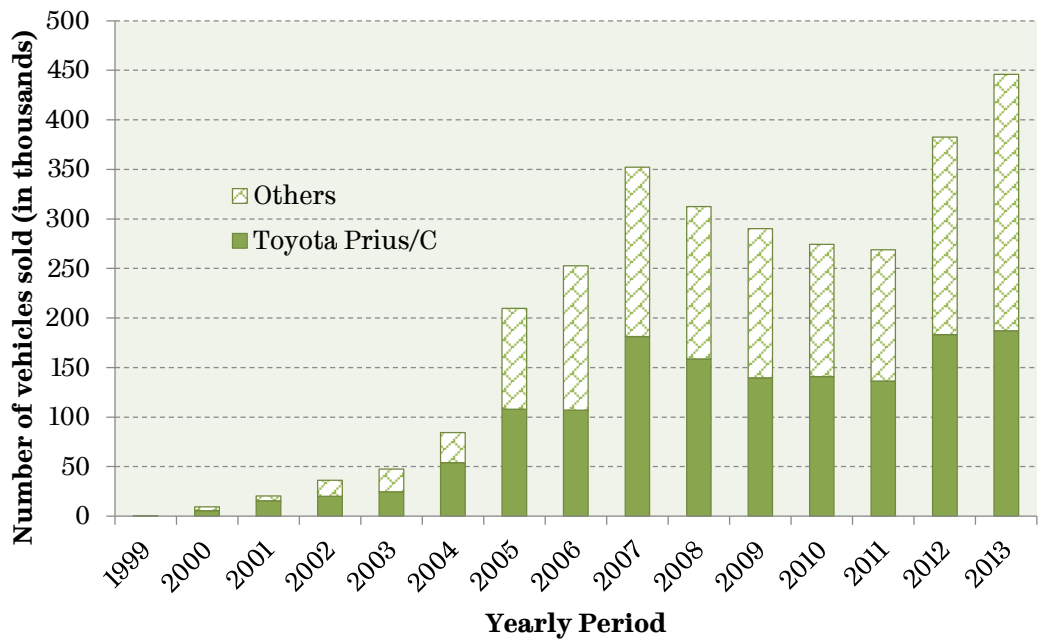


Figure 1.4. Sales of HEV in United States³

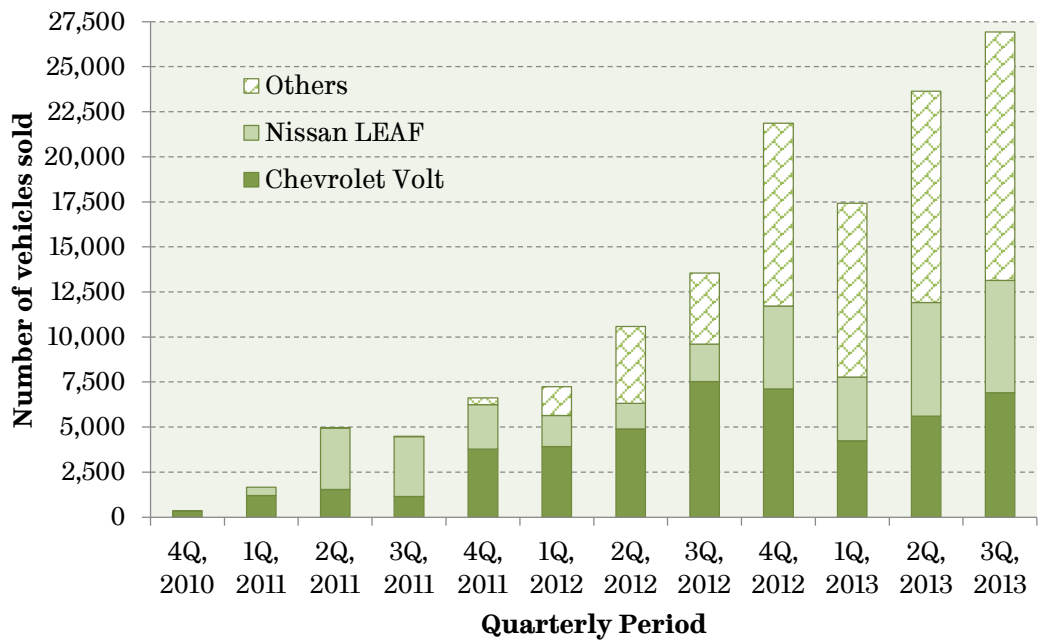


Figure 1.5. Sales of PEV in United States⁴

In recent years, greener and cleaner vehicles are pushed up by various international initiatives such as The Electric Vehicles Initiative (EVI), The

^{3,4} US Dept. of Energy, Alternative Fuels Data Center, <http://www.afdc.energy.gov/data/>

European Union Climate and Energy Package, Energy Security Through Improved Vehicle Fuel Economy of US Energy Independence and Security Act, etc. All initiatives and/or acts are dedicated to accelerating the introduction and adoption of electric vehicles worldwide. For example, the EVI seeks to facilitate the global deployment of at least 20 million passenger car EVs, including plug-in hybrid and fuel cell electric vehicles, by 2020. As per the EVI, the global EV sales in 2012 is more than doubled compared to 2011 [4]. Figure 1.4 and Figure 1.5 shows the sales of hybrid electric vehicles (HEV) and plug-in electric vehicles (PEV) in United States respectively [7]. The HEV sales includes plug-in HEV (PHEV), battery operated electric vehicles (BEV), but do not include neighbourhood or low speed electric vehicles or two-wheeled electric vehicles.

1.1.2 Types of electric vehicles

There are mainly three types of electric vehicles: (1) Hybrid Electric Vehicle (HEV), (2) Plug-in Hybrid Electric Vehicle (PEHV), and (3) Battery operated Electric Vehicle (BEV, which is also referred to EV in the literature).

HEV utilizes propulsion from both ICE and an electric machine. The on-board primary energy source in HEV can be petrol, diesel, natural gas, etc. while the electrical energy is stored in batteries and super capacitors. In addition to primary energy source, PHEV employs rechargeable batteries, which can be charged by connecting a plug to an external electric power source. BEV uses the chemical energy stored in rechargeable battery packs, which is converted to mechanical energy with the use of electric machines and their controllers, to propel the vehicle. The energy for electrical propulsion may also be provided by fuel cells and flywheel energy storage systems.

1.1.3 Merits and challenges of electric vehicles

Electric vehicles have following merits compared to conventional ICE powered vehicles:

1. Economic fuel consumption by (a) optimizing operating point of ICE, and (b) recovering kinetic energy during braking of the vehicle.
2. Overall size reduction of ICE in HEVs.

3. Minimized emissions of harmful pollutants in HEVs, whereas BEVs have zero tail pipe emissions.
4. Quiet operation. For HEVs, the ICE stops at low speed operations and only electric machines are operating. Naturally, the electrical machines are less noisy than the ICE.
5. Lower maintenance as optimized ICE design in HEV results into fewer oil and spark-plug changes, etc. On the other hand, BEVs have almost no maintenance except change of cooling medium, bearings of an electrical machine after their life, etc.

However, there are certain engineering challenges on the design and implementation of EVs as summarized below:

1. High initial cost due to battery, electric machines, and their controllers.
2. Reliability concerns due to increased number of components including additional sensors employed for protection of power drivetrain components.
3. Availability of fast charging stations.
4. Range anxiety in vehicle drivers of BEVs as they're fully dependent on energy stored in the battery packs.

The public-private partnership including government, academia and industry throughout the world are seeking to help technological innovation reach full market potential through research, development, and demonstration by addressing the above challenges.

High initial cost is mainly due to battery cost. However, they're coming down rapidly, more than halving in the past four years [4]. The reliability and safety concerns are greatly improved due to advanced improved controllers for the torque generated by the electric machines. The charging stations are being set-up in the countries having EV presence with different approaches for fast and slow charging. The on-going research and development activities for high energy density battery packs and high power dense electric machines will improve the range of EVs to a great extent from the present values.

1.2 Architectures of electric vehicles

The major challenges, which are being overcome by the automotive industry, are management of battery and multiple energy sources in case of HEVs that are highly dependent on driving cycles and vehicle driver. The electric vehicles are classified by the division of power between multiple energy sources; and, both or more sources may operate in parallel or series or in combination to provide acceleration to the vehicle. One of the sources may act as the primary source for providing the acceleration, whereas the other source/s may be used to augment the first source's power reserve. The architecture of electric vehicles depends on the type of electric vehicles, i.e. HEV or BEV.

1.2.1 Architectures of hybrid electric vehicles

HEVs can be classified based on the architecture of power drivetrain as shown in Figure 1.6: (a) Series, (b) Parallel, and (c) Series-Parallel or Combined. The electrical power transmission is shown in green arrows, whereas blue arrows show the mechanical power transmission.

1.2.1.1 Series hybrid

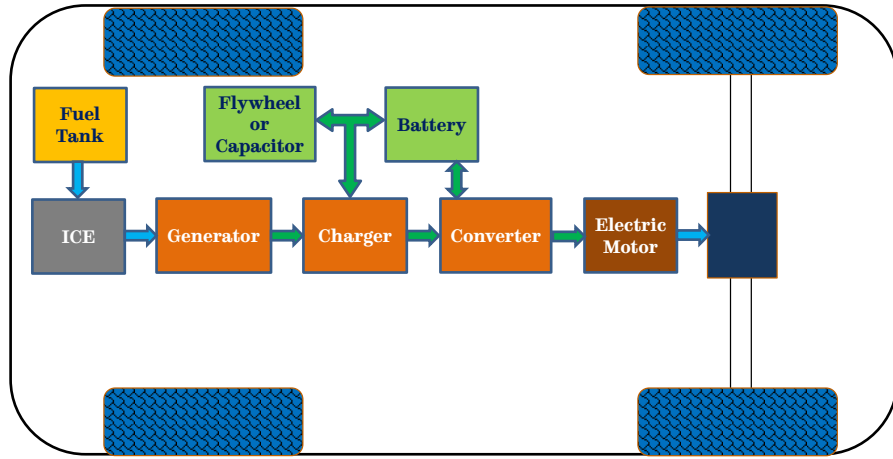
In series architecture of HEV, an ICE via generator produces an electric power to drive an electric motor, which in turn provides the tractive effort to the vehicle. This architecture requires more components and full electrical traction power, making it more expensive.

1.2.1.2 Parallel hybrid

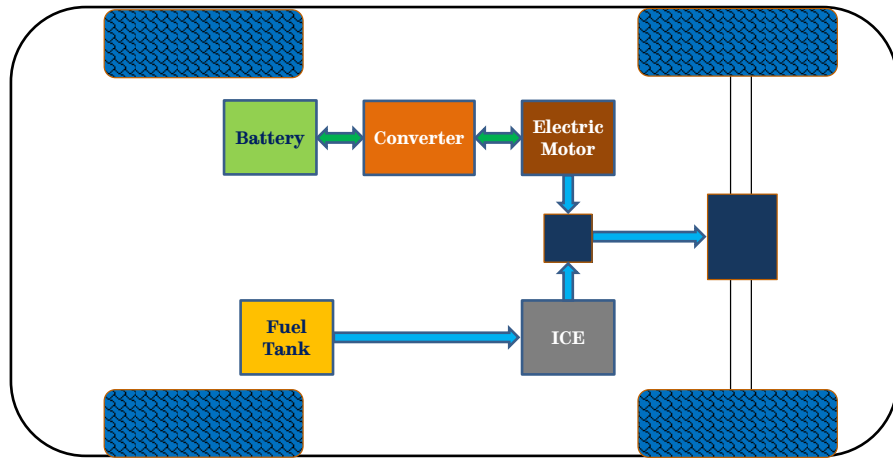
In parallel architecture of HEV, both ICE and electric motor provide the tractive effort to the vehicle. The kinetic energy while braking is used to regenerate electrical energy to charge the battery through motor and converter. This architecture is most commonly used in commercial HEVs of the present day.

1.2.1.3 Series-parallel or combined or power-split hybrid

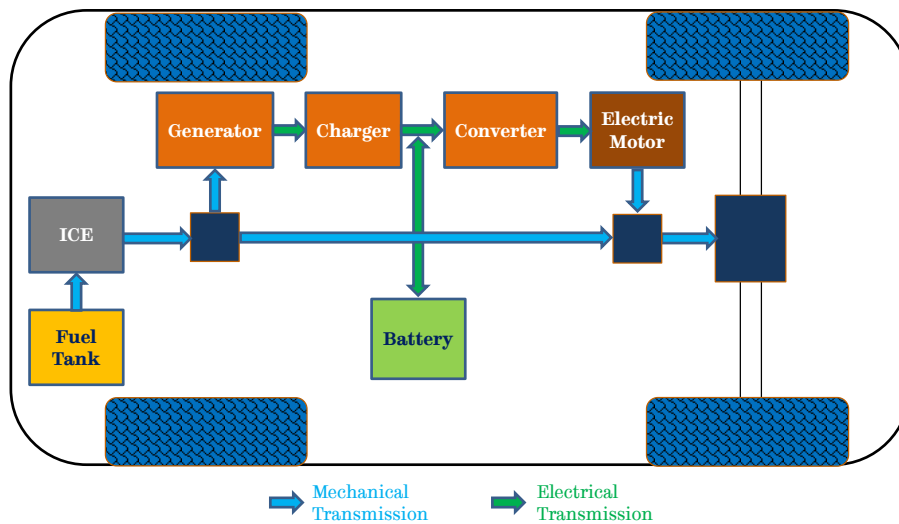
In series-parallel or combined or power-split architecture of HEV, the power is split between ICE and electric motor allowing power flow from the engine to the wheels that can be either mechanical or electrical or combined. However, this



(a) Series architecture of HEV



(b) Parallel architecture of HEV



(c) Series-parallel (or combined) architecture of HEV

Figure 1.6. Architecture of HEVs

flexibility is offset by cost and complexity of power split.

1.2.2 Architectures of battery electric vehicles

Unlike HEVs, BEVs have only one source of tractive effort – an electric motor. A fault in electric drive (motor and/or converter) of BEVs will result in a complete loss of power and may lead to an accident. In order to avoid such dangerous situation while driving, the multiple electric drives in BEVs are favourable as they provide a degree of fault-tolerance. Hence, the BEVs can be mainly classified based on number of electric drives employed for the tractive effort as shown in Figure 1.7 and Figure 1.8.

1.2.2.1 Four power drivetrains

In this architecture, each wheel of the vehicle is being driven by an independent electric motor and the converter. Usually, they share power equally. The use of similar sized motor and converter in this power drivetrain enables easy maintenance, easy replacement and interchangeable parts. However, it adds the complexity of controlling the four wheel drive simultaneously. Many researchers are investigating benefits of using two different type of electric motors that may result into effective lower usage of rare-earth PM, and higher energy efficiency of the vehicle over driving cycles.

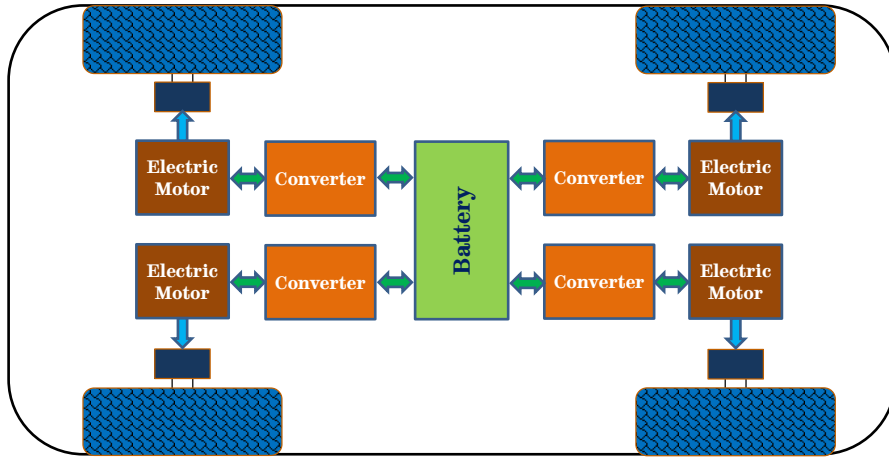
1.2.2.2 Three power drivetrains

In this architecture, usually front wheels are driven by a single drive whereas rear wheels have their own independent drives. Usually in this configuration, 40% power is shared by front wheel drive whereas rear wheel drive share 30% power each.

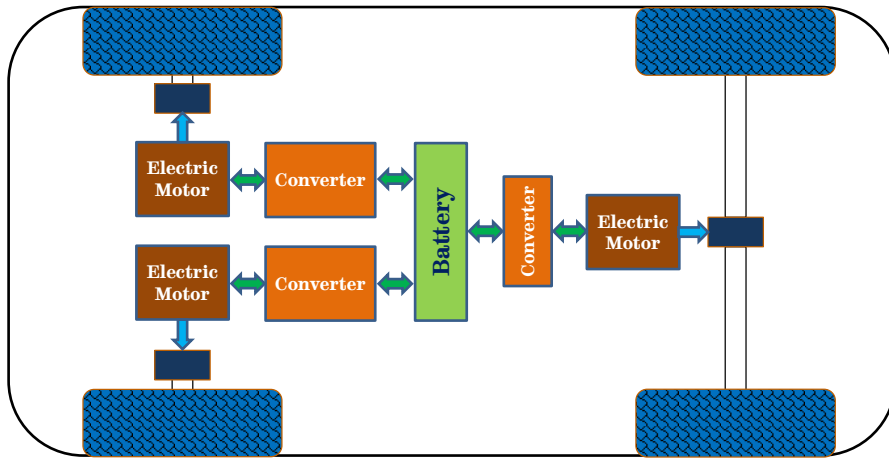
1.2.2.3 Two power drivetrains

Two separate drives are used in this architecture, one each for front and rear wheels. They share the power equally, i.e. 50%.

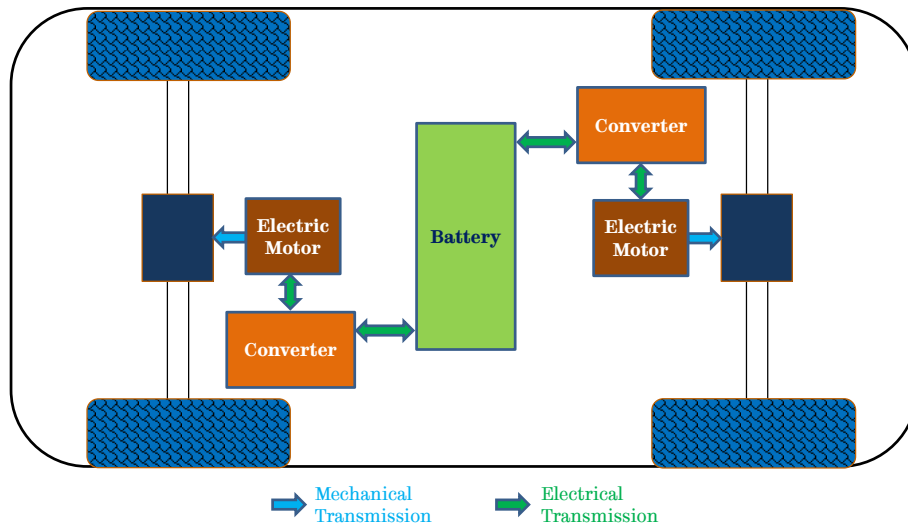
Above all architectures of BEVs are fault-tolerant as they continue to provide the traction power even if one drive fails. However, the implementation of these power drivetrains is always challenging due to larger foot print of the power



(a) Four power drivetrains



(b) Three power drivetrains



→ Mechanical Transmission
 → Electrical Transmission

(c) Two power drivetrains

Figure 1.7. Architecture of BEVs

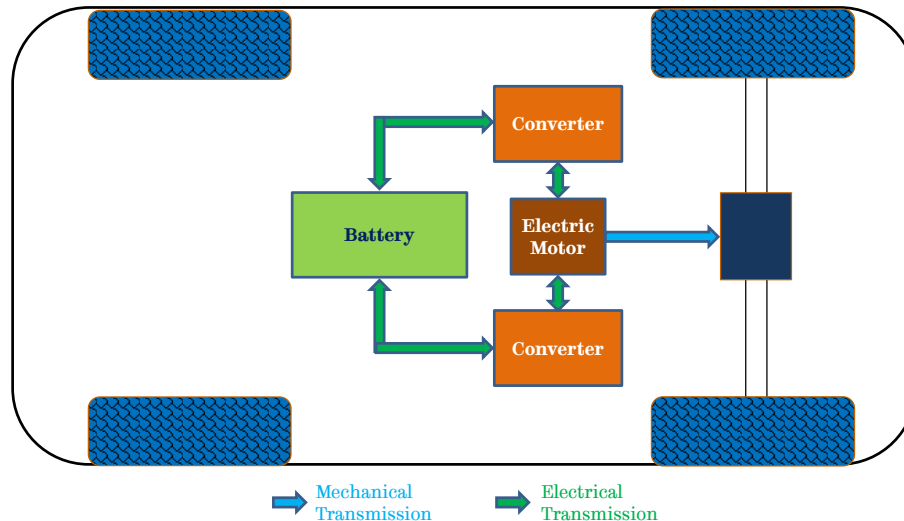


Figure 1.8. Centralized power drivetrain for a small BEV

drivetrain components. For small size vehicles, an alternate solution must be sought which is not only compact, but also fault-tolerant.

1.2.2.4 Centralized power drivetrain for small BEVs

Figure 1.8 shows the centralized power drivetrain for a small BEV having a degree of fault-tolerance. It employs one 6-phase electric motor coupled to the front or the rear axle via a differential and a reduction gearbox. The six phases of the motor are controlled as two separate and independent 3-phase systems, which are fed by two independent inverters. In the event of a fault on one of the drive system, the vehicle can continue to operate using the remaining second set of 3-phase system without any sudden stops or compromising vehicle stability and passenger safety.

1.2.3 Classification of EVs based on the car size

The EVs can generally be classified based on the size of the car. Various governments around the world have established a vehicle classification system for determining tax amount, mainly using curb weight. Other factors such as type of engines, type of fuel, emissions, purpose, etc. are also given the due consideration in the classification [7]. Table 1.1 shows the general classification of the vehicles adopted by the Euro Car Market Segment [8]. The market share is of 2011 car sales in the Europe market [9]. Based on the engine power of the various vehicle segments, nominal power and voltage ratings can be determined for a specific

architecture for EVs. Table 1.2 shows the general classification of EVs based on the power rating of the vehicle.

Table 1.1. Classification of cars [8, 9]

Segment	Class	~ Market Share (%)	Power (kW)
A	Mini cars	8.8	53
B	Small cars	28.2	64
C	Medium cars	30.5	87
D	Large cars	11.6	114
E	Executive cars	3.2	152
F	Luxury cars	0.5	235
S	Sports coupes	1.3	177
M	Multi-purpose	14.6	92-118
J	Sport utility	1.3	177

Table 1.2. Classification of EVs [7]

Class	Power Rating of Motor (kW)	Battery Voltage (V)
Micro	2-3	12-20
Mild	10-35	100-200
Full	40-130	200-350

It is worthwhile to note that power requirements for higher segment vehicles can be met by employing multiple power trains in order to deploy 100% electric traction in them.

1.3 Recent commercial electric vehicles

As seen from Figure 1.4 and Figure 1.5, the sale of EVs has increased exponentially in past 10 years. Various models of cars are being introduced by leading automakers around the world every year. Table 1.3 shows the list of most popular electric cars across the world. It lists power and torque of an electric motor, battery capacity and all-electric range. All-electric range is the driving range of a vehicle using power from its electric battery pack only to traverse a given driving cycle. For BEV, all-electric range means the total range per charge; whereas for HEV, it means the range of the vehicle in charge-depleting mode [10].

Table 1.3. Most popular electric cars across the world

Car Model	Manufacturer	Type	Drivetrain	Curb weight (kg)	Power (kW)	Battery (kW-h)	Range (km)	Release	Top market countries ⁵ as of Sep., 2013
Prius (XW30)	Toyota	PHEV	Power-split	1,420	60	4.4	18-26.4	2012	US, JP, EU, CA
Chevrolet Volt (Opel Ampera)	General Motors	PHEV	Series	1,715	1 x 111, 1 x 55	16 16.5	56-83	2011-12 2013	US, CA, EU, CH AU, NZ
C-Max Hybrid	Ford Motor	HEV	Power-split	1,477 –	35	1.4	-	2012	US
C-Max Energi		PHEV		1,697	68	7.6	34	2012	
Fusion Energi	Ford Motor	PHEV	Power-split	1,690	88	7.6	34	2013	US
Civic Hybrid	Honda	HEV	Parallel	1,294- 1,304	17	20		2011	US, CA, JP, EU, Asia, CH
Nissan Leaf	Nissan	BEV	Front	1,521	80	24	117-175	2011-12	JP, US, EU, CA
Tesla Model S	Tesla Motors	BEV	Rear	2,108	310	60 85	335-375 426-500	2012	US, CA, EU
Mitsubishi i-MiEV	Mitsubishi	BEV	Rear	1,080	47	16	100-160	2009	US, CA, AU, EU, JP, Asia
Smart Fortwo	Smart	BEV	-	730	55	17.6	140	2012	US, CA, EU
Chevrolet Spark	General Motors	BEV	-	1,356	97	21.3	132	2012	US, KO, CA, EU
Renault Zoe	Renault	BEV	-	1,468	65	22	210	2012	EU

⁵ AU-Australia, CA-Canada, CH-China, EU-Europe including UK, JP-Japan, KO-Korea, NZ-New Zealand, US-United States

Automotive industries follow various driving cycles depending on the target marketplace for their EVs. Hence, the range of an EV may not be a fixed value, as it is determined using a specific driving cycle. As seen from Table 1.3, the peak power requirement of an electric motor, to meet the peak torque and acceleration targets set by various automakers, varies widely with respect to the curb weight of the car. The battery capacity also depends on the size of the electric motor, and desired all-electric range of an EV.

Many auto-makers have already announced improved EVs based on the cutting-edge technology in the fields of electric machines, power electronics, and battery storage systems. The new announcements of hybrid, plug-in hybrid, or battery operated electric vehicles in recent past and the near future are listed in Table 1.4.

Table 1.4. New EV announcements in recent past and the near future

Timeline	Car model	Manufacturer	Type	Range (km)
3Q, 2013	McLaren P1	McLaren Automotive	PHEV	20
	BMW i3	BMW AG	PHEV, BEV	130-160, 240-300
	VW e-up	Volkswagen	BEV	160
	VW XLI	Volkswagen	PHEV	50
	BYD Qin	BYD Auto	PHEV	50
	Audi A3 e-tron	Audi	PHEV	50
2014	Rimac Concept One (Sports car)	Rimac	BEV	499
	Porsche 918 (Sports car)	Porsche	PHEV	24
	B-class electric drive	Mercedes	BEV	185
	BMW i8	BMW AG	PHEV	35
	Detroit Electric SP.01	Anderson Electric Car Company	BEV	290
	Tesla Model X	Tesla Motors	BEV	340-430

1.4 Target goals for traction drive in future EVs

The electric vehicles with advanced technologies and reduced cost are the key to meet international energy security goals, and reduction in CO₂ footprint. Achieving these goals will require cutting-edge research and development in the following areas:

- Power electronic devices with wide band-gap
- Advanced motor designs to reduce or to eliminate rare-earth PM
- Novel and compact packaging for battery packs
- Improved heat transfer and thermal management
- Integrated power electronics in vehicle architectures

The EV Everywhere Blueprint [11] of the Department of Energy, US describes the major goals of essentials (electric machines, power electronics, and battery storage) to reach the levels, as shown in Table 1.5, by 2020.

Table 1.5. Target goals for traction drive system in future EVs [11]

	Reduce Cost	Reduce Weight	Reduce Volume	Reduce Energy Storage Requirements
Year	Cost (\$/kW)	Specific Power (kW/kg)	Power Density (kW/l)	Efficiency (%)
2010	19	1.06	2.6	>90
2013	16	1.15	3.1	>91
2015	12	1.2	3.5	>93
2020	8	1.4	4.0	>94

It may be deduced from Table 1.5 that each component of the power drivetrain has to meet its own goals to reduce cost, weight and volume, and has to be more efficient. Hence, power-dense, high efficient electric traction machines pave the way for the development and swift realization of EVs. As of today, in applications requiring low and medium power range, permanent magnet (PM) machines exhibit high torque/power density and energy efficiency. Although the PM machines have gained increased attention of research industries in past two decades, their history

goes back to 19th century.

1.5 History of permanent magnet motors

PM materials were discovered long ago, during the Gregorian calendar BC, but it was not until 1917 when the first artificial permanent magnet was invented by Korato Honda that attracted attention of many researchers around the world to develop various permanent magnets suitable for various industrial applications. This magnet was named KS steel.

In 1930s, Kato and Takei invented the OP magnet, which served as a base for the development of Ferrite magnets in late 1960s. The foundation for the development of Al-Ni-Co magnets were laid by Tokushichi Mishima when he invented MK steel in 1932. The performance of permanent magnets made a big leap forward thanks to the development of rare-earth samarium-cobalt (Sm-Co) magnets in 1968 by the United States Air Force Research Laboratory. The performance of Sm-Co magnets have improved significantly due to contribution made by the Japanese researchers. In 1983, Masato Sagawa invented the neodymium magnet, which is the strongest permanent magnet in the world ever since. Today, permanent magnets in terms of energy product are 60 times as strong as they were about 90 years ago [12].

Although the commercial PM were introduced in 20th century, the earliest inventors of 19th century used PM in their laboratory devices, which they termed as electrical rotating machines, later called as electric motors. Based on ideas from Hans Christian Oersted and William Wollaston, Michael Faraday built a device that used both fixed and rotating permanent magnets with wires attached to bowls of mercury and a battery. When a battery was connected to the wires, current flowed in the circuit and the generated electromagnetic field interacted with the permanent magnets to produce torque and hence, mechanical rotation. Many other inventors quickly followed Faraday's motor with improvements, which include J. Henry (1831), H. Pixii (1832), W. Ritchie (1833), F. Watkins (1835), etc. In 1837, Thomas Davenport was granted the first patent for an electric motor.

All these motors had very limited scope for practical or industrial applications because of very poor quality of hard magnetic materials [13]. This made inventors to use alternate source of excitation using electromagnets in the electric motors in the late 19th and early 20th century. Nikola Tesla's electromagnetic AC motor in 1889 fundamentally changed the popularity of direct current as the primary source of power. With only two parts in an electric motor, a stationary part known as stator, and a rotating part known as rotor, the AC motors were much simpler than electromagnetic DC motors. DC motors made their presence felt in industrial applications for many decades because of their ease of controllability and operability compared to AC motors, despite the simplicity offered by AC motors. The return of PM motors was almost inevitable in mid-20th century as the development of high energy PM had already begun.

In 1950s, the use of ferrite magnets in the electric motors for small appliances was first reported. It was not until 1970s that brushless PM DC motors started appearing in the market. The delay was due to (a) the development of high energy PM, and (b) the development of power electronic devices and controllers [14]. The continuous improvement in energy products of rare-earth magnets along with the advancement in power electronic devices and controllers have made the use of PM brushless motors more attractive and viable compared to conventional motors like induction motors, etc.

At present, in the low and medium power rating, the PM brushless motors exhibit higher performance in terms of torque/power density, energy efficiency, and dynamic response. As a result, the PM brushless motors have been increasingly used in a variety of applications ranging from high speed manufacturing, electric and hybrid vehicle traction, ship propulsion, aerospace actuation to wind power generation.

1.6 Motivation for the doctoral research work

The growing demand for internal combustion engine (ICE) based vehicles for personal mobility has led to significant increase in crude oil consumption resulting in to concern on energy security and global warming. To address these concerns, the only way forward is to employ electric vehicles at large in personal

mobility as they are less dependent on crude oil and have zero propulsion emissions. In recent past, the automotive industries, driven by low carbon emission legislations, are also advancing rapidly to commercialize fully electric vehicles (EV).

Recent developments in EVs have revolved around fault tolerant motor drives employing permanent magnet machines. This increased attention is due to the emphasis on passenger comfort and safety by the automotive industry around the world. Although fully electric vehicles are hailed as fuel economic and low- or no-emissions, their ability to tolerate fault is very critical as a fault in the electric drive will result in a complete loss of power and may lead to an accident. Due to their high torque/power density and higher efficiency compared to other machine technologies, permanent magnet (PM) brushless machines are preferred technology in traction applications, provided they could continue to operate following isolated failures in power drivetrain [15].

For traction applications, it is an attractive option to employ relatively newer winding configurations of PM brushless machines often referred to as "*fractional-slot concentrated winding*" or "*modular winding*" [16, 17], because of their numerous advantages over the overlapped distributed windings in the conventional brushless AC machines.

In the field of electric traction applications involving permanent magnet machines, several topics are being researched by the research community internationally.

The aim of this doctoral research work is to develop novel machine topology that has high efficiency over wide operating speed range and also has a degree of fault-tolerance. The objectives of the research work can be summarized as below:

1. To develop novel fractional-slot winding configuration for PM synchronous machines, having low space harmonics content in the stator magneto-motive-force (MMF).
2. To investigate the arrangement of 6-phase winding configuration as dual 3-phase windings in order to provide fault-tolerant capability,

and to evaluate how the d -axis inductance influence the efficiency over the wide operating speed range.

3. To design and optimize the machine geometry with the proposed winding configuration against a given set of specifications under electrical, thermal and volumetric constraints.
4. To underpin the research by extensive simulation studies using 2-D finite element analysis (FEA) tools and to validate them by a series of experimental measurements on a prototype machine.
5. To investigate other important design aspects of PM machine having the proposed winding configuration, which include demagnetization assessment, thermal analyses over various driving cycles, and evaluation of unbalanced magnetic pull.

The doctoral research work has been accomplished at the Electrical Machines & Drives Group within the Department of Electronic & Electrical Engineering of The University of Sheffield. The research work was sponsored by the European Commission for **CAr Multi PropulSion InTegrated POver TRain** (CASTOR) project under European Green Vehicles Initiative (EGVI) through grant no. 260176.

1.7 Main contributions of the thesis

The main contributions of this thesis in the field of multi-phase fractional-slot PM synchronous machines for EV application are as below.

1. Novel fractional-slot per pole per phase winding configuration with low space harmonics content, which is applicable to not only PM brushless synchronous machines (PMSM), but also to PM assisted Synchronous Reluctance Machines, Synchronous Reluctance Machines, Induction Machines, and Synchronous Wound-field Machines with benefits of low copper loss and high torque density.
2. Ability to configure the proposed winding configuration using multiple 3-phase systems, which brings a degree of fault-tolerance.

3. A comprehensive design procedure for PMSM targeted for electric vehicle applications under electrical, thermal and volumetric constraints.
4. Effect of phase shifts between two sets of 3-phase windings on machine performance indicators, viz. eddy current loss in PM, unbalanced magnetic pull, etc.
5. Comprehensive demagnetization assessment of PMSM with fractional-slot winding configuration.

1.8 Outline of the thesis

The thesis is organized in 8 chapters. The brief summary of each chapter is presented below:

This Chapter introduced the global drive towards electric vehicle and their adoption in the transportation sector as the answer to the issue of ever increasing harmful pollutant emissions and the global warming. The electric vehicles are classified with respect to architecture of the power drivetrain. The recent commercial examples of electric vehicles are presented, which gives an overall idea of the various design requirements and performance expectations by the automotive industries.

Various electrical machine technologies and their topologies for electric vehicle applications are illustrated in **Chapter 2**. First, the key design requirements for an electric traction motor are discussed. Then, a comprehensive literature survey on electrical machine technologies and their comparison is presented, which is followed by the selection of most promising advanced machine technologies for electric vehicle application.

The most promising machine technologies are assessed for their suitability for a 10kW (peak) traction drive for a micro size electric vehicle with a distributed power train in **Chapter 3**. The design for each machine technology is optimized using 2-D finite element analysis (FEA) under the same electrical, thermal and volumetric constraints and the key limitations are highlighted by comparing their

performance at the rated and the peak torque operation as well as over the driving cycle against one another.

Chapter 4 introduces fractional-slot per pole per phase winding configurations for permanent magnet machines. The development of novel fractional-slot per pole per phase winding configuration having low space harmonic contents is presented. This winding configuration is applied to a segment-A vehicle with centralized power drivetrain to design multi-phase electric motor, which enhances the availability of the power drivetrain. The optimum phase shifts between two sets of 3-phase systems is also evaluated.

The design and analysis of 6-phase fractional-slot PM machine for segment-A EV is presented in **Chapter 5**. The geometrical parameters of the motor are optimized against the design specifications and the thermal constraints to maximize energy efficiency over the New European Driving Cycle (NEDC) using the finite element analysis (FE) based design technique.

Chapter 6 presents the prototyping of the optimized design. Various design analysis and performance prediction models are validated using a series of experiments on the prototype machine. Investigation of partial demagnetization of the prototype motor along with the adopted preventive measures is described. Finally, the comparison of two prototype motors with different magnet and rotor steel material is presented, which is followed by the experimental validation of 2nd prototype motor.

Various important design aspects of the developed fractional-slot per pole per phase winding configuration with 18-slot, 8-pole topology for EV applications are illustrated in **Chapter 7**, which includes (a) effect of phase shifts between two sets of 3-phase windings on eddy current loss in PM and unbalanced magnetic pull of this novel winding configuration, (b) demagnetization assessment of fractional-slot per pole per phase winding PM machines, and (c) thermal analyses of the motor over driving cycles.

Chapter 8 concludes the research work on the novel 6-phase fractional-slot per pole per phase PM machine, which is followed by the future scope of work on PM machines having similar winding configurations for various applications.

1.9 List of publications

Several parts of the research work reported in this thesis have been presented by the author in international conferences and journals during the course of his doctoral research. The various publications are listed as below. The patent application is preceded by **P**. The conference and journal papers are preceded by **C** and **J** respectively. The research work disseminated in various platforms through presentations is preceded by **PR**.

- P** J. Wang, "An Electric Machine", *UK Patent*, Application no. GB1221635.4, filed on 30th Nov. 2012.
- C1** **V. I. Patel**, J. Wang, W. Wang, and X. Chen, "Analysis and design of 6-phase fractional-slot per pole per phase permanent magnet machines with low space harmonics," in *IEEE International Electric Machines & Drives Conference (IEMDC)*, pp. 386-393, 12-15 May 2013.
- C2** **V. I. Patel**, and J. Wang, "Assessment of 12-slot, 14-pole permanent magnet flux switching machine with hybrid excitation for electric vehicle application," in *IEEE International Energy Conversion and Congress Expo (ECCE)*, pp. 5092-5099, 15-19 Sep. 2013.
- PR1** **V. I. Patel**, J. Wang, C. Gould, D. T. Nugraha, R. Vuletic, J. Tousen, and J. Klenner, "6-phase fault-tolerant permanent magnet traction drive for electric vehicles", *European Conference on Nanoelectronics and Embedded Systems for Electric Mobility*, 25-26 Sept. 2013, Toulouse, France, 2013 [18].
- J1** J. Wang, **V. I. Patel**, and W. Wang, "Fractional-slot permanent magnet brushless machines with low space harmonic contents," in *IEEE Transactions on Magnetics*, vol. 50, no. 1, pp. 1-9, Jan. 2014.
- C3** **V. I. Patel**, and J. Wang, "Demagnetization assessment of 6-phase fractional-slot per pole per phase permanent magnet machines with low space harmonics for various fault conditions at different speeds," accepted for publication in *IET International Power Electronics, Machines and Drives Conference (PEMD)*, 8-10 Apr. 2014.

- C4** V. I. Patel, J. Wang, W. Wang, and X. Chen, "Thermal design and analysis of 6-phase fractional-slot permanent magnet machines considering driving cycles," accepted for publication in *IET International Power Electronics, Machines and Drives Conference (PEMD)*, 8-10 Apr. 2014.
- C5** V. I. Patel, and J. Wang, "Effect of phase shifts on PM eddy current loss and unbalanced magnetic force in 6-phase fractional-slot PM machines with low space harmonics content," in *IEEE International Magnetics Conference (INTERMAG)*, pp. 3079-3080, 4-8 May 2014.
- J2** V. I. Patel, J. Wang, W. Wang, and X. Chen, "6-phase fractional-slot per pole per phase permanent magnet machines with low space harmonics for electric vehicle application," in *IEEE Transactions on Industry Applications*, Accepted for publication in future issue of the journal, vol. 50, no. 5, Sep-Oct. 2014.

The following research publications are under preparation by the author.

- J3** V. I. Patel, and J. Wang, "Effect of phase shifts on PM eddy current loss and unbalanced magnetic force in 6-phase fractional-slot PM machines with low space harmonics content," planned to submit to, *IEEE Transactions on Magnetics*.
- J4** V. I. Patel, J. Wang, and S. S. Nair, "Comparison of demagnetization assessment between fractional-slot and distributed wound 6-phase permanent magnet machines," planned to submit to, *IEEE Transactions on Magnetics*.
- J5** V. I. Patel, J. Wang, D. T. Nugraha, R. Vuletic, and J. Tousen, "Multi-phase permanent magnet machine drive for electric vehicle traction," planned to submit to special issue of, *IEEE Transactions on Industrial Electronics*.

Chapter 2

Electrical Machine Technologies and Topologies for EV

In this chapter, key requirements for an EV traction machine are discussed. Various electrical machine technologies and topologies are assessed and compared qualitatively for electric vehicle application through a comprehensive literature survey, which is followed by the selection of most promising machine technologies for preliminary design study targeting micro-sized electric vehicle.

2.1 Basic requirements for an electrical machine for EV

Electrical machines and power electronic drives are essential for any EV. The basic characteristics required from an electrical machine for traction applications are [19-21]:

1. High torque and power density (typically >20 N·m/kg peak, >10 N·m/kg continuous, > 5 kW/kg continuous)
2. High starting torque at low speed
3. Sufficient peak torque capability to meet vehicle acceleration for drive away and climbing up the slope
4. High efficiency over wide speed and torque range (typically $> 94\%$)
5. Wide speed range with constant power operation up to 3 to 4 times the base speed
6. Acceptable torque ripple (typically $\leq 5\%$)
7. High reliability
8. A degree of fault-tolerance
9. Flexibility of control
10. Manufacturability and maturity

Figure 2.1 shows the typical torque-speed characteristics for an EV traction motor. It has three distinct region based on power delivered by the traction motor: (a) constant torque region, (b) constant power region, and (c) reducing power region. In constant torque region, the maximum torque capability is determined by the requirement for peak acceleration and slope-climbing but also limited by the peak current rating of the inverter which controls the motor. In constant power region, the maximum power is specified by the requirement at top speed of the vehicle, i.e. cruise speed. For PMSM and induction machine drives, flux weakening control is often employed because of limit on voltage and current rating of the inverter. In reducing power region, with increasing speed, both torque and power have to be reduced due to increase in back EMF of the motor.

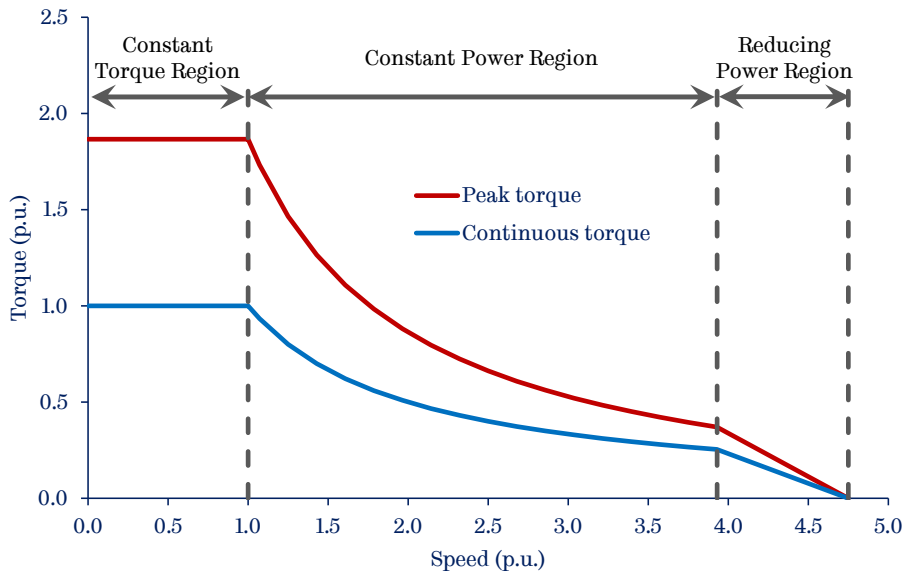


Figure 2.1. Typical torque-speed characteristics of EV traction motor

With reference to the above characteristics and requirements, comparative studies of various electrical machine technologies and topologies are undertaken by the author in his research work. First, comparison of conventional machine technologies and/or topologies is presented. Then, state-of-the-art technologies for EV are described. Based on the detail design comparison of promising machine technologies, the best candidates have been selected for the preliminary design study for micro-sized EV application.

2.2 Conventional machine technologies

The conventional machine technologies for EV traction include five major types, namely (1) DC machines – DCM, (2) Induction machines – IM, (3) Switched reluctance machines – SRM, (4) Permanent magnet machines – PM machines, and (5) Synchronous wound field machines – SM, as illustrated in Figure 2.2. The stator and rotor laminations are shown in grey and dark grey respectively, whereas the armature and field windings are shown in coral and chartreuse respectively. The permanent magnets are shown in red and blue for north and south polarity respectively.

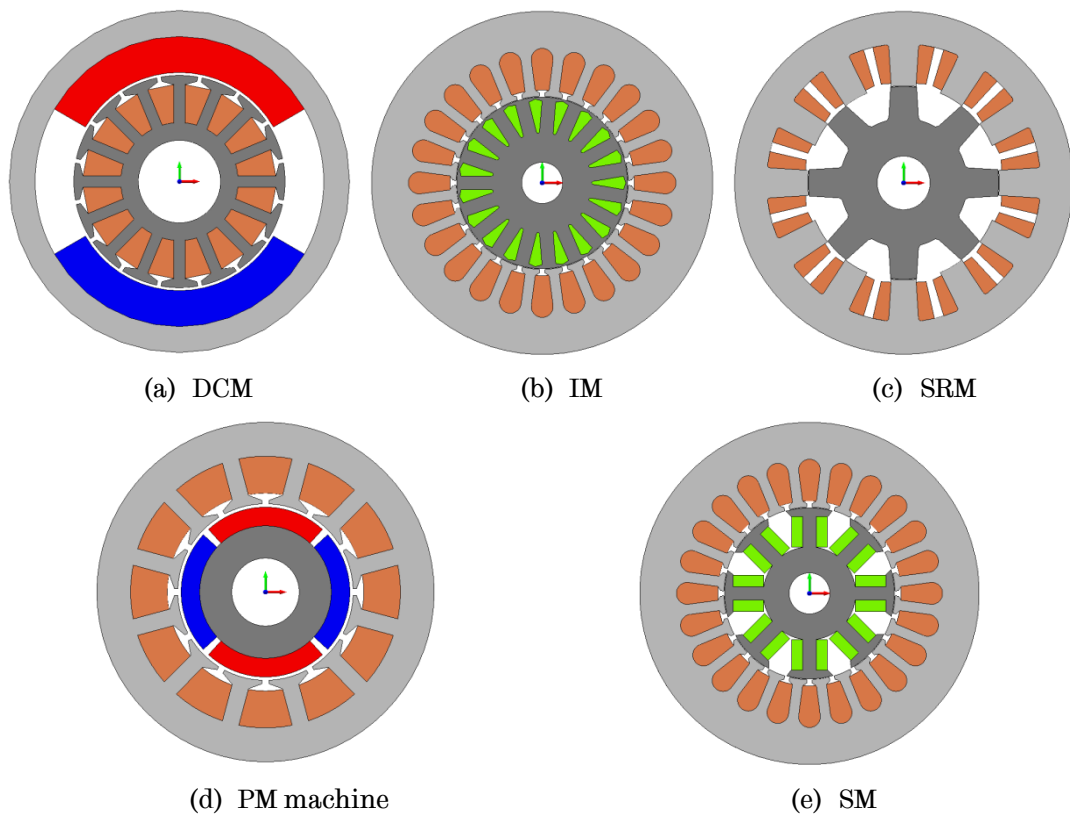


Figure 2.2. Cross-section of conventional electrical machine technologies

2.2.1 DC machines (DCM)

The brushed direct current electrical machine generates torque directly from DC power supplied to the motor by using a mechanical commutator, stationary electromagnets or permanent magnets, and rotating electromagnetic armature.

The advantages of DCM include low initial cost, technology maturity, high reliability, simple speed-control of motor, good speed regulation, and frequent starting, braking and reversing.

The disadvantages of DCM are high maintenance and low life-span for high intensity use due to presence of commutator and brushes. Also, winding excited DC machines have low power density.

2.2.2 Induction machines (IM)

The induction machines are widely used in industrial drives as they are robust, have no friction caused by brushes, and can have the easy speed-control due to advances in power electronic devices. There are two type of IM, namely, wound rotor and squirrel cage, where later is the most common type in which aluminium or copper bars are cast into slots in the outer periphery of the rotor.

The advantages of IM include robust structure, light weight, small volume, high efficiency, low cost, and well established manufacturing techniques. Good dynamic torque control can be achieved by either vector control or direct torque control. For IM, the constant power range typically extends to 2 to 3 times the base speed. However, for EV traction, this shall be extended to 4 to 5 times the base speed, which calls for complicated design. Also, the control schemes are more complex due to variable motor parameters.

Distributed overlapping windings are employed in IM where coils belong to each phase are often separated by insulation materials. Thus failures in one phase coil, e.g., a short circuit, are likely to propagate to other phases due to the extra heat being generated. On the other hand, an open circuit failure gives rise to unbalanced magnetic field in the air-gap, which in turn induces extra loss in the rotor conducting bars. Thus, the conventional induction machines are not fault tolerant.

Recently, fractional-slot wound IM are reported in the literature [22], [23] with wound rotor configuration to reduce stator magneto-motive-force (MMF) harmonics and to improve the torque ripple. The comparison between distributed wound and fractional-slot wound IM with a squirrel cage rotor is presented in [24],

which concludes that distributed wound IM outperforms fractional-slot IM mainly due to MMF harmonics.

2.2.3 Switched reluctance machines (SRM)

SRM are usually operated in discontinuous current mode, although continuous current operation may be advantageous under reduced power range operation of EV traction at high speed.

The main advantages of SRM include simple and robust structure without magnets or windings on the rotor making it suitable for high speed and high temperature operation, low cost, and inherent fault tolerance capability. Further, phase coils in SRM are wrapped around a single tooth and are not directly in contact with other phase coils. Thus, a failure in one coil can be isolated and a multi-phase SRM can continue to produce torque at reduced amount in the event of a single phase failure.

The key disadvantages are high torque ripple, vibration, noise due to sequential excitation of coils, requires complex profiling of phase current waveforms and accurate rotor position, and highly saturated magnetic circuit. The torque capability of SRM is often an issue of concern.

2.2.4 Permanent magnet (PM) machines

Conventional PM machines are brushless machines that include sinusoidal and trapezoidal back EMF machines, also known as brushless AC (BLAC) and brushless DC (BLDC) respectively. BLDC have surface mounted PM on the rotor, and a concentrated fractional-slot winding resulting into low copper losses. In BLAC, the stator slots or rotor magnets may be skewed, and PM could be appropriately shaped or magnetized.

In PM machines, the magnetic field, which is essential for electromechanical energy conversion, is provided by the permanent magnets without extra electrical power input or loss of energy. With high energy-product rare earth magnets, such as NdFeB, the magnetic field in a PM machine can be established with relatively small amount of magnets. Thus, PM machines not only have high power density and high efficiency, but also are compact and light weight.

These properties are particularly attractive for applications which require high efficiency and light weight, such as EV traction.

The disadvantages of PM machines are narrow range of constant power operation due to difficulty in weakening the air gap flux, relatively high cost due to rare earth PM, and risk of demagnetization.

For PM machines with distributed windings, their fault-tolerant property is similar to IM. However, by employing concentrated winding configuration, it is possible to design a PM machine in which each phase is physically, electrically, and thermally isolated improving fault tolerant capability significantly.

2.2.5 Synchronous wound field machines (SM)

Synchronous wound field machines have field coils on rotor. The power is supplied through slip-rings and brushes to energize the coils which in turn produces the magnetic field for electromechanical energy conversion. For SM in a few kilowatts to a few tens of kilowatts range, the available volume for field coils is limited and hence they are less volumetric efficient. Further, energizing the field coils incurs additional copper loss and reduces their efficiency. The presence of slip-rings and brushes, and their maintenance are additional issues of concern for high speed operation, and compromises the reliability. Very little literature exists about the use of conventional synchronous wound field machines for EV traction, although this machine technology has been employed in commercial EVs such as Renault ZOE, etc.

The advantages of SM are, however, a wider range for constant power operation for EV traction, and freedom in adjusting the field coil excitation to achieve high efficiency over a wide operating speed range.

2.2.6 Comparison of conventional machine technologies

There are quite a few research papers on comparison of various machine technologies and their topologies for electrical vehicles in general.

Neudorfer *et al.* [25] reports that maximum efficiency of induction machine, permanent magnet synchronous machine, and switched reluctance machines

differs from 90% to 93%, but these values are at different operational area of torque-speed characteristics. SRM has higher torque density compared to PM and IM. However, power density is slightly high in PM compared to SRM and considerably higher compared to IM. The paper also compares IM, PM, and SRM technologies for fuel consumption for HEV. However, other criteria such as torque ripple, manufacturing and maintenance cost of the vehicle power train, complexity of control, and easy integration of power electronics are not taken into account. Also, these designs are not optimized for increased torque and power density to reduce size and mass. The above reported results are also compared to those reported in [26] for electric go-kart application.

Table 2.1 summarizes the performance comparison of IM, PM and SRM as reported in [25].

Table 2.1. Performance comparison of IM, PM and SRM [25]

Performance Attribute	Unit	IM	PM	SRM
Torque density	Nm/l	11.4	11.9	17.1 ⁶
Power density	kW/l	3.9	4.4	4.3
Efficiency	%	90.1	92.7	92.5
Max. efficiency region (Speed – N , Torque – T)	-	Med. N Low T	Base N Rated T	High N Low T
Active mass	kg	28.7	28.9	25.7
Total mass	kg	39	41	38

The main conclusions drawn from various research papers [21, 27-29] are as below:

1. Induction machine and PM brushless machine drives are the most widely used in EV.
2. Induction machine drives are the best in terms of cost compared to PM, SRM, and DCM drives.
3. PM brushless machine drives are the most efficient compared to IM, SRM, DCM, and SM drives.

⁶ SRM torque density is higher but it is unable to provide peak power requirement at the base speed. One can say that SRM torque density is almost same as PM for the same peak power requirement at the base speed, as seen from Figure 3 of [25].

4. DC machine drives enjoy benefit of most mature technology. This may also apply to IM drives as they're also in existence since many years.
5. IM drives and SRM drives are the most reliable technologies and require least maintenance compared to other conventional motor drives.
6. SRM drives have worst torque ripple even after employing various design and/or control strategies for torque ripple reduction.

Based on the understanding of their operating principles, issues, advantages, and published literature, the author has compared the conventional machine technologies qualitatively using figure of merit (FoM) from 1 to 10, 10 being the best, and 1 being the worst, against each requirement for EV listed in section 2.1. The comparison is presented in Table 2.2

Table 2.2. Qualitative comparison of conventional machine technologies

Performance Attribute	DCM	IM	SRM	PM	SM
Torque/power density	5	7	8	10	8
Torque ripple	10	9	4	8	8
Efficiency	6	7	8	10	8
Cost	7	10	7	6	8
Sub-total FoM	28	33	27	34	32
High speed operability	7	8	10	7	8
Fault tolerance	6	6	10	8	7
Controllability	10	7	7	8	8
Reliability	5	10	10	8	7
Maturity	10	10	7	8	10
Manufacturability	8	9	10	7	8
Total FoM	79	90	88	90	88

As seen from the above table, PM machines and induction machines are more competitive for EV compared to other conventional machine technologies. Also, SRM and SM compete closely with IM and PM machines considering the total qualitative figure of merit. However, SRM have very low score for torque ripple, relatively low power density compared to PM machines. For an example, if one has to consider most important performance attribute (torque/power density, torque

ripple, efficiency, and cost), then competitive score of IM, SRM, PM, and SM is shown as sub-total FoM in Table 2.2.

It is evident that PM machines and induction machines are competitive for these four requirements. For induction machines, the key benefit is low cost, but its power density and efficiency are relatively low; whereas PM machines have high power density and efficiency, but the cost is high, particularly with the dramatic increase in rare earth magnets in recent past, however, the price is declining in the present time. Hence, it is advisable that one shall look into the comparative figure of merit for most important requirements based on application and chose the machine technology accordingly.

For most EV power trains, acceptable torque ripple is below 5% of peak torque. This requirement is beyond the achievable value of the current state-of-the-art technology for SRM.

2.3 State-of-the-art technologies for EV

Most of the series production models include Toyota Prius, Chevrolet Volt (Opel Ampera), Nissan Leaf, Tesla Model S, Mitsubishi i-MiEV, Honda Civic Hybrid, and Renault ZOE as listed in Table 1.3. All of these models employ either induction machine, or PM machine or synchronous would field machines as their drive machine technology with either rear wheel or front wheel drive and/or series or parallel or power-split configuration [30-35].

2.3.1 Multi-phase induction machines

As discussed before, conventional induction machines have very limited fault tolerance and lower efficiency compared to PM machines. In order to compensate for these demerits, multi-phase induction motors have become popular in research community in the past decade. This has predominantly resulted from the recent developments in electric ship propulsion, traction, and the concept of 'more-electric' aircraft [36]. The advantages of multi-phase induction machines are:

1. The stator excitation in a multi-phase induction machine produces a field with a lower space harmonic content, which makes it more efficient than a 3-phase machine.
2. Multi-phase machine has a greater fault tolerance capability than a 3-phase machine during open circuit.
3. Time harmonic components in excitation waveform create fewer problems in multi-phase machine than in a 3-phase machine. These components produce pulsating torques at even multiples of fundamental frequency of excitation.

Increasing number of phases to 6 from 3 reduces stator joule losses by 6.7% whereas 15 phase machine has 8.5% reduction in stator joule losses [36, 37]. Also, there are various strategies available to control output power and loss during open-circuit fault conditions for multi-phase machine by controlling current in each non-faulty phase [36]. The implementation of these strategies might be problematic considering the rating of the power electronic devices and limitation of DC link voltage. Vector control and direct torque control can be employed in multi-phase induction machine to control variable speed. Advances in drives make it possible to use 5-phase induction machines, and asymmetric 6-phase induction machines.

A. Matyas *et al.* [38] reported the design comparison between 6-phase IM and PMSM for electrical power steering (EPS) application. For the same value of stator current, 6-phase PMSM produces 10% higher torque compared to 6-phase IM. However, EPS application requires much low torque compared to EV traction.

D. G. Dorrel *et al.* [39] analysed electrical machine employed in the 2004 Toyota Prius to assess its characteristics, which is a fluid cooled interior mounted permanent magnet machine (IPM). They have produced an alternative induction machine design that is operationally close to that of the current PM motor design and is also cheaper to build due to absence of PM. The efficiency of the IM design is 7.5% lower than that of PM machine at the rated torque and speed.

The latest advancements in the field of induction machine design suggest that IM will continue to be considered while designing an electric vehicle power drivetrain.

2.3.2 Switched reluctance machines

Switched reluctance machines employ simple and robust rotor structure without magnets or windings that makes them suitable for high speed and high temperature operation. They are of low cost, and inherent fault tolerant. However, large torque ripple, typically around 20% of the peak torque, is a key limiting factor for their application in EV. Various strategies using design and/or control are reported in current state-of-the-art for reducing the torque ripple in SRM.

With respect to design of SRM, optimized pole tip shape reduces torque ripple by 24.1% in short-pitched wound SRM and by 22.6% in full-pitched wound SRM. Average torque output at low and medium current level also increases with this design technique [40]. Also, a segment type SRM with 2-steps slide rotor is reported to reduce torque ripple by 19%, although with compromise on average torque, which is reduced by 10% [41].

With respect to control, fuzzy logic control for current waveform and fuzzy logic rules for noise and torque ripple reduction using piece-wise linear torque characteristics approach is reported to reduce torque ripple to 38% from 57% in [42]. Direct torque control of SRM has reported torque ripple reduction to 10% from 71.4% [43]. SRM drive circuit with boost capacitors in parallel to stator windings to generate desirable current waveform has reported torque ripple reduction by 14% compared to conventional drive with voltage control, whereas 34.6% reduction compared to conventional drive with current control; also, it has resulted in higher torque per stator current of 1.37 compared to conventional of 1.01-1.05 [44].

It is evident from the published literature that even after employing best control and best design optimization, torque ripple of switched reluctance machine is not at par with other competing candidate electrical machines for EV.

2.3.3 Synchronous reluctance machines

Synchronous reluctance machines employ conventional induction machine stator with a loss-free rotor constructed from axially stacked steel laminations without any copper windings on it. The rotor with no cage or windings is simple and robust than IM and PM machines. Because of absence of PM, no back EMF and

hence no risk of demagnetization caused by over-heating or other failures, making them inherently safe. This is also advantageous by ruling out the need to protect power electronics. Also, these machines may operate without rotor position sensors, which make them robust and reliable. Figure 2.3 shows the cross-section of a typical synchronous reluctance machine.

In April, 2011, ABB unveiled two ranges of synchronous reluctance technology for new generations of high efficiency and high power density machines at Hannover Fair. One designed to operate at the *super premium* levels of efficiency (IE4 specifications), and the other optimized to deliver a high output from a small frame [45]. The published results show that efficiency of synchronous reluctance machine is ~2% higher in the range of 1-10 kW power, ~1% higher in the range of 10-100 kW power and ~0.5% higher in the range of 100-800 kW power compared to induction machines.

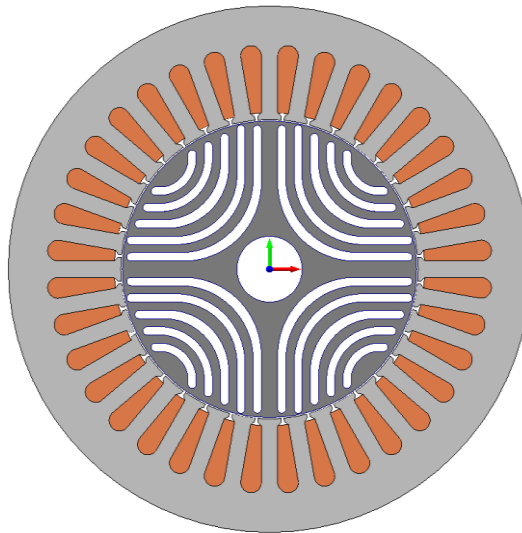


Figure 2.3 Cross-section of synchronous reluctance machine

Within two months of its introduction by ABB, one of the pilot users reported energy savings of 5-10% with synchronous reluctance drive technology, on top of the 25% achieved with a standard ABB motor and drive [46]. A German pump manufacturer, KSB Aktiengesellschaft, started producing a range of synchronous reluctance machines to drive its own pumping equipment, which dissipate 13% less power than IE3 machines, meeting IE4 efficiency target. These motors can operate at speeds from 0 to 4200 rpm [47]. In Dec., 2012, the world's first commercial IE4

synchronous reluctance motor-drive package was installed on a pump operated by a UK water utility, at South Staff Water's Somerford pumping station [48]. The new system, called SynRM by ABB, has replaced a 20-year old, 115 kW, IE2 induction machine used to control a vertical shaft driven borehole pump, which abstracts 2.5 million litres of water every day. The utility reported every saving of 6% with the SynRM technology compared to induction machine technology [48].

Another attraction of synchronous reluctance machine is high efficiency even at partial loads, which is useful for fan and drive pump applications. This can also be useful for EV traction during high speed operation.

Direct torque control (DTC) is employed by ABB to control synchronous reluctance motors at speed up to 6000 rpm. This control technology works in the field-weakening range and can reach speeds 1.5 times the nominal rating. It also allows the motor to reach much higher torque densities than induction machines.

Although recent research and development suggests that synchronous reluctance machines can outplay induction machines, it remains to see if they match PM machines for EV application.

2.3.4 Permanent magnet machines

Due to their high power density and high efficiency, PM machines have been researched extensively in past two decades for various applications including EV. For better understanding, the author has classified PM machines as shown in Figure 2.4.

Permanent magnet machines are broadly classified into constant flux PM machines and variable flux PM machines. Constant flux PM machines are further classified into concentrated winding and distributed winding PM machines. All these classes can have rotor with PM on surface, i.e. surface mounted PM machines (SPM) or buried inside the rotor, i.e. interior PM machine (IPM).

2.3.4.1 SPM versus IPM

In SPM machines, the torque is produced by the interaction of permanent magnet flux and winding current. In IPM machines, in addition to the torque due

to permanent magnets, a reluctance torque component due to the anisotropic effect of reluctance seen by the stator windings is also produced. Because of the extra reluctance torque, IPM machines can produce the same torque with lower current than the SPM counterpart. Based on the machine design, the reluctance torque contribution may be negative or positive in IPM machines. Compared to SPM machines, IPM machines have lower fault current and uncontrolled generation in the event of a fault due to lower magnet volume than SPM machines for the same design specifications.

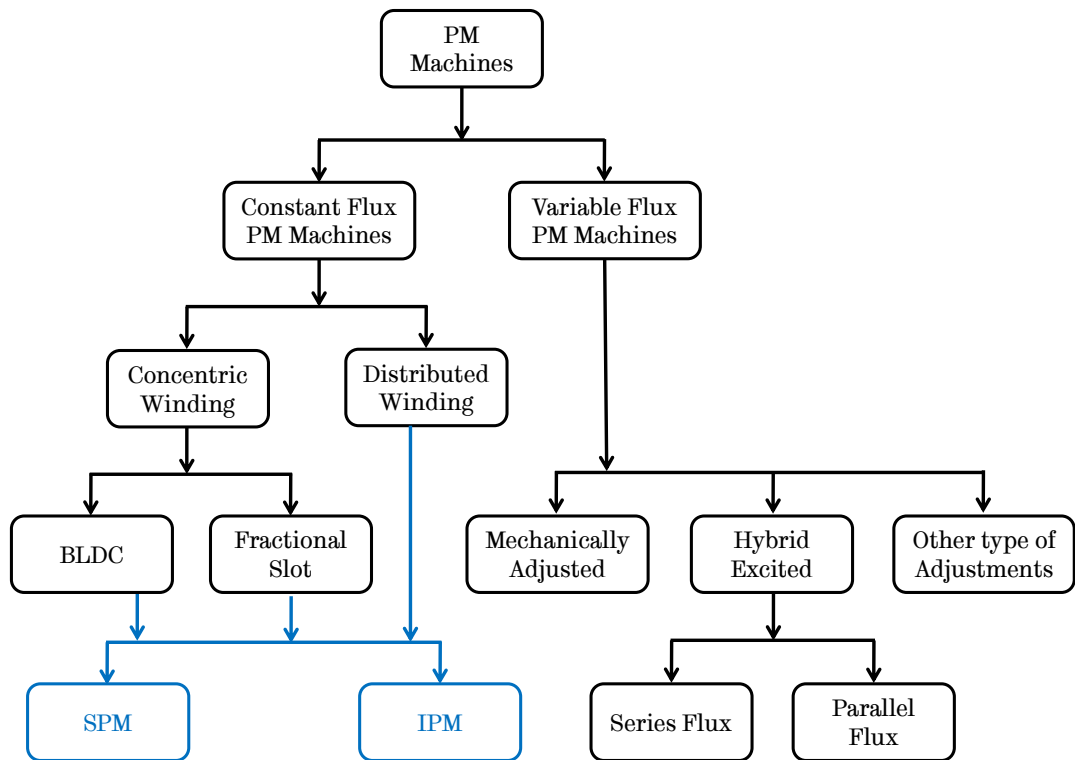


Figure 2.4 Classification of permanent magnet machines

Thus, SPM machines require higher inverter VA rating, higher peak current, and has low saturation level than IPM machines. Since the inverter loss is more significantly affected by current level, SPM design will also lead to higher inverter losses. If the winding configuration of both SPM and IPM designs is similar, then it is highly unlikely that SPM design can lead to low winding resistance. Hence, IPM design outperforms SPM design. However, if SPM design is to outperform IPM design, then its winding resistance has to be lower, which may be achieved by employing *fractional-slot per pole* winding configuration with high number of pole

pairs. This makes more room for slot area, and shortens the stack length and end winding. However, high number of pole pairs may lead to higher iron losses. Figure 2.5 shows typical cross-section of IPM and SPM machines. Both employ fractional-slot per pole winding configuration. The stator and rotor laminations are shown in dark grey and grey respectively, whereas PM is shown in red and green to indicate their polarity. For clarity, stator windings are not shown.

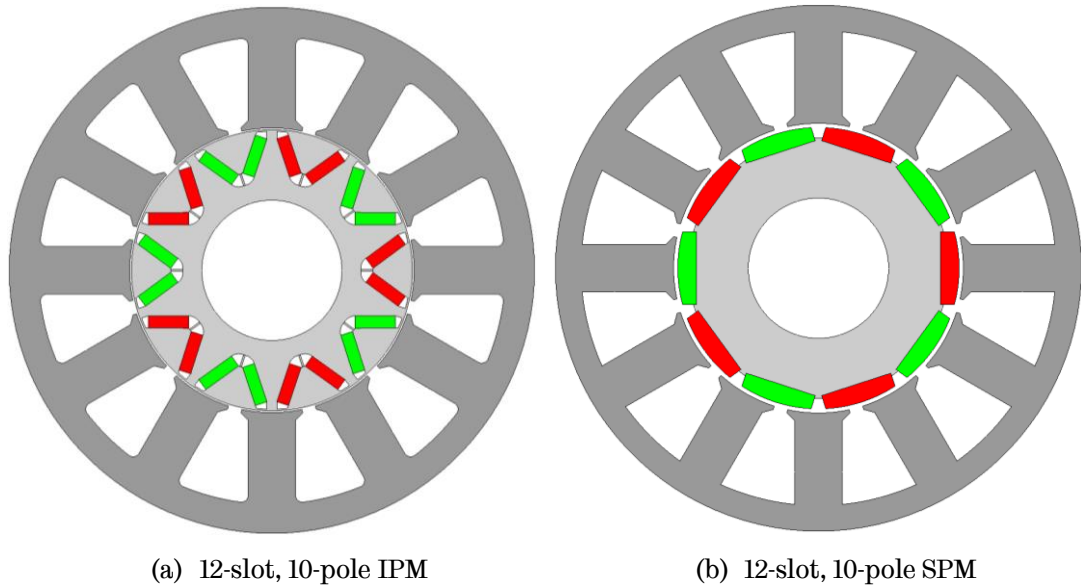


Figure 2.5 Cross-section of IPM and SPM machines

As shown in the classification, both SPM and IPM machines may employ distributed winding with integer slot per pole or concentrated winding with fractional-slot per pole. Various research papers are published with different topologies of the winding configuration and fractional-slot per pole winding configurations in the past decade.

Table 2.3 shows the qualitative comparison of SPM and IPM machines with distributed and fractional-slot windings for EV application using figure of merit (FoM) from 1 to 10, 10 being the best, and 1 being the worst.

SPM machines with distributed windings result in low inductance, poor flux weakening capability (high speed operability) and high inverter VA rating. Therefore, they are considered unsuitable for EV application. The three remaining candidates are SPM with fractional-slot concentrated windings, IPM with distributed windings, and IPM with fractional-slot concentrated windings.

Longer end windings of machines having distributed windings may lead to lower torque density and lower efficiency. They also have higher torque ripple and higher cogging torque compared to machines with fractional-slot concentrated windings. Also, relatively lower attainable number of pole-pairs for a given number of slots with distributed winding design yields thicker yoke and thicker rotor back iron, which in turn, reduces the slot area, and hence lower torque density and efficiency. Thus, while both IPM designs and SPM with fractional-slot windings have good field weakening capability (high speed operability), IPM topology with distributed winding may yield low torque density, lower efficiency and larger torque ripple than the fractional-slot counterpart.

Table 2.3. Qualitative comparison of SPM and IPM with different winding configurations

Performance Attribute	SPM Distributed	SPM Fractional-slot	IPM Distributed	IPM Fractional-slot
Torque/power density	9	10	9	10
Torque ripple	9	10	8	9
Efficiency	8	9	8	9
Cost	7	6	8	8
Sub-total FoM	33	35	33	36
High speed operability	8	8	10	10
Fault tolerance	9	10	9	10
Controllability	9	9	8	8
Reliability	8	8	8	8
Maturity	9	8	9	8
Manufacturability	7	7	8	8
Total FoM	83	85	85	88

On contrary, the lower and higher order space harmonics in the stator magneto-motive-force (MMF) which rotate at different speeds relative to the rotor in fractional-slot machines will induce significant eddy currents in the rotor magnets. However, the eddy current loss can be effectively reduced to very small amount by both circumferential and axial segmentation of rotor magnets, especially when the machine speed or electrical frequency is not very high. This will increase manufacturing cost for SPM machines. For IPM machines with fractional-slot windings, high order magneto-motive force (MMF) space harmonics

are generally shielded by the rotor core, and hence the magnets are not segmented circumferentially, but are assembled axially using smaller length magnets, making handling easier and reducing additional cost of manufacturing due to segmentation.

Other important design issue between SPM and IPM machines to consider is the containment of magnets. In IPM machines, the magnets are buried inside the rotor lamination, which calls for specific attention to mechanical design and structural analysis in order to ensure the structural integrity of the rotor. For SPM machines with fractional-slot windings, the magnets are usually retained by either a metallic sleeve or glass/carbon fibre banding layer, which in turn, increases the manufacturing cost of SPM machines.

Hence, it is a matter of trade-off between performance and cost when it comes to selecting SPM or IPM machines with fractional-slot windings. It is evident from Table 2.3, with fractional-slot windings, IPM machines have slightly better edge compared to SPM machines, mainly due to manufacturability and cost attributes. Also, high torque demand at low speed and low back EMF requirement at high speed for safety conflicts with each other, and cannot be met simultaneously for SPM machines, making them less attractive than IPM machines.

2.3.4.2 Variable flux PM machines

One of the key challenges faced by constant flux PM machines is to achieve desired range of constant power operation, usually 3 to 4 times the base speed, for EV application, because of the uncontrollable permanent magnet flux. Many researchers strived to devise various PM machines with variable air-gap flux capability through various means including mechanical adjustments, hybrid excitation, and other type of adjustments, as depicted in the classification of PM machines in Figure 2.4.

The memory machine, shown in Figure 2.6 (a), having special magnetic qualities of AlNiCo magnets, can control its air-gap flux by applying a short pulse of negative d -axis current in the motor winding which in turn regulates its magnetization levels [49]. Extensive research has been carried out on this machine

with respect to modelling, effect of shape of AlNiCo magnets, and combination of NdFeB and AlNiCo magnets, etc. on its performance.

In recent past, memory machine concept is extended to the hybrid field doubly salient PM (HF-DSPM) machine making it flux-nemonic PM brushless (FM-PMBL) machine, which offers effective and efficient control of the air-gap flux [50]. Figure 2.6 (b) shows the cross-section of FM-PMBL machine. An attempt is made to compare FM-PMBL machine with HF-DSPM machine in [51]. FM-PMBL machine has no cogging torque, high short circuit fault tolerance, simple handling of PMs and overall high power density compared to HF-DSPM machine. Although the cost of AlNiCo magnets is lower than the NdFeB, more permanent magnet material in FM-PMBL machine makes it little expensive than HF-DSPM [51]. Also, the manufacturing process still remains complicated and poses a challenge for its use in EV application.

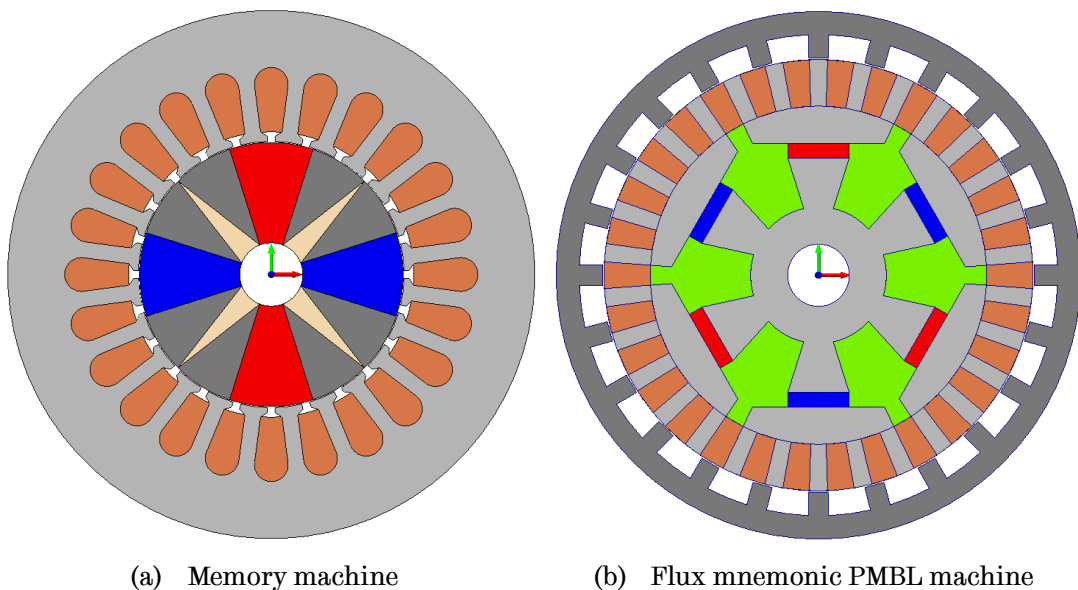


Figure 2.6 Cross-section of different types of variable flux machines

In order to provide flux regulation in PM machines, various mechanical adjustments are also studied and analysed. In these machines, the mechanical structure of the machine is changed to regulate the air-gap flux. This can be achieved by (a) rotating rotor sections, (b) rotating stator sections, (c) axially adjusting the air-gap, (d) adjusting flux barriers in IPM machines or (e) adding more leakage paths for the air-gap flux, an example of which is shown in Figure 2.7.

In all these methods, only flux-weakening is possible as original PM excitation is weakened by misaligning the actual flux path. Also, these machines have additional mechanical structures in place, making power drivetrain for EV application bulky and less reliable.

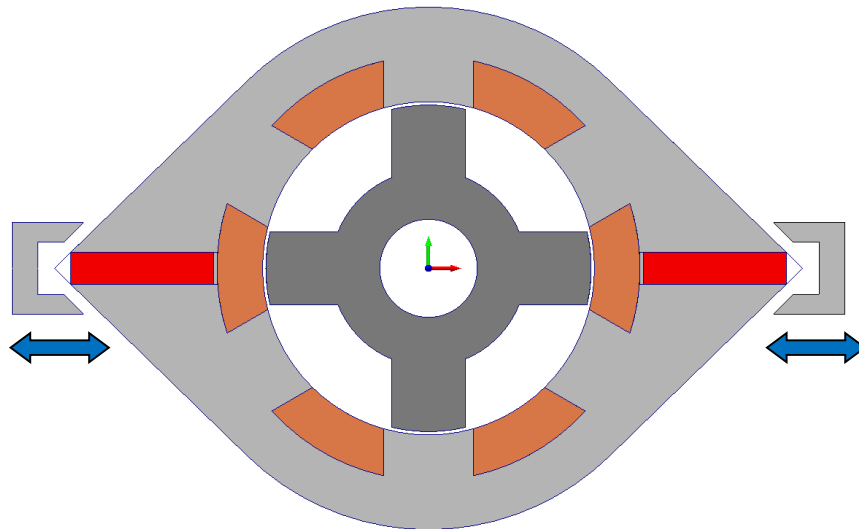


Figure 2.7 Cross-section of mechanically adjusted DSPM machines

Summarizing, in general, the variable flux PM machines have complex geometries to design and analyse, and to manufacture. Hence, the above machine topologies are not so attractive for a practical EV application considering manufacturing cost, maintenance requirements, and reliability concerns. However, some variable flux PM machine topologies under hybrid excited configuration may be promising for EV application.

2.3.4.3 Hybrid excited PM machines

The hybrid excited PM machines derive their name due to hybrid excitation using both PM and field coils. They can be divided into series flux path hybrid excited PM machines and parallel flux path hybrid excited PM machines depending on whether the PM flux is in series or in parallel with field coil excitation. It is most common to use parallel flux hybrid excited PM machines to avoid permanently demagnetizing the magnets, and to incorporate field windings in stator to avoid the need for slip rings and brushes.

2.3.4.3.1 Series flux path hybrid excited PM machines

Although series flux path hybrid excited PM machines have simple structure and good flux regulation (weakening and boosting), the high risk of PM demagnetization does not make them suitable candidate for EV application. The doubly excited synchronous machine (DESM), Figure 2.8 (a), has both field excitation sources in the rotor – PM is fixed to the end of rotor teeth that are wound with DC field coils [52]. The doubly salient PM machine (DSPM), whose topology is similar to that shown in Figure 2.6 (b), has both excitation sources in the stator to avoid the need for slip rings and brushes [53]. The hybrid stepper machine, shown in Figure 2.8 (b), does not suffer from demagnetization issue as DC coil flux passes through the magnets only in the direction of magnetization of magnets [54]. However, the hybrid stepper machine requires additional component in stator to provide the flux path for the field coil, generally known as soft magnetic composite (SMC). This is an additional cost driver for such machines.

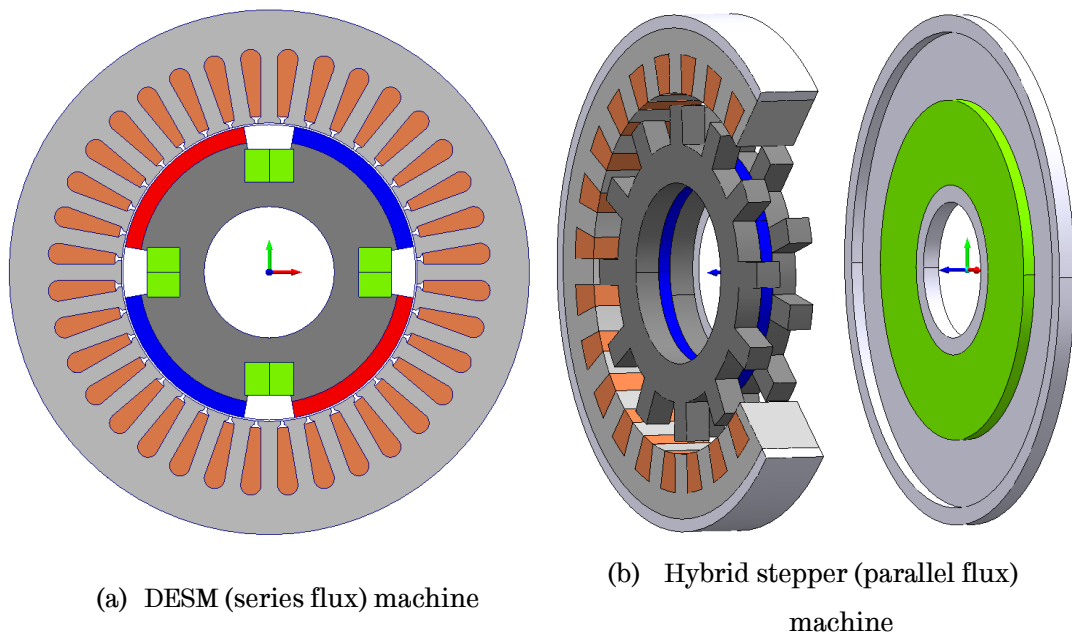


Figure 2.8 Cross-section of different types of hybrid excited PM machines

2.3.4.3.2 Parallel flux path hybrid excited PM machines

Parallel flux path hybrid excited PM machines can be classified based on their configuration of placing field coils and magnets, as shown in Figure 2.9.

Most of the hybrid excited PM machines are found under category of having field coils on stator and PM on rotor, eliminating slip rings and brushes. They are relatively complex to analyse and manufacture, which in turn, limits their application for EV.

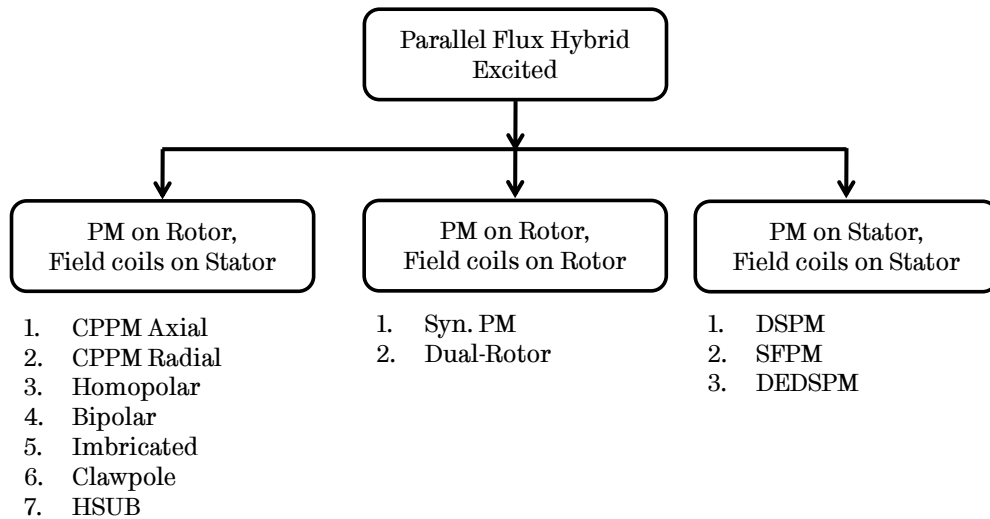


Figure 2.9 Classification of parallel flux path hybrid excited PM machines

The consequent pole PM (CPPM) machines have toroidal field coil in the stator back iron. They can either be axial [55] or radial [56] field designs. The rotor has alternating PM and consequent iron poles attached to rotor back iron.

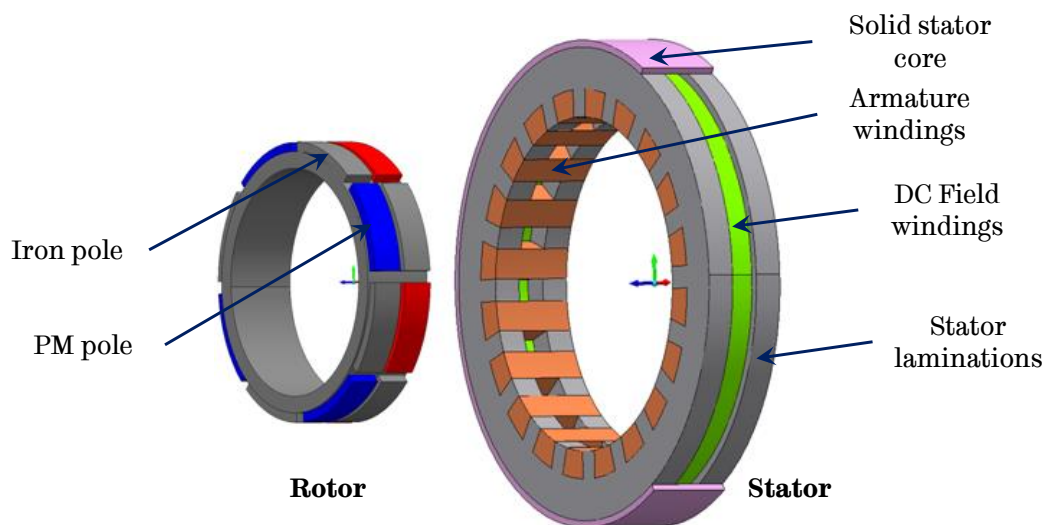
Figure 2.10 (a) shows the radial flux CPPM machine. Since additional space is required to accommodate the field coil on the stator, the volumetric efficiency and torque /power density of the machine is compromised.

Homopolar [57] or bipolar [58] embedded PM topologies have ferrite magnets embedded in the rotor with circumferential magnetization. The field excitation coil has a complex flux path, and hence less efficient in flux variation control. Like CPPM machines, these topologies are also very complicated to manufacture.

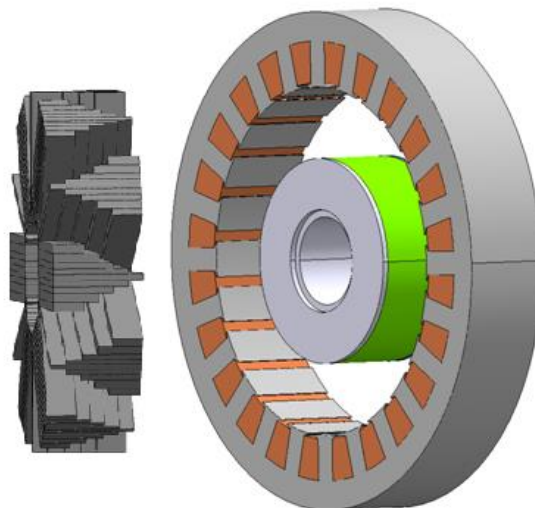
Imbricated hybrid excited machine [59] consists of a rotor with two parts, which are magnetically separated, the outer cylinder and an inner core with magnets, and has teeth that extend to the rotor surface through holes in cylinder. The stator too has two parts joined by a yoke. It employs toroidal field coils located adjacent to stator yoke.

Claw pole rotor machines [60] also have stationary toroidal windings located outside the rotor structure. The rotor is claw pole type with magnets either on or between the claw poles. This topology is extremely complicated to manufacture. Figure 2.10 (b) shows the claw pole rotor machine.

The high strength undiffused brushless (HSUB) machine [61] is nothing but an IPM machine with toroidal field coils included in the stator. Both axial and radial field designs are possible. It has a very good flux boosting capability due to well positioned magnets helping DC field flux to reach main air-gap of machine and not leaking away. However, it has a slightly poor flux weakening performance.



(a) Radial flux CPPM machine



(b) Claw pole PM machine

Figure 2.10 Radial flux CPMM machine and Claw pole machine (shown without PMs)

Usually, it has cheaper magnet material than rare earth magnets.

For variable flux machines with magnets on rotor and field coil on stator, the flux produced by current in the field coil has to pass an additional air-gap to reach the rotor. This results in less efficient field excitation, and larger volume.

Hybrid excited PM machines with field coils on the rotor are very rare considering need of slip rings and brushes requiring additional maintenance cost. However, it is possible to eliminate the slip ring by employing high frequency rotating transformer. The synchronous PM (SynPM) machine [62] has both wound DC field coils and PM poles on the rotor. A variant of synchronous PM machine having interior PM is also reported in literature [63]. The dual rotor machine [64] includes field coils and permanent magnets on axially separated rotor sections with a common stator. The large inductance of magnets ensures that both flux paths remain parallel. Wide range of control is possible with small amount of DC current as reported in publications. Figure 2.11 shows the typical SynPM machine and dual-rotors machine. The permanent magnets are shown in red and blue to indicate their polarity, whereas armature windings and field coils are shown in coral and chartreuse respectively.

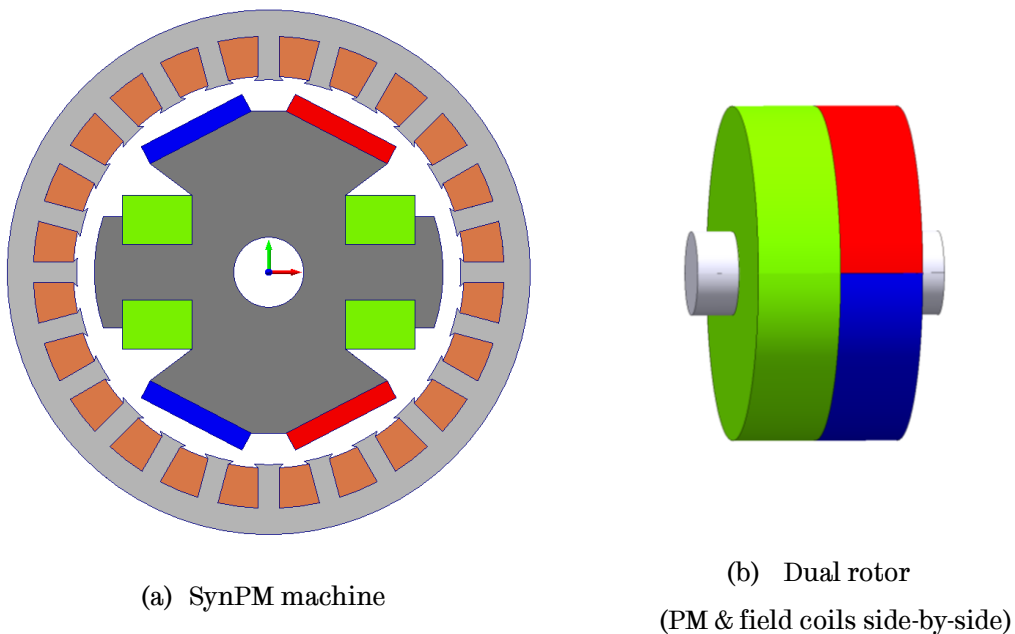


Figure 2.11 Typical SynRM machine and dual-rotors machine

The last type of parallel flux path hybrid excited PM machines can be achieved by three different machine types: (i) the doubly salient PM (DSPM) machine as shown in Figure 2.12 (a), (ii) the permanent magnet flux switching (PMFS) machine as shown in Figure 2.12 (b), and (iii) the double-excited, dual-stator permanent magnet (DEDSPM) machine as shown in Figure 2.12 (c). In these machines, both PM and field coils are located on the stator. Therefore, they have simple and robust rotor structure like switched reluctance machine (SRM), and have good flux control at the expense of torque density.

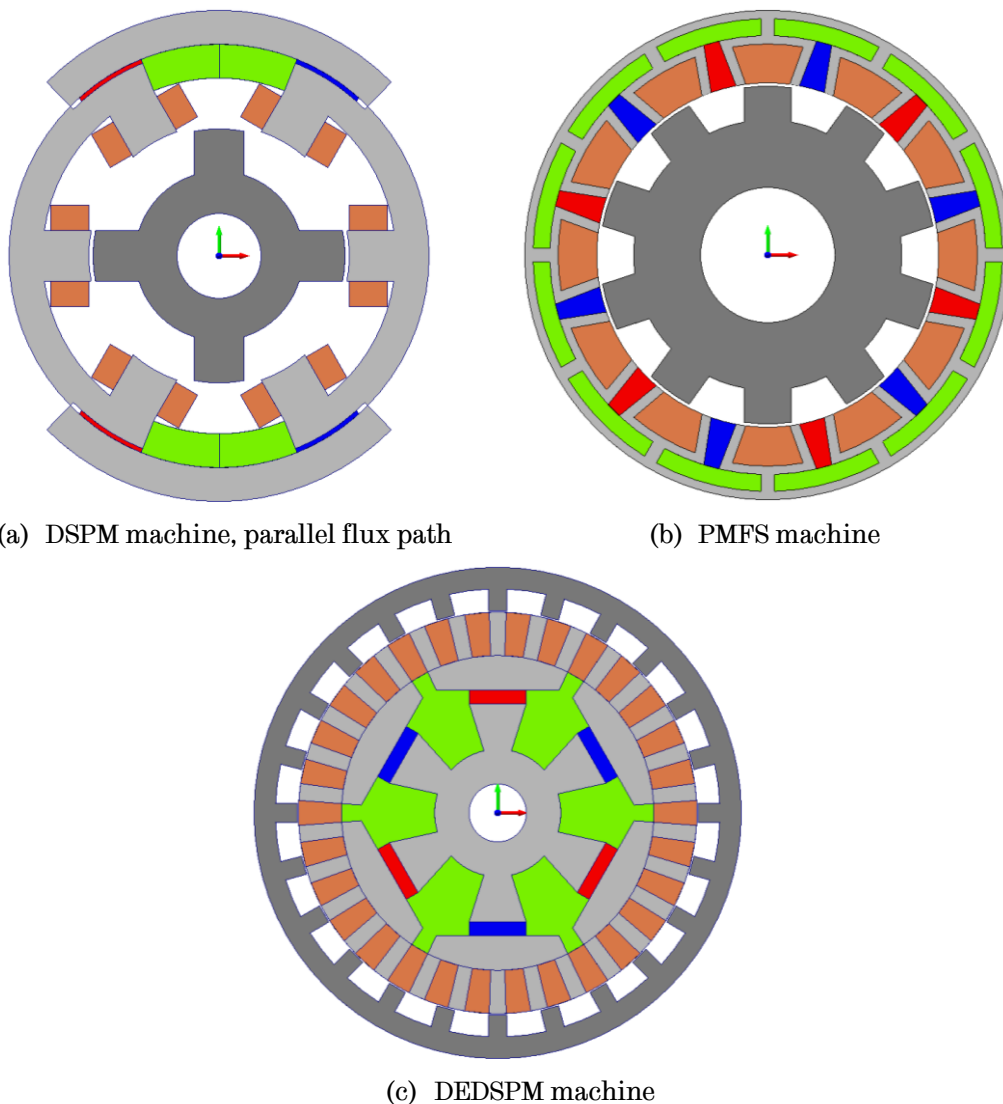


Figure 2.12 Cross-section of parallel flux hybrid excited PM machines having PM and field coils on the stator

Parallel flux path hybrid excited PM machine can have either distributed or toroidal field coils and utilize small amount of magnet material [65].

The hybrid field doubly salient PM (HF-DSPM) machine employs field windings into traditional DSPM machine [66]. This can not only weaken the air-gap flux, but also strengthens it [67]. Even though DSPM machine has high torque density, high efficiency, small VA rating of converter, rugged structure, high speed operability and fast response, their torque ripple is quite high due to pulsed excitation. Due to complex motor structure and additional field windings, HF-DSPM manufacturing process will be demanding and challenging.

Hybrid excited PMFS machine [68] can be formed by replacing permanent magnet materials with field coils or by increasing the overall volume of the machine to accommodate the field coils along with permanent magnets. In this machine, it is possible to modulate the flux-linkage of armature windings by changing or reversing the field coil excitation. This helps in regulating torque output of the machine and also the flux during field weakening mode.

The DEDSPM machine [69] is an external rotor machine with stator in two parts, having inner part with field coils and outer part with armature windings. Results show that a wide range of flux control is possible with air-gap flux density ranging from 0.1T under field weakening to 0.9T under flux boosting. Due to complex structure of the stator, its manufacturing will be challenging.

A common feature for all hybrid-excited or variable flux PM machines is additional space/volume to accommodate flux adjusting devices, either mechanically or electrically. This may lead to lower torque density, more complex structure, higher cost and additional copper loss if electrically adjusted. Whether the benefits outweigh the cost and other penalties remains a question to be addressed.

2.4 Selection of advanced machine technologies for a micro-sized EV

Based on the comprehensive literature survey and the current state-of-the-art technologies for EV application, the author has selected the following advanced machine technologies to assess them through preliminary design studies for a micro-sized EV application.

1. Fractional-slot per pole per phase winding PM machine
 - a. 12-slot, 14-pole SPM
 - b. 24-slot, 14-pole IPM
2. Hybrid excited permanent magnet flux switching machine (HE-PMFSM)
 - a. 12-slot, 14-pole HE-PMFSM

Fractional-slot per pole per phase winding configurations are advantageous over conventional distributed winding configurations as outlined in section 2.3.4.1. It has been shown that 12-slot, 10-pole and 12-slot, 14-pole design variants for SPM and/or IPM represents very good slot-pole number combinations for the electric vehicle application in [16] and [17]. Although 10-pole design will have lower iron loss, the author has selected 14-pole topology in order to have fair comparison between these advanced machine technologies. Hence, 12-slot, 14-pole fractional-slot SPM machine is considered for the preliminary design study as a benchmark.

A novel 24-slot, 10-pole winding topology is reported to reduce/eliminate stator MMF sub-harmonics of the fractional-slot concentrated windings [70]. In this configuration, conventional 12-slot, 10-pole concentrated winding, divided into two separate identical winding systems, are connected in series and are supplied by the same inverter. The second set of winding is shifted by an appropriate mechanical angle with reference to the first set of winding in such a manner to cancel out the undesirable harmonics in the stator MMF. The results show that this new winding topology clearly has better performance compared with standard distributed windings in PM machines for EV traction. This winding can also be applied to induction machines and wound-field synchronous machines. Hence, this

new topology (24-slot, 14-pole) of fractional-slot PM machine is also a candidate for the preliminary design study.

Recently, development of permanent magnet flux switching machines for electric vehicle applications has gained popularity among the researchers [71-74]. As discussed before, PMFSM employs both PM and armature windings in the stator and a robust rotor similar to that of an SRM, making it advantageous for easier cooling of all active parts, and a great potential for high speed operation compared to conventional PM machines. A common problem of all PM machines is, however, fixed excitation which may lead to high losses in the frequent operating regions of an EV traction machine when torque is low or speed is high. To enable PMFSM for variable flux controllability to improve maximum torque and power, and efficiency, E. Hoang *et al.* [68, 75] reported a PMFSM with 12-slot, 10-pole having an additional excitation located on the stator. This machine topology is also known as hybrid excited machines [76]. E. Sulaiman *et al.* [77, 78] have investigated the PMFSM design possibility with hybrid excitation having 6-slot, 5-pole topology for traction drives in HEV. It is designed with an aim to produce maximum torque and is reported to have better efficiency over 5 representative points for EV traction with 9.1% lower volume of PM compared to conventional IPM machine. However, comprehensive comparisons based on the same volumetric and thermal constraints have not been reported. Hence, the author has also selected hybrid excited PMFSM machine for the preliminary design study.

Chapter 3

Preliminary Design Study on Advanced Machine Technologies for a Micro-sized EV

The most promising machine technologies are assessed for their suitability for a 10kW (peak) traction drive for a micro-sized electric vehicle with a distributed power train. The design for each machine technology is optimized using 2-D finite element analysis (FEA) under the same electrical, thermal and volumetric constraints and the key limitations are highlighted by comparing their performance at the rated and the peak torque operation as well as over the driving cycle against one another.

Part of this chapter is published by the author in [79].

3.1 Most promising machine technologies for EV

Fractional-slot PM machines (SPM and IPM) and Hybrid excited flux switching machines being most promising are selected for preliminary design study. The details of their characteristics features, topologies and geometry are described as below.

3.1.1 Fractional-slot SPM – 12 slot, 14-pole

Among numerous PM machine technologies that differ in PM rotor structure and stator winding arrangements [25], an SPM with fractional-slot (per pole) concentrated winding (FSCW) is emerging as a promising candidate suitable for EV applications due to its good field-weakening and over-load capability compared to distributed winding SPM machine [16, 80].

Figure 3.1 shows the cross-section of a typical SPM machine having 12-slot, 14-pole topology. The stator and rotor laminations are shown in dark grey and grey

respectively. The armature windings are inserted in the 12 stator slots which comprise 3 phases denoted as A, B, and C. Each phase winding consists of four series connected concentrated coils which are wound on consecutive teeth so that the phase windings do not overlap. The polarity of armature windings is indicated by '+' and '-', whereas the magnetizing direction of PM is indicated by red and green for north and south pole respectively.

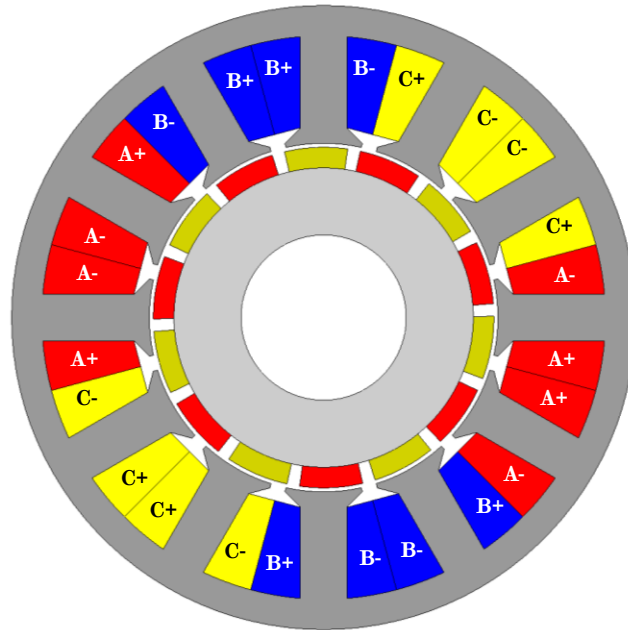


Figure 3.1. Cross-section of a 12-slot, 14-pole, SPM machine

3.1.1.1 Characteristic features of FSCW SPM machines

As seen from the above figure, an SPM rotor employs permanent magnets on the surface of the rotor back-iron. Hence, to contain and to protect the magnets in an SPM machine, a thin layer of glass or carbon fibre with high temperature epoxy or a thin sleeve using non-magnetic stainless steel or other high tensile strength materials is often employed. This increases the cost of manufacturing and restricts the application of SPM for high speed operations.

Since the relative permeability of magnet materials is close to that of an air, the effective air-gap seen by the stator magneto-motive-force (MMF) is uniform and relatively large for SPM machines. The resultant armature reaction field is weak, and, the harmonics resulting from the FSCW in the stator do not cause significant torque ripple. The phase inductances (self and mutual) are independent of the rotor

position. The use of concentrated winding configuration result in relative large self and mutual inductances compared with those of distributed windings. The d - and q -axis inductances are equal, making the reluctance torque production virtually zero in SPM machines. In addition, the SPM machines with FSCW have a relatively linear torque-current characteristics, a high peak torque capability and good over-load capacity.

In addition, FSCW produce a large number of additional space harmonics in the stator MMF, which cause undesirable effects that include localized core saturation, eddy current losses in magnets, acoustic noise and vibrations [81, 82]. To mitigate these detrimental effects, the most common approach is to segment the rotor magnet axially and circumferentially in order to reduce the eddy current loss in the rotor and/or PM. However, this brings an additional penalty in terms of manufacturing cost and material usage (material being wasted during the segmentation process), and does not address the other undesirable effects. While this machine topology has a good field weakening capability [83], the absence of reluctance torque means that the requirements for high torque at low speeds and low back EMF at high speeds for safety become conflicting, making it difficult to satisfy both.

3.1.2 Fractional-slot IPM – 24 slot, 14-pole

One way to mitigate the conflicting requirements and to reduce the manufacturing cost of PM machine technologies for high speed applications is to use IPM machines. However, IPM machines with fractional-slot windings exhibit very poor reluctance torque capability [84]. G. Dajaku *et al.* [70] reported a new 24-slot, 10-pole machine topology to reduce the sub- and high order stator MMF harmonics of the conventional 12-slot, 10-pole FSCW by dividing the 3-phase windings into two sets and placing an appropriate phase shift between the two. Hence, the IPM machine with FSCW is selected with 24-slot, 14-pole topology to assess it for EV application.

Figure 3.2 shows the cross-section of a typical IPM machine with 24-slot, 14-pole topology. The stator and rotor laminations are shown in dark grey and grey respectively. The armature windings are inserted in the 24 stator slots which

comprise 3 phases denoted as A, B, and C. Each phase winding consists of eight series connected coils which are wound on alternate teeth resulting into overlapping phase windings. The polarity of armature windings is indicated by '+' and '-', whereas the magnetizing direction of PM is indicated by red and green for north and south pole respectively.

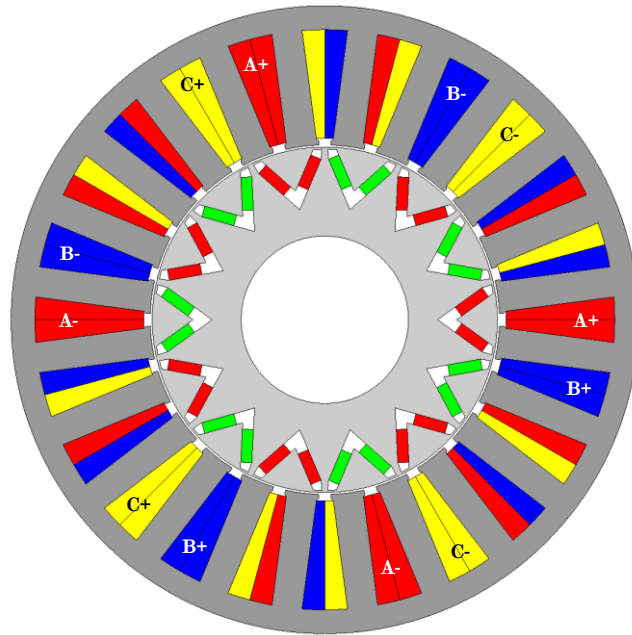


Figure 3.2. Cross-section of a 24-slot, 14-pole, IPM machine

3.1.2.1 Characteristic features of FSCW IPM machines

As the magnets are buried inside the rotor lamination for IPM machines, the armature reaction field becomes anisotropic because the flux perpendicular to the magnetic axis (d -axis) has a lower reluctance than that parallel to the d -axis. Hence, the reluctance seen by the stator winding varies with the rotor position, and the difference in d - and q -axis inductances gives rise to a reluctance torque component in IPM machines with distributed windings. So, in order to produce same torque, the permanent magnet flux can be lower in IPM machines than that of SPM machines.

Since the effective air-gap in IPM machines is much smaller, the resultant inductance is much higher than that of SPM machines. In addition, the strong armature reaction together with localized core saturation (due to very thin posts and bridges to contain magnets) in the rotor structure makes IPM machines more

prone to reaching magnetic saturation limits, which may limit its peak torque capability. Presence of stator MMF space harmonics also make it difficult to obtain high reluctance torque from IPM machines with FSCW [84].

3.1.3 Hybrid excited flux switching machines

Although the PM synchronous machines (PMSM) have high torque and/or power density and high efficiency, the rotor geometry and construction of PMSM is complicated due to the need for bonding and containing the magnets in SPM rotors as well as exploiting the reluctance torque in IPM rotors. This leads to high manufacturing cost for SPM rotors and compromises on rotor mechanical integrity for IPM rotors. The hybrid excited PM flux switching machines (HE-PMFSM) offers advantages of easier cooling of all active parts such as armature windings, field windings and PM, and have a great potential for high speed operation compared to conventional PM machines. Additional field coils on the stator provides variable flux control capability to improve maximum torque and power, and efficiency [77, 85].

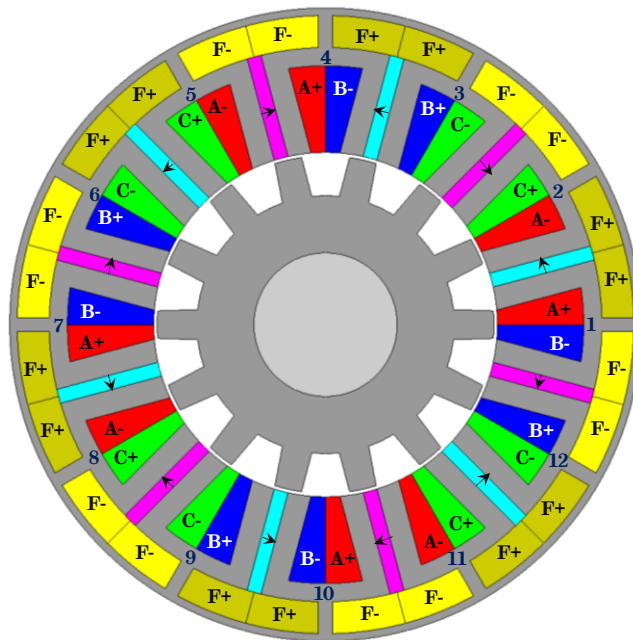


Figure 3.3. Cross-section of a 12-slot, 14-pole HE-PMFSM

Figure 3.3 shows the cross-section of a typical PMFSM with hybrid excitation which employs 12-slot, 14-pole topology. The machine is composed of 12 PM and 12

field excitation coils denoted as F, distributed across the stator, supplied by a DC source. The magnetizing direction of PM in magenta and turquoise is indicated by arrows, whereas polarity of field winding is indicated by '+' and '-'. The armature windings which are inserted in the 12 stator slots comprise 3 phases denoted as A, B, and C. Each phase winding consists of four series connected coils wired around the adjacent tooth with polarity as indicated by '+' and '-'.

3.1.3.1 Principle of operation of HE-PMFSM

The hybrid excited PMFSM uses the principle of both flux switching and flux concentration [72-74]. In order to understand the principle of operation of a HE-PMFSM, a section of a full geometry show in Figure 3.4, is used.

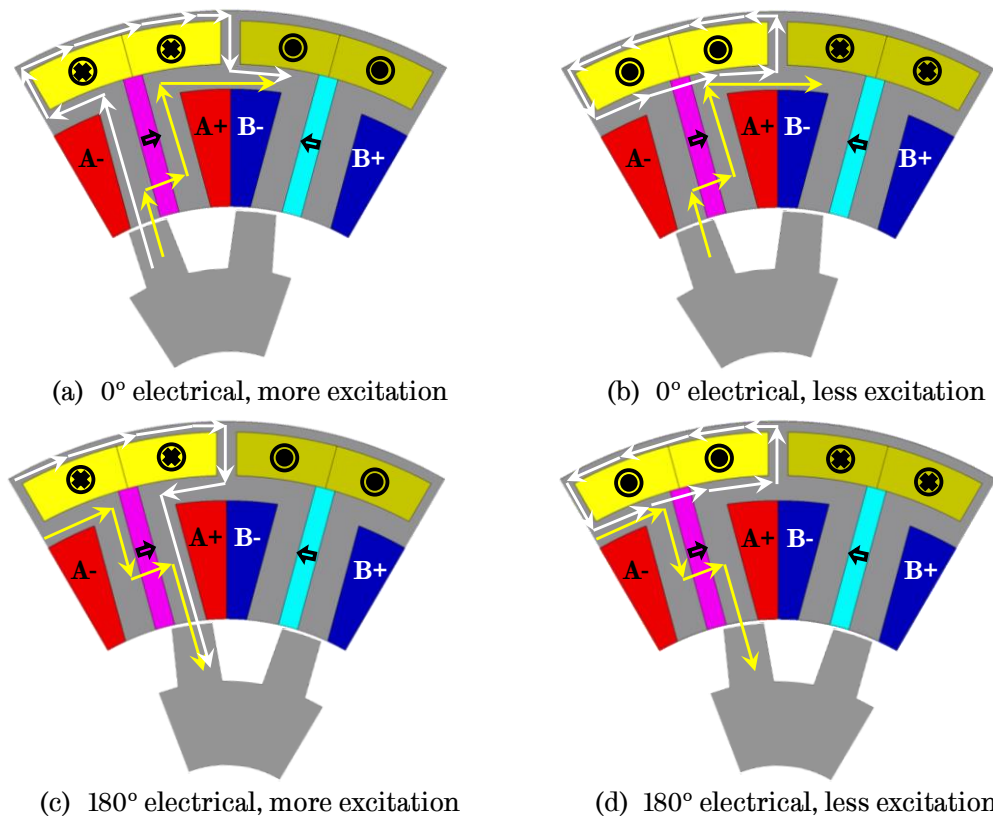


Figure 3.4. Principle of flux switching and flux concentration

In the above figure, the dot and cross symbols indicate the directions of the field excitation currents, whereas polarity of currents in phase windings are denoted as '+' and '-'. The yellow arrows indicate the path of flux created by PM whereas the white arrows indicate the path of flux created by field excitation.

If the flux linkage in the phase windings is considered as positive when the rotor tooth aligns with the stator tooth on the left side of the PM as seen in Figure 3.4 (a) and (b), then the flux linkage becomes negative when the rotor tooth aligns with the stator tooth on the right side of the PM as seen in Figure 3.4 (c) and (d). Thus the flux linkage alternate in nature when the rotor rotates and the term *flux switching* is derived.

It is also possible to modulate the flux linkage in the phase windings by changing or reversing the field excitation as seen in Figure 3.4 (a) and (b) or (c) and (d). This helps in regulating the torque output of the machine and also the flux during the field weakening operations at high speed.

3.1.3.2 Characteristic features of HE-PMFSM

Although the slot area is reduced in the HE-PMFSM compared with PMFSM or PMSM because of presence of field windings and PM in the stator, it is comparatively easy to dissipate the heat generated from the stator, which helps limit temperature rise of PM [72]. For micro or medium segment vehicle applications involving HE-PMFSM, natural air cooling is a cost effective way by integrating cooling fins on to the stator frame. For high power range, water cooling with a nominal flow rate shall be employed via a cooling jacket surrounding the stator. The additional field excitation coils on the stator helps to enhance torque and power with the variable flux control capability [77, 85].

The effect of armature reaction on the PM is less significant in HE-PMFSM as the flux produced by the armature windings and PM are in parallel magnetically. This is conducive to increasing the electrical loading of the machine. Due to high winding inductance of HE-PMFSM, they are readily suitable for constant power operation over a wide speed range, which is one of the desired characteristics for EV traction [72].

Mechanically robust rotor structure of a HE-PMFSM helps to achieve (a) higher speeds, and (b) simple and cost effective manufacturing, albeit high iron loss in the rotor may become problematic and reduce efficiency at high speed. However, the torque ripple of such rotors is comparatively higher than PMSM.

3.2 Power drivetrain of a micro-sized EV

To assess the suitability of the most promising advanced machine technologies for electric vehicle application, 10kW (peak) traction machines for a micro-sized electric car with distributed power drivetrain architecture having the front and rear drives are considered. The vehicle employs two traction motors that are connected to the front and the rear axle via a differential, as shown in Figure 2.1. In the event of a front- or rear-drive system failure, the vehicle can continue to operate with no sudden stops and without compromising vehicle stability and passenger safety as the front and the rear wheels are driven independently. Both the traction machines are under torque control, and their speed ratings are automatically synchronized against vehicle speed and tire interaction with the road surface [86].

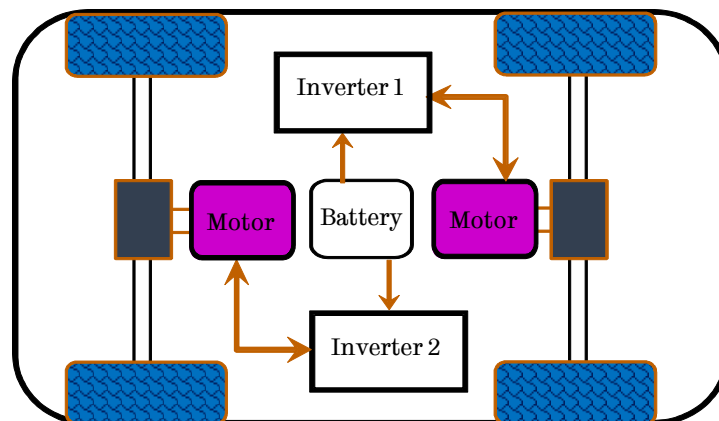


Figure 3.5. Architecture of distributed power drivetrain for preliminary design study

3.3 Design specifications and constraints

From the vehicle data and the acceleration performance requirements, the torque-speed envelopes for one motor with 50% torque split ratio between the front and the rear axles are established using the procedure described in [87]. The New European Driving Cycle (NEDC), shown in Figure 3.6, is employed as a reference driving cycle against which the design optimization of the promising machine technologies should be performed. The design specifications of the electric motor are depicted in terms of the torque-speed characteristics as shown in Figure 3.7.

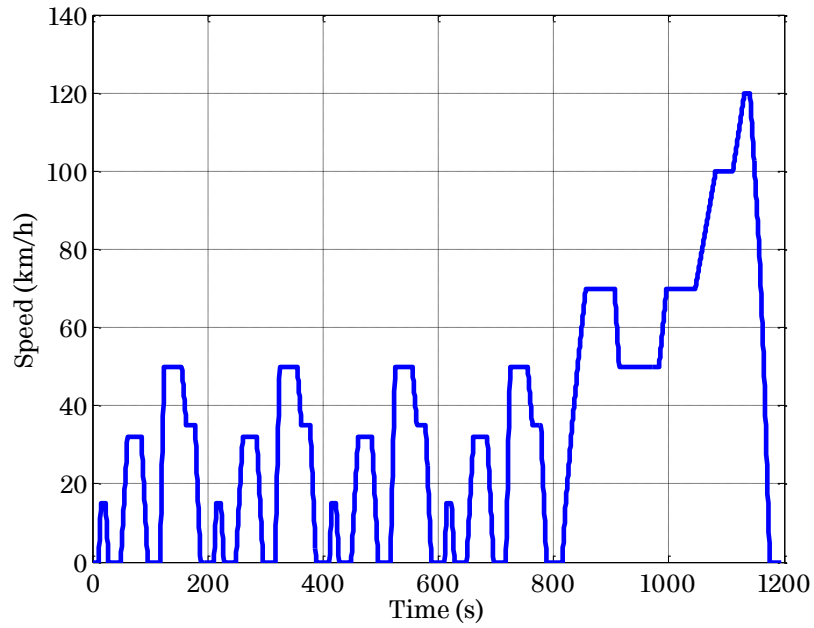


Figure 3.6. The New European Driving Cycle (NEDC)

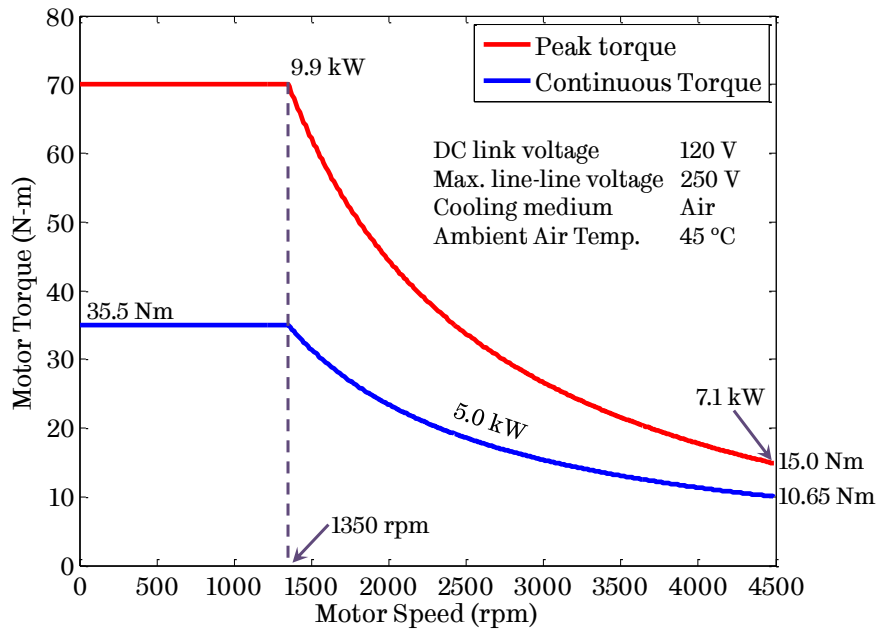


Figure 3.7. Target torque-speed characteristics for the preliminary design study

The geometry constraints, limitation on use of PM material, and thermal constraints listed in Table 1.1 are imposed to have a fair comparison of the performance of 24-slot, 14-pole IPM and 12-slot, 14-pole HE-PMFSM with that of a 12-slot, 14-pole SPM. For all the designs, a slot fill factor (or packing factor) of 0.4 is considered.

Table 3.1. Design constraints for the preliminary design study

Design Constraint	Unit	Value
Stator outer diameter	<i>mm</i>	150.0
Motor stack length	<i>mm</i>	118.0
Mass of PM material (NdFeB)	<i>kg</i>	0.9
Average winding temperature	$^{\circ}\text{C}$	≤ 120.0
Max. PM temperature	$^{\circ}\text{C}$	≤ 150.0
Max steel temperature	$^{\circ}\text{C}$	≤ 225.0

3.4 Design process and optimization

The design process involves the scanning of various geometrical parameters of the electrical machine over a defined range and selecting the optimum values which yields the best performance of the machine.

Preliminary scans on influential geometrical parameters of the promising machine technologies are carried out using 2-D finite element analysis (FEA) through commercial FEA software package, FLUX ver. 10.4, released by CEDRAT, France. M270-35A electrical steel is used for the stator and the rotor laminations, whereas the permanent magnet is defined as NdFeB with residual flux density and relative permeability of 1.1T and 1.04 respectively.

The design optimization of each of the promising machine technologies for a micro-sized EV is described below in detail.

3.4.1 Design optimization of FSCW SPM with 12-slot, 14-pole

In order to compare the performance of the machine technologies for a micro-sized EV under consideration, the author has selected the optimized design of FSCW SPM with 12-slot, 14-pole as a benchmark from [86], which describes the design, analysis and performance prediction in detail.

3.4.2 Design optimization of FSCW IPM with 24-slot, 14-pole

For a given stator outer radius of 75 mm and stack length of 118 mm, the geometrical parameters that have most significant influence on the performance of the FSCW IPM having 24-slot, 14-pole topology are shown in Figure 3.8, which

include rotor radius $RADI$, magnet pole arc β_m , magnet cap depth $IPMHQ$, length of magnet LM , width of magnet per pole $MAGWID$, slot depth SD , stator tooth width TWS , and stator back iron BI . Both the required stator tooth width TWS , and stator back iron BI , are a function of SD and $RADI$, and are dependent on the air-gap flux density and maximum permissible flux density in the teeth and the yoke. In addition, the bridge thickness of the rotor structure and air barriers are also considered to fine tune the design performance during the design process. The air-gap of the machine is assumed to be constant, at 0.5 mm, considering the manufacturing tolerances, and static and dynamic clearances.

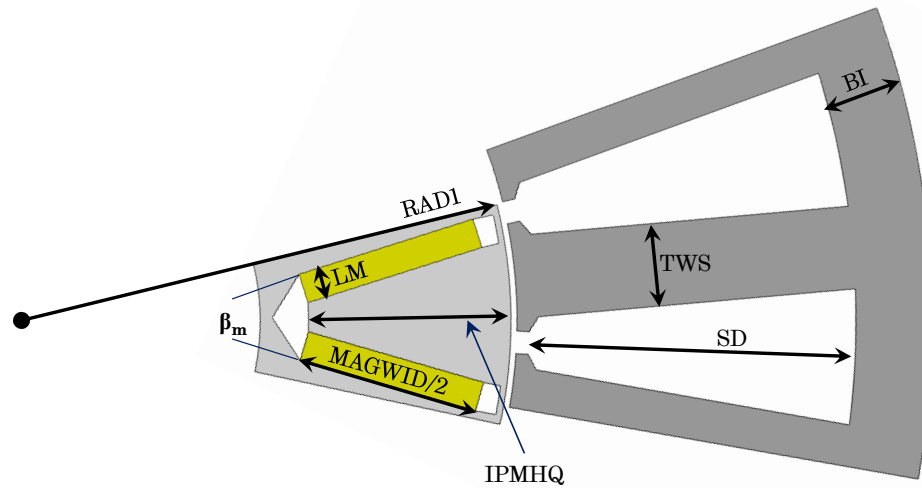


Figure 3.8. Cross-section of FSCW 24-slot, 14-pole IPM with influential geometrical parameters

The design optimization is carried out with an objective to achieve the best possible torque production at the base speed whilst minimizing the losses over the representative driving cycle, NEDC.

Since the torque production is greatly influenced by the rotor radius $RADI$, the stator slot depth SD , and the stator tooth width TWS , these parameters are varied while the current density and magnet volume is kept constant. As the rotor radius increases, the torque production increases. However, there is an optimum rotor radius, beyond which the torque production decreases. This is mainly due to reduction in back iron area resulting into reduced flux linkage when the current density is kept constant. Similar trends are observed for the stator tooth width and

the stator back iron, which are a function of slot depth and current density. Figure 3.9 shows the optimization trends for the FSCW 24-slot, 14-pole IPM. It is seen that for a rotor radius of 40.75 mm, the optimum stator tooth width is found out to be 6.85 mm. Although the optimum stator back iron is 4.296 mm, the back iron thickness is selected to be 6.296 mm in order to keep the peak current per phase at the peak torque and the base speed below the limit of 200 A.

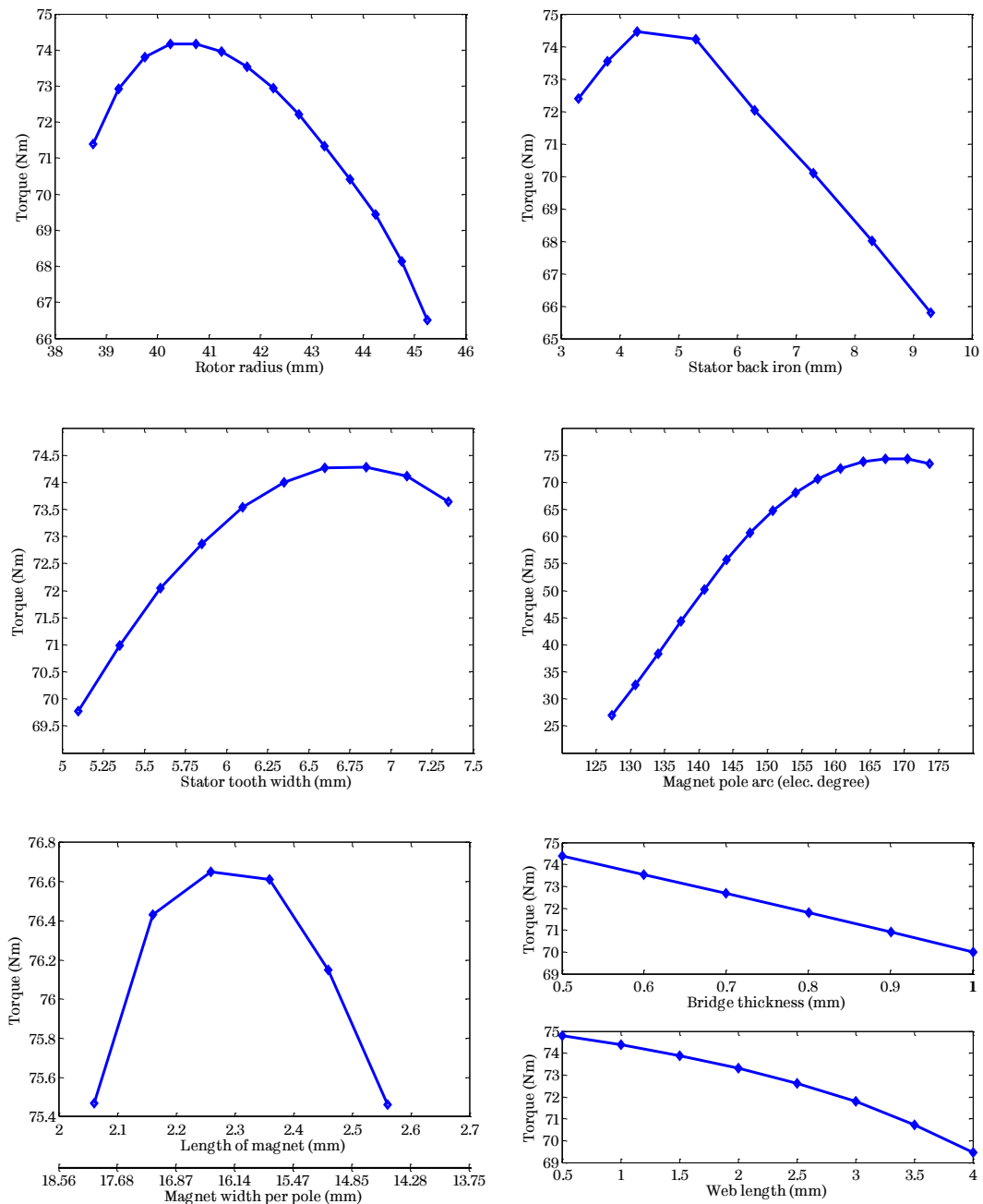


Figure 3.9. Design optimization trends for FSCW 24-slot, 14-pole IPM

The magnet pole arc β_m is optimized to minimize the torque ripple which results from the cogging torque and electro-motive force (EMF) harmonics [88]. For a given magnet mass of 0.9 kg, an optimum combination of magnet length LM and width per pole $MAGWID$ is found out for minimum energy loss over the NEDC without compromising the peak torque and the rated torque performance. The rotor bridge and web are also iterated during the design optimization to achieve best electromagnetic performance without compromising mechanical and structural integrity.

Table 3.2 shows the optimized geometrical parameters of the FSCW 24-slot, 14-pole IPM, whereas the cross-section of the optimized design is shown in Figure 3.10. The performance of the optimized design is discussed in section 3.5.

Table 3.2. Optimized geometrical parameters of FSCW 24-slot, 14-pole IPM

Symbol	Unit	Value	Symbol	Unit	Value
$RADI$	mm	40.75	β_m	deg	167.2
BI	mm	6.296	$IPMHQ$	mm	16.75
TWS	mm	6.85	LM	mm	2.46
SD	mm	26.31	$MAGWID$	mm	30.18
$BRIDGE$	mm	0.5	WEB	mm	1.405

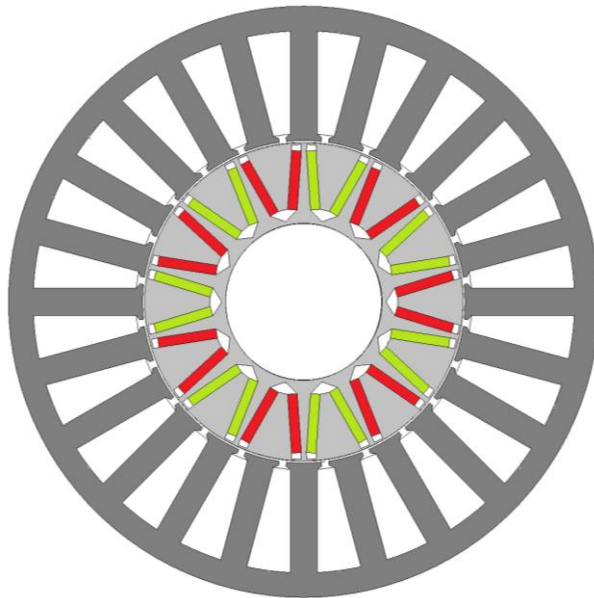


Figure 3.10. Cross-section of the optimized design for FSCW 24-slot, 14-pole IPM

3.4.3 Design optimization of HE-PMFSM with 12-slot, 14-pole

Another promising machine technology selected for assessing its suitability for EV traction is Hybrid Excited Permanent Magnet Flux Switching Machine (HE-PMFSM) having 12-slot, 14-pole topology. For the same volumetric constraints (stator outer diameter of 150 mm and stack length of 118 mm), the geometrical parameters that have most significant influence on the performance are shown in Figure 3.11, which include shaft radius, r_{sh} , rotor outer radius, r_r , rotor pole depth, d_p , rotor pole width, w_p , air-gap length, l_g , height and width of armature slot, h_a and w_a respectively, height and width of PM, h_{pm} and w_{pm} respectively, thickness of stator back iron, w_{bi} , and a parameter defined as f_{offset} , which controls the area of field windings.

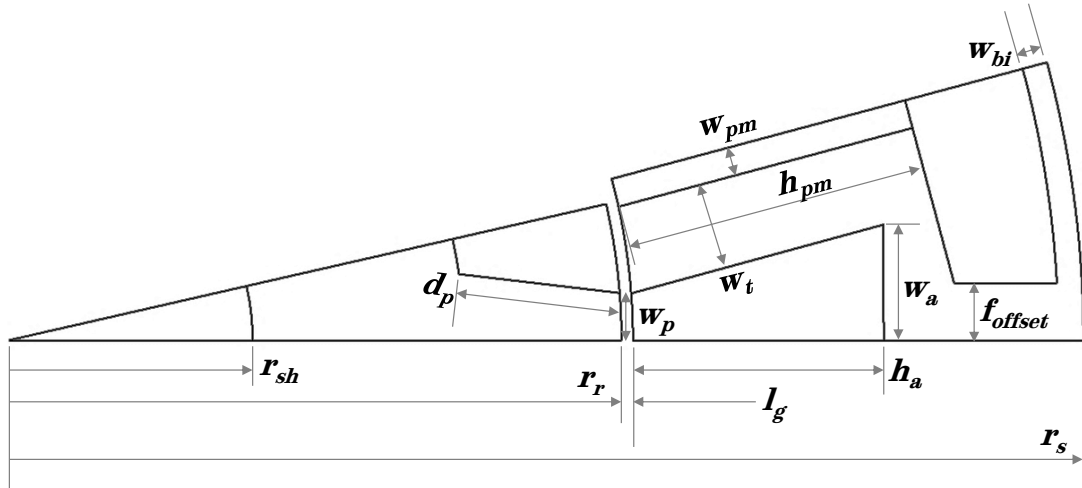


Figure 3.11. Influential geometrical parameters of 12-slot, 14-pole HE-PMFSM

The air-gap of the machine is assumed to be 0.5 mm considering the manufacturing tolerances, and static and dynamic radial clearances. As discussed before, the required stator tooth width and back iron thickness are dependent on the air-gap flux density and maximum permissible flux density in the stator teeth and the back iron.

The design optimization is carried out as per the following steps with an objective to achieve the best possible torque production at the base speed whilst minimizing the losses over the representative driving cycle, NEDC:

- 1) Optimizing the split ratio (r_r/r_s) fixes the outer radius of the rotor. With optimized rotor radius, the best combination for depth and width of the rotor pole (d_p and w_p) is determined.
- 2) Keeping the above parameters fixed, field slot area and its shape is optimized by varying height and width of PM (h_{pm} and w_{pm}), thickness of stator back iron (w_{bi}), and field offset (f_{offset}) with the field current density constrained at 20 A/mm².
- 3) Last, the armature slot area and its shape is optimized by varying tooth width (w_t), height and width of armature slot (h_a and w_a) keeping the parameters optimized in (1) and (2) fixed and with the armature current density constrained at 20 A/mm².

For forced air cooled machines, the continuous current density should be limited to 5-8 A/mm². However, for the peak torque production, the current density of 20 A/mm² will not be thermally challenging as peak torque/power operation is allowed for 1 to 2 minutes as per the IEEE standards.

Figure 3.12 shows the selected design optimization trends with influential geometrical parameters, which are obtained through above design optimization steps. Figure 3.12 (a) shows the peak torque variation with the rotor radius and field current density at 0 A/mm² and 20 A/mm² while maintaining armature current density at 20 A/mm². To illustrate the effect of field control in a hybrid excited PMFSM, torque regulation which is defined as a ratio of the torque at zero field current density to that at the maximum field current density in percentage is also plotted. As the rotor radius increases, the torque production of the motor increases while the torque regulation decreases. The maximum torque regulation is found to be at the rotor radius of 37 mm. In order to optimize the field winding slot area, parameters f_{offset} and w_{pm} are varied over a defined range as shown in Figure 3.12 (b). A decrease in f_{offset} and an increase in w_{pm} increases the field slot area for a constant PM volume. As seen, the torque production peaks with both f_{offset} and w_{pm} at 1.7 mm. Similarly, the armature slot area is optimized by varying w_t , h_a , and w_a over a defined range while maintaining constant armature current density. The change in these parameters affect the saturation level in the armature teeth which in turn impacts the flux linkages, and hence the torque production. As seen in

Figure 3.12 (c), the highest torque production is achieved when h_a and w_a are 20.5 mm and 5.5 mm respectively.

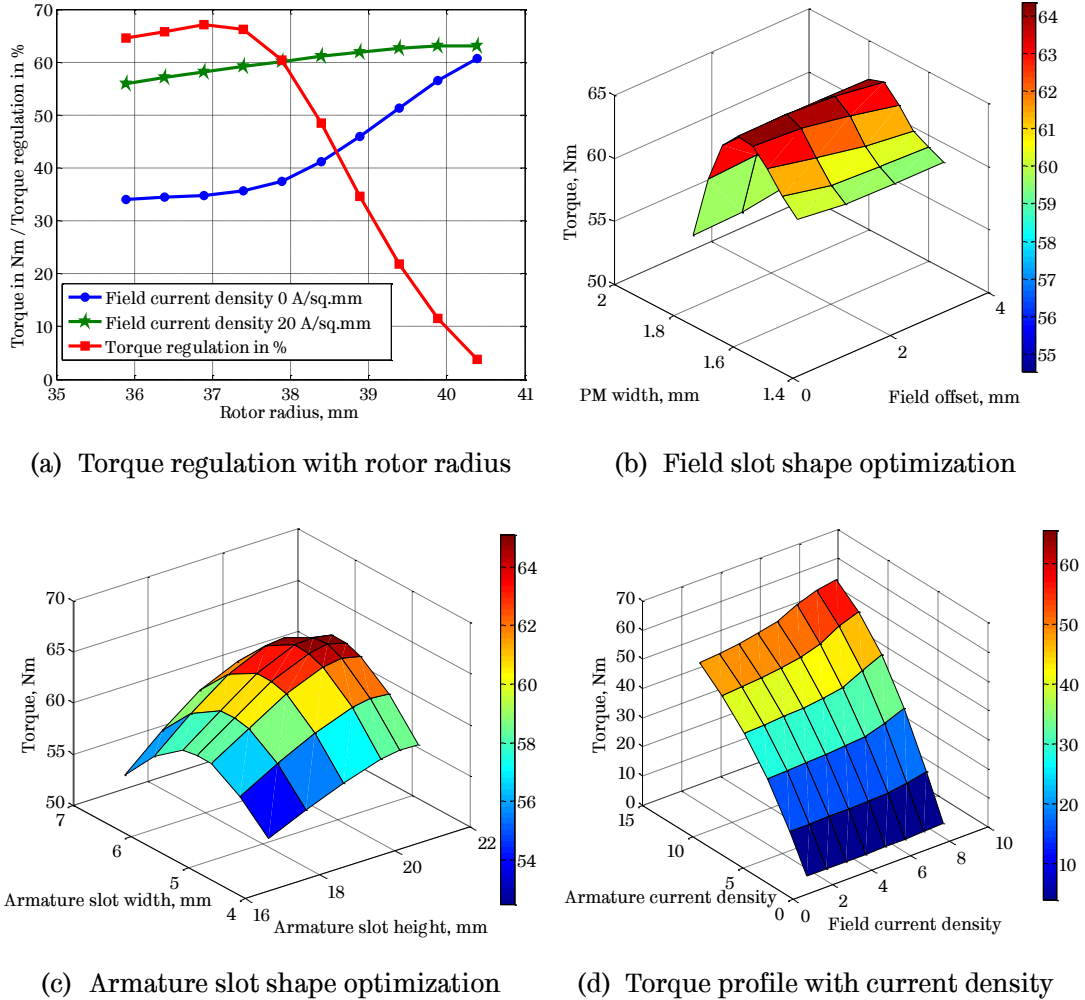


Figure 3.12. Design optimization trends for 12-slot, 14-pole HE-PMFSM

Because of field controllability in a HE-PMFSM, the torque production is greatly influenced by field winding excitation. In order to find the optimum field and armature currents at any given torque, the torque profile is generated by varying both the armature and field current densities as shown in Figure 3.12 (d). For simplicity, torque variation with only positive field current density is shown. The complete torque profile with positive and negative field current density forms an integral part of control system for a HE-PMFSM, which facilitates efficient motor operations at the most optimal combination of armature and field currents. For a specific torque-speed operating point, the optimal combination of iron loss,

and copper loss (both in armature and field) can be obtained by selecting optimum field and armature currents using the loss models, as explained in [89].

During the design optimization process, it becomes apparent that the HE-PMFSM is unable to meet the peak torque requirement with the defined set of the constraints. This is due to the fact that the field regulation is achieved at the expense of reduced volume for the magnets and armature winding. Hence, the optimization is aimed at maximizing the peak torque capability.

Table 3.3 lists the optimized geometrical parameters of the HE-PMFSM which yields a maximum peak torque of 63.8 Nm. Figure 3.13 shows the cross-section of the optimized design for HE-PMFSM. The performance of the optimized design is discussed in section 3.5.

Table 3.3. Optimized geometrical parameters of 12-slot, 14-pole HE-PMFSM

Symbol	Unit	Value	Symbol	Unit	Value
r_r	mm	40.0	w_{bi}	mm	1.8
d_p	mm	9.4	f_{offset}	mm	1.7
w_p	mm	3.25	w_t	mm	5.5
h_{pm}	mm	24.8	w_a	mm	8.8
w_{pm}	mm	1.7	h_a	mm	20.5

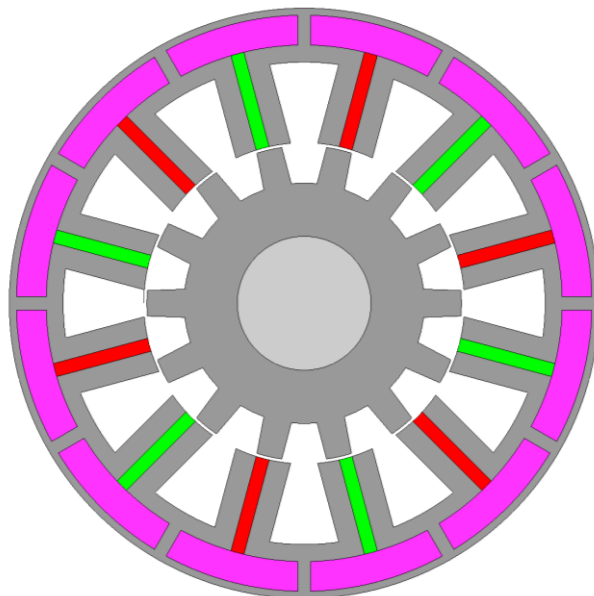


Figure 3.13. Cross-section of the optimized design for 12-slot, 14-pole HE-PMFSM (armature windings are not shown for clarity)

3.5 Performance evaluation of the promising machine technologies

The performance of the optimized design for each of the promising machine technologies is evaluated using 2-D transient FEA.

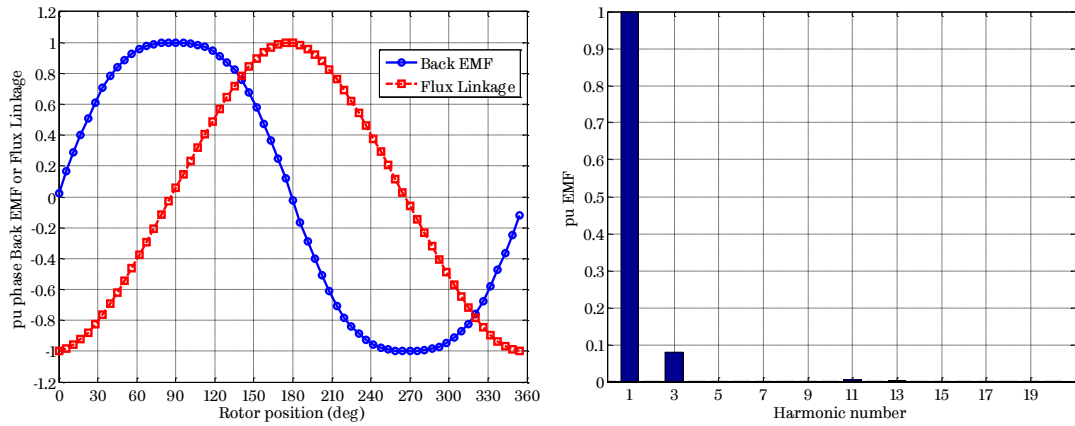
Per unit flux linkage and back EMF of one of the three phases for each of the promising machine technologies is shown in Figure 3.14. The other two phases are not shown for clarity and simplicity. As seen, the FSCW with both SPM and IPM configuration have 3rd EMF harmonic present in its phase back EMF, and its amplitude is higher in IPM than SPM. However, the 3rd harmonic will not affect the machine operation significantly for star-connected 3-phase machines. It is also evident from Figure 3.14 (c) that the phase back EMF and the phase flux linkage waveforms of HE-PMFSM are almost sinusoidal.

The industrial standard for EV traction machines requires the torque ripple be limited below 5% of the peak torque. Hence, it is worthwhile to evaluate the torque ripple of these machine technologies. Figure 3.15 shows the torque ripple over an electrical cycle of the promising machine technologies at the rated and the peak torque operation at the base speed of 1350 rpm.

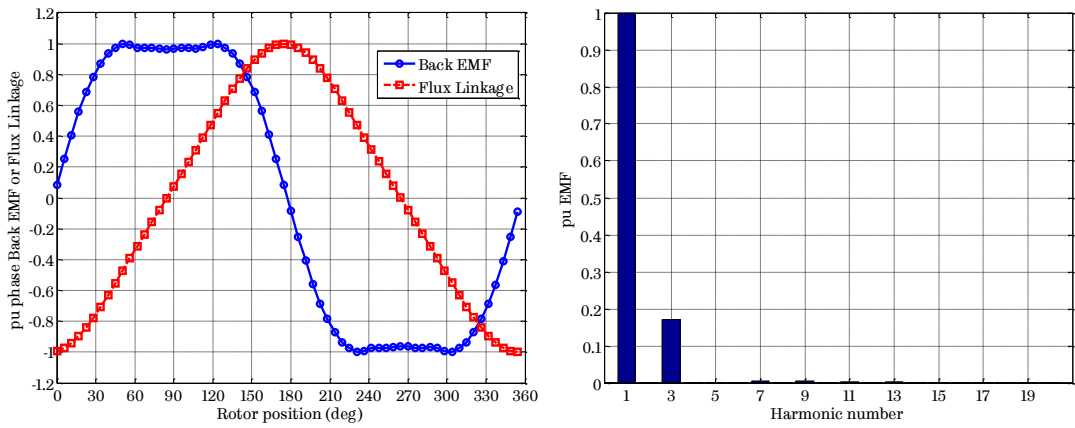
The machine performance at the rated torque and the peak torque when operating at the base speed of 1350 rpm is tabulated in Table 3.4. The energy efficiency over the NEDC is calculated using “*energy centre of gravity*” principle described in [90]. The principle represents the entire NEDC shown in Figure 3.6 into 12 energy concentrated torque-speed points having equivalent energy consumption over the NEDC. The energy efficiency of the motor over the NEDC can be evaluated against these points by ((3.1).

$$\eta_{NEDC} = \frac{\sum_{i=1}^{12} \omega_i T_i dt_i}{\sum_{i=1}^{12} \omega_i T_i dt_i + \sum_{i=1}^{12} (P_{cu-i} + P_{fe-i}) dt_i} \quad (3.1)$$

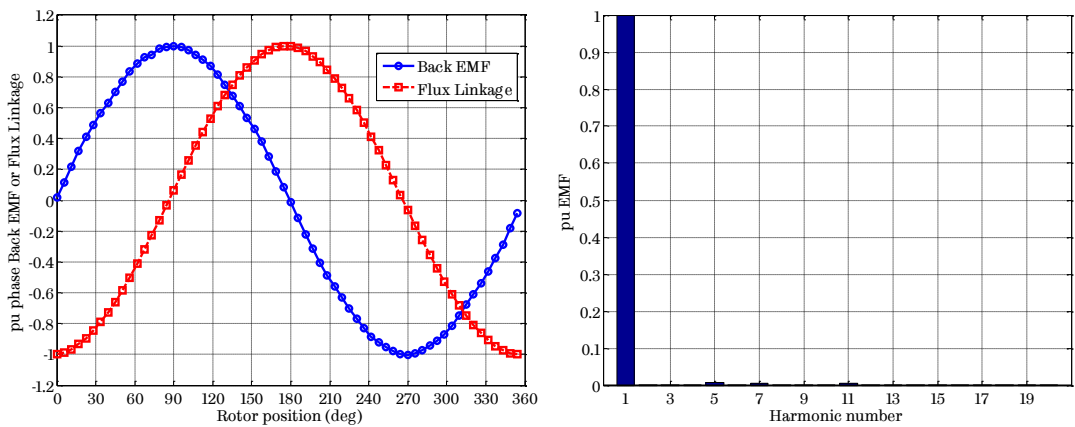
where ω_i and T_i are speed and torque for a specific point i respectively, P_{cu-i} and P_{fe-i} are respective copper loss and iron loss, and dt_i is the time duration for the specific torque-speed point.



(a) SPM 12-slot, 14-pole

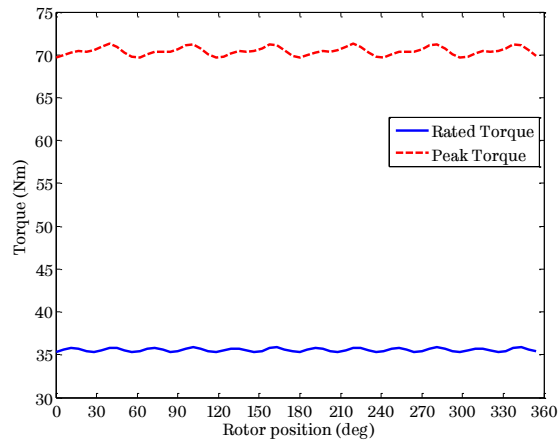


(b) IPM 24-slot, 14-pole

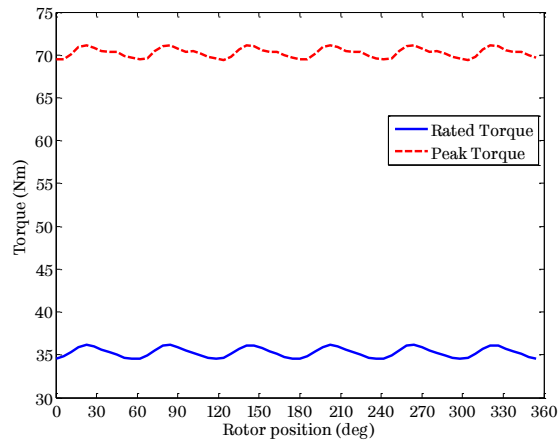


(c) HE-PMFSM 12-slot, 14-pole

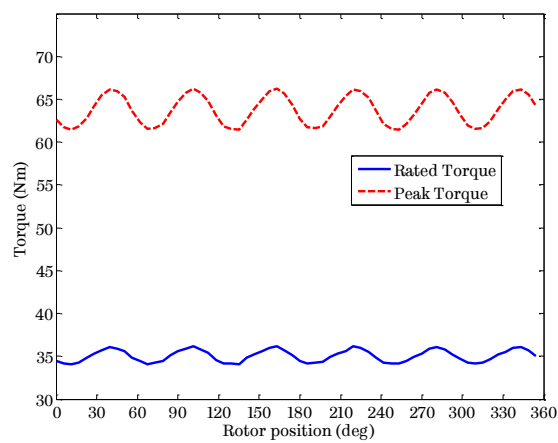
Figure 3.14. Per unit flux linkage, back EMF and EMF harmonics of the promising machine technologies at the base speed of 1350 rpm



(a) SPM 12-slot, 14-pole



(b) IPM 24-slot, 14-pole



(c) HE-PMFSM 12-slot, 14-pole

Figure 3.15. Torque waveforms of the promising machine technologies at the base speed of 1350 rpm

Table 3.4. Performance comparison of the promising machine technologies for EV traction

	Unit	SPM 12s14p		IPM 24s14p		PMFSM 12s14p	
		RT ⁷	PT ⁸	RT	PT	RT	PT
Torque	N·m	35.0	70.0	35.0	70.0	35.0	63.8
Torque ripple	%	0.8	2.3	2.4	2.5	3.1	6.9
Speed	rpm	1350	1350	1350	1350	1350	1350
Peak phase current	A	80.0	165.0	65.0	141.0	46.8	89.1
Peak field current	A	-	-	-	-	0.0	111.1
Total copper loss	W	230	930	203	954	239	2827
Iron loss	W	50	89	92	115	107	200
Efficiency	%	94.5	90.5	94.4	90.3	93.5	74.9
Torque regulation	%	-	-	-	-	19.4	-
Energy Efficiency over NEDC	%	94.0	-	93.5	-	91.7	-

As seen from the above table, the performance of the FSCW SPM and FSCW IPM is comparable, whereas the HE-PMFSM does not meet the peak torque requirement for the selected EV application. In order to achieve the peak torque,

Table 3.5. Performance comparison of the promising machine technologies for EV traction

	Unit	SPM 12s14p		IPM 24s14p		PMFSM 12s14p	
		RT	PT	RT	PT	RT	PT
Stack length	mm	118.0		118.0		129.5	
Torque	N·m	35.0	70.0	35.0	70.0	35.0	70.0
Torque ripple	%	0.8	2.3	2.4	2.5	2.9	6.8
Speed	rpm	1350	1350	1350	1350	1350	1350
Peak phase current	A	80.0	165.0	65.0	141.0	42.0	89.1
Peak field current	A	-	-	-	-	0.0	111.1
Total copper loss	W	230	930	203	954	204	3005
Iron loss	W	50	89	92	115	111	218
Efficiency	%	94.5	90.5	94.4	90.3	94.1	75.4
Torque regulation	%	-	-	-	-	19.4	-
Energy Efficiency over NEDC	%	94.0	-	93.5	-	90.9	-

⁷ RT – Rated torque operation

⁸ PT – Peak torque operation

the stack length of the machine is increased to 129.5 mm from 118.0 mm and the complete design optimization process is repeated. The performance of the HE-PMFSM with longer stack length is shown in Table 3.5. The efficiency at the rated and the peak torque has increased mainly due to lower copper loss and increased torque production on account of increased stack length of the HE-PMFSM machine respectively. However, the NEDC efficiency of the longer HE-PMFSM is about 0.8% lower because of the increased iron loss due to increased stack length of the machine. It should be noted that the torque regulation is independent of the machine stack length.

3.6 Assessment of the promising machine technologies for a micro-sized EV application

In this section, the promising machine technologies are assessed for a micro-sized EV application with respect to various attributes as below:

- 1) Peak torque capability
- 2) Torque ripple
- 3) Efficiency at the rated and the peak torque operation and over the NEDC
- 4) Power electronics converter
- 5) Mechanical structure

The end effects of FSCW SPM and HE-PMFSM will be very similar due to (a) similar slot-pole topology, (b) similar stator outer diameter and stack length, (c) similar tooth wound or concentrated coils in the stator. However, the end effects of FSCW IPM may differ from the above two machine technologies as it employs 24-slot, 14-pole topology with coils wound on the alternate teeth.

Use of simplified 3-D model of end region of machine involving end-windings may be employed to estimate the inductance of end-windings. The resistance of end-winding is estimated by assuming perfect circular end-windings and is accounted in the per phase resistance for the performance estimation.

3.6.1 Peak torque capability

It is evident from Table 3.4 that with the same volumetric and thermal constraints, the optimized FSCW SPM and FSCW IPM machines satisfy the peak torque requirement, whereas the optimized HE-PMFSM does not satisfy the requirement of the peak torque capability. This is mainly due to the fact that excitation using electric coils is less efficient and effective than that of permanent magnets, leading to torque limitation and low efficiency because of (a) higher copper losses and (b) higher iron losses due to saturation in the stator steel. In order to meet the peak torque capability, the active volume of HE-PMFSM must be higher than that of FSCW SPM or FSCW IPM. This can be achieved by increasing either stack length or stator diameter with an additional penalty on efficiency due to increased iron loss.

Although both FSCW SPM and FSCW IPM machines satisfy the requirement of the peak torque capability, FSCW IPM require lesser current to produce the same torque because of the anisotropic effect for the armature reaction field, also known as saliency in the IPM rotors. To produce the same torque, the required phase flux linkage is less in IPM than that in SPM machines, and therefore, the induced EMF at the maximum speed is also lower in IPM than that in SPM machines. Hence, it would be easier to satisfy both the peak torque capability and maximum EMF requirements with IPM than SPM machine technologies.

3.6.2 Torque ripple

In PM machines, the torque ripple results from the cogging torque and/or the EMF harmonics [88]. As seen from Table 3.4 and Table 3.5, the torque ripple of FSCW SPM and FSCW IPM is within the requirement of 5% for EV traction application at both the rated and the peak torque operation. The lower torque ripple in FSCW PM machines may be attributed to (a) lower EMF harmonics as seen from Figure 3.14, and (b) extremely low cogging torque which is achieved by the modular structure of FSCW resulting in to a high winding factor for the fundamental EMF, while reducing the effect on 5th and 7th EMF harmonics

significantly [91]. Also, the saliency of IPM machines results into slightly higher torque ripple than that of SPM machines.

On contrary, although the torque ripple of HE-PMFMSM with 12-slot, 14-pole topology is within the requirement of 5% at the rated torque operation, it is higher than that of FSCW SPM and FSCW IPM machines. Further, the HE-PMFMSM does not meet the torque ripple requirements at the peak torque operation. It is worthwhile to note that other topologies of HE-PMFMSM having 6-slot, 5-/7-pole will exhibit much higher torque ripple than 12-slot, 10-/14-pole topologies. The higher torque ripple for HE-PMFMSM may be attributed to its salient structure of the rotor similar to Switched Reluctance Machines (SRM).

3.6.3 Efficiency at the rated and the peak torque operation and over the NEDC

From Table 3.5, it is clear that the optimized FSCW IPM has slightly lower efficiency at the rated and the peak torque operation than its SPM counterpart. At the rated torque operation, FSCW IPM has lower copper loss due to lower current required to produce the same torque compared to SPM because of the reluctance torque capability of IPM machines. Whereas, at the peak torque operation, FSCW IPM has higher copper loss because (a) it requires more current to produce the peak torque because of localized saturation in rotor magnetic structure and stronger armature reaction, and (b) higher per phase resistance due to longer end windings compared to FSCW SPM. The susceptibility of FSCW IPM to magnetic saturation also results into higher iron loss in FSCW IPM at both the rated and the peak torque operation compared to FSCW SPM.

Among all three promising machine technologies, HE-PMFMSM is inferior to both FSCW SPM and FSCW IPM with respect to efficiency at the rated and the peak torque operation. The efficiency of the optimized HE-PMFMSM at the rated torque operation is slightly lower (~0.4%) than that of FSCW SPM, however, at the peak torque operation, the efficiency is significantly lower (~15.1%) compared to FSCW SPM.

The energy efficiency over the NEDC calculated using *energy centre of gravity* principle for all the three machine technologies is also compared in Table

3.5. The FSCW SPM and FSCW IPM clearly outshine the HE-PMFSM with respect to energy efficiency over the NEDC. The lower energy efficiency of HE-PMFSM is mainly due to higher iron loss of HE-PMFSM in continuous torque-speed envelope as almost all the NEDC points are within the continuous torque-speed envelope of the machine for the selected micro-sized EV application as shown in Figure 3.16. A significant portion of the iron loss is from the rotor which experiences alternating magnetic field. In the continuous torque range, the total copper loss of HE-PMFSM is slightly lower than that of FSCW SPM, however, for the peak power/torque operation at all speeds, the copper loss will be higher as more current is required to generate the demand torque because of saturation. The HE-PMFSM with 6-slot, 5-/7-pole configuration will have almost half the iron losses compared to 12-slot, 10-/14-pole configuration as the fundamental frequency is half, however, they have large torque ripple. Unless skewing is employed with penalty in manufacturing cost, 6-slot, 5-/7-pole HE-PMFSM will not be an attractive option for EV application.

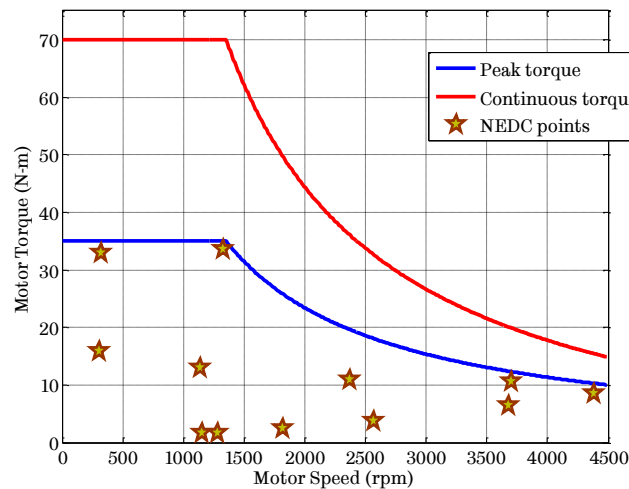


Figure 3.16. Torque-speed characteristics of the machine with 12 NEDC points

3.6.4 Power electronics converter

As discussed, due to lower current requirement to produce the same torque for FSCW IPM than its SPM counterpart, the inverter VA rating of the FSCW IPM design will be lower than the FSCW SPM design.

HE-PMFSM will require additional power electronics to control the bi-directional DC field excitation. This can be achieved by a simple H-bridge DC-DC

converter as part of the drive. Hence, the cost of power electronics is higher than that of FSCW SPM or FSCW IPM.

3.6.5 Mechanical structure

For EV traction applications, a robust mechanical structure is required for both the stator and the rotor. It is easier and simpler to design such a structure as an integral part of the stator frame for FSCW IPM and HE-PMFSM than to contain PM on the rotor surface with either a metallic non-magnetic sleeve or glass/carbon fibre banding layer in FSCW SPM. Also, both FSCW IPM and SPM will require additional detailed mechanical and rotor dynamics analysis during the design process if they are to use in EV applications having high speed requirements.

3.7 Summary

This chapter has presented comprehensive assessment of the FSCW SPM, FSCW IPM, and HE-PMFSM for a micro-sized EV application. For each of them, the characteristic features are discussed and the design optimization is described. It has been shown that while the HE-PMFSM is an attractive concept for EV application, this machine technology has a number of drawbacks compared to other competing PM machine technologies. First, it has a lower torque density since the field windings are less effective in producing magnetic field in the air-gap than the permanent magnets and they compete with the armature windings and the magnets for limited space on the stator under a given thermal and volumetric constraints. In addition, significant amount of iron loss which exists on the rotor compromises the machine efficiency at higher speeds. These drawbacks tend to outweigh the benefits of variable field excitation, particularly when the machine size is relatively small. Consequently, its peak torque capability, efficiency at the rated and the peak torque operations, and energy efficiency over the NEDC are lower, while torque ripple is higher than that of FSCW PM machines (SPM and IPM). It remains to be challenging to realize a competitive hybrid excited permanent magnet flux switching machine for EV applications.

Although FSCW SPM and FSCW IPM machines are very competitive for EV applications, selection of SPM or IPM rotors depends on various requirements,

which include controllability and high speed operability. SPM has better controllability due to low saturation level and less operation-dependent parameter variations compared to IPM. For EV application, high torque requirement at low speed conflicts with low back EMF requirement at high speed for safety which cannot be met simultaneously, making FSCW SPM less attractive than FSCW IPM.

Chapter 4

Novel Fractional-slot per Pole per Phase Winding Configuration with Low Space Harmonics Content

This chapter introduces fractional-slot per pole per phase winding configurations for permanent magnet machines. The development of novel fractional-slot per pole per phase winding configuration having low space harmonics content is presented. This winding configuration is applied to a segment-A vehicle with centralized power drivetrain to design multi-phase electric traction machine, which enhances the availability of the power drivetrain. The optimum phase shifts between two sets of 3-phase systems is also evaluated.

The main contents of this chapter has been published by the author in [92] and [93].

The fractional-slot per pole per phase winding configurations were first conceptualized by Tingley in 1915 [94], who devised a means of laying out winding by the lowest common multiple (LCM) method. Later on, in 1940, Malati *et al.* [95] developed theory underlying m -phase fractional-slot in order to define rules of procedure for the designer. All these fractional-slot windings were distributed in nature and are still being used in medium and large 3-phase synchronous machines. Recently, a relatively newer winding configuration for permanent magnet (PM) brushless machines, which is often referred to as “fractional-slot concentrated” or “modular”, has emerged [16, 17, 88, 96].

4.1 Characteristic features of fractional-slot per pole per phase PM machines

The characteristic features of fractional-slot concentrated winding (FSCW) offers a number of significant advantages, over conventional PM brushless machines, which are particularly suitable for many applications.

- 1) The coils which belong to each phase are concentrated and wound on consecutive teeth or alternate teeth, so that the phase windings do not overlap. This is not only a distinctive manufacturing advantage [97], but also conducive to a high copper packing factor and lower end-winding losses, and, hence, high efficiency [91], and to reducing the likelihood of an inter-phase fault.
- 2) It results in a small number of slots for a given number of poles, e.g., 18 slots for a 16-pole machine, as compared to 24 slots for a conventional 16-pole brushless DC winding, and a minimum 48 slots for a conventional 16-pole brushless AC winding.
- 3) The modular structure of the winding configuration gives rise to a high winding factor for the fundamental electromotive force (EMF), while the effect on the 5th and 7th EMF harmonics is being significantly reduced. This yields extremely low cogging torque without the use of skew [98].

Hence, a fractional-slot PM brushless machine has a higher torque capability, high efficiency and a lower torque ripple than PM brushless machine equipped with conventional windings.

In fractional-slot PM brushless machines, however, the stator magnetomotive-force (MMF) distribution contains a large number of space harmonics [16, 17, 99]. The electromagnetic torque results from the interaction of a high order stator MMF harmonic, known as working harmonic, with the field produced by the permanent magnets. Lower and higher order stator MMF harmonics, relative to the working harmonic, which rotate at different speeds relative to the rotor, will, therefore, cause undesirable effects, such as localized core saturation, eddy current loss in permanent magnets [100, 101], and acoustic noise and vibrations, which are the main disadvantages of the fractional-slot PM machines. These space harmonics also make it difficult to obtain high reluctance torque from IPM machines with fractional-slot winding configurations [84]. Table 4.1 compares the total harmonic distortion (THD) and most dominant MMF space harmonics of the fractional-slot PM machines and conventional distributed PM machines.

Table 4.1. Comparison of working harmonic, most dominant higher and lower order space harmonics, and total harmonic distortion for various slot-pole combinations

	Working harmonic	Higher order	Lower order	Lower order	THD (%)
9-slot, 8-pole	4 1.0 pu	5 0.8 pu	2 0.296 pu	1 0.257 pu	107.0 %
9-slot, 10-pole	5 1.0 pu	13 0.385 pu	4 1.563 pu	2 0.37 pu	153.4 %
12-slot, 10-pole	5 1.0 pu	7 0.714 pu	1 0.359 pu	-	96.2 %
12-slot, 14-pole	7 1.0 pu	17 0.412 pu	5 1.4 pu	1 0.503 pu	166.5 %
18-slot, 16-pole	8 1.0 pu	10 0.8 pu	4 0.296 pu	2 0.257 pu	105.6 %
18-slot, 20-pole	10 1.0 pu	26 0.385 pu	8 1.25 pu	4 0.37 pu	151.8 %
48-slot, 8-pole	4 1.0 pu	20 0.054 pu	-	-	15.0 %
48-slot, 16-pole	8 1.0 pu	40 0.2 pu	-	-	26.2 %

As seen from the above table, the fractional-slot per pole per phase windings (listed in black) produce a large number of stator MMF space harmonics compared to conventional integral slot per pole per phase distributed windings (listed in blue).

4.1.1 Mitigation of the demerits of FSCW configuration

To fully exploit the advantages of FSCW configuration, it is necessary to mitigate its detrimental effects. Among a number of techniques reported in the literature to mitigate them, the most common approach is to segment the rotor magnets both axially and circumferentially in order to reduce the eddy current loss on the rotor [102]. Without this, the heat generated by the eddy current loss in the rotor magnets may be excessive and may result in irreversible partial demagnetization [103]. However, this significantly increases the manufacturing cost and material usage (materials being wasted during segmentation process), and does not address the other undesirable effects of the FSCW configuration.

As mentioned in section 3.1.2, Dajaku *et al.* [104] have reported a new 24-slot, 10-pole machine topology to reduce the sub- (low order) and high order stator MMF harmonics of the conventional 12-slot, 10-pole FSCW by dividing the 3-phase windings into two sets and placing an appropriate phase shift between the two. However, this is achieved with a small reduction of the winding factor for the fundamental EMF component, which compromises the torque density and efficiency (as seen from the preliminary design study in Chapter 3), while the first space harmonic is not much affected. To reduce these harmonics, further methods have been described in [70] by (a) using different number of turns per coil for the neighbouring phase coils or (b) employing coil windings with different number of turns per coil side. This leads to uneven stator tooth width and more complex winding configuration with further reduction in the fundamental EMF winding factor. Further, for a variety of applications, 24-slot, 10-pole may not be the best slot-pole combination which yields the optimal performance. An alternate approach to reduce the most harmful MMF space harmonics (1st and 7th) is described in [105] by developing 18-slot, 10-pole winding configuration with two sets of concentrated windings with star-delta (Y- Δ) connections, which helps in reducing radial force mode of the machine by completely eliminating 7th MMF space harmonics. However, this configuration has very low winding factor for fundamental EMF (~ 0.76) and employs different number of turns for star (Y) and delta (Δ) windings, which impose challenges to achieve (a) higher torque density, and (b) ease of manufacturing.

The concept of stator shifting is investigated in [106] to assess its effect on various harmonic components of stator MMF, winding factor, power density, and efficiency (both at low speeds and in flux-weakening region) as well as torque ripple for various slot-pole combinations of FSCW configurations. This technique works more effectively in designs with a single sub-harmonic (low order harmonic), whereas the improvement is compromised for slot-pole combinations having multiple sub-harmonics. Also, it introduces uneven tooth width in the stator, which may lead to reduction of peak torque capability due to uneven flux density levels in the stator teeth.

In order to eliminate the most harmful space harmonics of FSCW configurations in a simple and cost-effective way, a novel fractional-slot per pole

per phase winding configuration for electrical machines has been devised in this chapter. It is applicable to a range of electrical machine technologies, viz. permanent magnet machines, induction machines, synchronous wound field machines, and synchronous reluctance machines; and also, improves both torque/power density and efficiency of these different machine technologies for a variety of applications.

4.2 Novel 3-phase fractional-slot per pole per phase winding configurations with low space harmonics

For the purpose of description, let p denotes the number of pole-pairs and q being defined as the ratio of the number of slots per phase to the number of poles. For an m -phase machine, q is given by (4.1).

$$q = \frac{N_s}{m(2p)} = \frac{N_s}{2mp} \quad (4.1)$$

where N_s denotes the number of stator slots.

For the conventional distributed winding configuration, q is an integer. For hydro-generators, the fractional-slot per pole per phase windings, having $q > 1$ but not integer, are usually employed, however, the windings are distributed in nature; usually referred to as “*fractional-slot distributed windings*”. For 3-phase machines with concentrated winding configurations in prior arts, q is a fractional number, from where the term “*fractional-slot per pole per phase*” is derived.

Many feasible slot-pole combinations exist for fractional-slot per pole per phase machines [95, 107]. In a subset of these combinations the slot number N_s is related to the number of pole-pairs p by $N_s = 2p \pm 1$. For 3-phase machines, N_s must be divisible by 3 and the phase shift in electrical degrees between phases must equal to $\pm 360k + 120$, where $k = 0, 1, 2, 3, \dots$. The resulting slot-pole combinations which are known in the prior art are listed in Table 4.2 for $p \geq 4$ and up to 25. It also lists the corresponding q for each slot-pole combination.

Table 4.2. Slot-pole combinations of prior art

No. of pole-pairs	Feasible slot number	q	No. of pole-pairs	Feasible slot number	q
4	9	3/8	16	33	11/32
5	9	3/10	17	33	11/34
7	15	5/14	19	39	13/38
8	15	5/16	20	39	13/40
10	21	7/20	22	45	15/44
11	21	7/22	23	45	15/46
13	27	9/26	25	51	17/50
14	27	9/28

It should be noted that any integer multiple of the slot and pole numbers of a given slot-pole combination in the above table also results in a feasible combination with the same q . For example, 18-slot, 16-pole, and 27-slot, 24-pole, etc. They all have the same $q = 3/8$. While the machine designs with these slot-pole combinations have all the advantages of fractional-slot per pole per phase PM machines, they also result in a large number of undesirable MMF harmonics and unbalanced radial magnetic force in the air-gap [82, 108].

In order to reduce the undesirable MMF space harmonics significantly and to eliminate the unbalanced magnetic force associated with the slot-pole combination listed in Table 4.2, and any other combination derived from integer multiple of a given combination, the proposed technique can be summarized in the following steps:

- 1) Configure a 3-phase winding for a given slot-pole combination described above according to the prior art.
- 2) Double the number of slots of the design.
- 3) Divide the 3-phase winding into two 3-phase sets denoted by A1-B1-C1 and A2-B2-C2. Each 3-phase winding is configured in the same pattern as that in step (1).
- 4) Position the second 3-phase winding (A2-B2-C2) 180 mechanical degrees away with respect to the first 3-phase winding (A1-B1-C1). A1 and A2 are connected either in series or in parallel with the same

polarity if the pole-pair number is even, or opposite polarity if pole-pair number is odd. Similar connections are made for B1 and B2, and C1 and C2.

It will become clear that the $N_s = 2p \pm 1$ slot-pole combination has a unique property in that by adopting the above steps, all even harmonics for odd pole-pair number p , or all odd harmonics for even pole-pair number p are eliminated without affecting the fundamental winding factor. For $N_s = 2p \pm 2$ slot-pole combination, this is not possible.

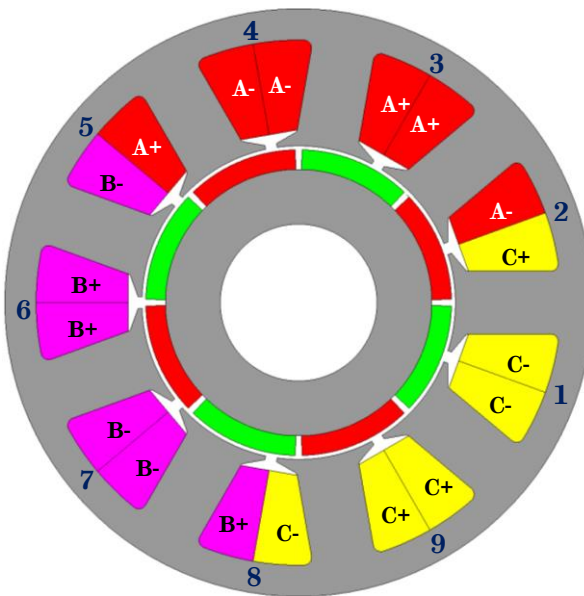


Figure 4.1. Schematic of 3-phase, 9-slot, 8-pole winding configuration as per prior art

Without the loss of generality, Figure 4.1 shows the stator with 9-slots and a surface mounted permanent magnet (SPM) rotor with 8-poles placed concentrically inside. The stator windings which are inserted in the stator slot comprise 3 phases denoted as A, B and C. Each phase winding consists of three series connected coils formed by windings wired around a tooth with the polarity indicated by “+” and “-“. The coil span is one slot-pitch or $360^\circ/9 = 40^\circ$ mechanical.

4.2.1 Proposed 3-phase, 18-slot, 8-pole winding configuration

To reduce the undesirable harmonics significantly and eliminate the unbalanced magnetic force, the number of slots is doubled to 18, and the stator windings are separated into two 3-phase sets, as shown in Figure 4.2. The first 3-

phase windings denoted as A1-B1-C1 and the second 3-phase windings as A2-B2-C2, follow the same pattern as in Figure 3.1. In this case, however, the coil span is now two slot-pitches instead of one slot-pitch because the number of slots have been doubled, but it has the same mechanical angle of 40° because one slot-pitch is 20° ($= 360^\circ/18$) mechanical. For an 8-pole rotor, the electrical degree of a slot-pitch is $360^\circ \times 4/18 = 80^\circ$.

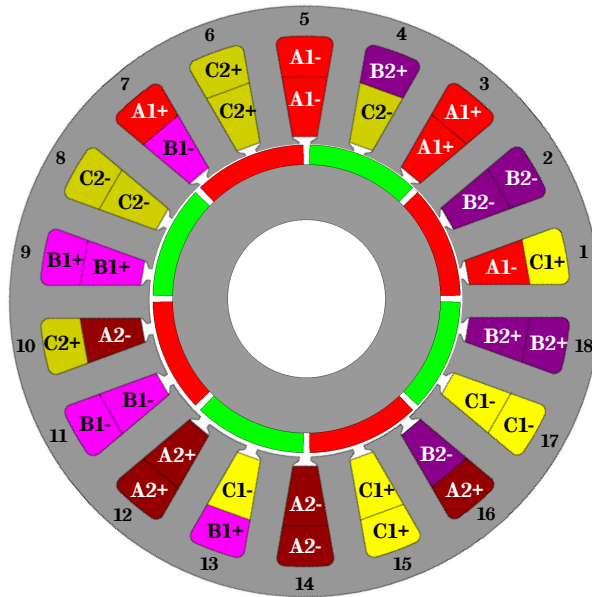


Figure 4.2. Schematic of proposed 3-phase, 18-slot, 8-pole winding configuration

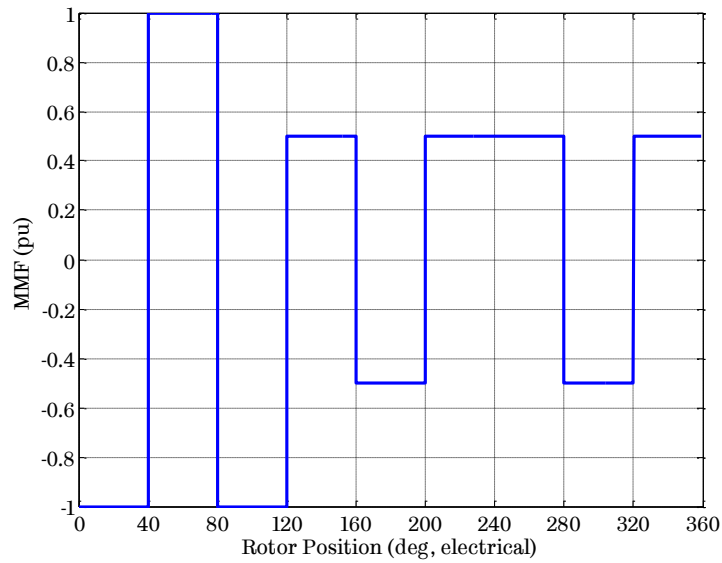
The second 3-phase windings A2-B2-C2 are positioned with respect to the first 3-phase windings A1-B1-C1 by an offset of 180° mechanical or 9 slot-pitches. The offset in electrical degree is 720° or 4π . Thus, if phase windings A1 and A2 are connected in series or in parallel with the same polarity, and similar connections are made for B1 and B2, and C1 and C2, respectively, the resultant 4th order MMF space harmonic produced by the first 3-phase windings (A1-B1-C1) and the second 3-phase windings (A2-B2-C2) are in phase with respect to each other. The 4th order space harmonic has the same number of pole-pairs as that of the rotor, and its interaction with the 4 pole-pair rotor magnetic field produces the electromagnetic torque. For all odd ($n = 1, 3, 5, 7, \dots$) space harmonics, the phase shift between the harmonics produced by the first 3-phase winding and those by the second 3-phase windings is $n\pi$. Thus these harmonics have the same magnitude but in the opposite

direction, and hence will be cancelled with each other by the proposed winding configuration.

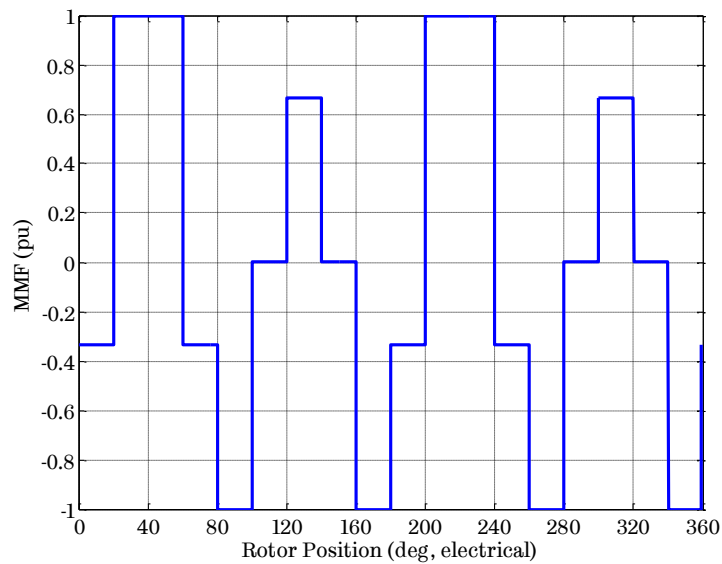
Thus, the winding configuration shown in Figure 4.2 results in the highest possible winding factor of 0.945 for the 4th order working space harmonic, and completely eliminates all odd space harmonics, while preserving the key advantages of the fractional-slot per pole per phase winding configuration. The end-windings are slightly longer than conventional concentrated windings, whereas they are much shorter than the distributed windings. Also, the end-windings of different phase coils, being in parallel, can be easily insulated using coil separators, which in turn reduce the likelihood of inter-phase faults. Further, the normal magnetic force produced by the first 3-phase windings is cancelled by that produced by the second 3-phase windings, thereby, eliminating unbalanced magnetic pull in the radial direction and reducing sensitivity to a rotor eccentricity. In addition, by eliminating the most significant harmonic due to armature reaction, the resultant radial force harmonics have also been greatly reduced. All these benefits of the proposed winding configuration are conducive for reducing bearing friction loss, noise and vibrations.

The stator MMF profile for 3-phase, 9-slot, 8-pole machine and the proposed 3-phase, 18-slot, 8-pole machine is shown in Figure 4.3 (a) and (b) respectively.

Figure 4.4 (a) shows the normalized stator MMF space harmonics distribution produced by 3-phase windings in Figure 3.1 or one of the 3-phase windings, viz. A1-B1-C1 or A2-B2-C2, in Figure 4.2. As will be seen, the MMF contains forward rotating harmonics for $n = 1, 4, 7, \dots$, backward rotating harmonics for $n = 2, 5, 8, \dots$, and zero triple harmonics. For the 8-pole machine, however, only the 4th MMF space harmonic interacts with the magnetic field of the rotor to produce continuous torque. The other harmonics, in particular, the backward rotating 5th, which has relatively large magnitude, and rotates at the twice of speed with respect to the rotor, may cause undesirable effects, such as localized core saturation, additional iron loss, and eddy current loss in the magnets, etc., as described before.



(a) 3-phase, 9-slot, 8-pole

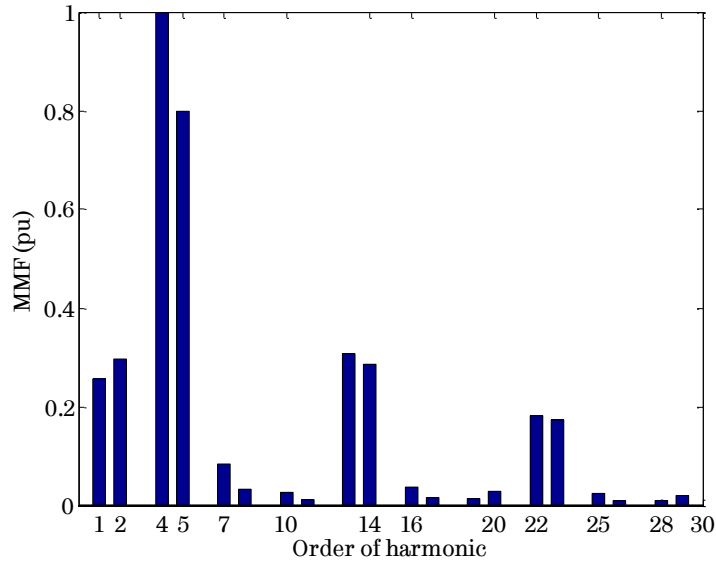


(b) 3-phase, 18-slot, 8-pole

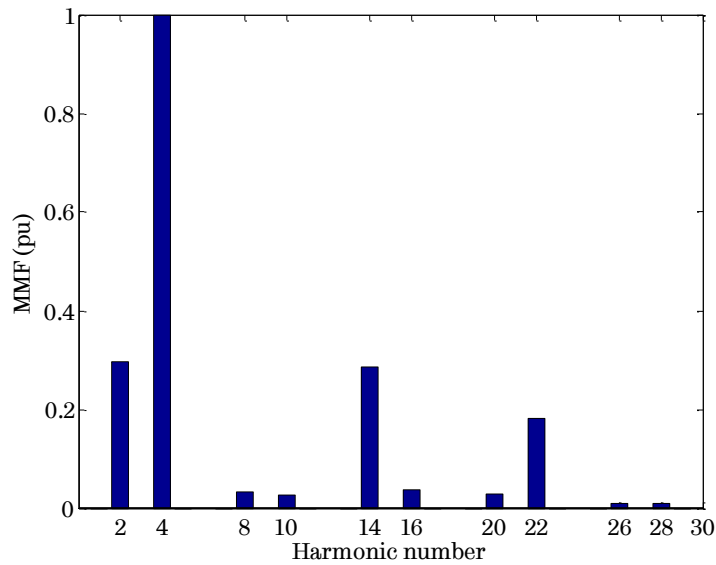
Figure 4.3. Stator MMF profiles of 9-slot, 8-pole and the proposed 18-slot, 8-pole winding configurations

Figure 4.4 (b) shows the normalized MMF space harmonic distribution produced by the two sets of 3-phase windings shown in Figure 4.2. As will be seen, all odd space harmonics have been eliminated. The remaining space harmonics have relatively low magnitude except for the 2nd, 14th, and 22nd. However, since the wave-length of the 14th and 22nd harmonics is relatively short, the resulting magnetic field due to these harmonics will be attenuated rapidly in the radial

direction towards the rotor, as can be seen from the analytical expression given in [16]. Therefore the undesirable effects caused by these harmonics will be much less significant. Likewise, the frequency of 2nd harmonic seen by the rotor is relatively low, and the resultant undesirable effect is also significantly less.



(a) 3-phase, 9-slot, 8-pole



(b) 3-phase, 18-slot, 8-pole

Figure 4.4. Normalized stator MMF space harmonics distribution

It is worthwhile to note that the total harmonic distortion (THD) of the proposed 3-phase, 18-slot, 8-pole winding configuration is 50.4 %, which is much

less than any of the conventional fractional-slot winding configuration, listed in Table 4.1.

4.2.2 Proposed 3-phase, 18-slot, 10-pole winding configuration

The same concept is applicable to form an 18-slot, 10-pole machine from 9-slot, 10-pole counterpart shown in Figure 4.5 (a). Compared with 9-slot, 8-pole design shown in Figure 3.1, the only difference in 9-slot, 10-pole design is that the positions of phases B and C are swapped. The resulting winding configuration is illustrated in Figure 4.5 (b), where the positions of coils pertaining to phase B and C are also swapped and the phase windings A1 and A2 are connected in series or in parallel with the opposite polarity. Similar connections are made for phase windings B1 and B2, and C1 and C2. For the 10-pole machine, the working MMF space harmonic is the 5th order, and the phase shift between the first 3-phase winding set, and the second 3-phase winding set is $(360^\circ/18) \times 5 \times 9 = 900^\circ$ or 5π . Thus by connecting the two windings in each phase with opposite polarity, the winding factor for the 5th harmonic is not affected, while all even harmonics are eliminated.

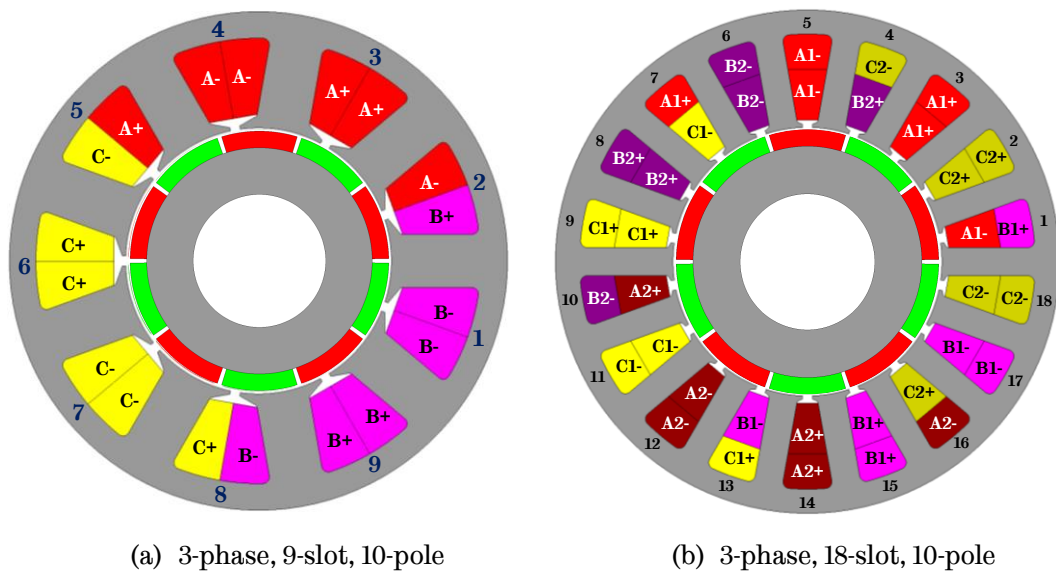


Figure 4.5. Schematic of 9-slot, 10-pole and proposed 18-slot, 10-pole winding configuration

Figure 4.6 shows the resultant normalized MMF space harmonic distribution produced by the two 3-phase windings for 10-pole machine shown in

Figure 4.5 (b). As will be seen, all even space harmonics have been cancelled. The remaining harmonics have relatively low magnitude except for the 1st, 13th, and 23rd. However, for the same reasons as explained for the 18-slot, 8-pole machine, the undesirable effects caused by these harmonics will be much less significant, and the unbalanced magnetic force in the radial direction is also eliminated.

It is worthwhile to note that the THD of the proposed 3-phase, 18-slot, 10-pole winding configuration is 62.6 %, which is much less than any of the conventional fractional-slot winding configuration, listed in Table 4.1.

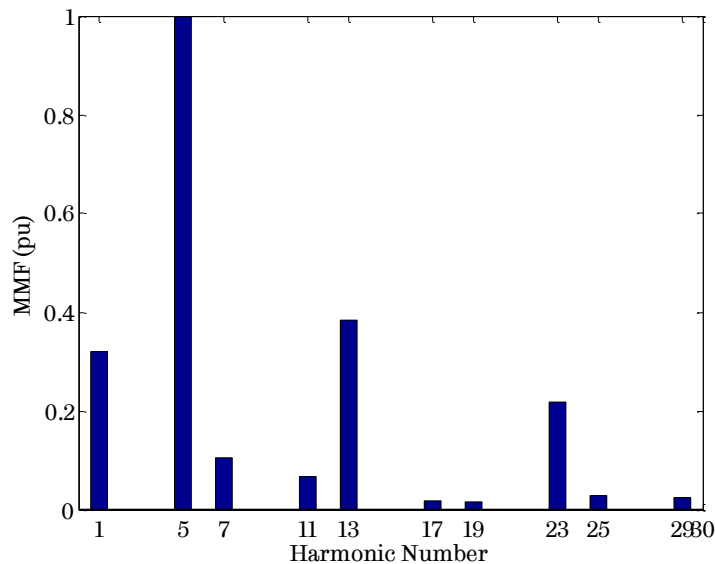


Figure 4.6. Normalized stator MMF space harmonics distribution for the proposed 3-phase, 18-slot, 10-pole winding configuration

By applying the similar concept to all slot-pole combinations listed in Table 4.2, a new set of slot-pole combinations in Table 4.3 are derived that yield significant reduction in undesirable MMF space harmonics and elimination of unbalanced magnetic force.

It is worthwhile to note that the effect of stator slotting on air-gap magnetic field is ignored in the harmonic distribution. However, as observed from 2-D FEA with magnet turned off, the effect of slotting for 18-slot, 8-pole machine is not significant. The winding functions for all these configurations are described in Appendix A.

Table 4.3. Proposed slot-pole combinations having low space harmonics in stator

MMF

No. of pole-pairs p	Slot number N_s	Slot/pole/phase q	Offset between two 3-phase windings (no. of slots)	Polarity between two 3-phase windings
4	18	3/4	$N_s/2 = 9$	same
5	18	3/5	$N_s/2 = 9$	opposite
7	30	5/7	$N_s/2 = 15$	opposite
8	30	5/8	$N_s/2 = 15$	same
10	42	7/10	$N_s/2 = 21$	same
11	42	7/11	$N_s/2 = 21$	opposite
13	54	9/13	$N_s/2 = 27$	opposite
14	54	9/14	$N_s/2 = 27$	same
16	66	11/16	$N_s/2 = 33$	same
17	66	11/17	$N_s/2 = 33$	opposite
19	78	13/19	$N_s/2 = 39$	opposite
20	78	13/20	$N_s/2 = 39$	same
22	90	15/22	$N_s/2 = 45$	same
23	90	15/23	$N_s/2 = 45$	opposite
25	102	17/25	$N_s/2 = 51$	opposite
...

4.2.3 Proposed 3-phase, 36-slot, 10-pole winding configuration

The same concept is applicable to any slot-pole combination with q listed in Table 4.3, for example, 36-slot 16-pole, 54-slot 24-pole, ..., etc., machines whose slot-pole number are integer multiples of 18-slot, 8-pole with $q = 3/4$. As will be seen, the phase shift between the two 3-phase windings is always equal to 180° mechanical or half of the number of slots, whilst the polarity of the two 3-phase windings is the same for even number of pole-pairs and opposite for odd number of pole-pairs.

For the slot-pole combinations with even number of pole-pairs, the same phase shifting technique can be employed to further eliminate undesirable harmonics. For an example of 18-slot, 8-pole design shown in Figure 4.2, the number of slots is first doubled to 36 as shown in Figure 4.7, and the stator winding is divided into two sets of 3-phase windings. The first 3-phase windings denoted as

A1-B1-C1 and the second 3-phase windings A2-B2-C2 follow the same pattern as that shown in Figure 4.2. In this case, the coil span is now 4 slot-pitches instead of 2 slot-pitches, because the number of slots is doubled, but it has the same mechanical angle of 40° . One slot-pitch spans $10^\circ (=360^\circ/36)$ mechanical. For an 8-pole rotor, the electrical degree of a slot-pitch is $360^\circ \times 4 / 36 = 40^\circ$.

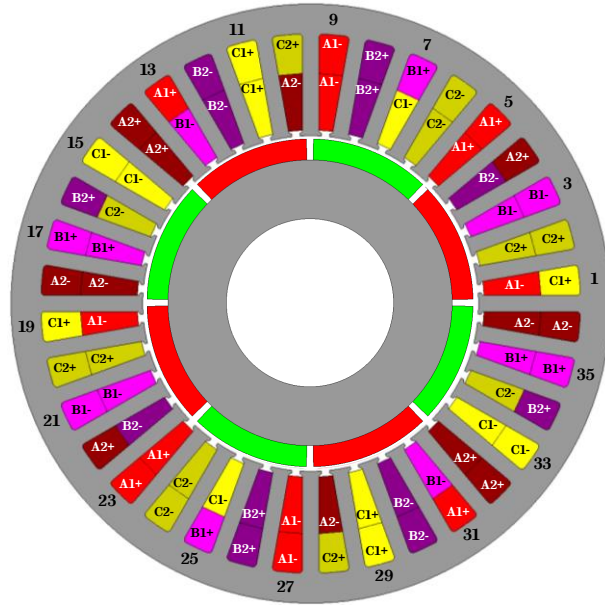


Figure 4.7. Schematic of the proposed 3-phase, 36-slot, 8-pole winding configuration

The second 3-phase windings A2-B2-C2 are positioned with respect to the first 3-phase windings A1-B1-C1 by an offset of 9 slot-pitches (or 90° mechanical). The offset in electrical degree is $9 \times 10 \times 4 = 360^\circ$ or 2π . Thus, the resultant 4th order working MMF space harmonics produced by the first and the second 3-phase windings are in phase with respect to each other. However, the phase shift between the n^{th} harmonics ($n = 2, 6, 10, 14, 18, 22, \dots$) produced by the first 3-phase windings and those by the second 3-phase windings is $n\pi/2$. Thus, these harmonics have the same magnitude but in the opposite direction and will be cancelled with each other by the proposed winding configuration. Figure 4.8 shows the resultant normalized stator MMF space harmonics distribution. It is evident that all odd harmonics and, in addition, even harmonics with order equal to 2, 6, 10, 14, 18, 22, 26, ... have been eliminated.

The THD of the proposed 3-phase, 36-slot, 8-pole winding configuration is just 18.9%, which is much lower than any of the conventional fractional-slot per pole per phase winding configurations listed in Table 4.1.

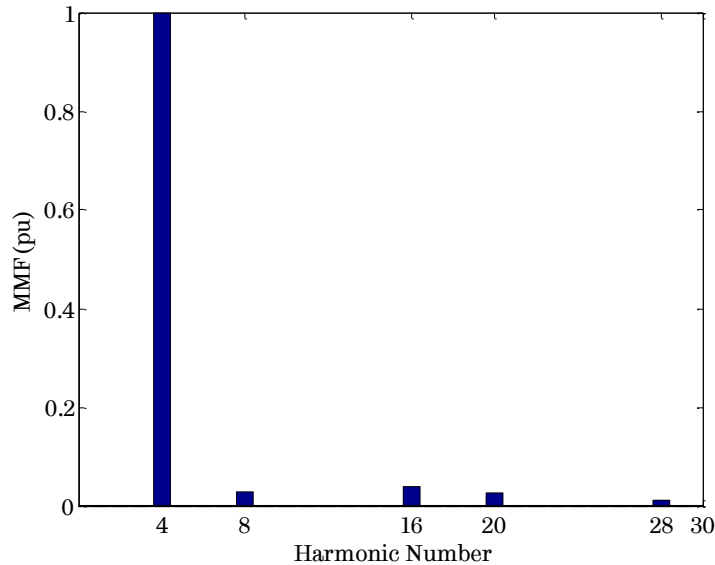
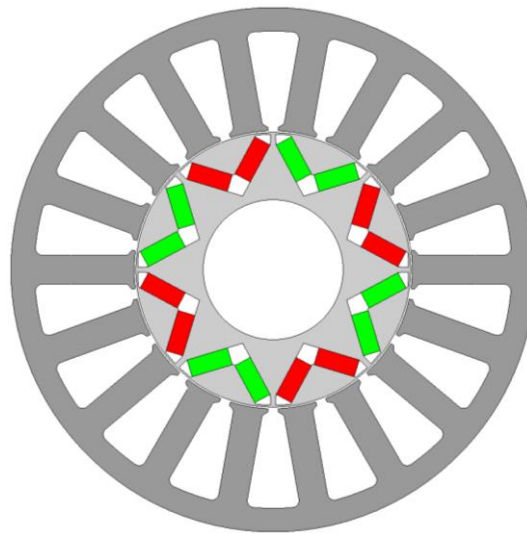


Figure 4.8. Normalized stator MMF space harmonics distribution of the proposed 3-phase, 36-slot, 8-pole winding configuration

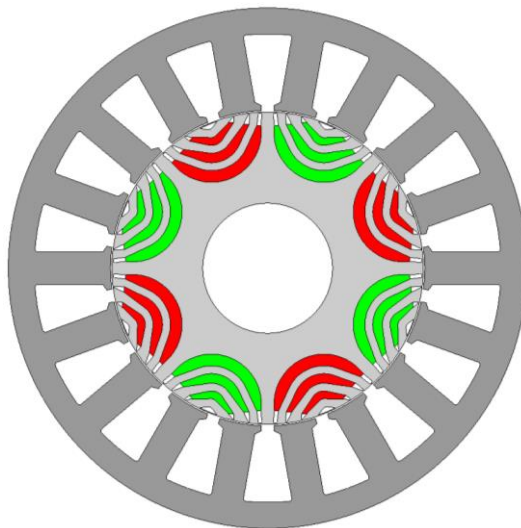
4.2.4 Applicability of novel fractional-slot per pole per phase winding configurations

These novel fractional-slot per pole per phase winding configurations can be employed to design various electrical machine technologies, as listed below, for a variety of applications, with the benefits of high torque/power density, high efficiency, and low torque ripple.

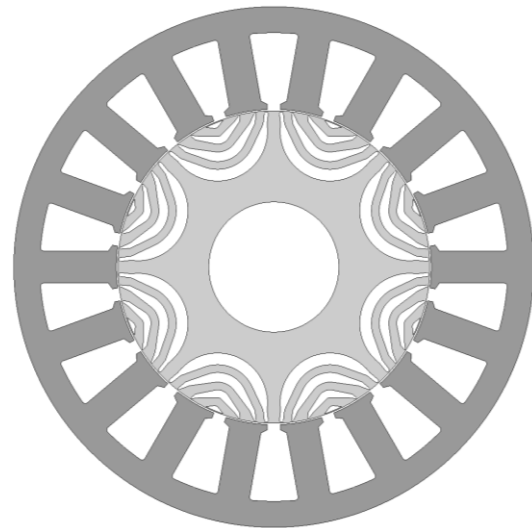
- 1) Permanent magnet brushless machines:
 - a. Surface mounted (SPM), Figure 4.2, Figure 4.5 (b), Figure 4.7
 - b. Interior mounted (IPM), Figure 4.9 (a).
- 2) Permanent magnet assisted synchronous reluctance machine, Figure 4.9 (b).
- 3) Synchronous reluctance machine, Figure 4.9 (c).
- 4) Induction machines with cage bar rotor, or wound rotor.
- 5) Wound-field synchronous machines including the claw type.



(a) Interior mounted PM machine



(b) PM assisted synchronous reluctance machine



(c) Synchronous reluctance machine

Figure 4.9. Application of proposed winding configurations to various machine technologies

Detailed comparisons of the permanent magnet assisted synchronous reluctance machines employing the proposed 18-slot, 8-pole design with 12-slot, 10-pole and 12-slot, 8-pole counterparts is given in [109] for electric vehicle application. It is shown that the 12-slot, 10-pole design suffers from low efficiency due to large iron loss caused by the 7th MMF space harmonic at high speeds while the 12-slot, 8-pole design exhibits excessive torque ripple of 49%. The proposed design with 18-slot, 8-pole yields high efficiency over a very wide torque-speed range, low torque

ripple, high reluctance ratio, and the good flux weakening capability, thereby being attractive for high speed and low torque ripple EV applications.

For the SPM machine shown in Figure 4.2, the key benefits are significant reduction in eddy current loss in rotor magnets due to elimination of most significant undesirable MMF space harmonics. This leads to low rotor loss and low cost manufacturing as circumferential and axial segmentations of the magnets are no longer necessary for low speed applications. The benefits for the IPM machine, shown in Figure 4.9 (a), are the increase in reluctance torque and reduction in rotor iron loss, which leads to high torque density, and high efficiency. High reluctance torque and low undesirable MMF space harmonics resulting from the proposed winding configurations can also be exploited in PM assisted synchronous reluctance machine, shown in Figure 4.9 (b), and synchronous reluctance machines, shown in Figure 4.9 (c), where the prime benefits are improved torque density and efficiency, and lower cost as compared to the current state-of-the-art.

Very low MMF space harmonics content as a result of the proposed winding configurations is also conducive to the design of induction machines, where the benefits is lower end-winding length, lower copper loss, and hence, high torque/power density and high efficiency. It should be noted that the process of construction and insertion of the windings is the same as that of conventional overlapping distributed windings, but the end-winding length of the proposed design is much shorter.

4.3 Configuration of the proposed winding as multiple 3-phase winding systems

To improve safety and availability in electric vehicle traction applications, multiple 3-phase motor drives are advantageous. Compared to conventional 3-phase motor drives, the multiple 3-phase motor drives are inherently fault tolerant, as loss of one 3-phase system will not lead to a complete loss of traction power. In addition, they have lower torque ripple, lower current per phase for the same voltage, lower DC link current harmonics, and improved torque per ampere capability [15].

4.3.1 Development of 6-phase, 18-slot, 8-pole winding

In order to reduce the undesirable stator MMF space harmonics significantly and to eliminate unbalanced magnetic forces associated with any slot-pole combinations listed in Table 4.2, the similar technique, as described in section 4.2, is applied to develop 6-phase, 18-slot, 8- or 10-pole winding configuration. The technique is summarized in the following steps:

- 1) Configure a 3-phase winding for a given slot-pole combinations according to the prior art, for example, 9-slot, 8-pole.
- 2) Double the number of slots of the design, i.e. $N_s = 18$.
- 3) Divide the 3-phase winding into two sets of 3-phase windings denoted by A-B-C and D-E-F. Each set of 3-phase winding is configured in the same pattern as that in step (1).
- 4) Position the second set of 3-phase winding, D-E-F, 180° mechanical away with respect to the first set of 3-phase winding, A-B-C.

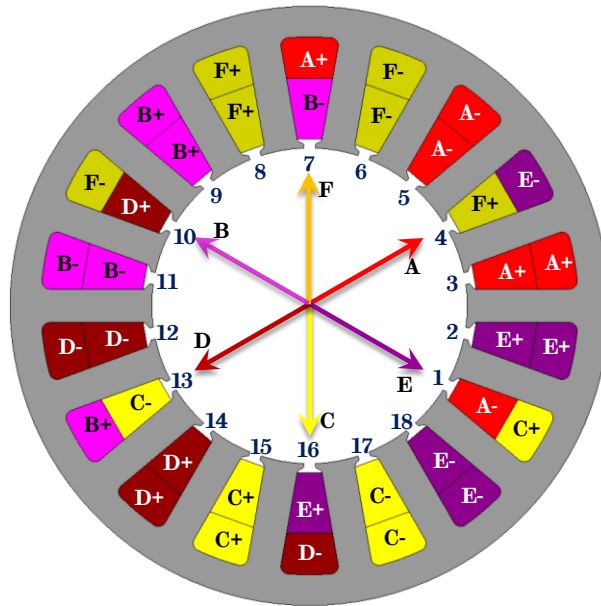
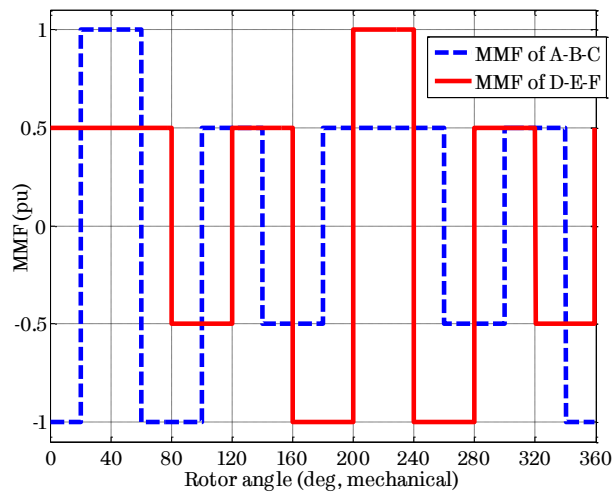


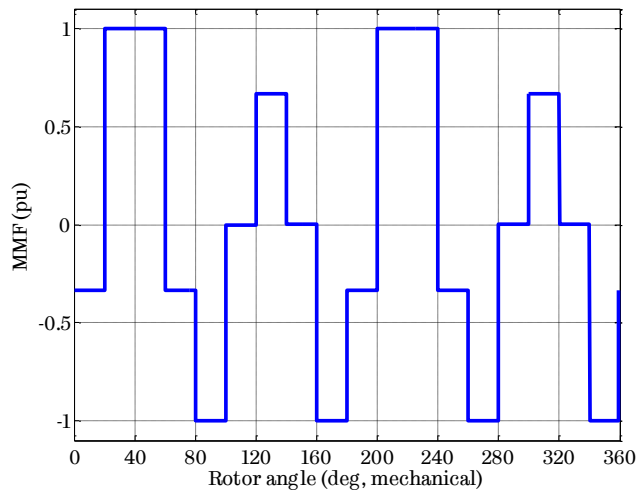
Figure 4.10. Schematic of the proposed 6-phase, 18-slot, 8-pole winding configuration

Figure 4.10 shows the schematic of 6-phase, 18-slot, 8/10-pole winding configuration. Each phase winding consists of three series connected coils wired around the adjacent teeth with the polarity as indicated by “+” and “-“. The coil span is two slot-pitches and the mechanical angle between two coil-sides is $360^\circ/9 = 40^\circ$.

The second 3-phase winding, D-E-F, is positioned with respect to the first 3-phase winding, A-B-C, by an offset of 180° mechanical or 9 slot-pitches. The offset in electrical degree is 720° or 4π . Thus, if phase windings A and D are arranged with the same polarity, and similar arrangements are made for B and E, and C and F, respectively, the resultant 4th order MMF space harmonics produced by the first 3-phase winding, A-B-C, and the second 3-phase winding, D-E-F, are in phase with respect to each other. The 4th order MMF space harmonic interacts with 4 pole-pair rotor magnetic field to produce the electromagnetic torque. For the similar reasons described in section 4.2, all odd harmonics are eliminated.



(a) MMF profile of A-B-C and D-E-F windings



(b) MMF profile of 6-phase, 18-slot, 8-pole machine with 180° phase shift between A-B-C and D-E-F windings

Figure 4.11. Stator MMF profile of 6-phase, 18-slot, 8-pole winding configuration

4.3.2 Stator MMF profile of 6-phase, 18-slot, 8-pole winding configuration

Figure 4.11 (a) shows the MMF profile of A-B-C and D-E-F windings of 6-phase, 18-slot, 8-pole machine when the currents in D-E-F are displaced from those in A-B-C by 180° electrical. The resultant MMF profile of 6-phase, 18-slot, 8-pole winding configuration is also shown in Figure 4.11 (b).

The resultant MMF space harmonics distribution is shown in Figure 4.12 along with that of 3-phase, 9-slot, 8-pole winding configuration. As will be seen, all odd MMF space harmonics have been eliminated. However, for the same reasons as explained in section 4.2, the undesirable effects caused by 2nd, 14th and 22nd harmonics will be much less significant, and the unbalanced magnetic force in the radial direction is also eliminated.

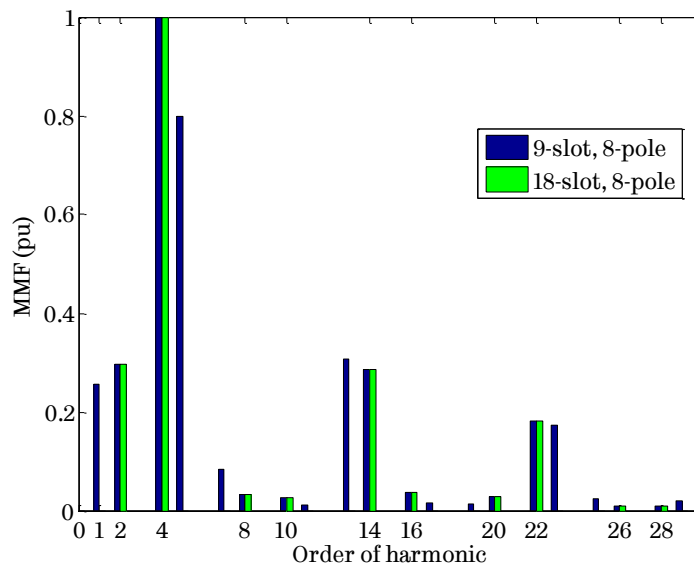


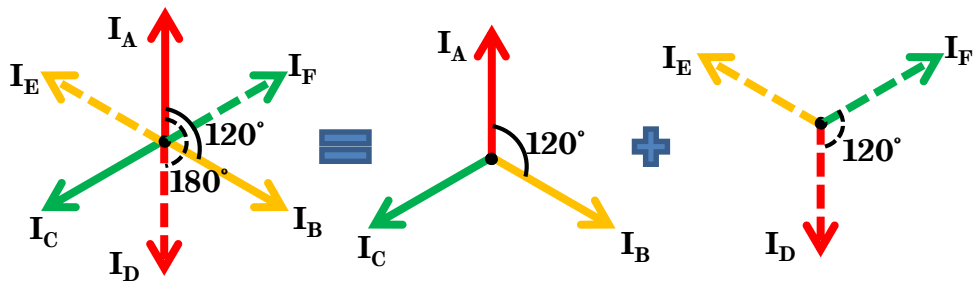
Figure 4.12. Comparison of normalized stator MMF space harmonics distribution

4.3.3 Optimal phase shift between two sets of 3-phase windings in the proposed 6-phase, 18-slot, 8-pole winding configuration

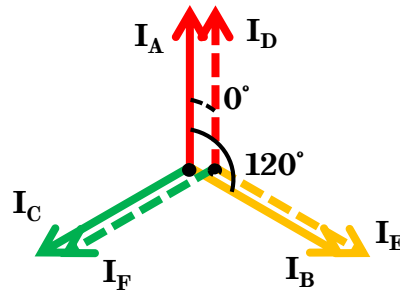
Conventionally, 6-phase machines employing distributed windings has phase shift of 60° electrical between each phase. This configuration can also be seen as two sets of 3-phase windings with a phase shift of 180° electrical between

the sets as illustrated in Figure 4.13 (a). The space vector positions of all the phases are of the winding configuration shown in Figure 4.10.

As seen from Figure 4.10, phase D is shifted from phase A by 9 slots, i.e. 180° mechanical, or 720° electrical. If we consider reversing the polarity of phase D, E, and F, the resultant phase shift between A-B-C and D-E-F becomes 0° , as shown in Figure 4.13 (b). With fractional-slot per pole per phase winding configuration, it is possible to have different phase shifts between two sets of 3-phase windings than the conventional phase shift of 180° electrical.



(a) 6-phase machine seen as two sets of 3-phase machines (180° phase shift)



(b) 6-phase machine seen as two sets of 3-phase machines (0° phase shift)

Figure 4.13. Phase shift between two sets of 3-phase windings in a 6-phase machine

For the proposed 6-phase, 18-slot, 8-pole winding configuration, each phase occupies the alternate slots. This will allow to make balanced 6-phase windings using two sets of 3-phase windings by shifting second set (D-E-F) from first set (A-B-C) by a slot-pitch or an integer multiple of a slot-pitch. Further phase shifts are also possible by reversing the polarity of either set of 3-phase winding. Let θ be defined as phase shift in electrical degrees between two sets of 3-phase windings A-B-C and D-E-F. The slot-pitch in electrical degrees is given by (4.2).

$$\theta_s = p \left(\frac{360}{N_s} \right) \quad (4.2)$$

Phase shift, θ , is then derived using the slot-shift, α_s , and slot-pitch, θ_s , as below:

$$\theta = \theta_s \times \alpha_s \quad (4.3)$$

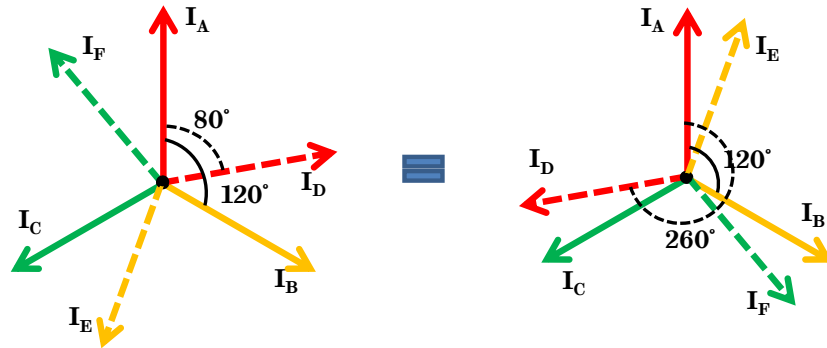
Hence, for the proposed winding configuration, there are 18 possible phase shifts between two sets of 3-phase windings as listed in Table 4.4. The winding configurations for each of the phase shifts are shown in Appendix B. It is worthwhile to note that even slot-shifts are not possible for the proposed winding configuration since these slots have already occupied by A-B-C windings.

Table 4.4. Possible phase shifts in 6-phase, 18-slot, 8-pole winding configuration

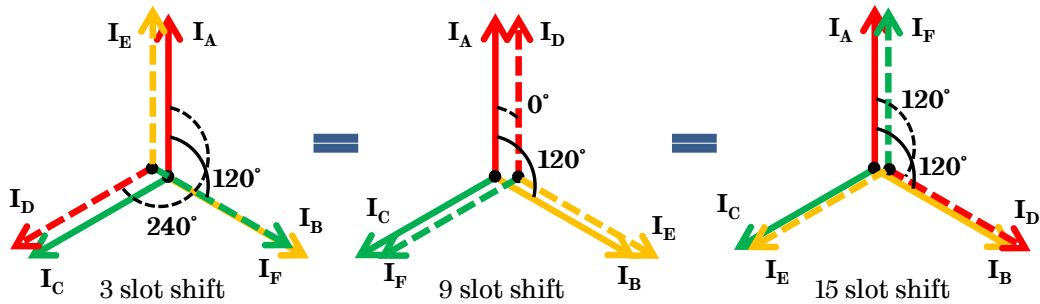
Slot-shift α_s	Phase shift θ	Slot-shift α_s	Phase shift θ
D-E-F polarity same as A-B-C		D-E-F polarity opposite to A-B-C	
1	80°	1	260°
3	240°	3	60°
5	40°	5	220°
7	200°	7	20°
9	0°	9	180°
11	160°	11	340°
13	320°	13	140°
15	120°	15	300°
17	280°	17	100°

In order to evaluate the optimum phase shift, vector diagrams of all phases with all possible phase shifts are examined. Figure 4.14 (a) shows the phase space vectors for 1 slot-shift having D-E-F polarity same as A-B-C, and opposite to A-B-C. Both these configurations produce same magnetic field in the air-gap as they change their spatial location by 180°. Figure 4.14 (b) shows the phase space vectors for three different slot-shifts, 3, 9, and 15, resulting in to 240°, 0°, and 120° phase shift respectively. All these configurations with D-E-F shifted from A-B-C by 3, 9, and 15 slots produce the same magnetic field in the air-gap as they occupy the same spatial position with respect to A-B-C. Therefore, the 18 possible phase shifts for 6-

phase, 18-slot, 8-pole machine, listed in Table 4.4, are reduced to only 3 different phase shifts, as listed in Table 4.5.



(a) Phase space vectors for 1 slot-shift (80° and 260° phase shifts)



(b) Phase space vectors for different slot-shifts (0° , 120° , 140° phase shifts)

Figure 4.14. Reduction technique by analysing phase space vectors in 6-phase machine

Table 4.5. Reduced phase shifts in 6-phase, 18-slot, 8-pole winding configuration

Slot-shift	Phase shift between A-B-C and D-E-F
α_s	θ
3-9-15	0°
1-7-13	20°
5-11-17	40°

The phase shifts listed in Table 4.5 results into balanced windings irrespective of whether the machine is operated with 6-phases or just one set of 3-phase. This feature enhances the capability of the proposed winding configuration for traction application as it is fault tolerant. In the event of a fault on one set of 3-phase system, other set of 3-phase will continue to operate as a balanced machine with half the torque/power output. The probability of having turn-to-turn fault in

the machine is higher than that of the terminal short-circuit. It is important to investigate the effect of turn-to-turn fault on machine behaviour including thermal impact on the shorted turn/s and resultant torque capability of the machine. The author has proposed this work as future scope of the work.

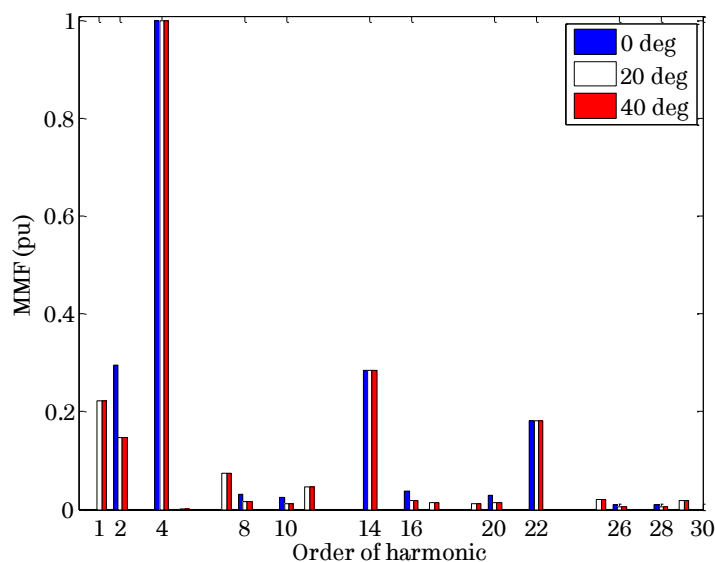


Figure 4.15. Comparison of normalized stator MMF space harmonics distribution for various phase shifts between A-B-C and D-E-F in 6-phase, 18-slot, 8-pole winding configuration

Figure 4.15 shows the normalized MMF space harmonics distribution for different phase shifts between A-B-C and D-E-F. As seen, the proposed winding configuration with 0° eliminates all odd MMF space harmonics that are present in the 9-slot, 8-/10-pole winding configuration, therefore results in much improved performance. The effect of 20° and 40° phase shifts is the same – both help in reducing the 2nd order MMF space harmonic by $\sim 50\%$, however, gives rise to other odd harmonics (1st, 7th, and 11th) that were otherwise not present with 0° phase shift. However, these odd harmonics are less significant due to their lower frequency (for 1st order) or lower magnitude (for 7th and 11th order).

Table 4.6 lists the total harmonic distortion (THD) of all three phase shifts between A-B-C and D-E-F. It is evident that the THD (considering harmonics up to 30th order) of 20° phase shift is 1.6% and 0.6% lower than that of 0° and 40° phase shift respectively. This is mainly because of reduction of low order harmonics (2nd

order) by 50% for 20° and 40° phase shifts. Lower THD of 20° phase shift will result into comparatively lower rotor iron loss including PM eddy current loss. Hence, 20° phase shift is selected as the optimum phase shift between A-B-C and D-E-F windings. This winding configuration is employed to design permanent magnet synchronous machine for segment-A electric vehicle application.

Table 4.6. Total harmonic distortion for various phase shifts

Phase shift	T.H.D	T.H.D.
θ	$n = 1 \text{ to } 100$	$n = 1 \text{ to } 30$
0°	50.4 %	45.4 %
20°	48.8 %	43.8 %
40°	49.4 %	44.4 %

Chapter 5

Design and Analysis of 6-phase, 18-slot, 8-pole IPM Machine for Segment-A Electric Vehicle

The design specifications for an electric traction machine from the vehicle data and acceleration performance requirements are derived. The design and analysis of 6-phase fractional-slot PM machine for Segment-A electric vehicle is presented. The geometrical parameters of the machine are optimized for the design specifications against the volumetric and thermal constraints to maximize energy efficiency over the New European Driving Cycle (NEDC) using the finite element analysis (FEA) based design technique.

The main contents of this chapter is published by the author in [93] and [110].

5.1 Drivetrain configuration

The proposed winding configuration, described in Chapter 4, is applied to the design of a traction machine for a segment-A sized electric vehicle. For the same, the centralized power drivetrain configuration is considered as shown in Figure 5.1. As will be seen, the vehicle employs only one traction machine coupled to the front or the rear axle via a differential and a reduction gearbox. The 6-phases of the electric traction machine are controlled as two separate and independent 3-phase systems, which are fed by two separate inverters. In the event of a fault on one of the 3-phase drive system, the vehicle can continue to operate using the remaining healthy set of 3-phase drive system without any sudden stops or compromising vehicle stability and passenger safety. The ability of the proposed winding topology with 18-slot, 8-/10-pole to configure it as two sets of 3-phase system enables the centralized power drivetrain to be inherently fault tolerant.

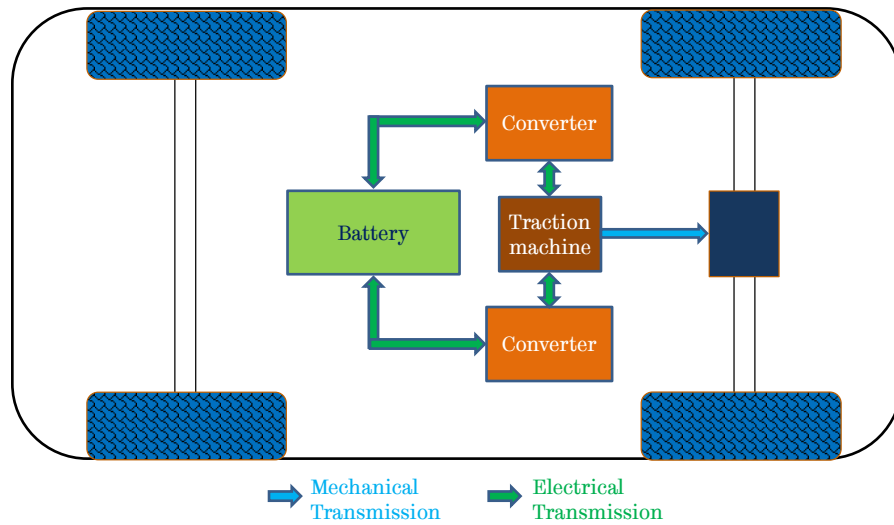


Figure 5.1. Centralized power drivetrain configuration for a segment-A vehicle

5.2 Vehicle data and target performance

To determine the machine design specifications, the New European Driving Cycle (NEDC), as shown in Figure 3.6, is used to estimate the continuous and the peak torque and power ratings of the vehicle propulsion system with the typical vehicle data of a segment-A car from the vehicle OEM [111], as listed in Table 5.1.

Table 5.1. Typical vehicle data of a segment-A vehicle

Parameter	Symbol	Value	Unit
Radius of the wheel	r_w	0.29	m
Vehicle mass	m_v	910.0	kg
Rolling resistance coefficient	k_r	0.008	
Product of drag coefficient and frontal area	$c_d A$	0.7	m ²
Air density	ρ	1.25	kg/m ³
Differential gear ratio	G_r	10	-
Efficiency of the differential (indicative)	η_g	97.0	%
Average auxiliary power		200	W
Weight load for performance evaluation		200	kg

In addition to the vehicle data, the acceleration performance requirements for a segment-A car is also specified, as listed in Table 5.2.

Table 5.2. Acceleration performance requirements for a segment-A vehicle

Parameter	Symbol	Value	Unit
Maximum speed	ω_b	120	km/h
Cruise speed	ω_{ms}	60	km/h
NEDC driving range	-	> 80	km
Driving range at cruise speed	-	> 60	km
Acceleration time, 0 to 50 km/h	-	< 5	s
Acceleration time, 0 to 90 km/h	-	< 15	s
Acceleration time, 0 to 400 m	-	< 20	s
Acceleration time, 0 to 1000 m	-	< 40	s
Maximum road slope at standstill	-	>20% at 0.8 m/s ²	

5.3 Motor design specifications

The vehicle model shall consider the mechanical parameters of the vehicle, as listed in Table 5.1, and its interaction with the road and the air to derive the force required to act against these resistances. Three different types of resistance forces are considered in the vehicle model: (1) the inertia, (2) the rolling resistance, and (3) the air drag. Hence, the net force required by the vehicle is given by (5.1):

$$F = F_i + F_r + F_a \quad (5.1)$$

where F_i , F_r , and F_a are the respective forces required to overcome the vehicle inertia, the rolling resistance, and the air drag resistance, all in N. The effect of tyre slip is neglected in this steady-state equation of the vehicle motion.

As per Newton's second law, any mass, which is accelerated, will oppose the acceleration with a force of inertia equal to product of mass and the acceleration, as defined in (5.2).

$$F_i = m_v \frac{dv}{dt} \quad (5.2)$$

where, F_i is the inertial force in N, m_v is the vehicle mass in kg, v is the velocity of the vehicle in m/s. The velocity is defined by the NEDC as shown in Figure 3.6.

The rolling resistance is proportional to the rolling resistance coefficient, which is a function of the normal force applied on the wheel [87].

$$F_r = m_v \cdot g \cdot k_r \quad (5.3)$$

where k_r is the rolling resistance coefficient, and g is the gravitational constant in m/s^2 .

The air drag is proportional to the aerodynamic drag coefficient, the cross-section frontal area of the vehicle, and the air density [87]. It is also proportional to square of the velocity.

$$F_a = \frac{1}{2} \cdot c_d A \cdot \rho v^2 \quad (5.4)$$

where $c_d A$ is the product of drag coefficient and the frontal area in m^2 , and ρ is the air density in kg/m^3 .

The net force required for the vehicle can be found out using (5.1)-(5.4). Then, the torque and angular speed of the wheel is given by (5.5) and (5.6) respectively.

$$T_w = F \cdot r_w \quad (5.5)$$

$$\omega_w = \frac{v}{r_w} \quad (5.6)$$

where T_w and ω_w are the torque and the angular speed of the wheel in $\text{N}\cdot\text{m}$ and in rad/s respectively, and r_w is the radius of the wheel in m .

Using the differential gear ratio and efficiency of the differential, the torque and angular speed of the wheel can be transferred to the machine torque and the machine angular speed using (5.7) and (5.8).

$$T_m = \frac{\left(\frac{T_w}{G_r}\right)}{\eta_g} \text{ for } T_w > 0 \quad (5.7)$$

$$T_m = \left(\frac{T_w}{G_r}\right) \eta_g \text{ for } T_w < 0$$

$$\omega_m = \omega_w \cdot G_r \quad (5.8)$$

where T_m and ω_m are the motor torque and the motor angular speed in $\text{N}\cdot\text{m}$ and in rad/s respectively.

5.3.1 Required wheel torque and power over the NEDC

Using the NEDC, the vehicle data (as listed in Table 5.1), and the above equations, the required torque on the wheels and the related power over the driving cycle, for the centralized power train configuration (shown in Figure 5.1), are derived as shown in Figure 5.2. As will be seen, the peak torque reaches 503 N·m during the NEDC, and the peak power and the continuous steady-state power at the maximum speed of 120 km/h are 27 kW and 18.6 kW, shown as P_p and P_c respectively.

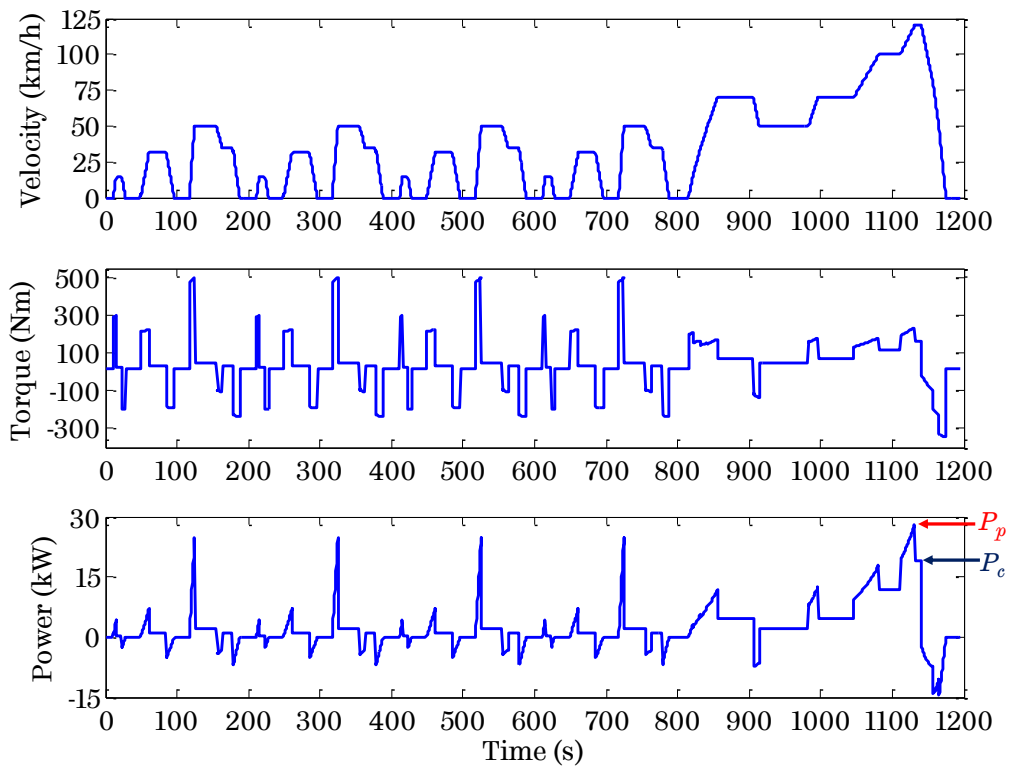


Figure 5.2. Required wheel torque, wheel power for the segment-A vehicle over the NEDC

5.3.2 Determining design specifications of the drive motor

The continuous power of the drive motor is therefore defined by the continuous steady-state power required at the maximum speed of 120 km/h. The minimum peak power of the drive motor, on the other hand, must be greater than the maximum power over the entire NEDC. To account for additional losses due to, for example, slightly higher drag or higher rolling resistance, and to provide a

degree of power redundancy for the drivetrain, 15% margin is given over the continuous and the peak power requirements while defining the continuous and the peak power of the drive motor. However, this will result into increased motor sizing and inverter rating. Hence, the peak and the continuous power of the drivetrain would be 31.1 kW and 21.4 kW respectively.

Once the continuous and the peak power are determined, the maximum motor speed is defined according to the maximum vehicle speed, the gear ratio, and the wheel size. An additional 5% margin is given to consider the wheel slip. The base speed (or the rated speed) is determined using constant power curves and the peak torque requirements.

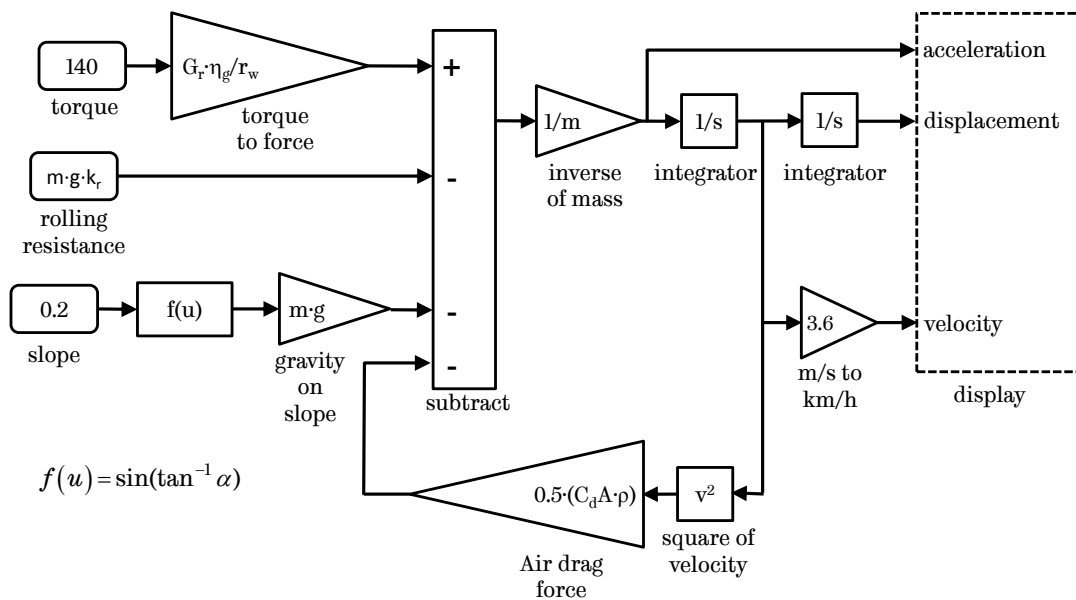


Figure 5.3. MATLAB Simulink model to check acceleration performance targets

Further, the peak torque or overload capacity is defined by the acceleration and drive-away performance for the worst case payload, i.e. 1310 kg considering the weight load of the passengers. A simple MATLAB Simulink model is developed, as shown in Figure 5.3, to determine the peak torque capability of the drive motor against acceleration targets listed in Table 5.2. The peak torque of 503 N·m as derived from the NEDC is not sufficient to achieve acceleration target of 50 km/h in 4.5 seconds. Repeated simulations have been performed to determine the peak torque rating against the acceleration and drive-away performance targets listed in

Table 5.2. It is found that if the peak torque reaches 1200 N·m, 10% margin will result for the most demanding acceleration performance, i.e. 0 to 50 km/h in less than 5 seconds. However, 20% margin is considered for the design specifications of the drive motor, yielding the peak torque requirement of 1370 N·m for a gear ratio of 1. Table 5.3 compares the acceleration and drive-away performance with 1200 N·m and 1370 N·m as the peak traction torque against the targets.

Table 5.3. Comparison of acceleration and drive-away performance for the segment-A vehicle for two different peak torque ratings

Parameter	Target	1200 N·m	% margin	1370 N·m	% margin
Acceleration time, 0 to 50 km/h	< 5s	4.5	10%	4.0	20%
Acceleration time, 0 to 90 km/h	< 15s	8.4	44%	7.2	52%
Acceleration time, 0 to 400 m	< 20s	16.5	17.5%	15.4	23%
Acceleration time, 0 to 1000 m	< 40s	26.9	33%	25.2	37%
Maximum road slope at standstill	>20% at 0.8 m/s ²	1.1	27%	1.6	100%

Given that the motor size and inverter VA (volt-ampere) rating are proportional to the peak torque, the determination of the peak torque rating of the drive motor is a trade-off between the % margin on the acceleration and drive-away performance target and cost of the machine drive. Figure 5.4 shows the torque-speed characteristics of the segment-A vehicle for 1200 N·m and 1370 N·m peak torques, respectively. Also, an additional 8% margin is given for the maximum speed to consider the wheel slip at that speed.

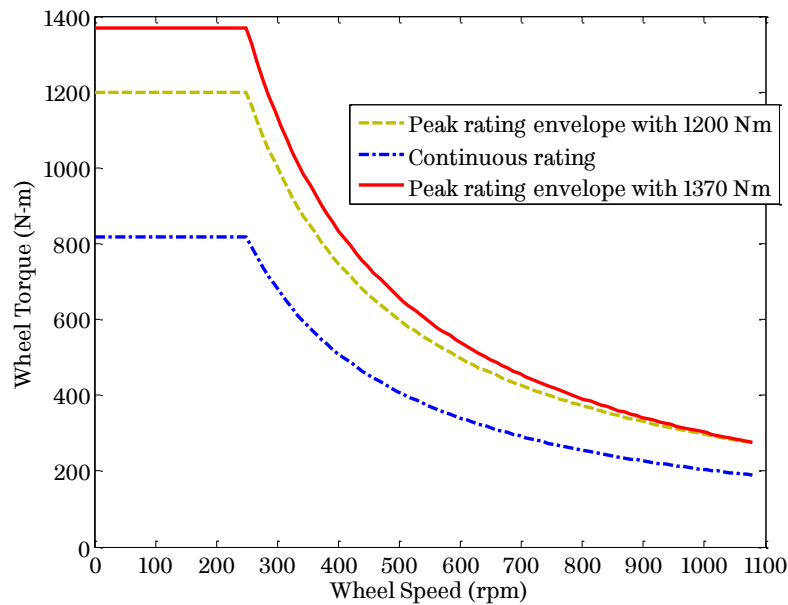


Figure 5.4. Torque-speed characteristics of the segment-A vehicle

The wheel torque-speed characteristics can be transferred to the torque-speed characteristics of the drive motor, for the centralized power drivetrain configuration, using the differential gear ratio and the efficiency of the differential, as in (5.7) and (5.8). Figure 5.5 shows the torque-speed characteristics of the drive motor of the segment-A vehicle having centralized power drivetrain. For the purpose of illustration, the torque-speed trajectory over the NEDC is also shown in dark yellow. As will be seen, most of the NEDC torque-speed trajectory lies within the continuous rating of the drive motor, which implies that the motor can operate over the NEDC continuously without violating any thermal design limits for various active parts of the motor.

In addition, the specifications of the drive motor are also compared with the Artemis Urban Driving Cycle (AUDC), which is derived as part of the European Commission Project, ARTEMIS, to set up and improve the European methods for estimating and quantifying the pollutant emissions from the vehicle transports [112]. As seen from Figure 5.6, the AUDC consists of five cycles, one each for urban dense, free-slow urban, congested stops, congested low speeds, and flowing stable [112]. It covers ~4.9 km with an average speed of 17.7 km/h. The torque-speed requirements over the AUDC is evaluated against the drive motor specifications

and the resulting variations of power and torque are shown in Figure 5.7 (a) and (b) respectively, assuming an average slope of 2.3° .

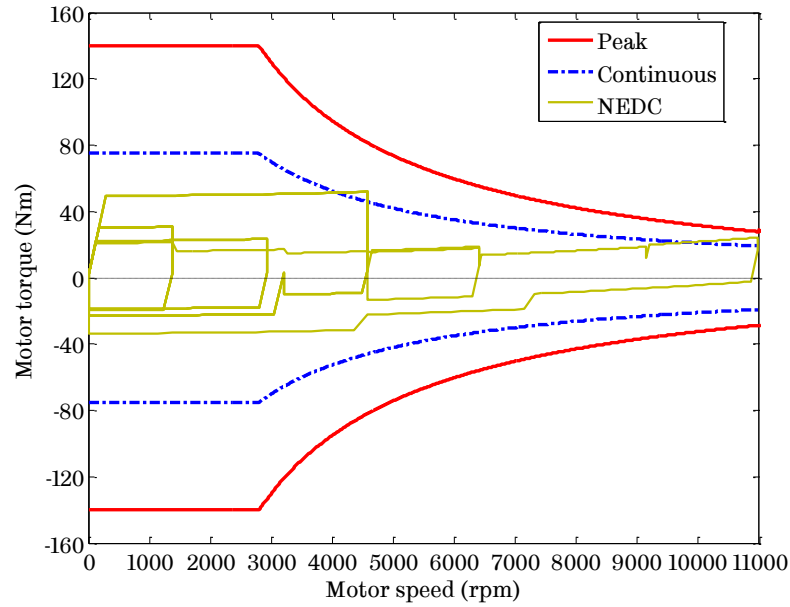


Figure 5.5. Torque-speed characteristics for the drive motor of the segment-A vehicle along with the NEDC envelope

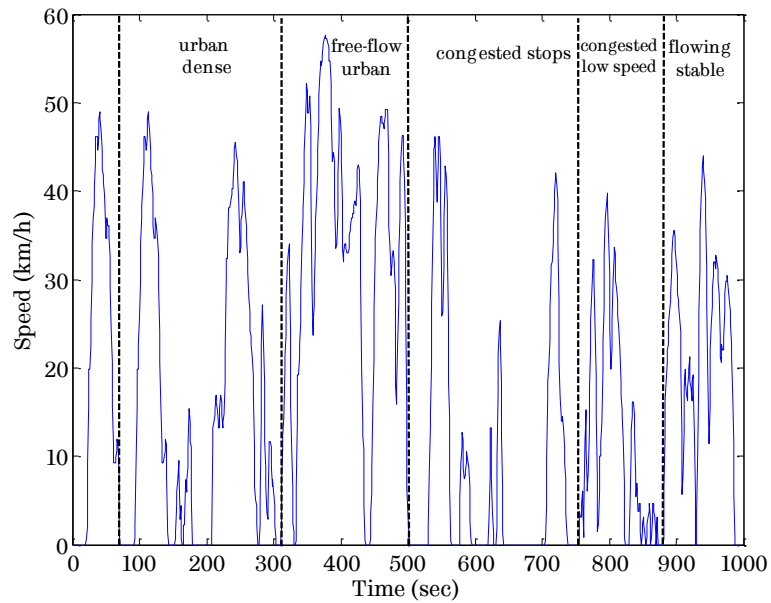
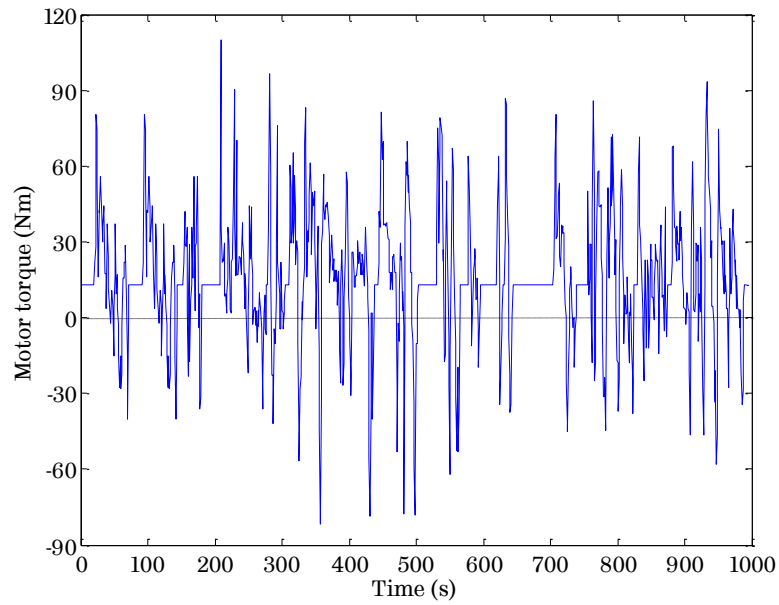
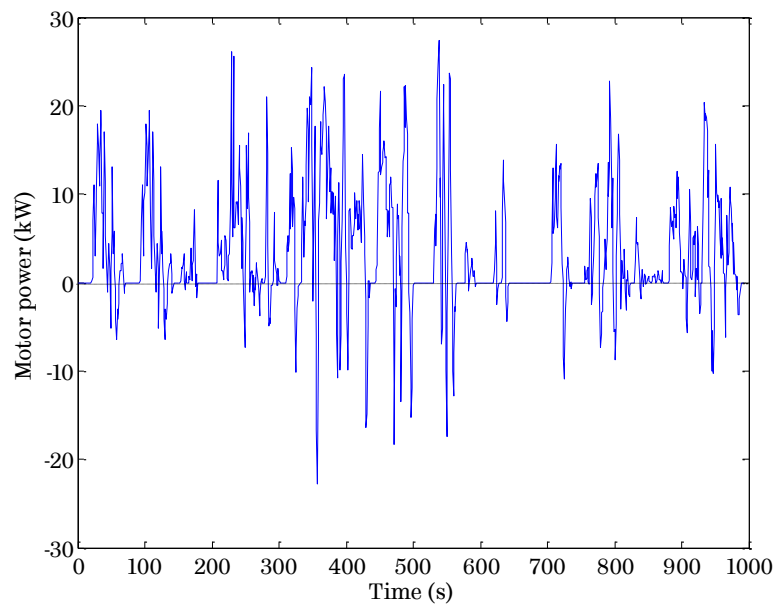


Figure 5.6. The Artemis Urban Driving Cycle (AUDC)

The torque-speed trajectory of the AUCD is shown as dark yellow dots in Figure 5.8 along with the torque-speed characteristics of the drive motor.



(a) Torque over the AUCD



(b) Power over the AUCD

Figure 5.7. Torque and power requirements over the AUCD

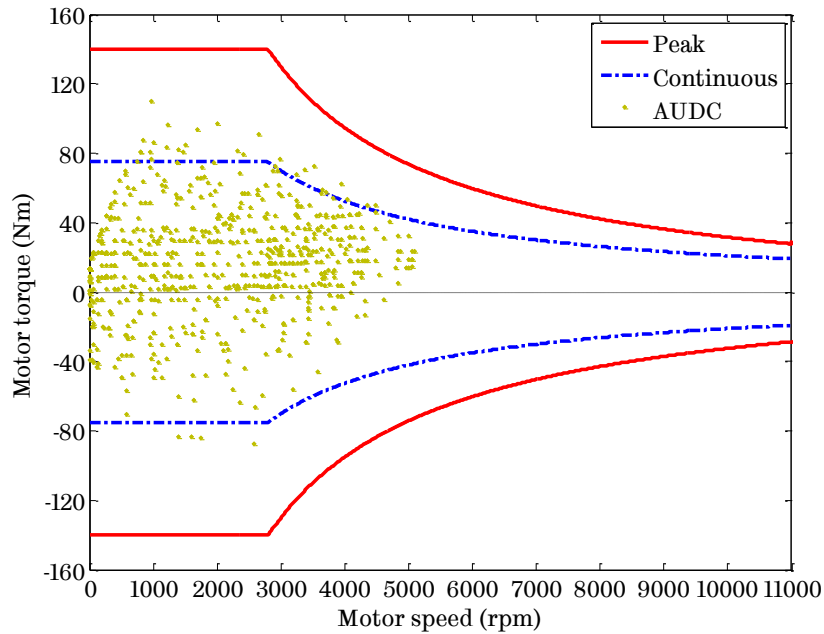


Figure 5.8. Torque-speed characteristics for the drive motor of the segment-A vehicle along with the Artemis Urban Driving Cycle envelope

As will be seen, the peak power of 26.6 kW, the peak torque of 109.7 N·m, and r.m.s. torque of 29.7 N·m over the AUDC are all within the specified peak and continuous torque-speed envelopes of the drive motor.

By employing water or liquid cooling, the active volume of the motor may be reduced to about half compared to air-cooling. Liquid cooling concept will be more attractive if it can be integrated with the cooling requirements of the inverter and battery system on board the vehicle.

5.3.3 Summary of motor design specifications

The motor design specifications derived for a centralized power drivetrain configuration employed in the segment-A vehicle are summarized in Table 5.4. The torque-speed characteristics of the traction motor is already shown in Figure 5.5 and Figure 5.8.

Table 5.4. Design specifications of the traction motor for a centralized power drivetrain in the segment-A electric vehicle

Parameter	Symbol	Value	Unit
No. of phases	m	6	-
Base speed or rated speed	ω_b	2800	rpm
Maximum cruise speed	ω_c	11000	rpm
Maximum speed	ω_m	12000	rpm
Peak torque below and at base speed	T_p	140	N·m
Rated torque below and at base speed	T_c	75	N·m
Peak power at base speed	P_{pb}	41	kW
Peak power at maximum cruise speed	P_{pc}	32	kW
Peak power at maximum speed	P_{pm}	0	kW
Continuous rated power	P_c	22	kW
Peak torque at maximum cruise speed	T_{pc}	27.8	N·m
Continuous torque at maximum cruise speed	T_{cc}	19.1	N·m
Nominal DC link voltage	V_{dc}	320	V
Maximum line-line voltage at maximum cruise speed	E_m	650	V
Cooling medium	-	Water	-

5.4 Distribution of energy consumption over the NEDC and equivalent energy distribution

It is important to note that since an EV operates over a wide torque-speed range, a design optimized against the rated torque at the base speed does not necessarily lead to an optimal design over a given driving cycle [86]. Likewise, a design optimized against a driving cycle does not yield the best performance when a different driving cycle or condition occurs. Thus, similar to the design of conventional internal combustion engine (ICE) driven vehicles, the design and performance of the electric vehicle are very much dependent on the drive styles and/or driving cycles (traffic variations). Hence, in order to optimize the electric machine design for a segment-A electric vehicle with a centralized power drivetrain, the best combination of design parameters should be selected against

the volumetric, electrical, thermal and mechanical constraints with the objective to minimize energy consumption of the traction drivetrain over the NEDC.

To evaluate the total energy loss of the electric traction machine over the NEDC with sufficient accuracy, the efficiency of the machine at each point in the NEDC for a given design must be predicted using the available design tools. As seen from Figure 5.2 (a), the NEDC, which includes four ECE-15 city cycles, contains 1198 operating points with a time interval between two adjacent points of one second, the design process requires enormous amount of computation time and efforts, if the efficiency at each point is to be evaluated by 2-D transient FEA.

By analysing the energy distribution of the vehicle under consideration as a function of machine torque and speed over the NEDC, it can be shown that energy is highly concentrated at six points, as shown in Figure 5.9. These six points, associated with the six highest peaks in the energy distribution, corresponds to the constant speed operations of the NEDC where the time duration for these operations is relatively long. The energy distribution of the vehicle under consideration, after excluding these six points, is illustrated in Figure 5.10. As seen, the energy levels for the remaining points are scattered and relatively low, hence they are lumped into another 6 operating points according to their “*energy centre of gravity*” as explained in [90]. The resulting 12 points to represent the entire NEDC with their energy distribution are shown in Table 5.5. The energy efficiency of the machine over the NEDC is evaluated against these 12 representative points using (5.9).

$$\eta_{NEDC} = \frac{\sum_{i=1}^{12} \omega_i T_i dt_i}{\sum_{i=1}^{12} \omega_i T_i dt_i + \sum_{i=1}^{12} (P_{cu-i} + P_{fe-i}) dt_i} \quad (5.9)$$

where ω_i is the angular speed in rad/s, T_i is the torque in N·m, dt_i is the time duration, P_{cu-i} and P_{fe-i} are the copper loss and the iron loss for the i^{th} point, respectively.

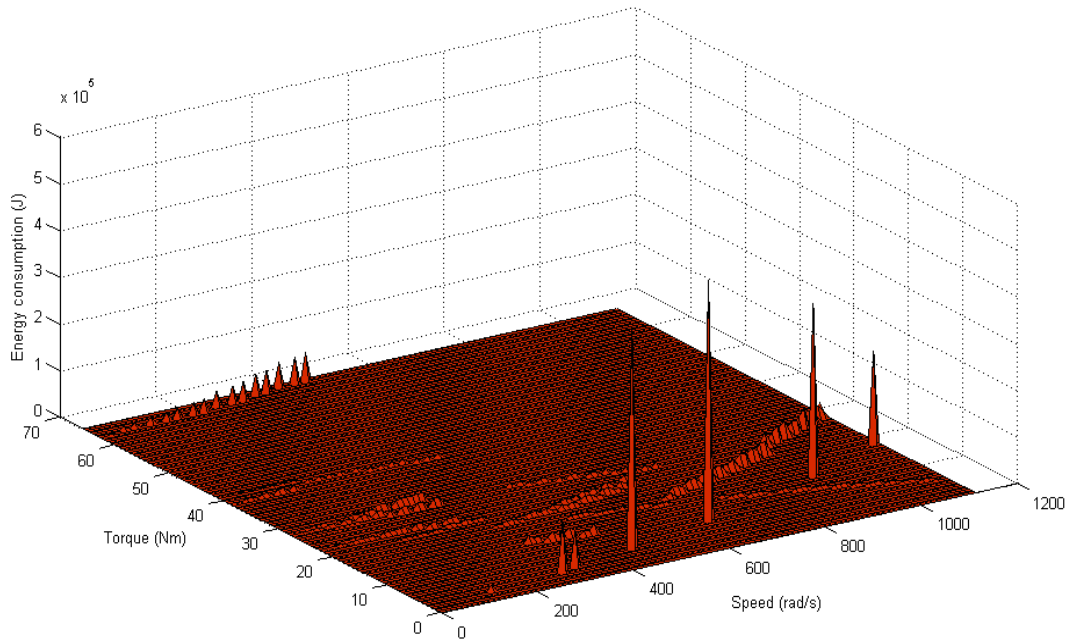


Figure 5.9. Energy distribution of the EV under consideration over the NEDC

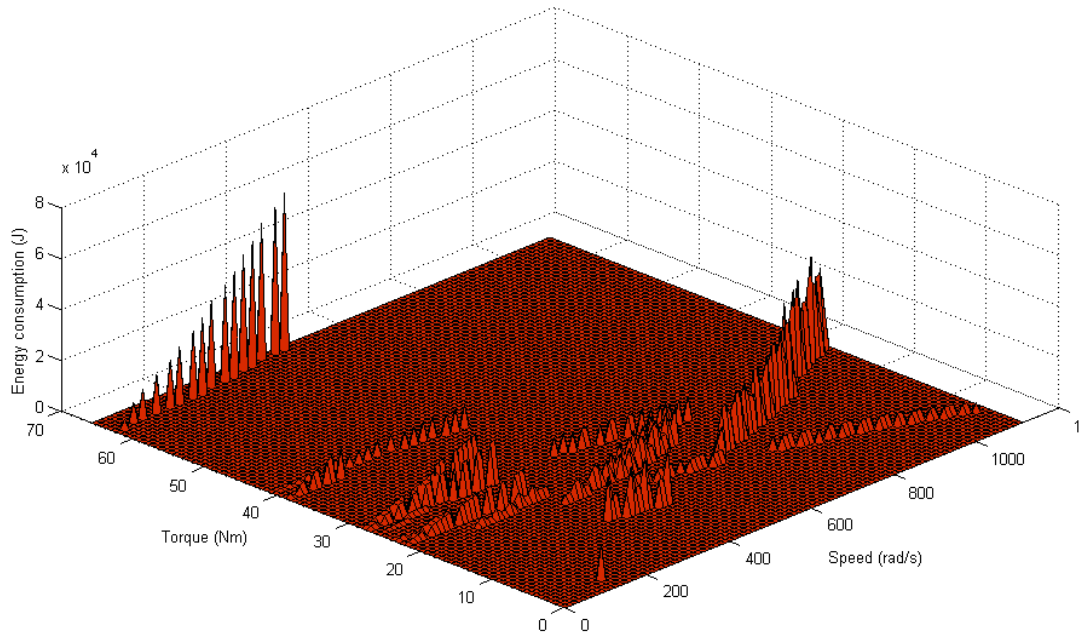


Figure 5.10. Energy distribution of the EV under consideration over the NEDC, excluding the six operating points having maximum energy

To calculate the copper loss and iron loss for these 12 points, the stator currents are determined to achieve specified torque according to MTPA (maximum torque per ampere) for low speed points. For high speed points, currents in d - and

q -axis (i_d and i_q) are properly chosen to operate in field weakening to satisfy voltage limit for a given torque demand. The maximum attainable torque in the field weakening region is either limited by the maximum permissible current or by the MTPV (maximum torque per voltage), also referred to as MPPA (maximum power per ampere) in literature under the voltage constraint. By following these strategies, the designed machine operates at maximum achievable efficiency at each of these 12 points. Also, this 12 points representation of the NEDC, significantly reduces the number of calculations over the NEDC from 1198 to 12, thus making it possible to perform design optimization in a reasonable time frame with a systematic approach.

Table 5.5. Representative points of the NEDC for the EV under consideration

Time (s)	Speed (rpm)	Torque (N·m)	Energy (kJ)	Normalized Energy (%)
5.7	583	63.0	21.9	0.4%
66.1	652	29.1	131.4	2.7%
134.0	2532	24.1	856.2	17.3%
114.0	2757	3.3	108.6	2.2%
62.4	3075	3.9	78.4	1.6%
23.2	3112	64.2	485.3	9.8%
195.5	4347	5.3	471.7	9.5%
42.1	5317	20.9	490.2	9.9%
101.3	6149	7.9	515.2	10.4%
64.9	8615	20.7	1211.4	24.5%
30.8	8800	13.1	371.8	7.5%
10.3	10496	17.8	200.8	4.1%
850.3	-	-	4942.9	100%

5.5 Design constraints for EV traction machine

As discussed in Chapter 3 and Chapter 4, the most suitable machine technology for the EV under consideration is PM brushless machines (IPM) with fractional-slot per pole per phase winding configurations having novel topology of 6-phase, 18-slot, 8-pole. Although PM machines have higher torque/power density, peak torque capability, and high efficiency, a very important design issue for them

is their field-weakening capability, since the traction machine is required to provide constant power operation over a wide speed range. In order to meet the field-weakening capability over a wide speed range for EV traction application, there are basic design constraints, as outlined below, that a given PM machine must satisfy:

- 1) Flux linkage due to permanent magnets (λ_m) must be constrained to limit the voltage below the maximum permissible peak value of line-line voltage in the event of an inverter fault, i.e. $V_{m-ll} < E_m$.
- 2) Maximum machine current (I_m) is limited by the inverter capability. $I_m \times V_{dc}$ defines the inverter VA rating.
- 3) Machine d -axis inductance (L_d) must be greater than $L_{d-\min}$ in order to achieve peak torque at the maximum cruise speed, under the current limit.
- 4) Machine d -axis inductance (L_d) must be smaller than $L_{d-\max}$ in order to achieve the peak torque at the base speed, under the DC link voltage limit.

5.5.1 Constraints on d -axis inductance for efficient field-weakening operations of an IPM machine

The induced back EMF, E , at the maximum speed, ω_m , in an IPM machine, is given by (5.10).

$$E = p\lambda_m\omega_m \tag{5.10}$$

where λ_m is permanent magnet flux-linkage in V·s (or Wb), and p is number of pole-pairs.

The back EMF must be limited to below the maximum permissible peak value of line-to-line voltage, E_m .

$$E = p\lambda_m\omega_m \leq \frac{E_m}{\sqrt{3}} \tag{5.11}$$

Alternatively, (5.11) can be re-written as:

$$p\lambda_m \leq \frac{E_m}{\sqrt{3}\omega_m} \quad (5.12)$$

The torque in an IPM machine consists of two components: one component due to the permanent magnets known as alignment torque or excitation torque, and another component due to the difference in d - and q -axis inductances referred to as reluctance torque, and is given by (5.13).

$$T = \frac{m}{2} p \left[\lambda_m i_q + (L_d - L_q) i_d i_q \right] \quad (5.13)$$

where m is number of phases, L_d and L_q are d - and q -axis inductances in H, i_d and i_q are d - and q -axis currents in A respectively. Also, for an IPM motor, the ratio of q -axis inductance to d -axis inductance is known as saliency ratio, k_s .

It can be inferred from (5.13) that for a given peak torque, the resulting maximum motor current, I_m , [86] is given by (5.14).

$$I_m \leq \frac{2}{m} \frac{T_p}{p\lambda_m} = \frac{2\sqrt{3}}{m} \frac{T_p \omega_m}{E_m} \quad (5.14)$$

For given values of the peak torque T_p , the saliency ratio k_s , and the peak torque T_{pc} , at the maximum cruise speed ω_c , the minimum and the maximum values of L_d and L_q , the maximum current I_m , the d - and q -axis currents, i_{db} , i_{qb} for T_p at the base speed ω_b , and the d - and q -axis currents, i_{dm} , i_{qm} for T_{pc} at the maximum cruise speed ω_c , can be found out iteratively as below.

$$\begin{aligned} i_{db} &= -\frac{\lambda_m}{4L_d(1-k_s)} - \frac{1}{2} \sqrt{\frac{\lambda_m^2}{4L_d^2(1-k_s)^2} + 2I_m^2} \\ i_{qb} &= \frac{T_p}{\frac{m}{2} p \left[\lambda_m + L_d(1-k_s) i_{db} \right]} \\ I_m &= \sqrt{i_{db}^2 + i_{qb}^2} \end{aligned} \quad (5.15)$$

$$i_{dm} = \frac{-\lambda_m L_d + \sqrt{(\lambda_m L_d)^2 - L_d^2 (1 - k_s^2) \left[(L_d k_s I_m)^2 - \left(\frac{V_m}{p \lambda_m} \right)^2 \right]}}{L_d^2 (1 - k_s^2)}$$

And,

$$i_{qm} = \sqrt{I_m^2 - i_{dm}^2} \quad (5.16)$$

$$L_{d-\min} = \frac{T_{pc} - \frac{m}{2} p \lambda_m i_{qm}}{\frac{m}{2} p (1 - k_s) i_{dm} i_{qm}}$$

Neglecting the effect of resistance, the maximum d -axis inductance for an IPM machine is determined by (5.17).

$$L_{d-\max} = \frac{-b + \sqrt{b^2 - 4ac}}{2a}$$

$$a = \left(\frac{2\pi}{60} p \omega_b i_{db} \right)^2 (k_s^2 + 1)$$

$$b = 2 \left(\frac{\omega_b}{\omega_m} \frac{E_m}{\sqrt{3}} \right) \left(\frac{2\pi}{60} p \omega_b i_{db} \right) \quad (5.17)$$

$$c = \left(\frac{\omega_b}{\omega_m} \frac{E_m}{\sqrt{3}} \right)^{2/3} - V_m^2$$

Equations (5.15), (5.16), and (5.17) define the range of d -axis inductance for an IPM machine which satisfies the peak torque requirements and the field-weakening capabilities.

For the design specifications given in Table 5.4, Figure 5.11 shows the maximum and the minimum d -axis inductance as a function of the number of pole pairs. The range of minimum and maximum d -axis inductance reduces with increase in number of pole pairs. It is desirable to have machine d -axis inductance to be as close to $L_{d-\max}$ as possible to achieve better efficiency over high speed range as the current required to weaken the permanent magnet field reduces with an increase in L_d . In fractional-slot per pole per phase machines, fine tuning of L_d is possible by controlling the leakage flux through stator slot opening or stator slot opening depth.

For 6-phase, 18-slot, 8-pole IPM machine design under consideration and a saliency ratio (k_s) of 1.45, the machine inductance should satisfy $0.237 \text{ mH} \leq L_d \leq$

0.682 mH, in order to achieve maximum possible efficiency over high speed region of the torque-speed envelope by employing flux weakening control within a current limit, and also to meet the peak torque capability ($T_p = 140 \text{ N}\cdot\text{m}$) at the base speed ($\omega_b = 2800 \text{ rpm}$) within the voltage limit ($V_{dc} = 320 \text{ V}$).

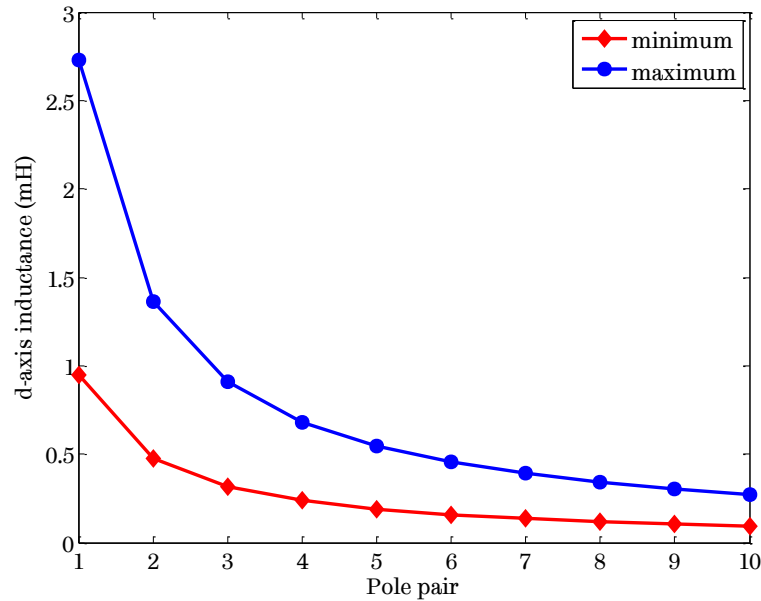


Figure 5.11. Variation of minimum and maximum d -axis inductance with number of pole pairs for 6-phase IPM machine

5.5.2 Volumetric, electrical, mechanical and thermal constraints

In addition to the constraints on d -axis inductance, the machine design under consideration must satisfy the volumetric, electrical, mechanical and thermal constraints as defined in Table 5.6.

Table 5.6. Volumetric, electrical, mechanical and thermal constraints

	<i>Symbol</i>	Value	Unit
Volumetric constraints			
Stator outer radius	r_s	75.0	mm
Stack length of the motor	L	≤ 150.0	mm
Electrical constraints			
Continuous current density	J_c	≤ 10.0	A/mm ²
Maximum flux-linkage	λ_m	≤ 74.7	mWb

Maximum motor current (peak)	I_m	≤ 200.0	A
Minimum d -axis inductance	$L_{d\text{-min}}$	0.237	mH
Maximum d -axis inductance	$L_{d\text{-max}}$	0.682	mH
Mechanical constraints			
Yield strength, M270-35A steel		450	MPa
Tensile strength, M270-35A steel		565	MPa
Thermal constraints			
Copper winding temperature	T_{cu}	≤ 180	$^{\circ}\text{C}$
Steel lamination temperature	T_{fe}	≤ 225	$^{\circ}\text{C}$
PM temperature (NdFeB, N35EH grade)	T_{pm}	≤ 180	$^{\circ}\text{C}$
Ambient air temperature	T_a	45	$^{\circ}\text{C}$
Water inlet temperature	T_{wi}	60	$^{\circ}\text{C}$

5.6 Design and analysis of 6-phase, 18-slot, 8-pole IPM machine for segment-A EV

For a given stator outer radius of 75 mm and stack length of 150 mm, the geometrical parameters that have most significant influence on the performance are shown in Figure 5.12, which include rotor radius r_r , magnet pole arc β_m , magnet cap depth h_q , length of magnet l_m , width of magnet per pole w_m , slot depth d_s , and stator tooth width w_t . The stator slot opening s_o and stator slot opening depth s_{od} are also considered to fine tune the d -axis inductance. It should be noted that the required tooth width w_t , and stator yoke depth, which are function of s_d and r_r , are dependent on the air-gap flux density and maximum permissible flux density in the stator teeth and the yoke.

Generally, the performance of a PM machine enhances as the length of magnet (l_m) is increased. This, however, increases the cost of the machine. Therefore, the mass of PM is to be minimized against the design specifications and demagnetization withstand-ability under the worst case conditions. The air-gap length is assumed to be constant, at 0.5 mm, considering the manufacturing tolerances, and static and dynamic radial clearances. As listed in Table 5.6, M270-35A electrical steel is used for both the stator and the rotor laminations, whereas the permanent magnet material NdFeB is considered with grade N35EH.

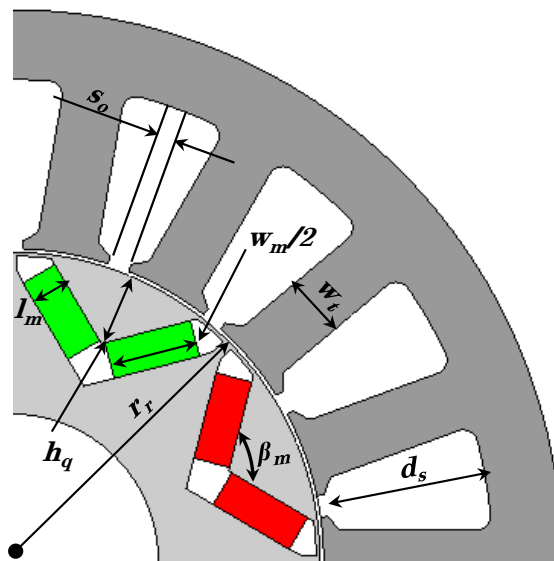


Figure 5.12. Cross-section of 18-slot, 8-pole IPM machine with influential geometrical parameters, phase windings are not shown for clarity.

5.6.1 Design optimization process

The objective of the design optimization is to achieve the best possible torque production at the base speed whilst minimizing the losses over the representative driving cycle, i.e. the NEDC in this case. The leading geometrical parameters are optimized against the objectives subject to the specifications and constraints through a combination of analytical through SPEED software and 2-D finite element analysis (FEA) through FLUX package. The design optimization is summarized as flow-chart in Figure 5.13.

As will be seen from Figure 5.13, the initial sizing and conceptual design was carried out using SPEED software to ensure the machine satisfies the basic design constraints to achieve the peak torque requirement, which are described in Table 5.6. Because of high speed operation requirements for this traction machine, the mechanical stress analysis is carried out using commercial software, ANSYS, at 1.5 times the maximum speed (i.e., 18000 rpm) as part of the design optimization to arrive at the best possible post and bridge geometry of the IPM rotor, which not only keeps the rotor stresses well below the yield strength of the steel material but also provides support to the permanent magnets during the operation.

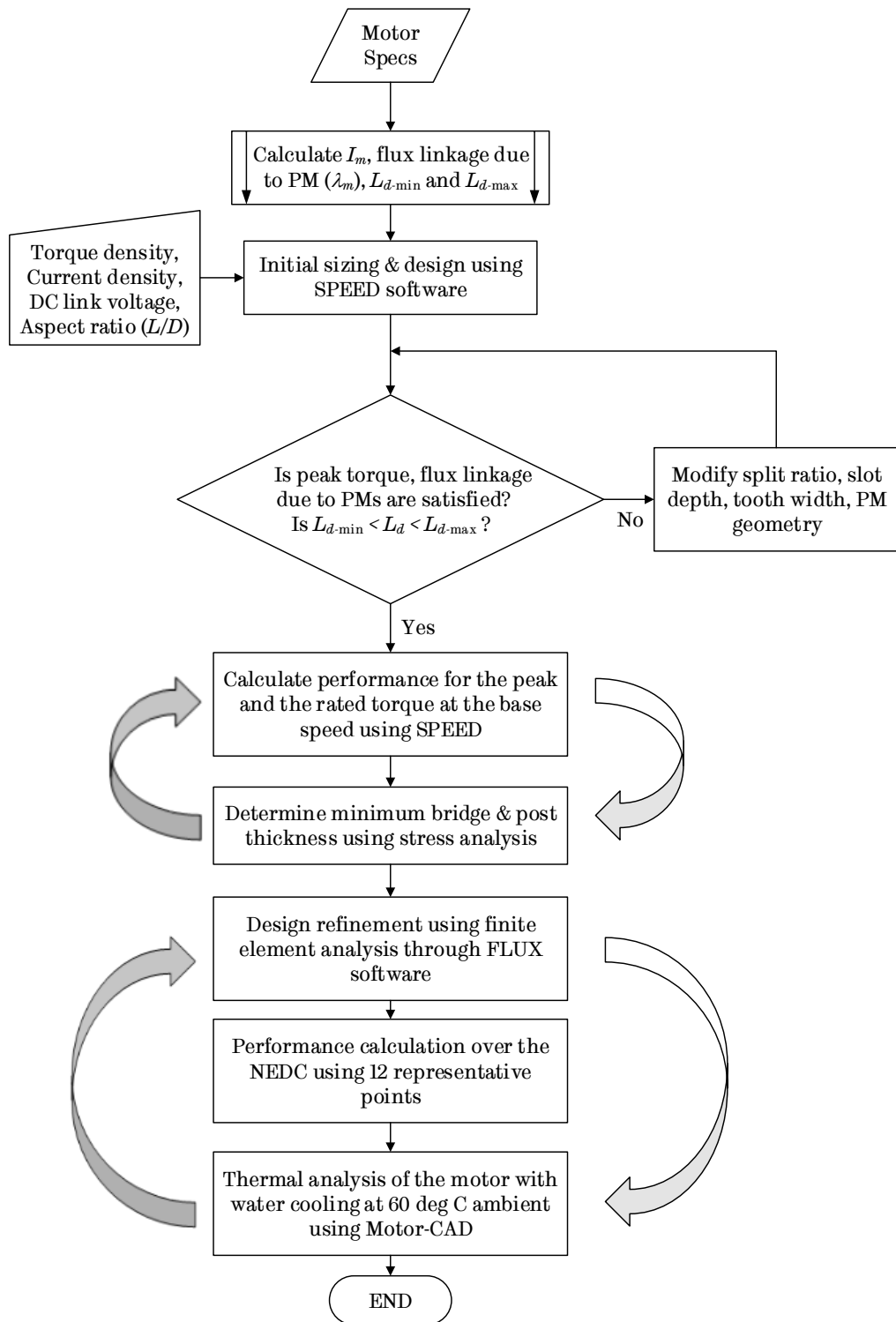


Figure 5.13. Flow-chart for the design of 6-phase, 18-slot, 8-pole IPM machine

It is worthwhile to note that the mechanical requirements for post and bridge dimensions conflict with electromagnetic requirements for better

performance. The iterative process between mechanical design and electromagnetic design is carried out to arrive at the best design that is within mechanical stress design limit with the best possible electromagnetic performance.

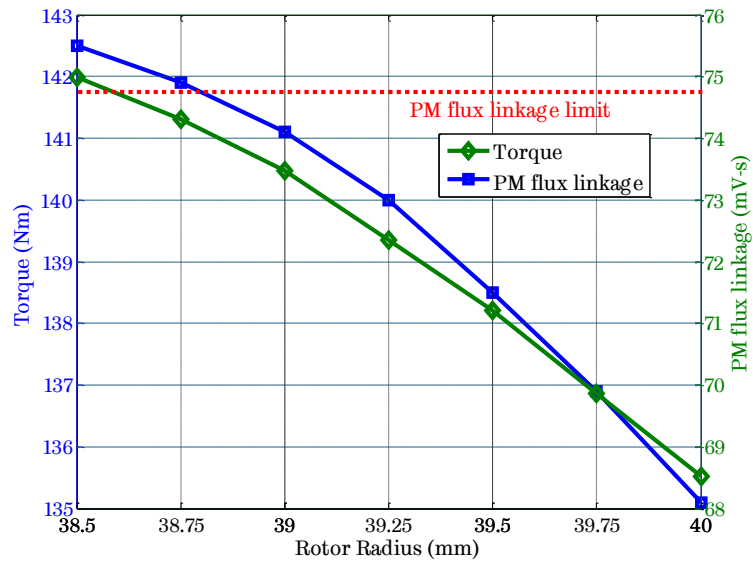
Then, 2-D transient electromagnetic FEA is performed to derive the performance of the machine geometry during the iterative design process over the 12 representative points of the NEDC (as listed in Table 5.5) as well as at the rated and the peak torque operation at the base speed. Once again, there is an iterative process between electromagnetic and thermal analysis to achieve best possible performance within the temperature limits of various parts of the machine, as listed in Table 5.6.

As seen from the flow-chart, the design of an electric machine for wide torque-speed range applications is comparatively complex and iterative with respect to electromagnetics, mechanical, and thermal constraints, requiring good amount of computation time and efforts to complete.

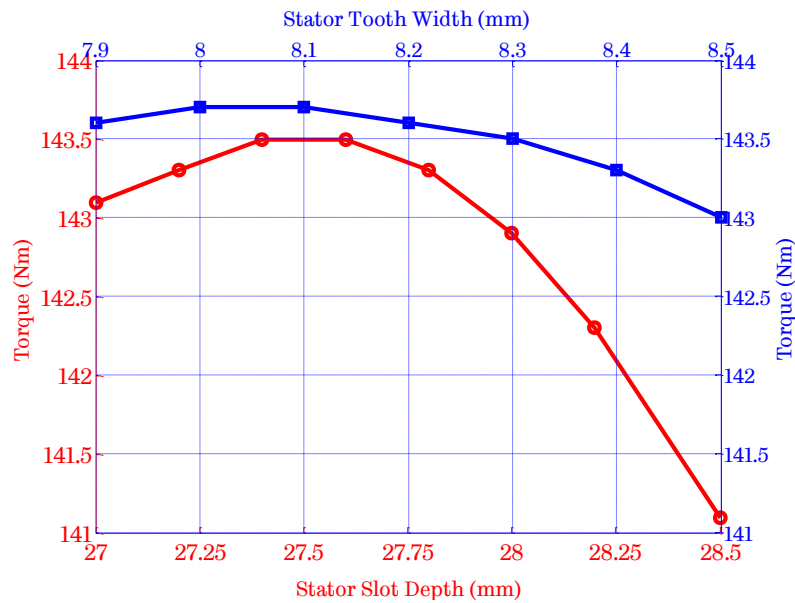
5.6.2 Design optimization trends

As discussed before, the conceptual design and sizing of the 6-phase, 18-slot, 8-pole IPM machine is carried out in SPEED design package, which satisfies the basic design constraints listed in Table 5.6.

Since the torque production is greatly influenced by the rotor radius r_r , stator slot depth d_s , and stator tooth width w_t , these parameters are varied while the current density and the magnet volume is kept constant. As the rotor radius reduces, while the magnet volume being kept constant, the stator yoke area increases, which in turn increases flux-linkage in windings, resulting in to increased torque production. However, the maximum flux-linkage due to PM also increases and impose a limit which restricts the rotor radius. The effect of rotor radius r_r , stator slot depth d_s , and stator tooth width w_t on the motor torque during one of the design iteration is shown in Figure 5.14. It is seen that PM flux-linkage limits the rotor radius at 39 mm, whereas the d_s and w_t are found out to be 27.5 mm and 8.1 mm respectively.



(a) Torque variation as a function of rotor radius with constant copper loss & magnet volume.



(b) Torque variation as a function of stator slot depth (red plot) and stator tooth width (blue plot) with constant copper loss & magnet volume.

Figure 5.14. Design optimization trends during one of the design iteration.

The magnet pole arc β_m , is optimized to minimize the torque ripple which results from the cogging torque and back EMF harmonics [88]. For a given magnet volume, an optimum combination of l_m and w_m is obtained for minimum energy

loss over the NEDC without compromising the peak torque and the rated torque performances.

During the design optimization, for each design iteration, the d -axis inductance is maintained within the range derived in section 5.5.1 to ensure the peak torque capability and efficient field-weakening operation. The leakage flux around the stator tooth is controlled by the stator slot opening s_o , and the stator slot opening depth s_{od} , which helps in refining L_d .

Also, as discussed in section 5.6.1, the mechanical design at 1.5 times the maximum speed, and thermal analysis at the maximum cruise speed operation, is carried out as an integral part of the iterative design process. However, the results of the mechanical and the thermal analyses of the final optimized design only are presented in this chapter. Figure 5.15 shows the cross-section of the optimized machine obtained after design refinements using 2-D FEA in FLUX. Table 5.7 compares the geometrical parameters obtained after initial design using SPEED with those of the final design optimization carried out using FLUX.

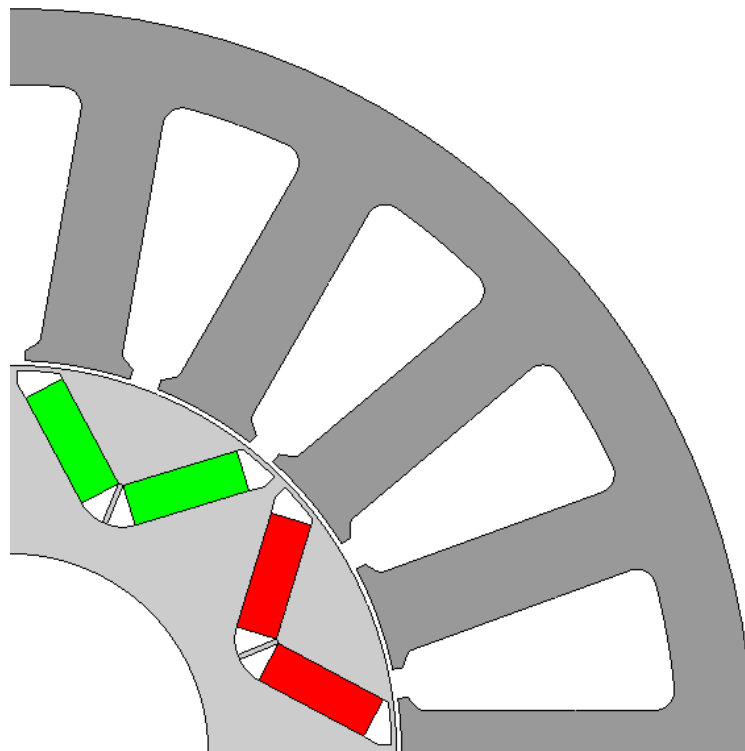


Figure 5.15. Cross-section of optimized 6-phase, 18-slot, 8-pole IPM machine.

Table 5.7. Geometrical parameters of the machine.

Parameter	Symbol	Unit	Initial Design	Optimized Design
Rotor radius	r_r	mm	39.25	39.00
Stator slot depth	d_s	mm	28.50	27.82
Stator tooth width	w_t	mm	8.30	8.38
Stator slot opening	s_o	mm	3.0	3.0
Stator slot opening depth	s_{od}	mm	1.0	1.0
Stator slot area		mm ²	283.6	269.2
Magnet pole arc	β_m	deg.	120°	120°
Magnet cap depth	h_q	mm	10.0	9.796
Length of PM	l_m	mm	5.0	4.2
Width of PM per pole	w_m	mm	24.0	24.0
Turns per coil	t_n	-	12	10
No. of coils per phase	N_c	-	3	3
Mass of PM material	m_{pm}	kg	1.066	0.900
NEDC energy efficiency*		%	94.4	94.9

*including PM eddy current loss over the NEDC

5.6.3 Mechanical design

The rotor mechanical design is carried out to ensure (1) stresses within the rotor material do not exceed the yield strength of the material at maximum operating speed, and (2) the critical speed of the rotor is away from the maximum operating speed. Although the mechanical design is integrated in the design optimization process as an iterative process, this section presents the mechanical design of the optimized rotor only.

5.6.3.1 Mechanical stress analysis

Several iterations of mechanical stress analysis are carried out in ANSYS to arrive at the best possible bridge and post geometry of the IPM rotor by achieving balance between the contradictory requirements of electromagnetic performance with mechanical stress limits. Young's modulus of 192,000 N/mm² is considered in the analysis. Figure 5.16 shows the rotor geometry of the optimized design for mechanical stress analysis. As discussed before, to have safety margin, the mechanical stress analysis is carried out at 1.5 times the maximum operating speed

(12000 rpm), i.e., at 18000 rpm. Figure 5.17 shows the contour plot of the Von Mises stresses in the rotor pole at 18000 rpm. It is seen that the maximum stress in the rotor lamination is about 391 MPa, well below the yield strength of 450 MPa, at the bridge. As expected, the posts are also under stress as the magnets being pulled away due to the centrifugal force while in operation. The safety factor is 1.15 (450/391) at 1.5 times the maximum operating speed of 12000 rpm (i.e., 18000 rpm).

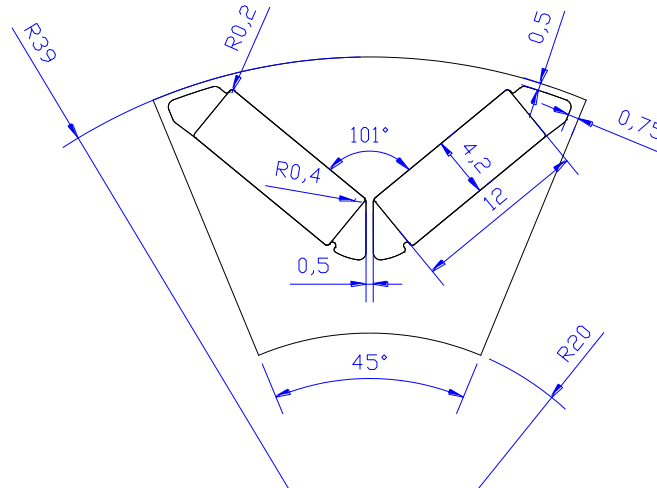


Figure 5.16. Geometry of the optimized rotor pole for mechanical stress analysis.

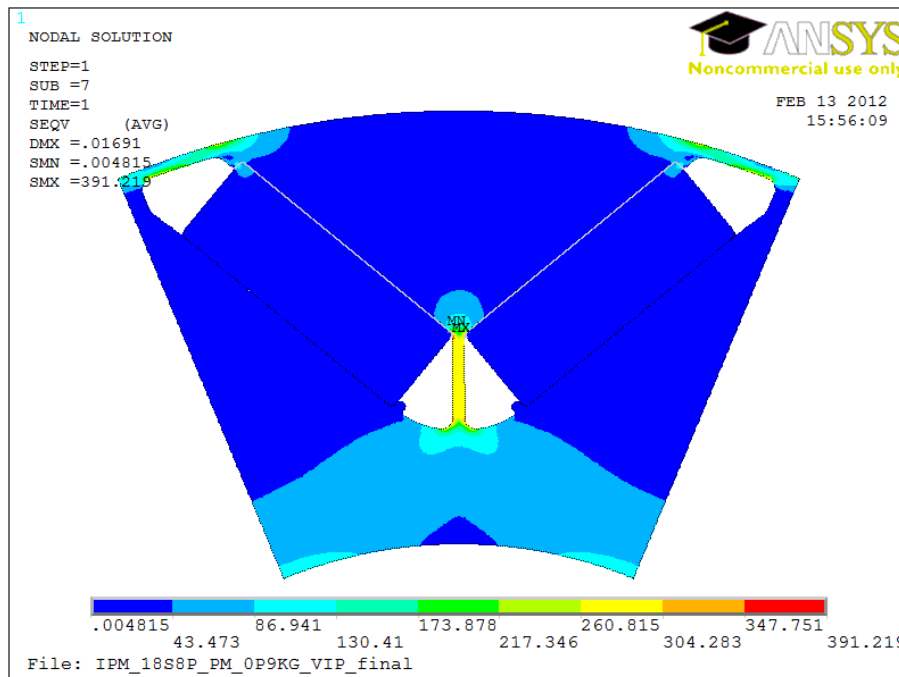


Figure 5.17. Von Mises stress plot of the optimized rotor lamination at 18000 rpm.

5.6.3.2 Rotor dynamics study

In order to determine the critical speed of the IPM rotor, and extended length of the shaft, rotor dynamic study is also carried out using ANSYS. The rotor geometry, shown in Figure 5.18, is considered for the study. The bearing stiffness is assumed to be 5.13×10^7 N/m from SKF bearing data-sheet [113] for a rotor mass of 6.6 kg. Figure 5.18 also shows the resulting first order bending modes in the rotor.

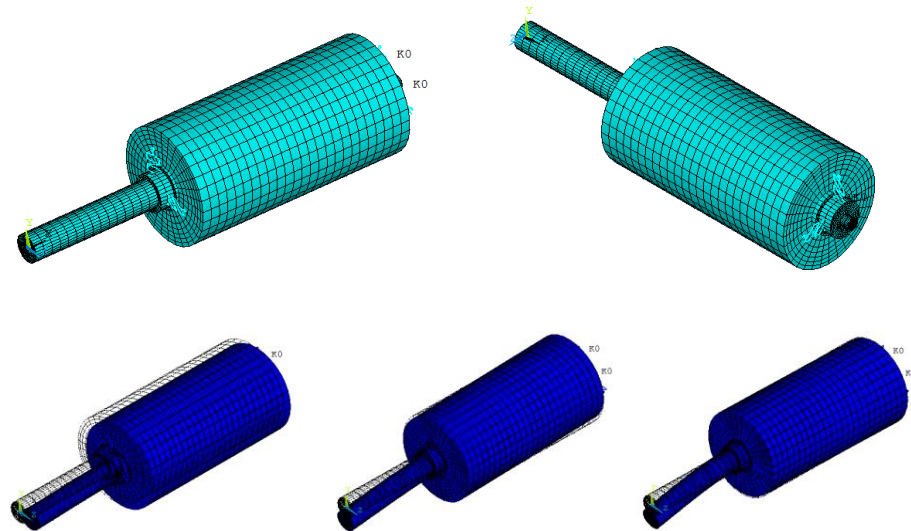


Figure 5.18. Rotor geometry for the rotor dynamics study and first order bending modes.

As a result of the rotor dynamics study, the Cambell diagram is generated showing various bending modes with the corresponding speeds, as in Figure 5.19. As will be seen from the Cambell diagram, the first order critical speed of the rotor is 34121 rpm, which is much higher than the 1.5 times the maximum operating speed of the rotor (i.e., 18000 rpm). In addition, sensitivity study is carried out with respect to the diameter of the shaft extension, and the bearing span. It is observed that the critical speed remains far away from the 1.5 times the maximum operating speed for various shaft extension and bearing span, as listed in Table 5.8.

As seen from Table 5.8, 1st order critical speed of the rotor reduces as the bearing span increases. It also reduces with increase in the diameter of the shaft extension. However, it remains far away from 18000 rpm for all the case studies. The optimized motor was selected with 24 mm diameter of the shaft extension and bearing span of 211.5 mm. If the rotor laminations are ignored in the analysis, the

effective mass of the rotor reduces to 2.6 kg, which in turn translates to radial force of 38.9 N ($m \cdot g + F_c$), where F_c is centrifugal force given by (5.18), e is eccentricity (G/ω) derived from the balance grade of the rotor (G16 considered).

$$F_c = me\omega^2 = me\left(\frac{2\pi}{60}N\right)^2 \quad (5.18)$$

This translates to bearing stiffness of 3.7×10^7 N/m, and the resultant first order critical speed is 42604 rpm. Hence, it is concluded that the rotor design is safe with respect to dynamics.

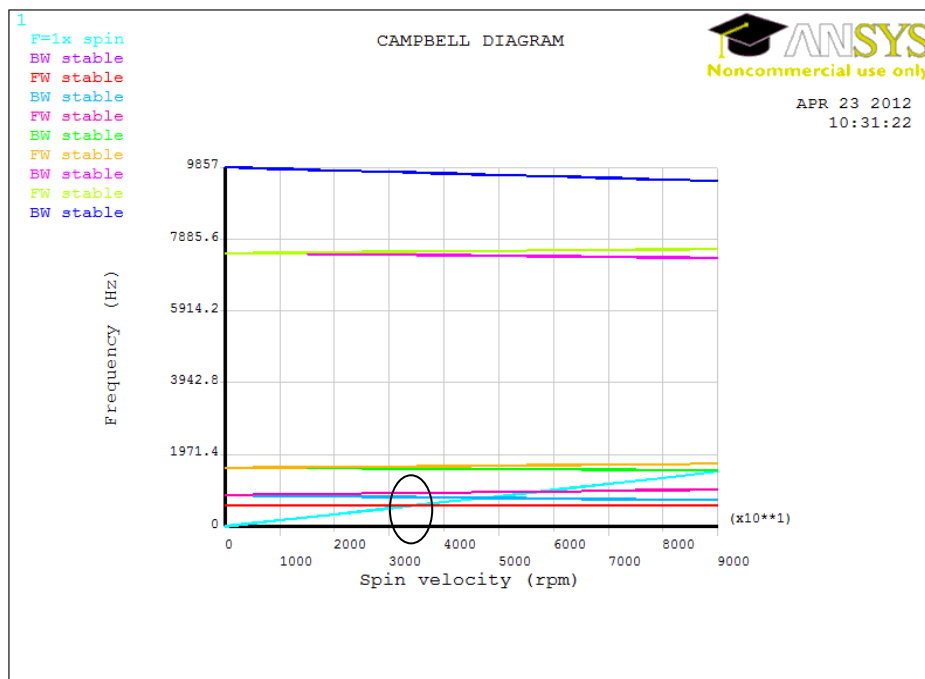


Figure 5.19. Campbell diagram of the optimized 18-slot, 8-pole IPM rotor.

Table 5.8. Sensitivity study for rotor dynamics

Case study	Diameter of shaft extension (mm)	Bearing Span (mm)	1 st order critical speed (rpm)
Original	19	171.5	34121
1	19	208.5	32857
2	19	211.5	32716
3	24	171.5	33135
4	24	211.5	32432

5.6.4 Cooling system design

As the thermal management in electrical machines impacts their life time, it is vital to consider the thermal design of the machine as part of the design procedure. It should be aimed to achieve an efficient and effective dissipation of the electromagnetic and mechanical losses generated in an electrical machine through direct or indirect cooling.

Although the use of a dedicated cooling would have cost and volume implications, it is desirable to make use of the machine enclosure as cooling mechanism, especially for liquid cooled machines. For the machine design under consideration, the machine enclosure is designed to carry cooling medium, i.e., water, around the machine housing in a sealed environment.

Figure 5.20 (a) shows the diagram of the cooling chamber, which also acts as a stator frame to house the stator laminations with copper windings inside the stator slots. The grooves on the cooling chamber are designed to carry water all around the stator periphery at a specific flow rate, and are made up of aluminium to avoid corrosion due to water over long time.

The cooling sleeve (Figure 5.20 (b)) fits outside of the cooling chamber, making it sealed environment for the coolant with the help of two O-rings, one at each end of the machine. As seen from Figure 5.20 (c), there is one water inlet and one water outlet for the water circulation using an external pump (if desired, depends on the required flow rate).

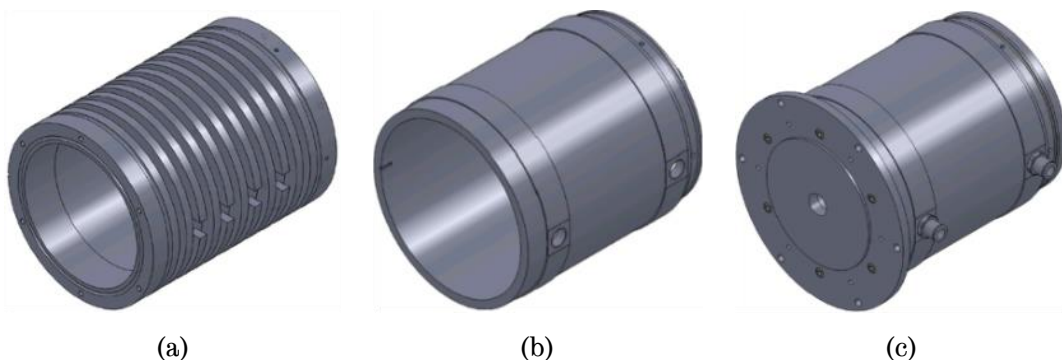


Figure 5.20. Machine enclosure designed for thermal cooling (a) cooling chamber, (b) cooling sleeve, (c) cooling jacket.

5.6.4.1 Design of cooling chamber

The inner diameter of the cooling chamber is determined by the heat shrink requirements as it houses the stator laminations by thermal fit. This results into very good contact between the stator laminations and inner surface of the cooling chamber, conducive to effective heat dissipation from the laminations to the cooling chamber. In order to dissipate heat generated by the machine at the most demanding load condition, the required surface area can be calculated by (5.19).

$$A = \frac{P}{h_c \Delta T} \quad (5.19)$$

where A is the surface area required for the heat dissipation in m^2 , P is the heat to be dissipated in W, h_c is the convection heat transfer coefficient in $W/m^2/^\circ C$, and ΔT is the temperature difference between the cooling chamber and the coolant in $^\circ C$.

Spiral groove water jackets are widely used for liquid cooled machines and provide easy flow path for the coolant. The groove and the channel wall are shown in Figure 5.21, where b_1 and b_2 are width of the groove and the channel wall in m, whereas h is the height of the groove or the channel wall in m. Assuming the number of grooves as N_g , the surface area required for each groove and channel wall is determined by (5.20).

$$A_{gc} = \frac{A}{N_g} \quad (5.20)$$

The surface area of one groove and channel wall can also be expressed by,

$$A_{gc} = 2\pi R_{gb} b_1 + 2\pi \left[(R_{gb} + h)^2 - R_{gb}^2 \right] + 2\pi (R_{gb} + h) b_1 \quad (5.21)$$

where R_{gb} is the groove bottom radius of the cooling chamber in m. The dimensions of the cooling chamber can be estimated using (5.20) and (5.21) for a specific water flow rate. Table 5.9 shows the calculation of the cooling chamber dimensions for the machine under consideration for a specific water flow rate of 6 litre/min.

5.6.4.2 Design of cooling sleeve

As seen from Figure 5.20 (c), the cooling sleeve forms the water circuit geometry, which is a hollow cylinder with an inlet and an outlet for the water. As

the cooling sleeve fits outside of the cooling chamber, the inner diameter of the cooling sleeve will be slightly higher than the outer diameter of the cooling chamber considering the O-ring clearance and the mechanical strength requirements. The difference between the internal diameter and the external diameter of the cooling sleeve, and the length of the cooling sleeve are limited by both the manufacturing process, the motor geometry, and the available space for the specific application.

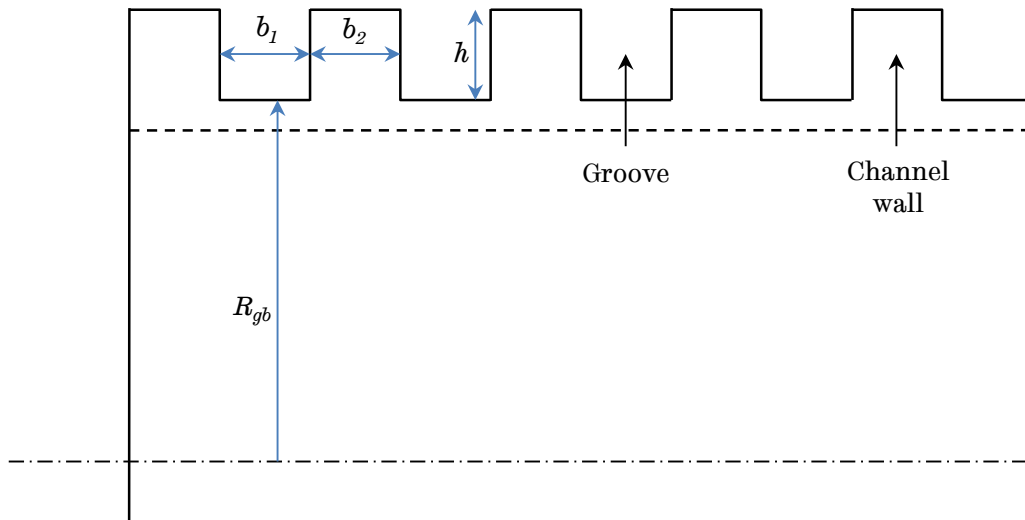


Figure 5.21. Representative cross-section of the cooling chamber.

Table 5.9. Design calculation for the cooling chamber.

Parameter	Symbol	Value	Unit
Losses to be dissipated	P	1300	W
Convection heat transfer coefficient	h_c	960	W/m ² /°C
Desired temperature difference	ΔT	6	°C
Surface area required for cooling	A	0.22	m ²
Number of grooves	N_g	10	-
Width of the groove	b_1	9	mm
Height of the groove or channel wall	h	10	mm
Width of the channel wall	b_2	9	mm
Flow area per channel		135	mm ²
Groove bottom radius	R_{gb}	160	mm
Thickness of the cooling sleeve		10	mm

5.6.5 Thermal analyses of the optimized machine

As explained in the design flow-chart (Figure 5.13), thermal analysis is also considered as a part of the iterative design process for the 6-phase, 18-slot, 8-pole IPM machine. Commercially available thermal analysis package, Motor-CAD, is employed to carry out transient or steady-state thermal analyses.

Although the thermal analysis can be carried out at various load points, the machine design must satisfy the thermal design limits, listed in Table 5.6, at the maximum cruise speed with continuous operation. This operating condition, 19.1 N·m at 11000 rpm, referred to as the maximum cruise speed operation, represents the maximum continuous power consumption of the vehicle. Various heat generating sources in the machine are quantified using 2-D transient electromagnetic FEA in FLUX. The mechanical losses because of bearing friction and windage are also accounted in thermal analysis. The thermal model of the motor is defined in Motor-CAD, and is shown in Figure 5.22. Table 5.10 shows the input to the Motor-CAD model for the thermal analysis.

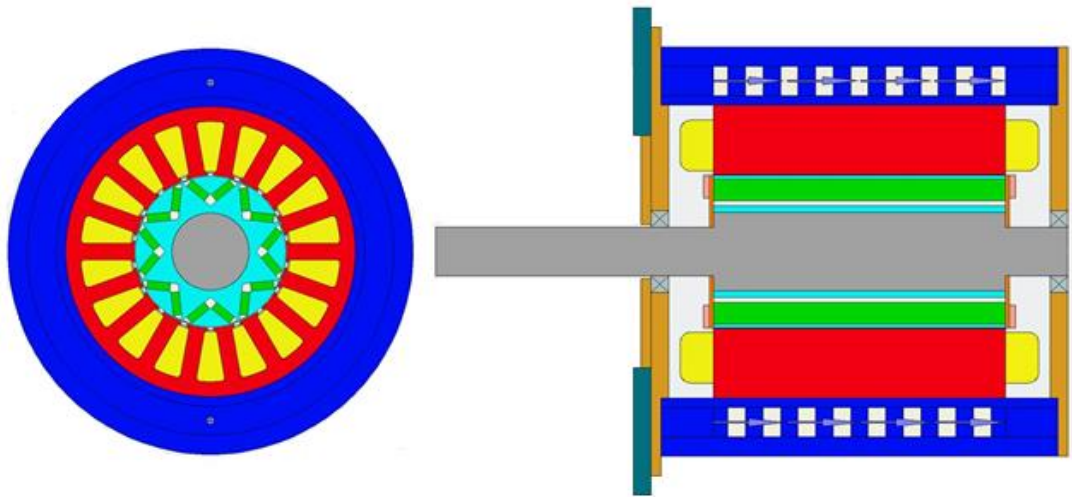


Figure 5.22. Radial and axial cross-section of the machine model in Motor-CAD.

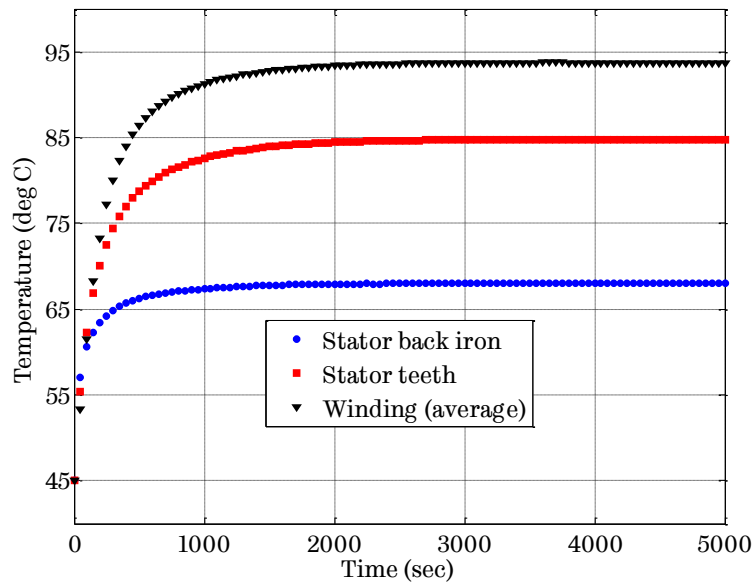
Table 5.10. Input data to Motor-CAD model for thermal analysis.

Parameter	Value	Unit
Maximum cruise speed	11000	rpm
Continuous torque	19.1	N·m

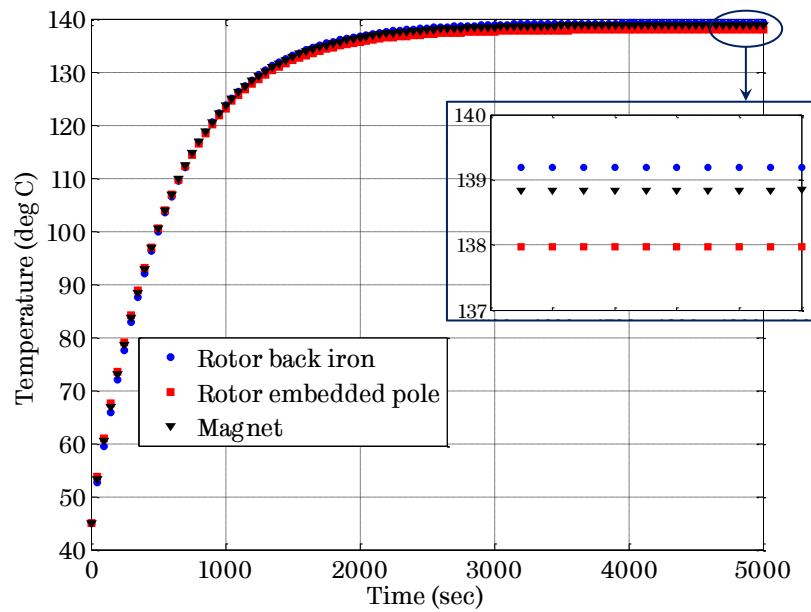
Continuous power	22.0	kW
Iron loss: stator yoke	182.0	W
Iron loss: stator teeth	365.6	W
Iron loss: rotor back iron	120.5	W
Iron loss: rotor embedded magnet pole	132.7	W
Eddy current loss in magnets	49.0	W
Copper loss in stator windings at 120°C	452.2	W
Friction loss in each bearing	2.0	W
Windage loss	150.0	W
Enclosure type	TENV	-
Ambient air temperature	45	°C
Water jacket: inlet temperature	60	°C
Water jacket: cooling flow rate	6	litre/min
Air-gap thermal model type	conduction & convection	
Interface gap between stator lamination and cooling chamber (thermal fit)	Very good (0.005 mm)	

Transient thermal analysis is carried out for the optimized machine for a period of 5000 seconds with 100 sampling points. The initial conditions for the transient analysis are set to the default ambient air temperature of 45 °C for various motor parts, and 60 °C as water inlet temperature.

The transient temperature response of various machine components are shown in Figure 5.23. As will be seen from the transient response of the machine components, the stator of the machine reaches steady-state earlier than the rotor. The stator winding, the stator back iron, and the stator teeth reach thermal steady-state after ~1800 seconds as the stator is cooled by the circulating water around the stator periphery. The rotor components (magnets, rotor back iron, rotor embedded pole) take longer time (~3000 seconds) to reach steady-state as most of the heat from the rotor has to be dissipated through air gap of the machine, and part to the machine end space through radial fins on the rotor end plates. From the transient analysis, it can be estimated that the thermal time constants [114] of the rotor magnets and the stator windings are 588 seconds and 285 seconds respectively.



(a) Transient temperature response of the stator components



(b) Transient temperature response of the rotor components

Figure 5.23. Transient temperature response of the machine components at maximum cruise speed operation (19.1 N·m, 22 kW, 11000 rpm).

The steady-state temperatures of the machine components at the maximum cruise speed operation derived from the transient analysis are listed in Table 5.11.

Table 5.11. Steady-state temperatures of the machine components at maximum cruise speed operation (19.1 N·m, 22 kW, 11000 rpm).

Machine component	Temperature (°C)	Machine component	Temperature (°C)
Stator winding – max.	98.6	Rotor surface	137.2
Stator winding – min.	90.6	Rotor embedded pole	138.0
Stator winding – avg.	93.8	Rotor magnets	138.9
Stator end winding	91.5	Rotor back iron	139.2
Stator back iron	68.0	Rotor shaft centre	137.8
Stator teeth – lower	88.5	Bearing	128.7
Stator teeth – mid	84.8	End plate	63.2
Stator teeth – upper	79.2	Housing	62.6
Stator bore surface	90.7	Coolant (water)	61.5

5.6.5.1 Comparison of the machine temperatures at the rated torque operation and at the maximum cruise speed operation

The thermal analysis at the rated torque operation is also carried out to compare the thermal behaviour of the machine at two different operating conditions. Table 5.12 compares the losses at the two different operating conditions: (1) the rated torque operation, and (2) the maximum cruise speed operation, whereas Table 5.13 compares the machine temperatures at these two operating conditions.

Table 5.12. Comparison of losses in machine at two different operating conditions.

	Rated torque operation	Maximum cruise speed operation
Speed	2800 rpm	11000 rpm
Torque	75.0 N·m	19.1 N·m
Power	22.0 kW	22.0 kW
Stator copper loss at 120 °C	870.0 W	452.2 W
Iron loss – stator back iron	67.3 W	182.0 W
Iron loss – stator teeth	88.1 W	365.6 W
Iron loss – rotor yoke	6.9 W	120.5 W
Iron loss – embedded pole	18.7 W	132.7 W
Eddy current loss in magnets	8.0 W	49.0 W

Table 5.13. Comparison of machine temperatures at two different operating conditions.

	Rated torque operation	Maximum cruise speed operation
Stator winding – average	101.3 °C	93.8 °C
Stator back iron	66.5 °C	68.0 °C
Stator teeth	79.4 °C	84.8 °C
Rotor magnets	87.4 °C	138.9 °C
Rotor back iron	87.4 °C	139.2 °C
Rotor embedded pole	87.3 °C	138.0 °C

As will be seen from the above table, the average winding temperature, the temperature of steel laminations, and the magnet temperatures are well below the respective design limits (listed in Table 5.6).

The winding temperature at the rated torque operation is slightly higher compared to that at the maximum cruise speed operation due to the higher copper loss at the rated torque operation. This is because large current is required to produce 75 N·m torque at the base speed. The total heat (losses) to be dissipated in the stator is almost same for both the operating conditions (1025.4 W for the rated torque operation versus 999.8 W for the maximum cruise speed operation). However, heat dissipation on the stator is quite effective due to water cooling. Consequently the winding temperature at the rated torque operation is marginally greater than that at the maximum cruise speed operation albeit the majority of the stator iron losses at the maximum cruise speed operation are concentrated towards air gap because of field weakening control in operation.

A significant difference in the rotor temperatures exists between the two operating conditions. At the rated torque operation, the low operating speed gives rise to much lower rotor loss and hence lower rotor temperature compared with the maximum cruise speed operation in which the iron loss becomes significant and the field weakening control forces the iron loss in the stator to concentrate at the stator bore, making the rotor heat dissipation further difficult. Hence, the rotor temperatures are much higher at the maximum cruise speed operation compared to the rated torque operation.

Overall, the operation at the maximum cruise speed with the continuous rated power (22 kW) is more demanding as rotor temperatures are closer to design limits and the rotor losses need to be dissipated indirectly via the stator. Thus this condition at the maximum cruise speed represents the worst case scenario among all the continuous power operations, at 22 kW, across the torque-speed envelope.

5.6.6 Sensitivity studies on the machine temperatures

In order to test the robustness of the results of the thermal analysis in the presence of (a) the uncertainties with respect to (i) actual losses in the prototype machine compared to design models, and (ii) difference in cooling conditions, and (b) various geometrical features in the machine, comprehensive sensitivity studies on the machine temperatures are considered.

5.6.6.1 Sensitivity of machine temperatures with losses

The sensitivity of copper loss and iron loss variation on machine temperatures has been studied by increasing copper loss and iron loss in the thermal analysis at the maximum cruise speed operation. Table 5.14 lists the temperatures of the machine components with different variation of copper and iron loss. Temperatures for the optimized design selected for prototyping are shown in **bold blue** letters.

Table 5.14. Sensitivity of machine temperatures with losses.

Copper loss	Iron loss	Winding (average)	Stator back iron	Stator teeth	Rotor magnets	Rotor back iron	Rotor embedded pole
		(°C)	(°C)	(°C)	(°C)	(°C)	(°C)
100%	100%	93.8	68.0	84.8	138.9	139.2	138.0
105%	115%	97.1	69.0	87.8	149.7	150.1	148.7
110%	125%	99.7	69.7	89.9	157.2	157.6	156.1
115%	150%	104.5	71.2	94.6	175.1	175.6	173.8

With 15% higher copper loss and 50% higher iron loss, the average winding temperature is still well below the design limit of 180°C. However, the design margin for the magnet temperature is reduced to only 5°C. Although NdFeB magnets are allowed to operate up to 180°C temperature, they shall not be operated

continuously at elevated temperature because of the risk of partial irreversible demagnetization.

5.6.6.2 Influence of steel lamination thickness on machine temperatures

As seen in the previous section, the machine temperatures will be quite high when the iron loss is increased by 50% and copper losses by 15%. In order to confine the machine temperatures with sufficient design margin, thinner laminations may be employed for the rotor core. The influence of stator and rotor lamination thickness on the machine temperatures is studied at the maximum cruise speed operation. Table 5.15 lists the losses in various components of the machine for different thicknesses of the stator and the rotor laminations. As expected, the iron loss reduces due to reduction in eddy current loss component, which is directly proportional to the thickness of the lamination. Table 5.16 lists the resulting temperatures of the machine components with different lamination thickness in the stator and the rotor.

Table 5.15. Losses in machine components with steel lamination thickness.

Stator lam.	Rotor lam.	Winding (average)	Stator back iron	Stator teeth	Rotor magnets	Rotor back iron	Rotor embedded pole
(mm)	(mm)	(W)	(W)	(W)	(W)	(W)	(W)
0.35	0.35	452.2	182.0	365.6	49.0	120.5	132.7
0.2	0.35	452.2	104.5	204.4	49.0	120.5	132.7
0.35	0.2	452.2	182.0	365.6	49.0	71.4	62.3
0.2	0.2	452.2	104.5	204.4	49.0	71.4	62.3

Table 5.16. Influence of lamination thickness on machine temperatures.

Stator lam.	Rotor lam.	Winding (average)	Stator back iron	Stator teeth	Rotor magnets	Rotor back iron	Rotor embedded pole
(mm)	(mm)	(°C)	(°C)	(°C)	(°C)	(°C)	(°C)
0.35	0.35	93.8	68.0	84.8	138.9	139.2	138.0
0.2	0.35	90.1	66.4	80.3	134.9	135.3	134.0
0.35	0.2	91.2	67.3	82.2	115.5	115.5	114.7
0.2	0.2	87.5	65.7	77.7	111.5	111.6	110.6

Losses and temperatures for the optimized design selected for prototyping are shown in **bold blue** letters in Table 5.15 and Table 5.16 respectively.

As will be seen from the above table, by employing 0.2 mm lamination for the rotor core, the rotor temperatures can be reduced by ~24°C. However, the 0.2 mm thick steel laminations are not commonly used for industrial applications and it is indeed difficult to purchase small quantity material within realistic time frame within the cost. Hence, the prototype machine has been built with 0.35 mm thick laminations. However, it is recommended to use 0.2 mm thick rotor laminations for the machine through established supply chain for its future mass production, so that enough design margin is achieved for the machine at the maximum cruise speed operation with uncertainty on the actual value of the iron loss. Table 5.17 shows the predicted temperatures with 0.2 mm thick rotor laminations with 15% higher copper loss and 50% higher iron loss. As will be seen, the temperature of the rotor magnet is now much below 180°C design limit, yielding design margin of 35.6°C.

Table 5.17. Machine temperatures with 0.2 mm thick rotor lamination with 115% copper loss and 150% iron loss.

Stator lam.	Rotor lam.	Winding (average)	Stator back iron	Stator teeth	Rotor magnets	Rotor back iron	Rotor embedded pole
(mm)	(mm)	(°C)	(°C)	(°C)	(°C)	(°C)	(°C)
0.35	0.20	100.6	70.2	90.6	139.6	139.7	138.4

5.6.6.3 Influence of vent holes in end plates on machine temperatures

Because of the harsh environmental conditions experienced by an electric vehicle during its life time, it is not advisable to have open vent holes in the traction machine for the cooling purpose. However, as part of the sensitivity study, its influence on the machine temperatures is worth to explore.

If ventilation holes are placed in the machine end-plates, they will allow air to flow in the machine end region, taking the heat away from the region (end windings, space around the rotor) thus enabling better heat transfer between the rotor end plate and the machine end region. The steady-state thermal analysis is

performed with opening of vent holes in the machine end plates and results are summarised in Table 5.18. The machine temperatures are obtained with an assumption of air flow rate of 0.02 m³/sec at 11000 rpm and the inlet temperature of the end plate vents as the ambient air temperature, i.e. 45°C. This flow rate is achieved with four vents of 25 mm diameter in the machine end plates. The velocity of air is assumed to be 10 m/sec. Temperatures for the optimized design selected for prototyping are shown in **bold blue** letters.

Table 5.18. Influence of vent holes on machine temperatures.

Front end plate	Rear end plate	Winding (average)	Stator back iron	Stator teeth	Rotor magnets	Rotor back iron	Rotor embedded pole
-	-	(°C)	(°C)	(°C)	(°C)	(°C)	(°C)
Close	Close	93.8	68.0	84.8	138.9	139.2	138.0
Close	Open	90.7	67.3	82.7	129.7	129.8	129.1
Open	Close	90.7	67.3	82.7	129.7	129.8	129.1
Open	Open	87.5	66.6	80.8	121.8	121.7	121.5

As seen from the above table, the opening of vent holes in the machine end plates results in ~10-20°C lower temperatures in the rotor due to increased heat transfer. This opens up another option to achieve better design margin at the maximum cruise speed operation with increased losses, as seen from Table 5.19.

Table 5.19. Machine temperatures with open vent holes (4 × Ø25 mm) in end plates with 115% copper loss and 150% iron loss.

Front end plate	Rear end plate	Winding (average)	Stator back iron	Stator teeth	Rotor magnets	Rotor back iron	Rotor embedded pole
-	-	(°C)	(°C)	(°C)	(°C)	(°C)	(°C)
Open	Open	96.4	69.4	89.5	153.0	153.0	152.4

As will be seen from Table 5.19, the temperatures of the winding and stator steel are still well below the design limits, whereas sufficient design margin (27°C) is achieved for the rotor magnets. The assumption of 10 m/sec air velocity at 11000

rpm shall be calibrated based on experiment data on the vehicle with the machine at the maximum vehicle cruise speed and continuous torque.

5.6.6.4 Sensitivity of the machine temperatures with water flow rate

The influence of water flow rate with the machine temperatures is considered to study robustness of the machine design in the event of variable coolant flow due to vehicle operation in varying environmental conditions. Table 5.20 shows the machine temperatures with varying water flow rate at the maximum cruise speed operation. Temperatures for the optimized design selected for prototyping are shown in **bold blue** letters.

Table 5.20. Influence of water flow rate on machine temperatures.





Flow rate	Convection Correlation	Winding (average)	Stator back iron	Stator teeth	Rotor magnets	Rotor back iron	Rotor embedded pole
(l/min)	-	(°C)	(°C)	(°C)	(°C)	(°C)	(°C)
0.5	laminar	134.0	106.3	123.6	178.1	178.4	177.2
0.75	laminar	127.0	99.6	116.9	171.3	171.6	170.4
1	turbulent	101.4	75.3	92.1	146.2	146.5	145.3
2	turbulent	98.8	72.8	89.7	143.7	144.1	142.9
4	turbulent	95.1	69.2	86.0	140.1	140.5	139.2
6	turbulent	93.8	68.0	84.8	138.9	139.2	138.0
8	turbulent	93.2	67.4	84.2	138.3	138.6	137.4
10	turbulent	92.8	67.1	83.8	137.9	138.3	137.0

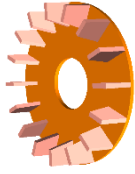
It is evident that as the flow rate increases, the temperatures of the machine components reduce. With flow rates less than 1 litre/min, laminar flow occurs due to low velocity of the water, and it is not effective for heat dissipation. For effective cooling, the turbulent flow is desirable inside the closed water jacket channels. The flow rate of 6 litre/min is a standard norm in most industrial applications, and with that, the machine temperatures are below the design limits with sufficient margin. With further increase in the flow rate from 6 litre/min, the reduction in the machine temperatures is much less significant.

5.6.6.5 Sensitivity of the machine temperatures with radial fins on the rotor end plates

The radial fins on the rotor end plate increase the surface area of the rotor for better heat dissipation at the expense of more drag or windage loss while in operation. The sensitivity of the machine temperatures with radial fins on the rotor end plates is also considered at the maximum cruise speed operation. The results are summarized in Table 5.21. Temperatures for the optimized design selected for prototyping are shown in **bold blue** letters.

Table 5.21. Sensitivity of the machine temperatures with rotor radial fins.

No. of fins /plate	Fin geometry L×W×T (mm)	Winding (average) (°C)	Stator back iron (°C)	Stator teeth (°C)	Rotor magnets (°C)	Rotor back iron (°C)	Rotor embedded pole (°C)
8	 3×11.5×3	93.8	68.0	84.8	138.9	139.2	138.0
8	 5×16.5×3	93.8	68.0	84.7	136.9	137.2	136.1
12	 3×11.5×3	93.8	68.0	84.8	137.9	138.2	137.1
12	 5×16.5×3	93.8	68.0	84.6	135.1	135.3	134.4

16		93.8	68.0	84.4	131.6	131.8	131.0
	12×11.5×2 Depth reduction 4 mm						

As will be seen from the above table, the fins on the rotor end plates can marginally reduce rotor temperatures by 2-5°C. However, they will also introduce extra drag or windage losses if the fins are made in form of fan blades (seen in last option in the above table). The optimization of radial fins on rotor end plates can be considered for future design improvements if desired.

5.7 Performance of the optimized design of 6-phase, 18-slot, 8-pole IPM machine

The optimized cross-section of 6-phase, 18-slot, 8-pole IPM machine is shown in Figure 5.24, whereas Table 5.22 lists the important design parameters of the machine. The detailed geometrical parameters are listed in Table 5.7.

Table 5.22. Important design parameters of the optimized machine.

Design parameter	Value	Design parameter	Value
Number of phases	6	No. of coils per phase	3
Number of slots	18	No. of turns per coil	10
Number of poles	8	Weight of laminations	10.6 kg
Stator diameter	150 mm	Weight of copper	3.8 kg
Stack length	150 mm	Weight of magnets	0.9 kg
Extended shaft diameter for couplings	24 mm	Phase shift between ABC and DEF	20°
Shaft diameter (active)	40 mm	Torque density*	52.8 N·m/l
Power density*	15.5 kw/l	Specific power*	2.67 kW/kg

*considering only active volume/weight and the peak power/torque.

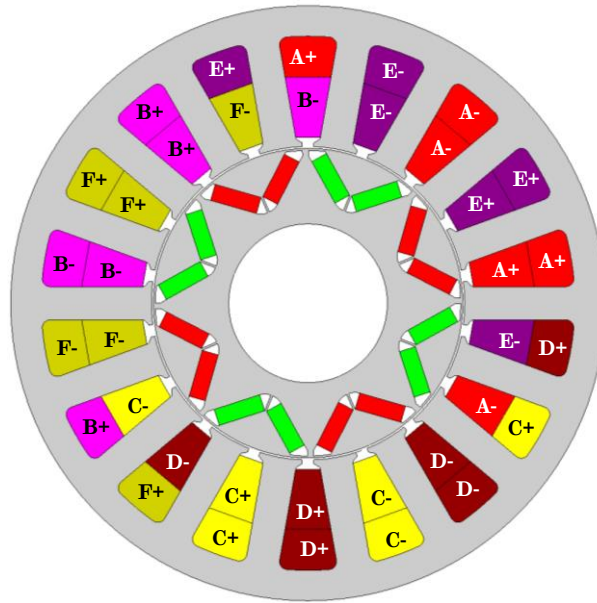


Figure 5.24. Optimized cross-section of 6-phase, 18-slot, 8-pole IPM machine.

5.7.1 Performance at the rated and the peak torque operation

The performance of the optimized machine is evaluated at the rated torque and the peak torque operation at the base speed and is shown in Table 5.23. The magnet temperature is considered as 85° C in the predictions.

Table 5.23. Performance of the optimized machine at the rated and the peak torque operation at the base speed.

Parameter	Rated torque	Peak torque	Unit
Torque	75.0	140.0	N·m
Speed	2800	2800	rpm
Power	22.0	41.0	kW
Torque ripple	2.7	4.4	%
Peak phase current	74.0	172.5	A
Line-line voltage (V_{u_1})	217.0	297.9	V
Current density	9.7	22.7	A/mm ²
Copper loss	870	4728	W
Iron loss – stator	155	230	W
Iron loss – rotor	26	44	W
PM eddy current loss	8	9	W
Power efficiency	95.4	89.1	%

As seen, the designed machine meets its peak torque capability within a voltage limit of 320 V and current limit of 200 A peak, and the rated torque capability within accepted continuous current density in order to have temperatures of the machine components within design limits. The torque ripple is also within 5%, which is one of the key requirements for EV traction machines.

5.7.2 Performance over the NEDC

Performance of the optimized machine is evaluated over the NEDC using energy efficiency. The 12 distinct points, obtained in section 5.4, are used to determine the losses in the machine using 2-D transient electromagnetic FEA in FLUX. Table 5.24 summarizes the losses and energy consumption at each of these 12 points of the NEDC, and energy efficiency over the NEDC determined by (5.9).

5.7.3 Torque ripple, flux lines and flux density plots

Figure 5.25 shows the torque profile over an electrical cycle at the rated torque and the peak torque operation at the base speed. As will be seen, the torque ripple is within acceptable range (below 5%) for EV application. Figure 5.26 shows the flux lines and flux density plots from 2-D FEA.

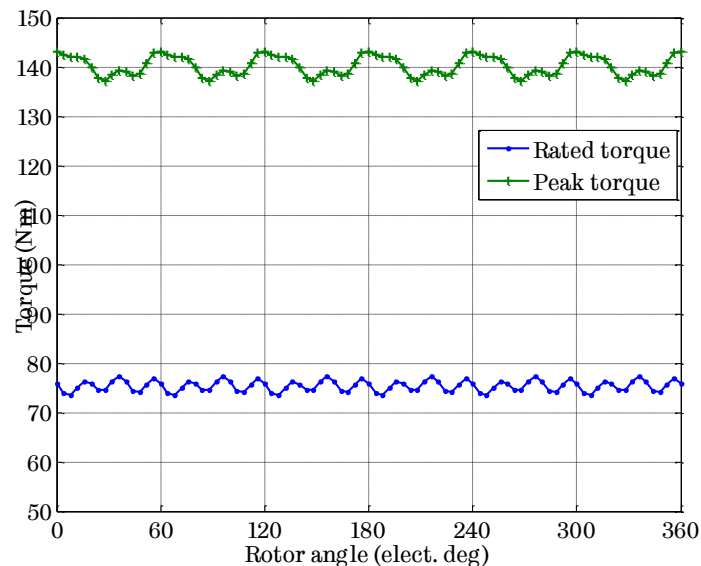
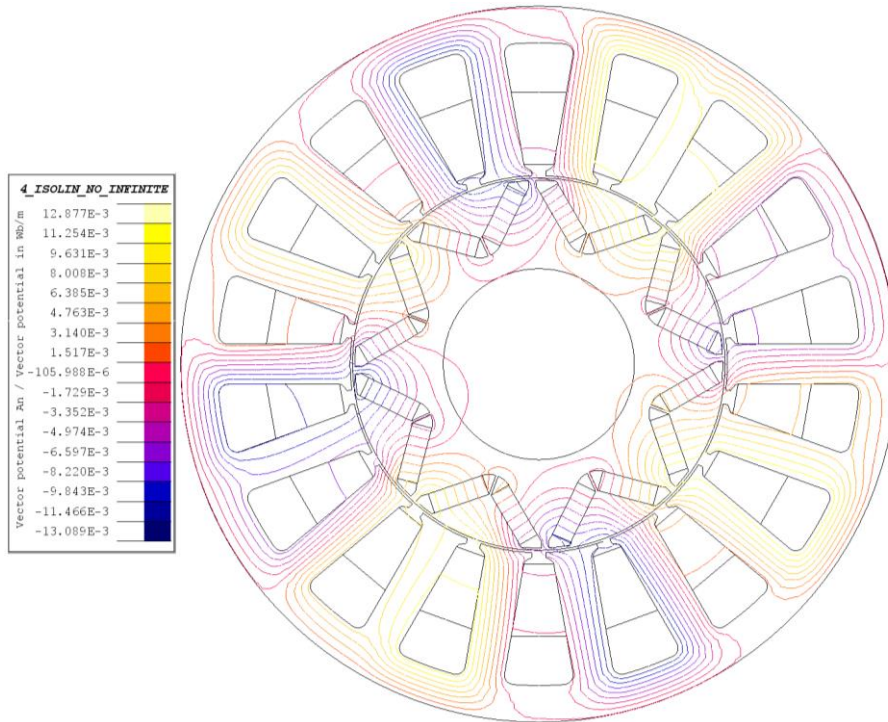


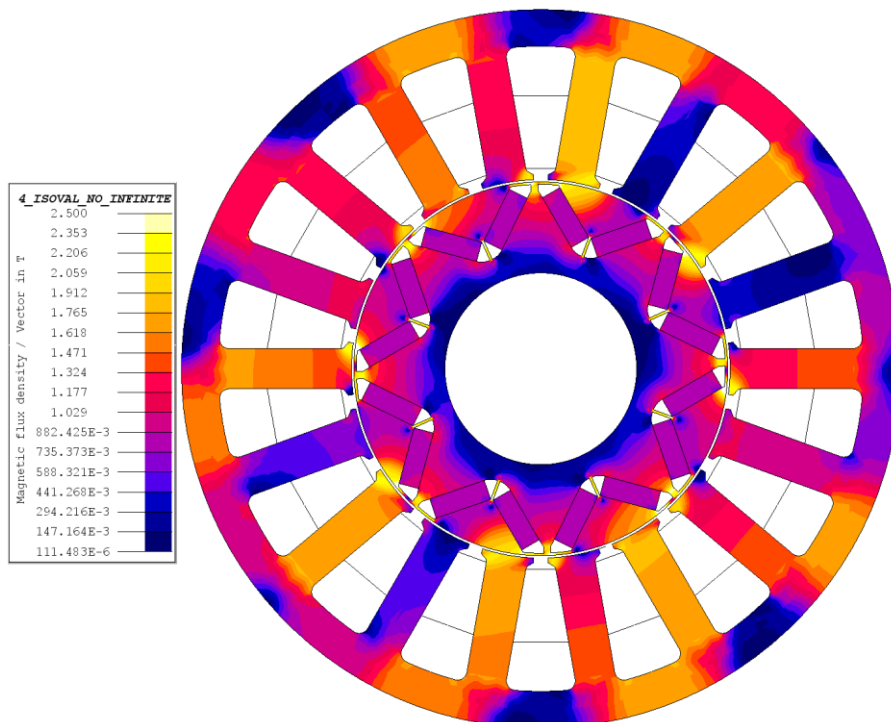
Figure 5.25. Torque profile of the optimized machine over an electrical cycle.

Table 5.24. Performance of the optimized machine over 12 representative points for the NEDC.

NEDC Point	Torque	Speed	Time	Peak current	Gamma	V_{IL1}	Rotor Iron loss	Stator iron loss	Copper loss	PM loss	Power efficiency	Total loss energy	Output energy
-	(N·m)	(rpm)	(sec)	(A)	(°)	(V)	(W)	(W)	(W)	(W)	(%)	(J)	(J)
1	63.0	583	5.7	61.0	30.5	46.8	3.1	19.3	591.2	0.2	86.3%	3492	21907
2	29.1	652	66.1	27.9	20.0	45.5	2.8	18.3	123.7	0.1	93.2%	9584	131379
3	24.1	2532	134.0	23.2	18.0	167.2	14.8	101.0	85.5	1.7	96.9%	27200	858716
4	3.3	2757	114.0	3.3	4.2	171.2	11.7	101.0	1.7	1.3	89.2%	13187	109330
5	3.9	3075	62.4	3.8	4.5	191.1	13.7	118.5	2.3	1.6	90.3%	8492	78717
6	64.2	3112	23.2	62.3	30.5	228.6	27.3	169.6	616.6	6.3	96.2%	19017	485545
7	5.3	4347	195.5	5.2	5.5	270.9	22.5	199.3	4.3	3.1	91.4%	44809	473636
8	20.9	5317	42.1	21.6	37.0	319.0	42.1	262.4	74.2	4.1	96.8%	16128	490886
9	7.9	6149	101.3	16.5	69.0	319.7	42.4	262.8	43.3	3.1	93.6%	35605	523220
10	20.7	8615	64.9	44.5	74.0	314.3	137.5	376.0	314.6	22.3	95.6%	55169	1211991
11	13.1	8800	30.8	38.0	78.5	320.4	126.0	361.3	229.4	16.8	94.3%	22592	372149
12	17.8	10496	10.3	49.5	78.7	320.3	216.9	493.8	389.3	38.6	94.5%	11686	200766
Total	-	-	850.3	-	-	-	-	-	-	-	-	266962	4958242
Energy efficiency over the NEDC												94.9%	



(a) Flux lines in the optimized machine



(b) Flux density plot in the optimized machine

Figure 5.26. Flux plots from 2-D FEA at the rated torque operation (74.0 N-m, 22 kW, 2800 rpm).

5.7.4 Efficiency map of the optimized machine

The efficiency map of the optimized machine is determined using the flux linkages derived from 2-D transient FEA and iron loss model developed using the method described in [115]. Figure 5.27 shows the predicted efficiency map of the machine. The 12 representative NEDC points are also shown as stars.

It is evident that the designed IPM machine with a novel topology of 18-slot, 8-pole has high efficiency over wide torque-speed range of the traction vehicle under consideration.

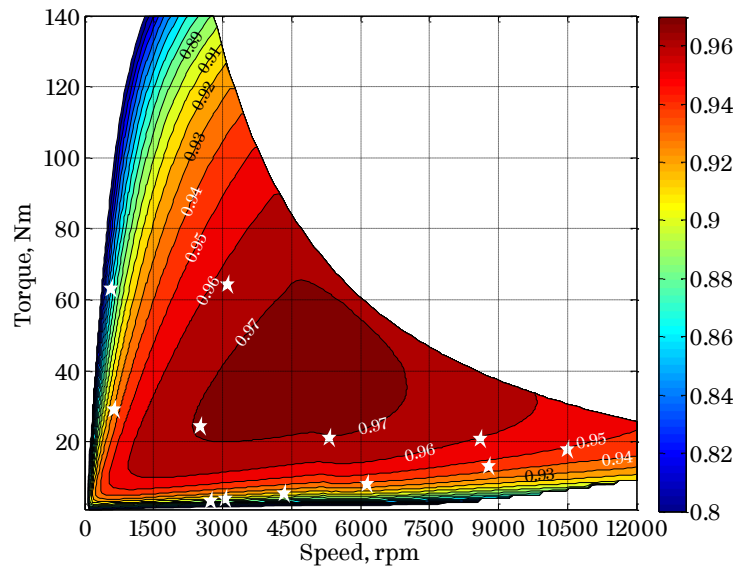


Figure 5.27. Predicted efficiency map of 6-phase, 18-slot, 8-pole IPM machine.

5.7.4.1 Fault tolerant capability

As described in Chapter 4, the designed machine having the proposed winding configuration with 6-phase, 18-slot, 8-pole exhibits the fault tolerant capability. In the event of a fault on one set of 3-phase system, other set of 3-phase will continue to operate with half the torque/power output. This enhances the fault tolerance capability of the electric traction machine without compromising vehicle stability and passenger safety. In this case, the machine will have an unbalanced magnetic pull (UMP) as it will not have other set of 3-phase winding (e.g., D-E-F) to eliminate the unbalanced magnetic pull generated by the healthy 3-phase winding (e.g., A-B-C) in operation. However, this may not be an adverse issue considering the

vehicle has to run only for short duration to reach the safe place for the fault mitigation.

In order to predict performance of the designed 6-phase, 18-slot, 8-pole IPM machine under 3-phase operation, one set of 3-phase winding (A-B-C) is supplied by the current sources in 2-D FEA, and the other set (D-E-F) is open circuited. Figure 5.28 shows the predicted efficiency map of 6-phase, 18-slot, 8-pole IPM machine under 3-phase operation. It is worthwhile to note that the copper loss reduces to almost half in 3-phase operation, whereas the iron loss also reduces albeit not to half value, compared to 6-phase operation. Hence, the efficiency of the machine is slightly lower in 3-phase operation compared to 6-phase operation (Figure 5.27), as the output power also reduces to half over the entire speed range.

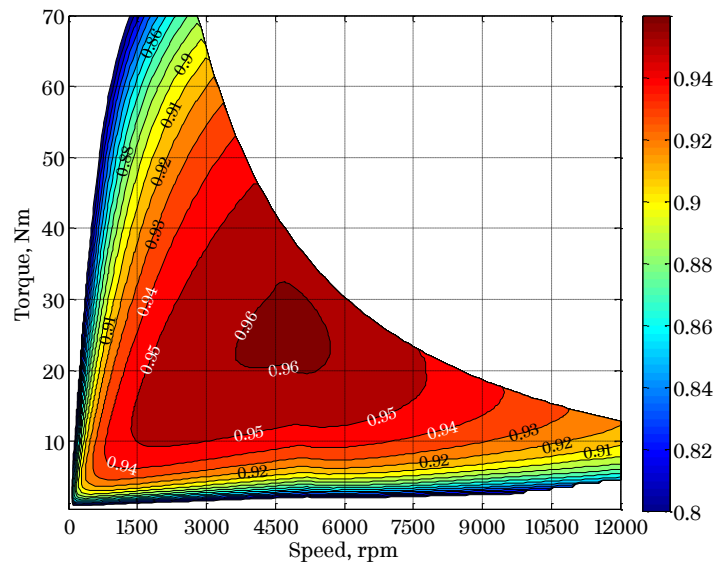


Figure 5.28. Predicted efficiency map of 6-phase, 18-slot, 8-pole IPM machine under 3-phase operation (A-B-C in operation, D-E-F open circuited).

5.8 d - q axis model and parameters of 6-phase, 18-slot, 8-pole IPM machine

5.8.1 d - q axis model of the machine

The designed 6-phase, 18-slot, 8-pole IPM machine has a phase shift of 20° electrical between A-B-C and D-E-F, and is achieved by 13 slot-shift. The d - q axis model of the machine is given by (5.22).

$$\begin{aligned} L_d \frac{di_d}{dt} + Ri_d &= v_d + \omega L_q i_q \\ L_q \frac{di_q}{dt} + Ri_q &= v_q - \omega L_d i_d - K_e \omega_m \end{aligned} \quad (5.22)$$

where V_d and V_q are d - and q -axis voltages respectively, i_d and i_q are d - and q -axis currents respectively, L_d and L_q are the d - and q -axis inductances respectively, ω and ω_m are the electrical and mechanical angular speed respectively, R is the phase resistance, $K_e (=p\lambda_m)$ is the back EMF constant, p is number of pole pairs, and λ_m is the peak flux linkage per phase due to permanent magnet field.

The electromagnetic torque expressed in d - q axis variables is given by (5.13).

The 6-phase to d - q axis transformation is given by (5.23).

$$C_{dq \leftarrow 6phase} = \frac{2}{6} \begin{bmatrix} -\cos\theta & -\cos(\theta-120^\circ) & -\cos(\theta+120^\circ) & -\cos(\theta-20^\circ) & -\cos(\theta-140^\circ) & -\cos(\theta+100^\circ) \\ \sin\theta & \sin(\theta-120^\circ) & \sin(\theta+120^\circ) & \sin(\theta-20^\circ) & \sin(\theta-140^\circ) & \sin(\theta+100^\circ) \end{bmatrix} \quad (5.23)$$

The inverse transformation is,

$$C_{6phase \leftarrow dq} = \begin{bmatrix} -\cos\theta & \sin\theta \\ -\cos(\theta-120^\circ) & \sin(\theta-120^\circ) \\ -\cos(\theta+120^\circ) & \sin(\theta+120^\circ) \\ -\cos(\theta-20^\circ) & \sin(\theta-20^\circ) \\ -\cos(\theta-140^\circ) & \sin(\theta-140^\circ) \\ -\cos(\theta+100^\circ) & \sin(\theta+100^\circ) \end{bmatrix} \quad (5.24)$$

Also, the mechanical torque balance equation for the system is given by

$$J \frac{d\omega_m}{dt} = (T_e - T_L - B\omega_m) \quad (5.25)$$

where J is the moment of inertia of the system, and B is the viscous friction coefficient, T_L is the load torque, and T_e is the electromagnetic torque of the motor whether it operates as a 6-phase machine, or as two independent 3-phase machines.

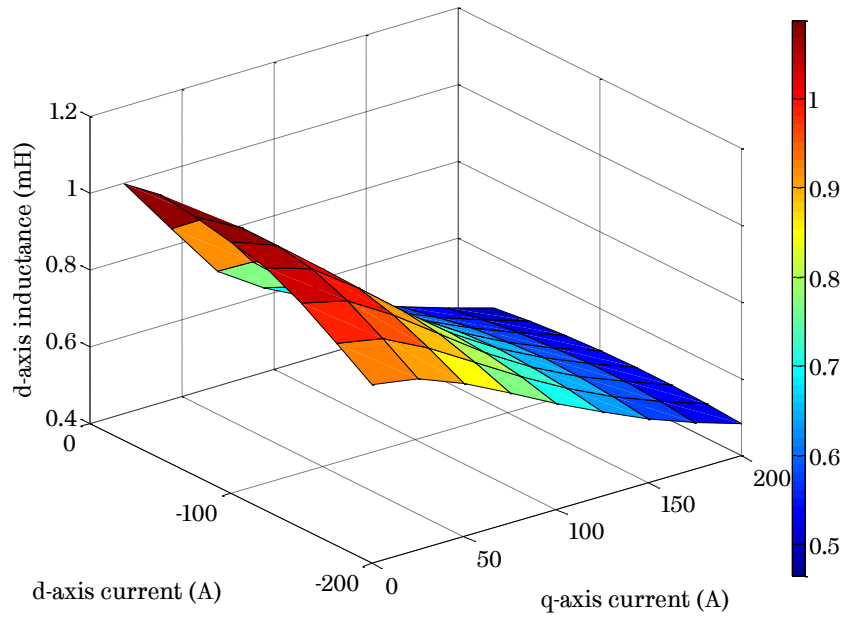
5.8.2 Parameters of the machine

Because of interior mounted PM structure of 6-phase, 18-slot, 8-pole machine, d - and q -axis inductances vary not only with motor currents but also with rotor position. In order to derive the inductance parameter map of the machine, 2-D static FEA with rotor rotation is carried out over an electric cycle (90° mechanical for this 8-pole machine) for a range of d - and q -axis currents. For deriving the parameters map, the following assumption is made.

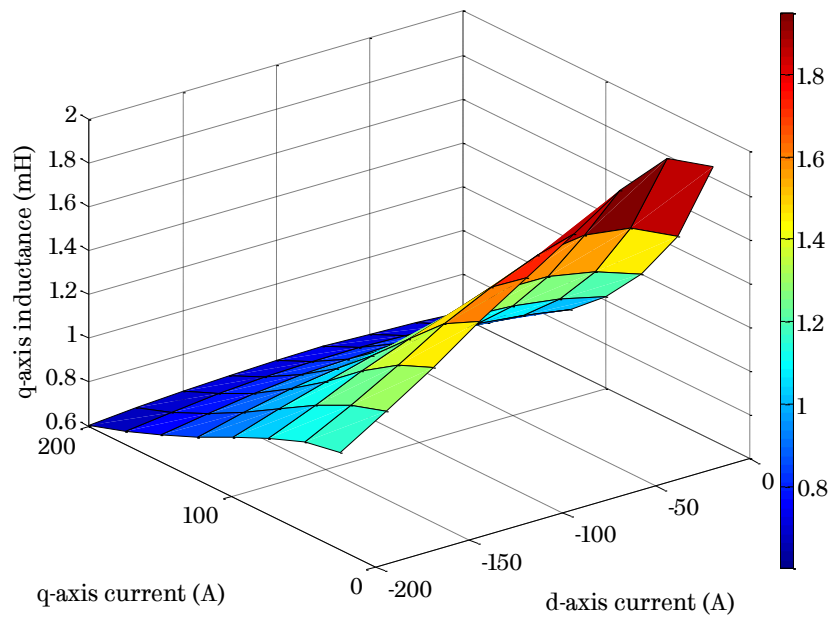
- 1) When the machine is modelled as two independent 3-phase systems, the cross-coupling between the two systems is neglected.

However, the variation of d -axis inductance (L_d) with d -axis current (I_d), q -axis inductance (L_q) with q -axis current (I_q), and cross-saturation effect on PM flux linkage (λ_m) due to q -axis current (I_q) are taken into account. Figure 5.29 shows the variation of d - and q -axis inductance with d - and q -axis currents respectively. Figure 5.30 shows the variation in d - and q -axis flux linkages with d - and q -axis currents respectively. The cross-saturation in PM flux linkage with q -axis current is shown in Figure 5.31.

These inductance maps along with cross-saturation in PM flux linkage are incorporated as look-up tables in the inverter controller to control the motor in various modes, viz. open loop, current control, torque control, and speed control. Appendix C tabulates the inductance and flux linkage maps for a range of d - and q -axis currents, obtained from 2-D FEA.

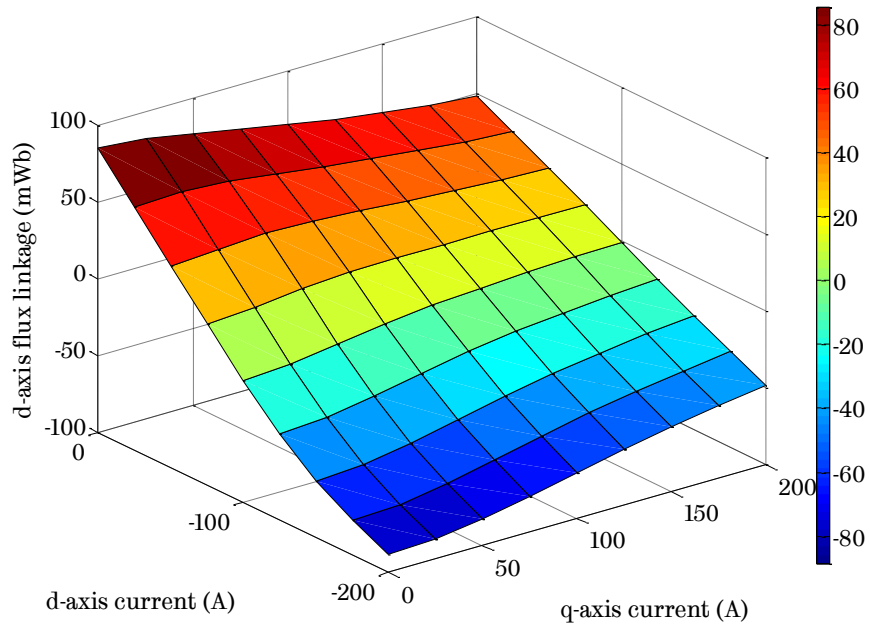


(a) d -axis inductance (L_d)

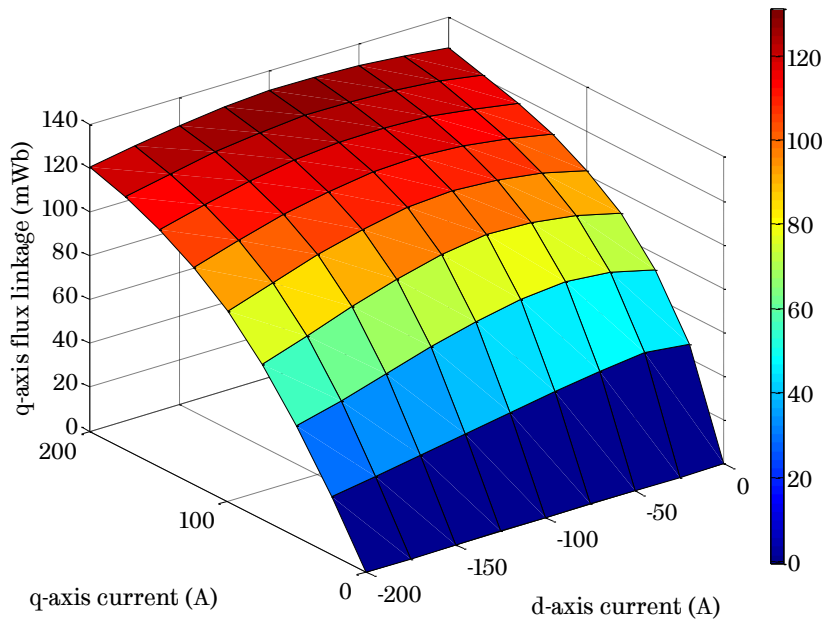


(b) q -axis inductance (L_q)

Figure 5.29. Inductance map of 6-phase, 18-slot, 8-pole IPM machine.

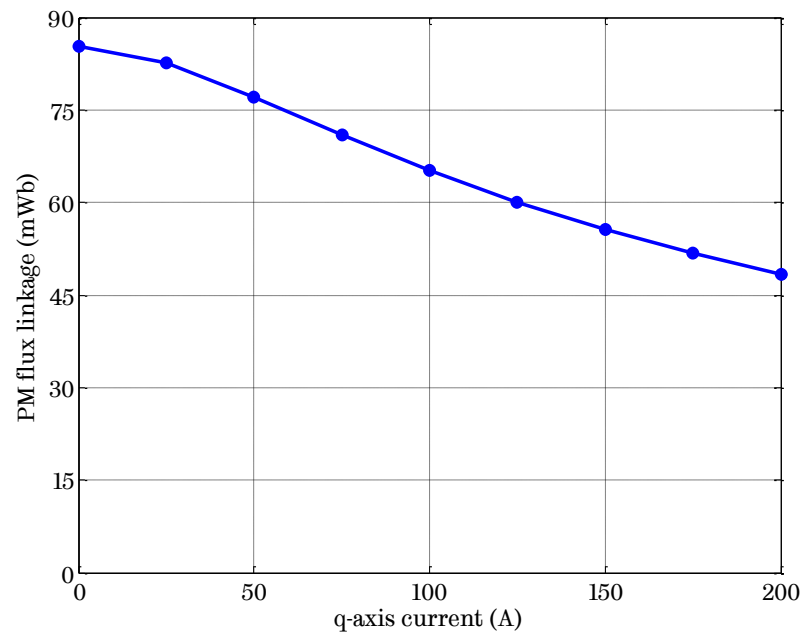


(a) d -axis flux linkage (λ_d)



(b) q -axis flux linkage (λ_q)

Figure 5.30. Flux-linkage map of 6-phase, 18-slot, 8-pole IPM machine.



(a) Cross-saturation in PM flux linkage (λ_m versus I_q)

Figure 5.31. PM flux-linkage map of 6-phase, 18-slot, 8-pole IPM machine.

Chapter 6

Prototyping and Experimental Validation of 6-phase, 18-slot, 8-pole IPM Machine

The prototyping of the optimized design of 6-phase, 18-slot, 8-pole IPM machine for the segment-A electric vehicle application is presented. Various design analysis and performance prediction models are validated using a series of experiments on the prototype machine. Investigation of partial demagnetization of the prototype motor along with the adopted preventive measures is presented. Finally, the comparison of two prototype machines with different magnet and rotor steel material is discussed, which is followed by the experimental validation of second prototype motor.

The main contents of this chapter is published by the author in [93] and [110].

6.1 Prototype of 6-phase, 18-slot, 8-pole IPM machine

The prototype of 6-phase, 18-slot, 8-pole IPM machine is built as per the optimized design, which is described in detail in Chapter 5.

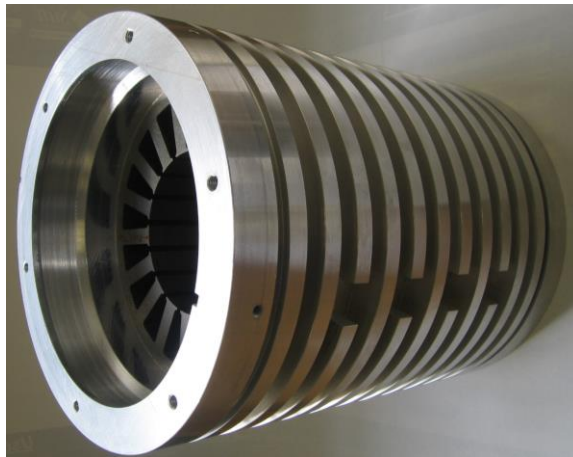
6.1.1 Components and assembly of the prototype machine

The stator laminations are stacked and housed inside the stator frame, which also forms an integral part of the cooling system, i.e. cooling chamber. The grooves are designed to carry the coolant (water) at a specific flow rate based on the thermal design of the machine, explained in section 5.6.4. The stator employs the novel winding design of 18-slot, 8-pole topology.

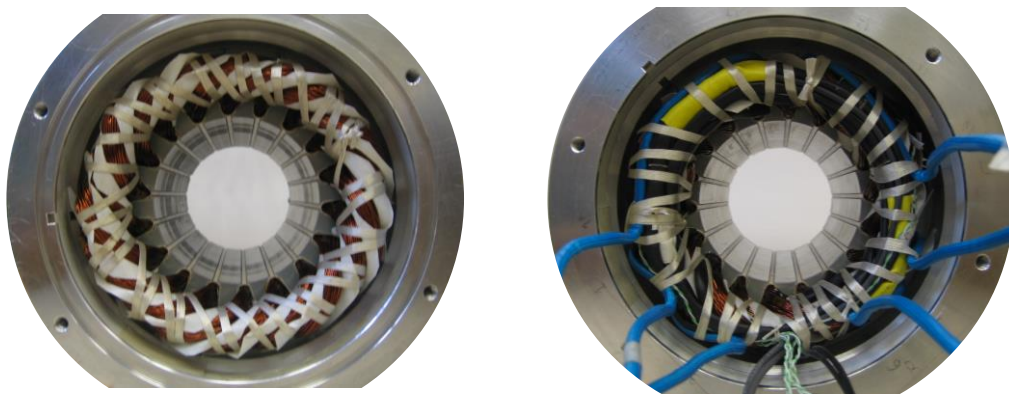
Figure 6.1 shows the components and sub-assembly of the stator of prototype machine. The detailed developed winding diagram of the novel fractional-slot per pole per phase topology is also shown in Figure 6.2 for reference.



(a) Stacks of stator and rotor laminations



(b) Stator frame with stator laminations (thermal fit)



(c) Stator assembly: (1) drive end, (2) non-drive end or connection end

Figure 6.1. Components and sub-assembly of the stator.

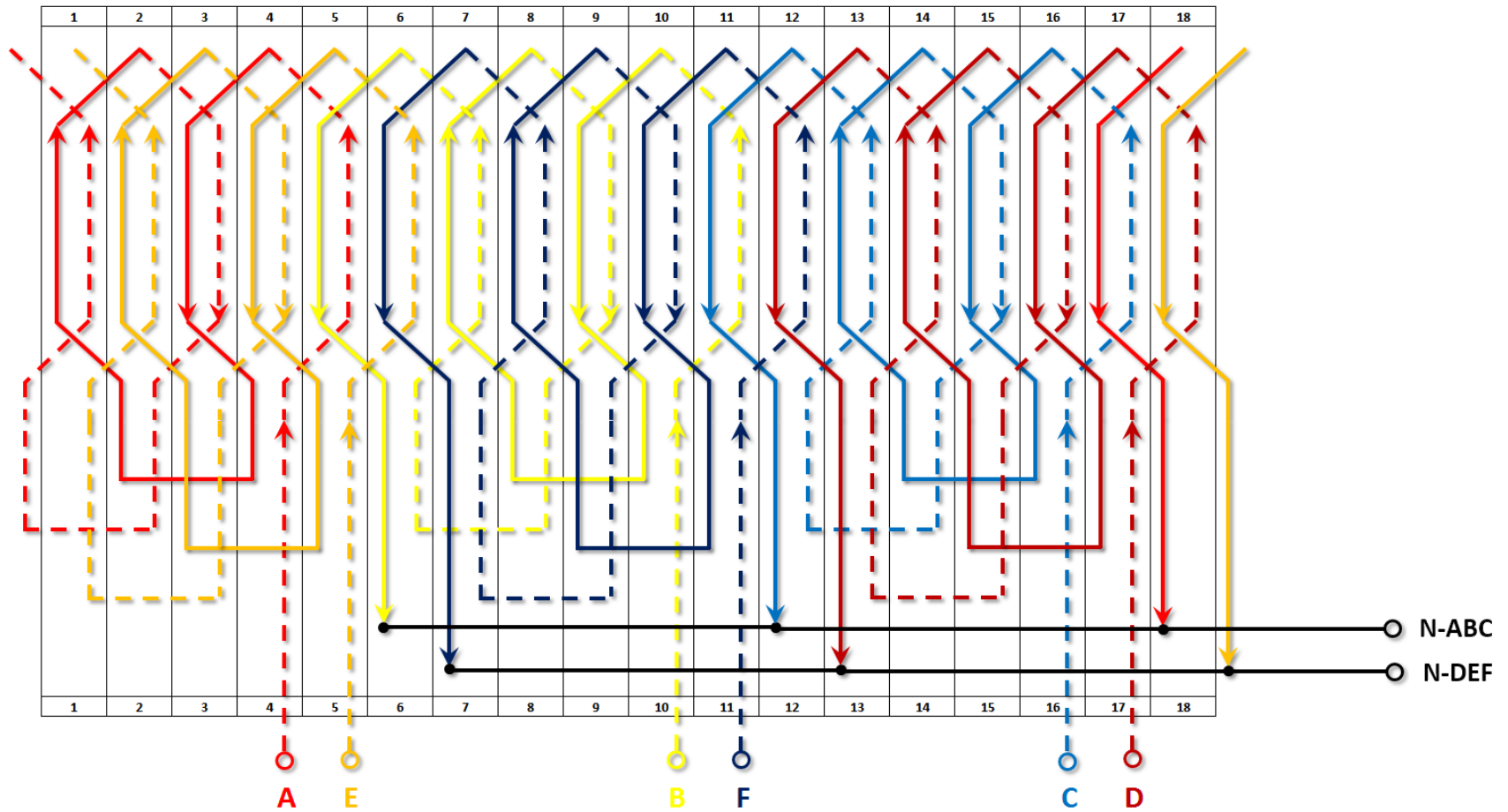
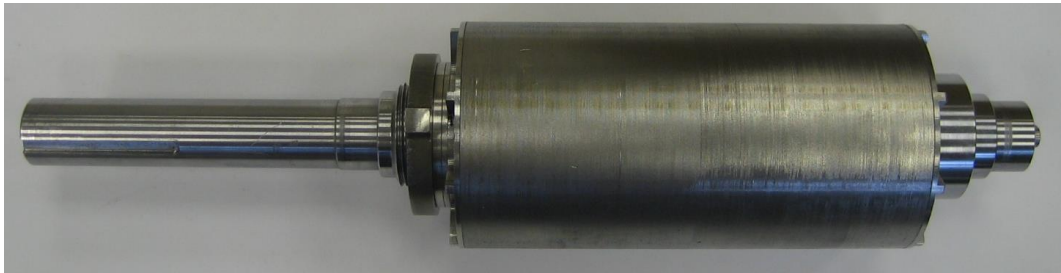


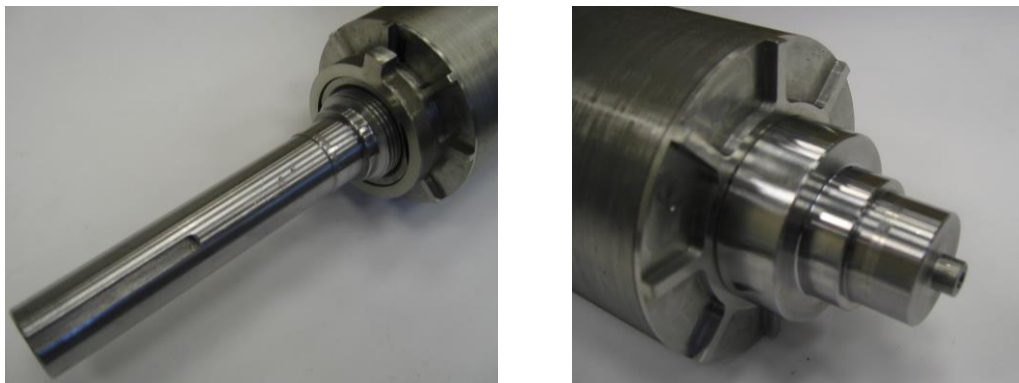
Figure 6.2. Developed winding diagram of the novel fractional-slot 6-phase, 18-slot, 8-pole topology.

6. Prototyping and Experimental Validation of 6-phase, 18-slot, 8-pole IPM

As will be seen from the winding diagram, the phase shift between A-B-C and D-E-F windings is 20° electrical and is achieved by 13 slot-shifts. The complete rotor assembly is shown in Figure 6.3. The rotor is V-shaped interior permanent magnet motor having single layer of magnets. The complete motor assembly with cooling sleeve, terminal box, and signal connector is shown in Figure 6.4.



(a) Complete rotor assembly



(b) Rotor assembly: (1) drive end, (2) non-drive end or connection end

Figure 6.3. Components and sub-assembly of the rotor.



Figure 6.4. Assembly of the prototype motor.

6.1.2 Instrumentation and feedback device

The instrumentation and feedback device for the rotor position, which are key essentials for preliminary tests on the prototype machine, are integrated during the manufacturing of the prototype machine. Table 6.1 lists the instrumentation installed on the prototype.

Table 6.1. Instrumentation and feedback device

Instrumentation	Part Number	Code	Location
K-type thermocouples	RS 621-2158	TC1	Slot # 3, Phase B
		TC2	Slot # 14, Phase D & E
		TC3	End winding (drive end)
		TC4	End winding (connection end)
PTC thermistors [116]	KTY84-130	TH1	Slot # 2, Phase E & F
		TH2	Slot # 9, Phase C
Rotary magnetic encoder [117]	RM44AC	-	Actuator on the rotor shaft
		-	Stationary encoder on end plate

Figure 6.5 shows the configuration of the signal connector comprising of 13 terminals. The signal connector is used to route the magnetic encoder terminals and thermistor terminals from inside the machine to outside.

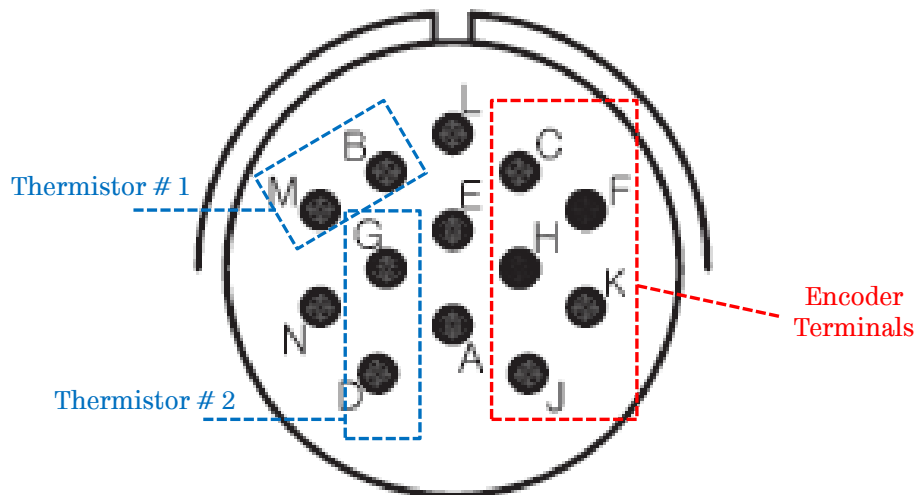


Figure 6.5. Configuration of signal connector.

Table 5.1 shows the terminal identification for the signal connector.

Table 6.2. Signal connector terminal identification

Terminal	Colour of wire	Description
B	Yellow	Thermistor # 1: Go
M	White	Thermistor # 1: Return
N	-	N/C
G	Blue	Thermistor # 2: Go
D	Black	Thermistor # 2: Return
L	-	N/C
E	-	N/C
A	-	N/C
C	Silver	Encoder shielding
F	Brown	Encoder Cosine output
H	Red	Encoder power supply +5 V
K	Black	Encoder Sine output
J	Orange	Encoder ground 0 V

In addition to the above instrumentation, two neutral points are also brought out for the preliminary tests. The accelerometer will also be mounted either on the motor or on the test bench to monitor the vibrations during the tests.

6.2 Instruments, test set-up and data acquisition

To perform a series of preliminary tests on the prototype motor, a test bench is developed using the AVL dynamometer available in Electrical Machines & Drives (EMD) group of Department of Electronic & Electrical Engineering at The University of Sheffield. The tests are performed under representative operating conditions and results are used to validate the design analysis models, control strategies and theoretical performance predictions.

6.2.1 Instruments for the test set-up

The various instruments and equipment employed in the test set-up are listed in Table 6.3 along with their purpose.

Table 6.3. List of instruments and equipment used in the test set-up

No.	Equipment/Instrument	Purpose
1	Prototype motor	The motor under test
2	AVL dynamometer	To drive the motor under test
3	6-phase Infineon inverter	To control the motor during load tests
4	R+W coupling	To couple the motor with the dynamometer and/or torque transducer
5	Bidirectional DC power supply	To supply power to the inverter
6	Magtrol torque transducer	To measure output of the motor under test (torque, speed and power) <ul style="list-style-type: none"> a. Magtrol 308 – for no load tests b. Magtrol 312 – for load tests
7	Yokogawa power analyser	To measure/analyse various quantities: <ul style="list-style-type: none"> a. Input power of inverter (I_{dc}, V_{dc}) b. Output power of inverter ($V_{ph}, I_{ph}, \cos \phi$) c. Output power of motor (T_m, N, P_m)
8	Current sensors	To measure currents through power analyser <ul style="list-style-type: none"> a. 3 sensors to measure $I_a, I_b,$ and I_c b. 1 sensor to measure I_{dc}
9	Voltage sensors	To measure voltages through power analyser <ul style="list-style-type: none"> a. 3 sensors to measure $V_a, V_b,$ and V_c b. 1 sensor to measure V_{dc}
10	Water flow rate meter	To monitor the water flow rate for cooling of the motor
11	Pico temperature logger	To record temperatures of the motor using thermocouples installed in the windings
12	Yokogawa / Tektronics scope	To observe/record signals through data acquisition
13	Accelerometer	To monitor vibrations of the motor under test

6.2.2 Test set-up

In order to measure the performance of the motor under various representative operating conditions, the test bench, involving the dynamometer and the motor-inverter equipped with the instruments listed in Table 6.3 to acquire

data (measured variables) during the tests in real time environment, is developed and its schematic is shown in Figure 6.6.

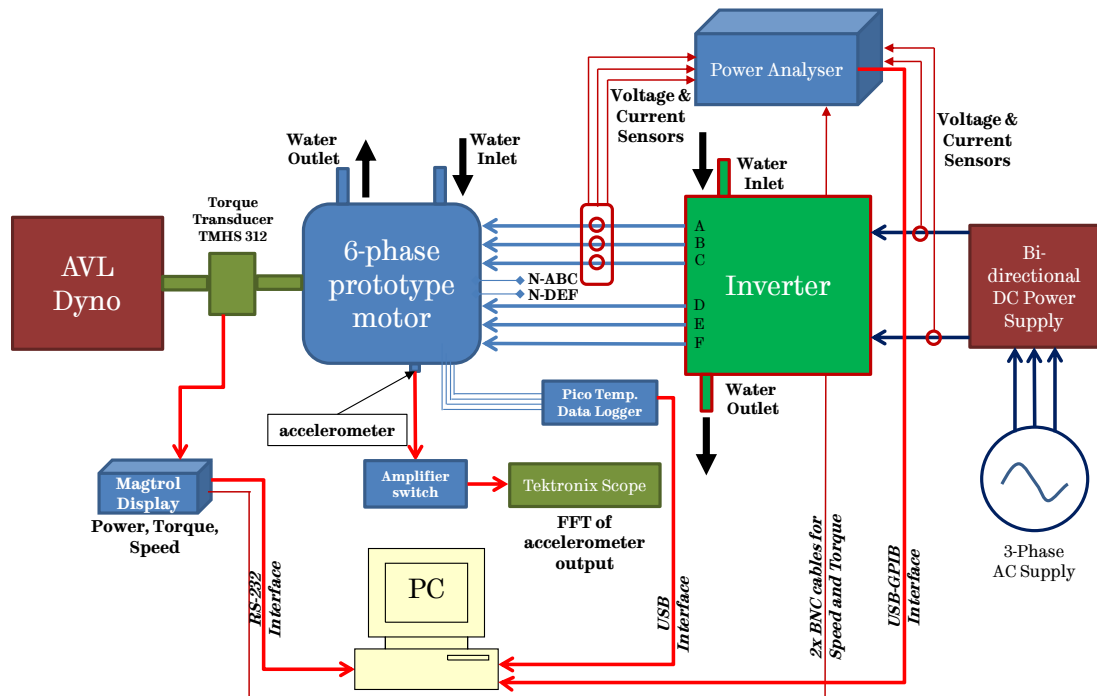


Figure 6.6. Schematic of test set-up with data acquisition system.

Figure 6.7 shows the photograph of the test bench on which the prototype motor is mounted. As will be seen, the 6-phase prototype motor is coupled to the AVL dynamometer using backlash-free, torsion-ally stiff metal bellow couplings and an in-line torque transducer. The AVL dynamometer, which is controlled by a bi-directional four-quadrant converter, is used to drive the motor at a given speed and provides load torque during the load tests. The motor is controlled by a 6-phase inverter configured as two independent 3-phase inverters that operates in torque control mode and can achieve flux weakening operation in a high speed range. The 6-phase inverter is developed by Infineon [118], as part of the FP7 CASTOR project [119]. The inverter DC link is fed by a programmable bi-directional DC power supply. Both the motor and the inverter are supplied with water as coolant in separate cooling circuits at constant flow rate. The 6-phase input power to the motor (from the inverter) is measured by a power analyser via the high precision ($\pm 0.02\%$ accuracy for power reading), high bandwidth voltage and zero flux current transducers. The motor output power is obtained through the in-line torque

transducer (accuracy of $< \pm 0.1\%$, temperature sensitivity of $\pm 0.2 \text{ N}\cdot\text{m}/10\text{K}$, range $0 - 200 \text{ N}\cdot\text{m}$) by measuring the torque and the speed. The test bench shown in Figure 6.7 allows direct and precise measurement of the motor efficiency.

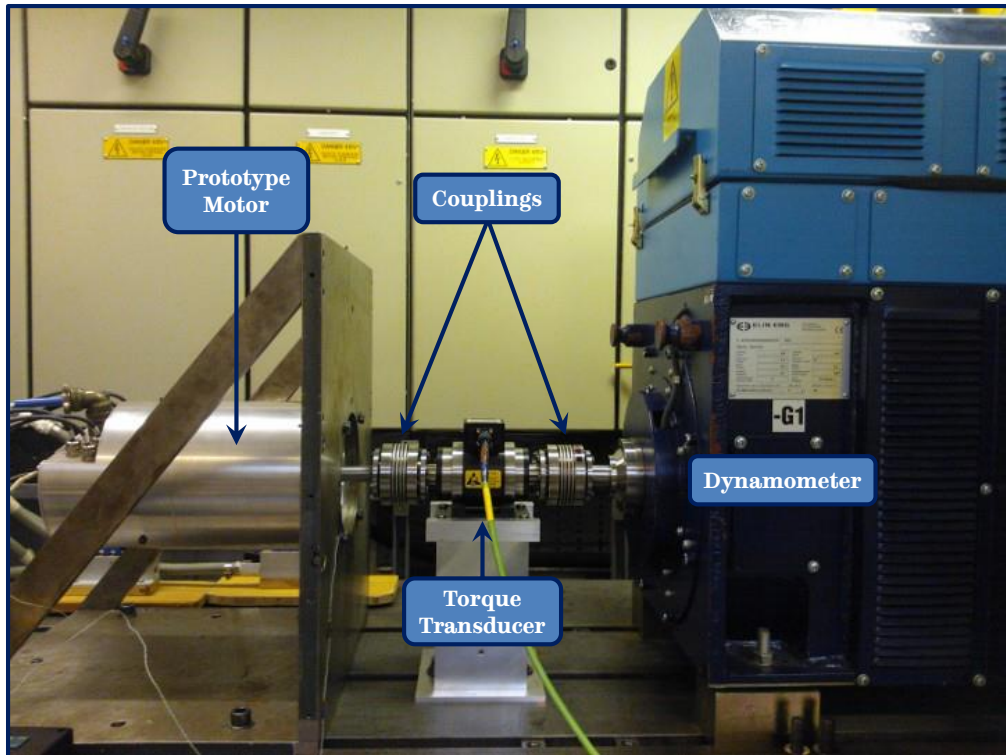


Figure 6.7. Prototype motor mounted on test bench with in-line torque transducer.

6.2.3 Data acquisition

As shown in Figure 6.6, the torque transducer TMHS 312 is connected to Magtrol display 3410 which displays torque on the shaft, the shaft speed, and hence power. Two BNC cables from Magtrol display 3410 are connected to Yokogawa power analyser to record the torque and the speed of the prototype motor respectively. The Magtrol display 3410 is also connected to PC through RS-232 cable to record the data in real-time environment on PC. Torque 1.0 software supplied with Magtrol display is used to record the torque, speed and power at every second in single .MDF file. This file contains the output of the prototype motor.

The four thermocouples located inside the windings of the motor are connected to Pico temperature data logger, which in turn is connected to PC

through USB port, to record the temperatures of the motor in real time. The temperature data at every second is recorded in a single .PLW file.

The accelerometer on the motor enclosure is connected to Tektronics scope via an amplifier switch or directly to Yokogawa scope, to display Fast Fourier Transform (FFT) of the motor vibrations. The motor vibrations are monitored throughout the tests to ensure safe loading and unloading of the motor.

The six voltage leads and three current sensors are connected to the output of the 6-phase inverter to measure the 3-phase voltages and currents respectively. It should be noted that due to limitation, the tests can only record 3 phase voltages and currents. These are recorded and processed in the Yokogawa power analyser. The purpose of this instrumentation is to measure the output power of the inverter, which is nothing but the input power of the motor including the copper losses in the motor cables and terminals.

The two voltage leads and one current sensor is connected to input of the inverter to measure the input power of the inverter by recording the DC link voltage and current respectively through the power analyser.

The Yokogawa power analyser analyses the voltage and current from the measurements and calculates the motor and the inverter efficiency. The power analyser is also connected to PC through GPIB-to-USB interface to record all the measured and analysed quantities in a single .CSV file.

Hence, for each test sequence, there are three files recording all the required data. Table 6.4 shows the list of files and the data they record during the tests.

6.2.3.1 Environmental conditions

The environmental conditions during the preliminary tests are observed and controlled throughout the tests and are listed in Table 6.5. It is worthwhile to note that although the machine is designed to operate continuously with 60°C water inlet temperature in ambient temperature of 45°C and 6 litre/min water flow rate, the prototype machine is tested at lower water inlet temperature and higher water flow rate to complete the testing of the prototype without any damage owing

to higher than the predicted temperatures due to uncertainties in iron losses and interface gap between the stator laminations and the stator frame.

Table 6.4. List of files acquiring real-time data during the tests

Equipment	Data file	Data
Power analyser	.csv	DC link – voltage, current and power
		Inverter output – voltage, current and power
		Motor output – Torque, speed and power
		Inverter efficiency
		Motor efficiency
Torque transducer	.mdf	Motor output – torque, speed and power
Temperature logger	.plw	Temperatures of the four thermocouples – TC1 to TC4.

Table 6.5. Environmental conditions during the preliminary tests

Environmental condition	Value	Controlled by
Ambient air temperature	20°C-25°C	Ventilator fans
Motor coolant temperature	20°C	Tool-temp machine
Motor coolant flow	15 litre/min	Tool-temp machine
Inverter coolant temperature	15°C	Chiller plant
Inverter coolant flow	9 litre/min	Chiller plant

6.3 List of preliminary tests

Various preliminary tests, listed in Table 6.6, on the 6-phase prototype motor having a novel winding topology of 18-slot, 8-pole are conducted.

Table 6.6. List of preliminary tests

No.	Test	Comments
A	No-load tests on the prototype motor	
1	Insulation testing	Megger test, Partial discharge test
2	Resistance measurement	At room temperature
3	Back EMF measurement	From 500 rpm to 7000 rpm
4	Check on mechanical integrity	Run the motor till max. speed of 11000 rpm
5	No load loss measurement	From standstill to max. speed of 11000 rpm

B Load tests on the prototype motor		
6	Validate control modes	Open loop, current control, torque control, etc.
7	Machine parameter characterization	At 1500 rpm in current control mode
8	Efficiency map measurement	From 500 rpm till 5000 rpm, 6-phase operation
9	Peak torque capability check	From 500 rpm till 3000 rpm, 3-phase operation
10	Thermal tests	At rated torque operation

6.4 No-load tests on the prototype motor

6.4.1 Insulation testing

As discussed in Chapter 5, each phase winding of the prototype machine consists of three series connected coils wired around the adjacent teeth. Each coil is made up of 10 series turns. In order to reduce losses due to skin effect and proximity effect, each turn consists of 13 parallel strands of double coated enamelled copper wires, as shown in Figure 6.8, having 0.75 mm diameter are used in the prototype machine to achieve slot packing (or fill) factor of 0.4157.

Due to double layer arrangement of the windings inside the slots, each layer of the winding is separated by a layer insulation made up of NOMEX insulating paper. End windings are also separated from one another by NOMEX insulating paper and tied securely to minimize the relative movement due to vibrations during the operation. The thickness of NOMEX insulating paper used in the prototype machine is 0.25 mm.

It is possible that two strands inside the stator slots have localized contacts because of rubbing of strands while inserting them inside the slots. The windings are potted with varnish to eliminate such potential problems between the strands.

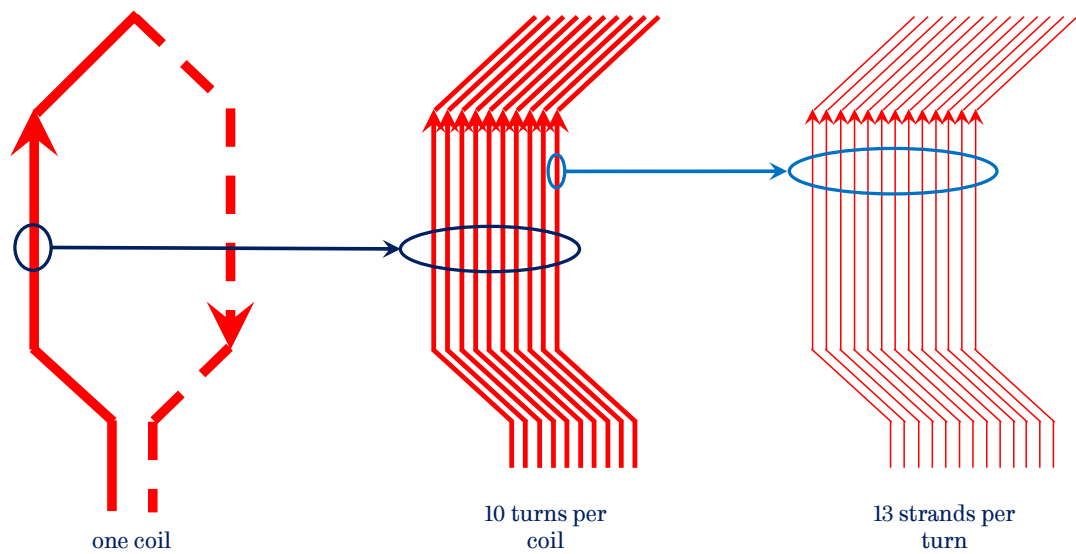


Figure 6.8. Development of a phase coil in the prototype machine.

In order to check insulation, megger is used and connected across each strand of the phase windings and motor enclosure as well as between strands of the same phase windings to determine if there is any leakage path. It was found that the insulation is adequate for the prototype machine. Also, when the machine was sent to Volkswagen's research facilities, partial discharge test is conducted to ensure insulation of the windings is adequate.

6.4.2 Resistance measurement

In order to predict performance of the machine during design phase accurately, it is vital to have accurate loss models of the machine. The main losses in an electric machine are copper loss, iron loss, and mechanical loss. To validate copper loss model, it is important to measure the resistance of the motor windings.

As part of tests, resistance measurement is carried out twice at different phases of the prototype assembly as below:

- 1) Resistance measurement before making neutral connections
- 2) Resistance measurement after connecting cables and terminals

The measured per phase resistance is compared against the predicted per phase resistance. The difference between them is investigated and various elements contributing to the difference are identified.

6.4.2.1 Resistance measurement before making neutral connections

As the prototype machine with novel winding configuration is designed as two independent 3-phase systems to enhance availability of the power drivetrain during fault conditions, two neutral points are made and taken out for the measurement purposes.

The resistance of the motor windings is measured before making the neutral points, at room temperature of 28°C. Table 6.7 compares the measured per phase resistance with that of calculated per phase resistance. The ratio T/C is defined as a ratio of the test or measured value of the quantity to the calculated or predicted value of the quantity.

Table 6.7. Resistance measurement before making neutral points at 28°C

Phase	Test Measurements at 28°C		Calculated per phase resistance at 28°C $C(\Omega)$	T/C
	Resistance of a strand (Ω)	Per phase resistance $T(\Omega)$		
A	0.535	0.04115	0.04033	1.020
B	0.534	0.04108	0.04033	1.019
C	0.540	0.04154	0.04033	1.030
D	0.536	0.04123	0.04033	1.022
E	0.538	0.04138	0.04033	1.026
F	0.535	0.04115	0.04033	1.020
Average	0.53633	0.04126	0.04033	1.023

As will be seen from the above table, the measured resistance of each phase differs slightly from one another. This is due to the difference in length of each phase windings. The average per phase measured resistance is 2.3% higher than that of calculated or predicted one. This is mainly due to increase in end-winding length because of the pull through method of the winding process by hands in the lab. However, it is worth to note that the higher packing factor (of 0.4157) than the designed one (i.e. 0.4), helps in offsetting the extra resistance coming from the longer end-winding (than ideal ones) by certain degree.

6.4.2.2 Resistance measurement after cable connections

In order to connect the cables with the phase windings, the extra length of the phase windings strands are cut and soldered to cables using crimp connectors. At the other end of the cables, the crimp terminals are also soldered to cables to make them suitable for connecting to the 6-phase inverter. The soldering of different strands together not only introduces the additional circulating currents around the soldered joints, but also increases the per phase resistance slightly.

The resistance of the motor windings is measured again after making cable connections at room temperature of 17°C. Table 6.8 tabulates the measured resistance between two phases to eliminate the resistance of the neutral wires. The measurements are repeated twice and average value is used to determine per phase resistance and to compare it with the calculated or predicted resistance. The winding resistance is obtained after deducting the cable resistance of 0.004425 Ω at 17°C.

Table 6.8. Resistance measurement after cable connections at 17°C

Measurement of resistance at 17°C				
Between Phases	Measurement I (Ω)	Measurement II (Ω)	Average value of Measurements (Ω)	Winding resistance (Ω)
A & B	0.087	0.088	0.0875	0.07865
B & C	0.089	0.089	0.089	0.08015
C & A	0.088	0.090	0.089	0.08015
D & E	0.089	0.090	0.0895	0.08065
E & F	0.088	0.090	0.089	0.08015
F & D	0.089	0.090	0.0895	0.08065

Table 6.9 compares the measured and the calculated phase resistance. From Table 6.9, it is seen that the per phase resistance of the prototype motor is 3.6% higher than the calculated resistance. This increase is due to two terminal connections via soldering, one between winding strands and the cable, and another between the cable and the motor power terminals. Table 6.10 summarises the per phase resistance of the motor at 17°C.

Table 6.9. Comparison of measured resistance with calculated one at 17°C

Phase	Measured resistance	Calculated resistance	T/C
	$T(\Omega)$	$C(\Omega)$	
A	0.039325	0.03864	1.018
B	0.039325	0.03864	1.018
C	0.040825	0.03864	1.057
D	0.040575	0.03864	1.050
E	0.040075	0.03864	1.037
F	0.040075	0.03864	1.037
Average	0.040033	0.03864	1.036

Table 6.10. Summary of measured per phase resistance at 17°C

	Measured value (Ω)	% of total value
Per phase resistance of the windings only	0.03948	88.80 %
Per phase resistance of the cable	0.004425	9.95 %
Per phase resistance of the cable terminals	0.000553	1.24 %
Per phase resistance of the motor including cable & terminals	0.044458	100%

It is important to note that per phase resistance of the windings only should be considered while evaluating the performance of the motor. Hence, the copper loss of the design machine will be 2.3% higher than the predicted loss.

6.4.3 Back EMF measurement

The back EMF of all phases are measured at room temperature at different speeds, i.e. 500 rpm, 1500 rpm, 2000 rpm, 3000 rpm till 7000 rpm, as per the procedure described in Appendix D. Figure 6.9 shows variation of the RMS and the peak values of the measured back EMF with speed. The back EMF in the plot is the average value of all phases together.

It is evident from Figure 6.9 that the back EMF of the PM machine has a linear relationship with speed. The back EMF constant (K_e) of the prototype motor is calculated as 32.944 mV/rpm from the peak values of the back EMF from the

measurements. From the back EMF constant, the calculated peak value of the open circuit line-to-line voltage at 11000 rpm is 627.7V, which is below the requirement of 650V limit set by the power electronics in the 6-phase inverter.

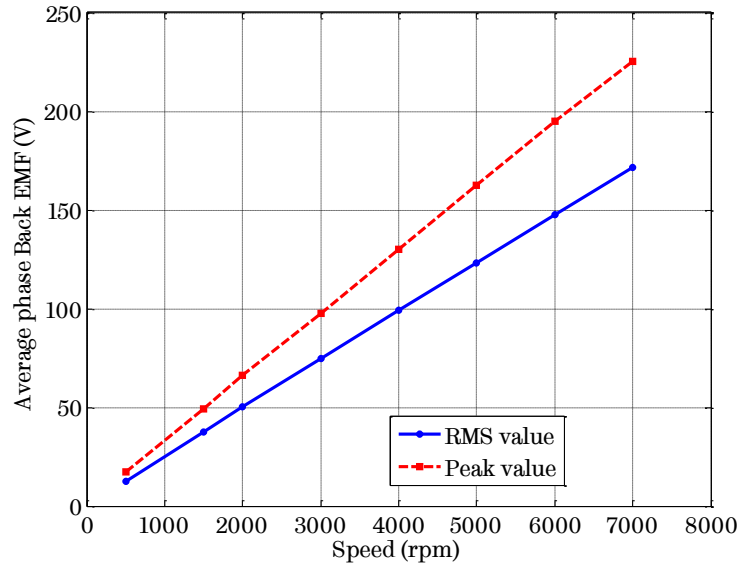


Figure 6.9. Measured back EMF at different speeds to determine back EMF constant.

Figure 6.10 shows the comparison of the back EMF waveforms of all the phases of the motor between the measurement (solid line) and the prediction by FEA. The FEA model is updated for the room temperature at which the back EMF was measured by changing the permanent magnet operating point ($B_r = 1.147$ T, $\mu_r = 1.05$) based on the data sheet of N35EH provided by the magnet supplier.

In order to quantify the difference, comparison of back EMF is carried out using RMS and peak value of the waveforms. Table 6.11 shows the comparison of RMS and peak value of back EMF obtained from the test with those of prediction.

From the comparison, it is evident that the RMS and the peak values of the measured back EMF are 2.7% and 2.4% lower than the prediction respectively. This can be attributed to lower permanent magnet length (l_m) in the prototype motor due to grinding or tolerance requirements for inserting them inside the rotor, as shown in Figure 5.15, and the resulting air gap between the magnets and rotor core, as well as slightly different BH characteristics of the magnets and the laminations between the data sheet and the actual materials used in the prototype motor. 3D

effect and axial leakage flux at both ends of the rotor may also contribute to the low measured back EMF, since the FE predictions are performed in 2D.

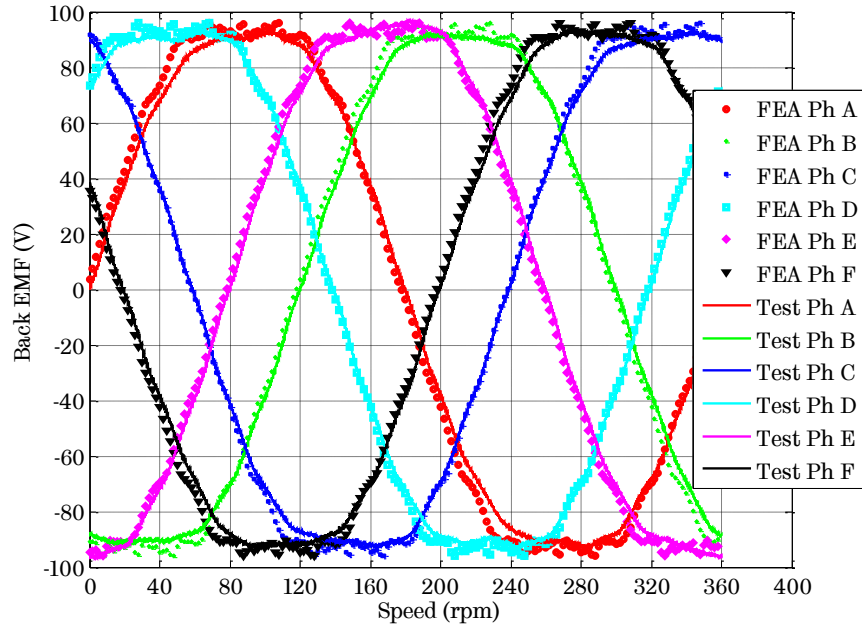


Figure 6.10. Measured and predicted back EMF waveform at 2800 rpm.

Table 6.11. Comparison of measured and predicted back EMF at room temperature

Phase	RMS value			Peak value		
	Test (V)	Calc. (V)	<i>T/C</i>	Test (V)	Calc. (V)	<i>T/C</i>
E_A	69.8	72.9	0.957	93.0	96.0	0.969
E_B	70.4	72.9	0.966	92.2	96.0	0.960
E_C	70.8	72.9	0.971	92.8	96.0	0.967
E_D	71.2	72.9	0.977	93.5	96.0	0.974
E_E	72.6	72.9	0.996	97.0	96.0	1.010
E_F	70.6	72.9	0.968	93.5	96.0	0.974
Average	70.9	72.9	0.973	93.7	96.0	0.976
Fundamental	98.5	102.8	0.958			

6.4.4 Check on mechanical integrity

The prototype motor is essentially a high speed electrical machine as it is required to operate at 11000 rpm continuously during the cruise speed of the vehicle. Hence, it is vital to check the mechanical integrity of the motor components before the load tests. This test will ensure the safe operation of the motor during high speed by observing any undesirable noise and vibrations as the speed increases.

Figure 6.11 shows the speed versus time curve of the prototype motor under no-load for this test. Using the AVL dynamometer, the motor speed is gradually increased till the maximum speed of 11000 rpm and was allowed to run continuously for about 13 minutes. The noise level and vibrations were observed throughout the test to ensure the operation at higher speeds is safe. No abnormal behaviour with respect to noise or vibrations is observed.

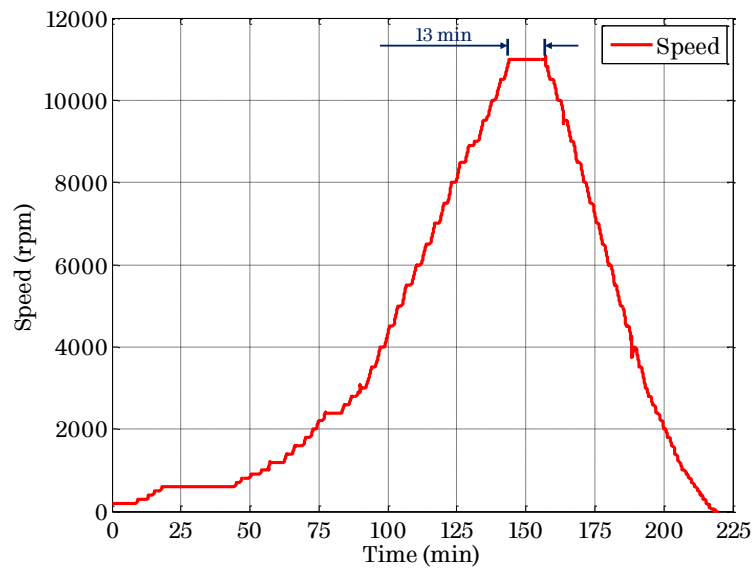


Figure 6.11. Speed versus time curve during the mechanical integrity check on the prototype motor.

6.4.5 No-load loss measurement

Losses in a permanent magnet machine can be divided into following three main categories:

- 1) Copper loss

- 2) Iron loss including eddy current loss in magnets
- 3) Mechanical loss

The copper loss includes conventional I^2R loss and stray load loss due to skin effect and proximity effect. Although the stray load loss for electrical machine of this size is not dominant, these losses can be computed using FEA or analytical methods.

The iron loss includes the iron loss in stator and rotor lamination. The iron loss consists of hysteresis loss, classical eddy current loss, and excess eddy current loss. Empirical equations or transient FEA with rotor rotation can be used to compute the iron loss in a machine. At no-load, due to slotting effect, the eddy currents are induced in the rotor magnets, which results into no-load eddy current loss in the magnets.

The mechanical loss includes frictional loss due to bearings, and windage loss due to shearing action of the cooling media between the rotor and the stator.

The no-load loss doesn't comprise of copper loss as there is no current flowing through machine windings. It is worthwhile to separate mechanical loss from no-load loss to compare the predicted iron loss with the measurements. The no-load loss tests were carried out using the in-line torque transducer with an accuracy of $\pm 0.1\%$, temperature sensitivity of $\pm 0.02 \text{ N}\cdot\text{m}/10\text{K}$ and the range of $0.1 \text{ N}\cdot\text{m} - 20 \text{ N}\cdot\text{m}$, as per the procedure described in Appendix D. Figure 6.12 shows the measured no-load loss of the prototype motor with increasing speed during the test.

6.4.5.1 Bearing friction and windage loss

The bearing friction and windage loss can be estimated using the bearing calculator developed by SKF [120] and empirical formulas [121]-[122] respectively. However, being empirical in nature, they may not provide the sufficient accuracy. In order to measure the bearing friction and windage loss in an electrical machine, it is necessary to build a dummy rotor with no magnets in it. The dummy rotor should be of same mass and mechanical dimensions and other geometrical features on the rotor surface as that of the prototype rotor. The dummy rotor will not have any no-load iron loss due to absence of any magnetic field.

The dummy rotor has been built to measure the bearing friction and windage loss for the prototype motor. Figure 6.13 shows the no-load loss of the dummy rotor obtained at different speeds. Using polynomial fit, the motor bearing friction and windage loss is expressed as a function of speed. The per unit speed and per unit loss is defined with base values of 11500 rpm and 150W respectively.

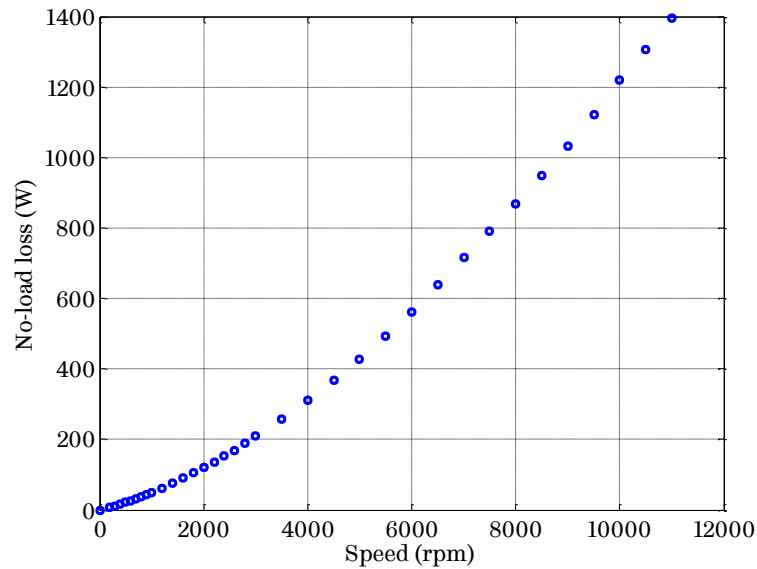


Figure 6.12. Measured no-load loss of the prototype motor.

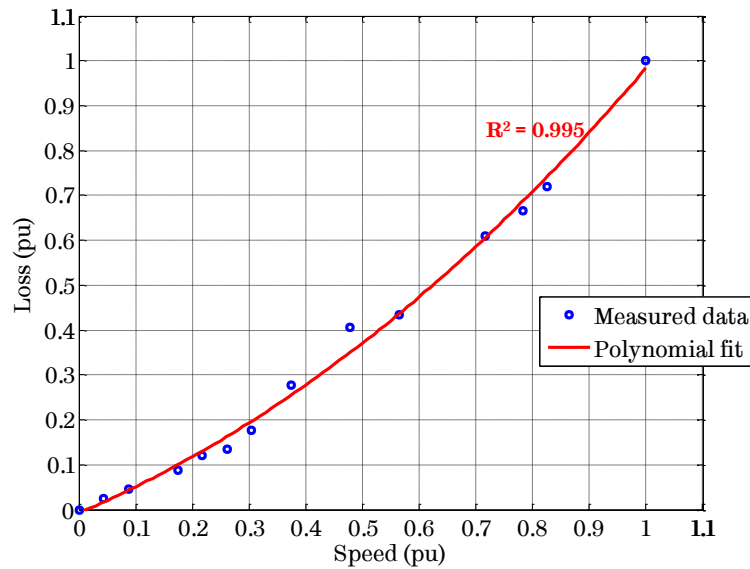


Figure 6.13. Measured bearing friction and windage loss using dummy rotor.

Thus, the motor bearing (P_{bf}) and windage loss (P_w) in per unit, is given by (6.1).

$$P_{bf} + P_w = 0.0433N^3 + 0.4041N^2 + 0.5445N - 0.0077 \quad (6.1)$$

where N is the motor speed in rpm. For maximum speed of 12000 rpm (*i.e.* 1.043 pu), the measured motor bearing friction and windage loss is 1.050 pu, *i.e.* 157.4 W.

6.4.5.2 Comparison of measured and predicted no-load iron loss

Assuming stray load loss to be negligible for the prototype motor, the no-load loss of the motor consists of no-load iron loss including no-load eddy current loss in the rotor magnets, bearing friction loss and windage loss, as shown in (6.2).

$$P_{nl} = P_{nl-fe} + P_{bf} + P_w \quad (6.2)$$

where P_{nl} is no-load loss of the motor in W, and P_{nl-fe} is no-load iron loss of the motor in W. As the bearing friction and windage loss are measured using the dummy rotor, the no-load iron loss can be found out by subtracting (6.1) from (6.2). Figure 6.14 shows the comparison of predicted and measured no-load iron loss from standstill to maximum cruise speed.

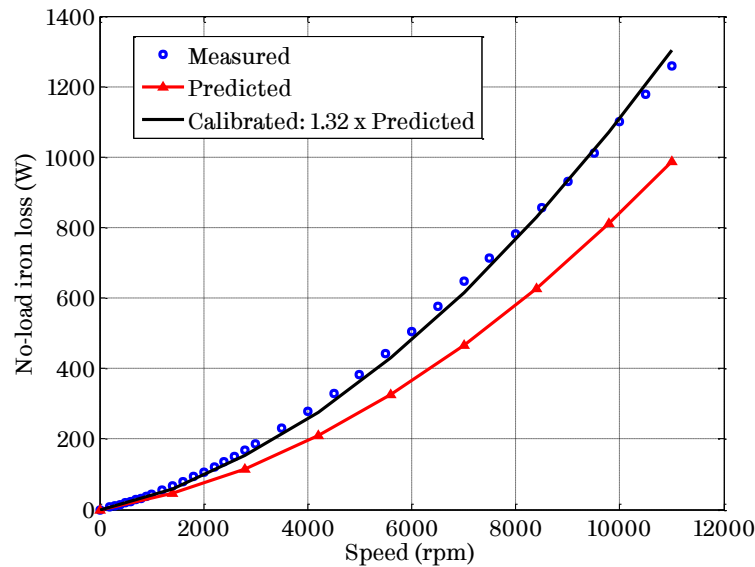


Figure 6.14. Comparison of measured and predicted no-load iron loss of the motor.

The difference between the measured and the predicted no-load iron loss varies from ~47% at lower speeds up to 2800 rpm to 28% at maximum cruise speed. The difference may be attributed to any degradation in the material properties of the steel laminations during the laser cutting (deburring) and thermal shrink-fit assembly. Usually, this can be accounted by manually adjusting the iron loss

prediction by a constant multiplier, generally known as *build factor* in the literature [115]. It can be seen that by introducing a build factor of 1.32 that accounts for any deterioration of material properties of laminations, the calibrated no-load iron loss model matches very well with the measured no-load iron loss.

6.5 Load tests on the prototype motor

The load tests are essential to evaluate the motor-drive operation and to measure their efficiency within the torque-speed envelope. The maximum torque that can be achieved at different speeds are also measured within the capability of the AVL dynamometer and the 6-phase inverter. It is worth to note that the achievable peak torque capability in the preliminary tests at the University of Sheffield is limited by the continuous torque rating of the AVL dynamometer, i.e. 100 N·m.

6.5.1 Validation of control modes

For the prototype motor, Infineon has designed and developed a prototype 6-phase inverter with two independent control for A-B-C and D-E-F phase systems [118]. Hence, it is important to validate various control modes developed and built as part of inverter control to ensure the inverter control operates as intended. The following control modes are incorporated in the prototype inverter:

- 1) Open loop control mode
- 2) Torque control mode
- 3) Current control mode
- 4) Speed control mode

As the inverter was not able to operate reliably at the rated DC link voltage of 320V due to electromagnetic interference problems in the IGBT protection circuit, most of the tests with the inverter are carried out at lower DC link voltage of 275V.

6.5.1.1 Open loop control mode

In the open loop control mode, the inverter controls the motor without taking any feedback from sensors such as rotor position, speed, and current

sensors. The motor is allowed to run with reference d -axis voltage and frequency set by the user inputs.

This control mode is validated by running the motor with $V_{dr} = 7$ V and $f_r = 7$ Hz. The AVL dynamometer does not operate during this validation allowing the motor to rotate as per the reference frequency. The motor speed was finally settled at 105 rpm, which corresponds to the frequency of 7 Hz ($60f/p$). The peak phase current measured in the power analyser was 36A, which is same as generated by the controller.

6.5.1.2 Torque control mode

In torque control mode, the current controller generates d - and q -axis currents from (a) the torque reference set by the user input, and (b) rotor position, speed and phase currents. In order to generate the torque reference, the motor model is incorporated in to the inverter control as various look-up tables (L_d versus I_d , L_q versus I_q , and λ_m versus I_q) derived from 2-D transient FEA, which are described in Chapter 5 and tabulated in Appendix C. The d - and q -axis currents are then converted to d - and q -axis voltages by the current controller. These voltages are used by space vector modulator to generate pulse-width-modulation (PWM) pulses, which are fed to the inverter to generate the phase voltages. These phase voltages are fed to the motor terminals.

During validation of torque control mode, the AVL dynamometer is operated at various speeds and the motor is controlled to generate the desired torque as per the reference torque (input). Table 6.12 shows the torque generated by the motor along with the reference torque at different speeds. It is seen that the generated torque by the motor is within ± 2 -4% of the reference torque. This validates the torque control mode of the inverter control as well as the motor model used in the inverter control.

6.5.1.3 Current control mode

In the current control mode, the current controller generates d - and q -axis voltages from (a) d - and q -axis current references set by user input, and (b) rotor position, speed and phase currents using the motor model. The phase voltages are generated as explained in section 6.5.1.2 and fed to the motor terminals.

Table 6.12. Validation of torque control mode at different speeds

Speed (rpm)	Measured torque T (Nm)	Reference torque C (Nm)	T/C
501	4.9	5.0	0.980
	25.4	25.0	1.016
	74.8	75.0	0.997
1501	9.8	10.0	0.980
	40.3	40.0	1.008
	85.0	85.0	1.000
2800	4.8	5.0	0.960
	45.7	45.0	1.016
	75.7	75.0	1.009

During validation of current control mode, the AVL dynamometer was run at different speeds and the motor is controlled to generate the desired torque as per the reference d - and q -axis currents (input). Table 6.13 shows the torque generated by the motor along with the reference d - and q -axis currents at different speeds and current references.

Table 6.13. Validation of current control mode at different speeds & currents

Speed (rpm)	Measured torque T (Nm)	Predicted torque C (Nm)	Reference current I_d (A)	Reference current I_q (A)	T/C
100	59.5	57.9	-25	50	1.028
500	58.3	57.9	-25	50	1.007
1000	58.5	57.9	-25	50	1.010
1500	64.7	60.6	0	70	1.068
	46.3	46.6	-20	40	0.994
	68.4	68.7	-30	60	0.996
	84.3	86.0	-50	70	0.980

As seen from the above table, the generated torque by the motor under current control mode is within $\pm 1-7\%$ of the expected torque from 2-D FEA for the

reference d - and q -axis currents. Table 6.14 shows the comparison of the measured and the reference d - and q -axis currents in current control modes.

Table 6.14. Comparison of measured and the reference currents in current control mode

Speed (rpm)	Measured	Reference	T/C	Measured	Reference	T/C
	current I_d	current I_d		current I_q	current I_q	
	$T(A)$	$C(A)$		$T(A)$	$C(A)$	
1500	-0.24	0	-	71.5	70	1.022
	-20.8	-20	1.040	40.9	40	1.023
	-31.4	-30	1.046	61.0	60	1.017
	-49.5	-50	0.989	72.7	70	1.039
	-80.7	-80	1.009	40.5	40	1.011

As seen from the above table, the generated d - and q -axis currents by the inverter controller are within $\pm 1-4\%$ of the reference d - and q -axis currents. It is worthwhile to note that the difference in actual currents affects the error in the torque generation marginally due to slight shift in the torque angle.

6.5.1.4 Speed control mode

In speed control mode, the speed controller generates the torque reference from the reference speed set by the user input. It works in conjunction with current control and torque control loops to generate the required d - and q -axis currents for the desired speed.

It was decided not to test the speed control mode as the motor essentially runs without any control except the speed input under this control mode. This could be dangerous for prototype testing considering very low inertia of the dynamometer-motor set as any malfunction of controller may lead to damage of the test bench.

6.5.2 Measurement of motor parameters (parameter characterization)

An IPM machine is a salient pole synchronous machine in which saliency is created by magnet arrangements in an IPM machine having a smooth uniform air-

gap. The torque generated by an IPM motor is given by (5.13). The first term in (5.13) is the excitation torque produced by the permanent magnets, whereas the second term is the reluctance torque produced by an IPM rotor due to its saliency. As the torque depends on d - and q -axis inductances, it is important to characterize the motor to account for variation of these inductances with currents.

The method described by K. M. Rahman *et al.* in [123] is adopted to characterize the prototype motor. The machine speed for the parameter characterization is selected carefully to minimize (a) the effect of resistive voltage drop, which is predominant at lower speeds, and (b) distortion in currents due to high back EMF of the machine at high speeds. Hence, the speed of 1500 rpm is selected for the experiment, which is below the base speed of the machine. The inverter is operated in current control mode and the entire possible range of d - and q -axis currents (resulting in to peak current below the design limit) is selected. The phase current I_a is measured with a current probe, and the phase voltage V_a is measured with a differential probe. For each set of d - and q -axis currents, the phase current and phase voltage waveforms are recorded along with the rotor position, derived from an absolute position sensor. Because of stator MMF space harmonics and slotting harmonics in actual machine, in order to produce the sinusoidal motor current, the applied voltages have to be non-sinusoidal [123], and they contain the MMF space harmonics and the slotting harmonics embedded along with the switching harmonics. The entire voltage waveform including harmonics is extracted. The machine phase currents also contain the PWM switching harmonics. The switching harmonics from the current waveform and the switching and the MMF space harmonics from the voltage waveform are eliminated using the Fast Fourier Transform (FFT). The amplitude and the phase angle information of the current and the voltage waveform are of interest to extract the machine parameters. The phase angles are obtained by using the fundamental voltage and the current waveform with respect to the position signal. The measured current and the voltage waveforms along with position signal is shown in Figure 6.15. From the measured amplitude and the phase angle information of the phase current and the phase voltage, d - and q -axis currents and voltages are calculated respectively. Then, d - and q -axis flux linkages (λ_d, λ_q) are derived using (6.3). The d - and q -axis inductances are then calculated using (6.4).

$$\begin{aligned} v_d &= i_d R_s - \omega_e \lambda_q \\ v_q &= i_q R_s + \omega_e \lambda_d \end{aligned} \quad (6.3)$$

$$L_d(i_d, i_q) = \frac{\lambda_m - \lambda_d}{i_d} \quad (6.4)$$

$$L_q(i_d, i_q) = \frac{\lambda_q}{i_q}$$

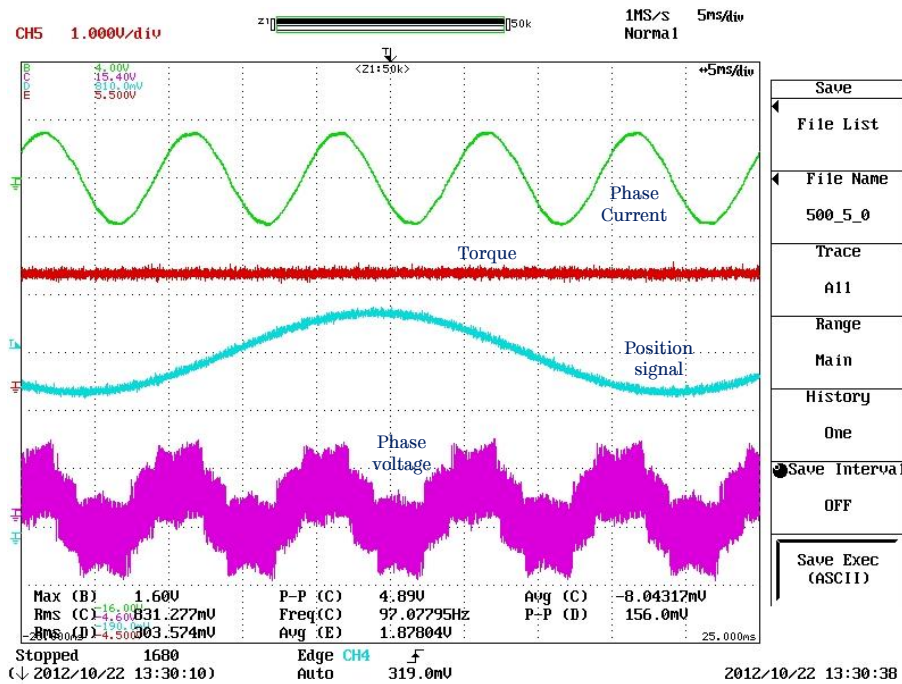


Figure 6.15. Measured phase current, phase voltage, and position signal at $I_d = -30$ A and $I_q = 70$ A.

Following the above method, the motor is characterized by measuring the position signals, back EMF waveforms and phase current for various set of d - and q -axis currents at 1500 rpm. The test procedure is described in Appendix D. Figure 6.16 and Figure 6.17 shows the comparison of d - and q -axis inductances with FEA prediction respectively.

As seen from the comparison of d - and q -axis inductances, d -axis inductance fairly matches with the prediction whereas q -axis inductance deviates considerably from the prediction mainly at lower q -axis currents. This may be attributed to several reasons such as (1) error and/or phase delay in position sensing, (2) phase

delay in current sensors, (3) error in data sampling for FFT analysis to derive fundamental quantities for parameter characterization, and (4) effect of iron loss resulting to increased current in actual tests. Similar trends have been observed for the inductances at higher d - and q -axis currents, which are shown in Appendix E.

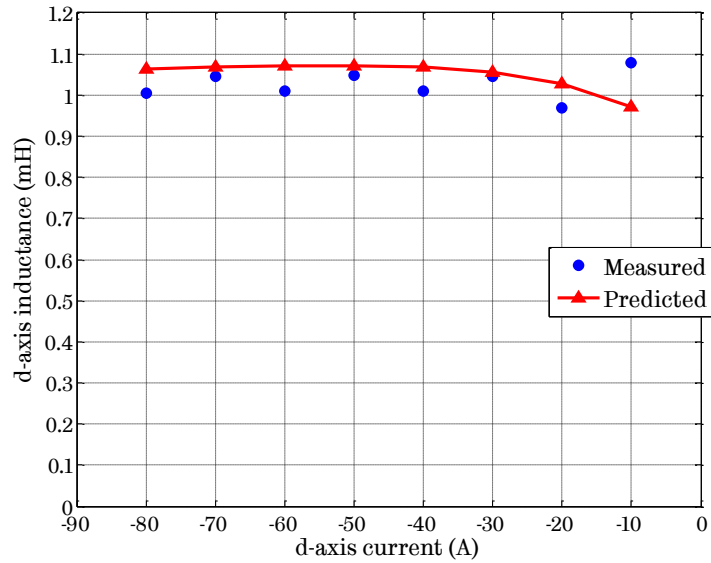


Figure 6.16. Comparison of measured and predicted d -axis inductance with $I_q = 10$ A.

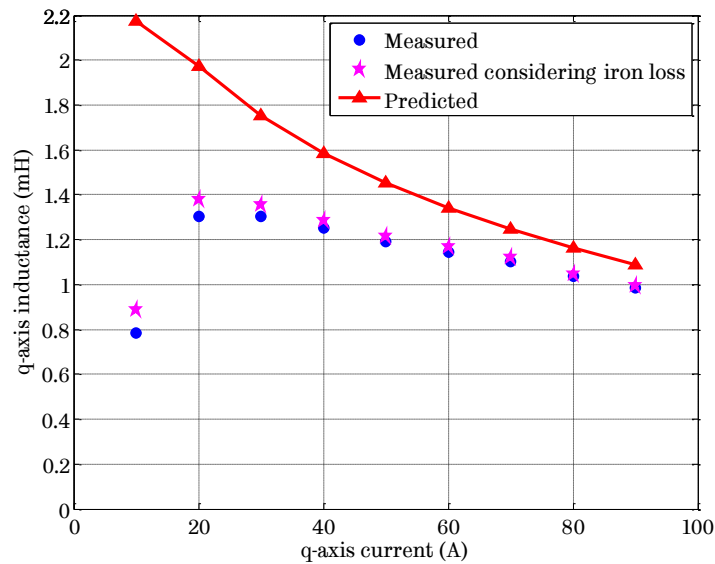


Figure 6.17. Comparison of measured and predicted q -axis inductance with $I_d = 0$ A.

6.5.2.1 Effect of iron loss on the measured inductances

In order to consider the effect of iron loss on the measured q -axis inductances, FEA based analytical iron loss model presented in [115, 124] is used, which is described by (6.5).

$$\begin{aligned} P_{fe-OC} &= a_h \frac{V_m}{2\pi\lambda_m} + a_e \left(\frac{V_m}{2\pi\lambda_m} \right)^2 + a_x \left(\frac{V_m}{2\pi\lambda_m} \right)^{1/2} \\ P_{fe-SC} &= b_h \frac{V_{da}}{2\pi\lambda_m} + b_e \left(\frac{V_{da}}{2\pi\lambda_m} \right)^2 + b_x \left(\frac{V_{da}}{2\pi\lambda_m} \right)^{1/2} \end{aligned} \quad (6.5)$$

where P_{fe-OC} and P_{fe-SC} are open-circuit and short-circuit losses respectively, a_h , a_e , a_x and b_h , b_e , b_x are open-circuit and short-circuit hysteresis, eddy current, and excess loss components respectively, and λ_m is permanent magnet flux linkage.

The voltage magnitude V_m and voltage drop due to the d -axis current V_{da} is given by (6.6).

$$\begin{aligned} V_m &= \omega_e \sqrt{\lambda_d^2 + \lambda_q^2} \\ V_{da} &= -\omega_e (\lambda_d - \lambda_q) \end{aligned} \quad (6.6)$$

where ω_e is electrical speed in rad/s.

Open-circuit loss in an IPM machine can be decomposed into d - and q -axis iron loss components, whereas short-circuit loss appears only in the d -axis iron loss component. Hence, the iron loss in d - and q -axis can be expressed by (6.7).

$$\begin{aligned} P_{fe-d} &= \frac{\lambda_q^2}{\lambda_d^2 + \lambda_q^2} P_{fe-OC} + P_{fe-SC} \\ P_{fe-q} &= \frac{\lambda_d^2}{\lambda_d^2 + \lambda_q^2} P_{fe-OC} \end{aligned} \quad (6.7)$$

During operation of the machine, the iron loss always comes from the supply side, i.e. in motoring, it comes from the electrical power supplied to the machine, whereas in generating, it comes from the mechanical power supplied to the machine. Hence, the equivalent circuit to represent iron loss in d - and q -axis can be modelled as shown in Figure 6.18.

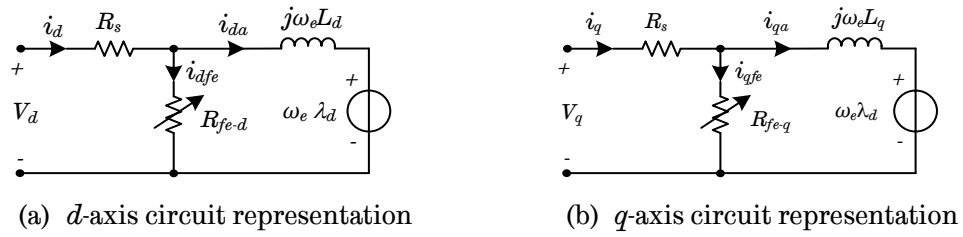


Figure 6.18. *d-q* axis circuit representation involving iron loss.

If the iron loss is considered as the equivalent current drop (as illustrated in circuit), the influence of the iron loss in *d*- and *q*-axis currents can be represented as (6.8).

$$\begin{aligned}
 i_{da} &= i_d \mp \frac{P_{fe-d}}{V_d - R_s i_d} \\
 i_{qa} &= i_q \mp \frac{P_{fe-q}}{V_q - R_s i_q}
 \end{aligned} \tag{6.8}$$

where i_{da} and i_{qa} are the *d*- and *q*-axis currents influenced by the iron loss, ‘-’ is for the motoring operation, whereas ‘+’ is for generating operation, R_s is phase resistance in Ω , V_d and V_q are *d*- and *q*-axis voltages of the machine.

The above concept is implemented to adjust the measured *q*-axis inductance of the Figure 6.18, as measurements involve the iron loss whereas the prediction using 2-D FEA does not include the iron loss. It is seen that iron loss does influence the measured *q*-axis inductance, more at the lower *q*-axis current than at higher *q*-axis current. However, there is still significant gap between the measurement and the prediction of *q*-axis inductance especially at the low *q*-axis current levels.

In order to understand the influence of the mismatch between the measured and the predicted parameters of the machine on the torque production, the motor is operated under the current control mode and the measured and predicted torque are compared, as shown in Table 6.15.

Table 6.15. Comparison of measured and predicted torque under current control mode

Reference current I_d (A)	Reference current I_q (A)	Computed torque from measured L_d, L_q (Nm)	Measured torque from the test T (Nm)	Predicted torque by FEA C (Nm)	T/C
0	10	10.8	10.3	10.2	1.010
0	90	77.7	77.5	72.9	1.063
-10	10	10.7	10.6	11.7	0.906
-10	90	82.3	81.8	78.1	1.047
-20	10	10.1	10.1	13.0	0.777
-20	90	88.5	86.8	83.4	1.041
-40	10	8.7	8.6	15.0	0.573
-40	20	23.6	23.4	29.3	0.799
-40	80	89.3	88.9	87.9	1.011
-60	10	6.7	6.5	16.2	0.401
-60	20	23.3	22.2	31.8	0.698
-60	60	80.2	77.3	82.0	0.943
-80	10	7.6	3.6	16.8	0.214
-80	20	24.2	20.0	33.4	0.599
-80	40	55.0	51.6	63.6	0.811

From Table 6.15 and comparison of inductances in Figure 6.16, Figure 6.17, and Appendix E, the following observations are made:

- 1) At lower d - and q -axis currents, even if the q -axis inductance does not match fairly well, the measured torque matches closely with the prediction.
- 2) At comparatively higher d -axis current with lower q -axis current, the measured torque does not match well with the prediction. However, with an increase in q -axis current, the difference between the measured and the predicted torque reduces. Please refer the bold red numbers in Table 6.15.

Although the difference between the measured and the predicted torque at higher d -axis current with lower q -axis current is high, this does not significantly impact the performance of the motor as the operating condition having comparatively higher d -axis current and lower q -axis current is rarely encountered and happens only during high speed operation where the deep flux weakening is employed.

Table 6.16 shows the comparison of measured torque with reference torque at 1500 rpm at which the parameters are measured with the motor-inverter drive under the current control mode. It is seen that the measured torque matches very well with the reference torque at 1500 rpm at which the parameters are measured. Figure 6.19 shows the comparison of the measured and the predicted flux linkage due to permanent magnets when d -axis current is zero. As will be seen, the measured permanent magnet flux linkage matches fairly well with the prediction for lower q -axis currents. However, with the increase in q -axis current, the measured PM flux linkage is higher than that of prediction by FEA resulting into lower cross-saturation at higher q -axis currents. The measured PM flux linkage at q -axis current of 90A peak is 7.2% higher than the prediction.

Table 6.16. Comparison of measured torque with reference torque at 1500 rpm

Reference torque $C(\text{Nm})$	Measured torque $T(\text{Nm})$	T/C	Reference torque $C(\text{Nm})$	Measured torque $T(\text{Nm})$	T/C
5	4.6	0.920	55	55.3	1.005
10	9.8	0.980	60	60.3	1.005
15	14.9	0.993	65	65.1	1.002
20	20.0	1.000	70	70.0	1.000
25	25.1	1.004	75	75.0	1.000
30	30.2	1.007	80	80.0	1.000
35	35.2	1.006	85	85.0	1.000
40	40.3	1.008	90	90.0	1.000
45	45.2	1.004	95	94.9	0.999
50	50.3	1.006	100	99.8	0.998

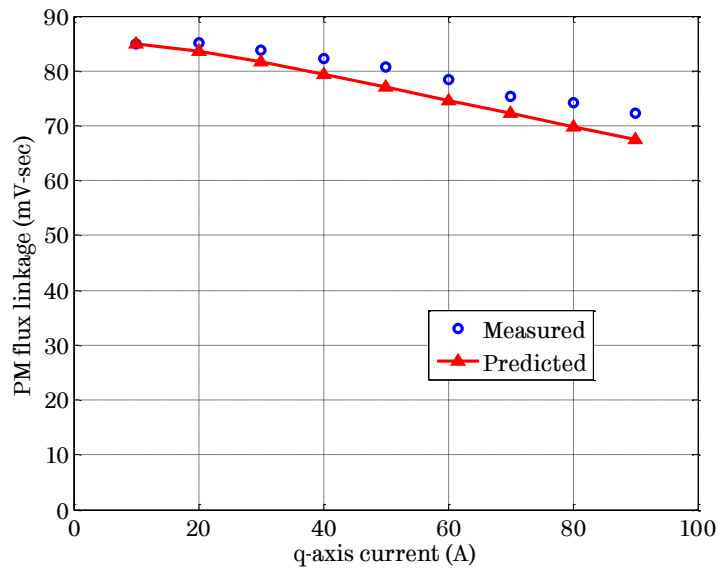


Figure 6.19. Comparison of permanent magnet flux linkage when $I_d = 0$ A.

6.5.3 Efficiency measurement

The load tests are conducted to evaluate the motor-drive operation and to measure their efficiency over the torque-speed envelope within the limitations of the dynamometer and the prototype inverter, as per the procedure described in Appendix D. Figure 6.20 compares the measured and the predicted efficiency at the base speed of 2800 rpm.

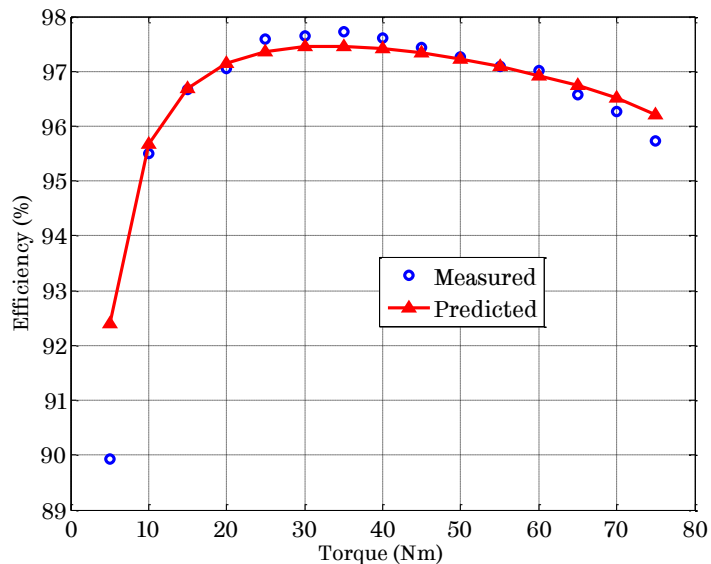


Figure 6.20. Comparison of measured and predicted efficiency of prototype IPM machine at base speed of 2800 rpm with DC link voltage of 275V.

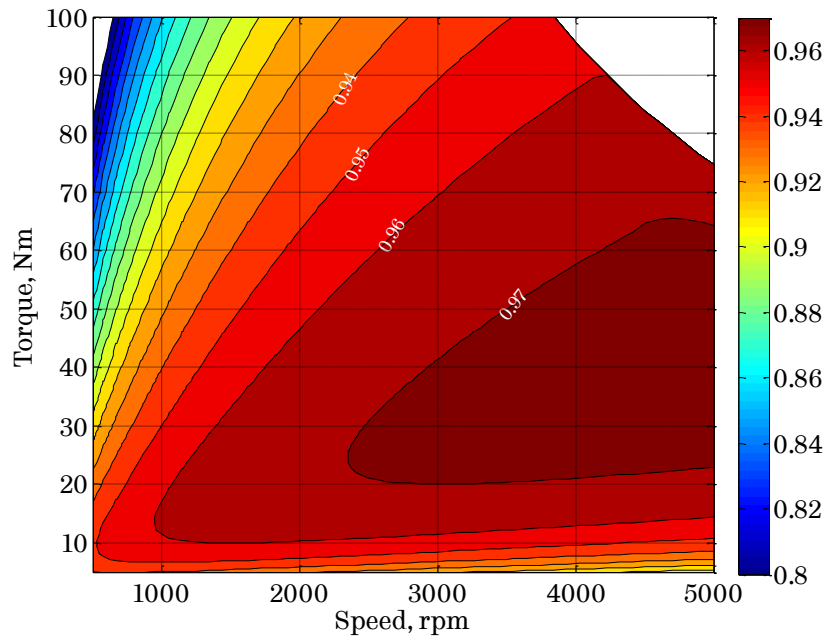
As observed, at the load torque of 5N·m, the measured efficiency is ~2.5% lower than the prediction. This is mainly due to lower accuracy of torque transducer at low torque level, and the friction and windage losses which are not accounted for in the prediction. At load torque greater than 60N·m, the measured efficiency is again slightly lower than the prediction. This is likely due to slightly lower measured back EMF as shown in Figure 6.10 and Table 6.11, and under estimation of iron loss prediction for the machine. The difference between the measured and the predicted efficiency at medium torque levels is very small and may be attributed to the combined effect of torque transducer accuracy, the error in copper and iron loss predictions, and mechanical losses due to friction and windage, which are neglected in the prediction.

6.5.3.1 Efficiency map

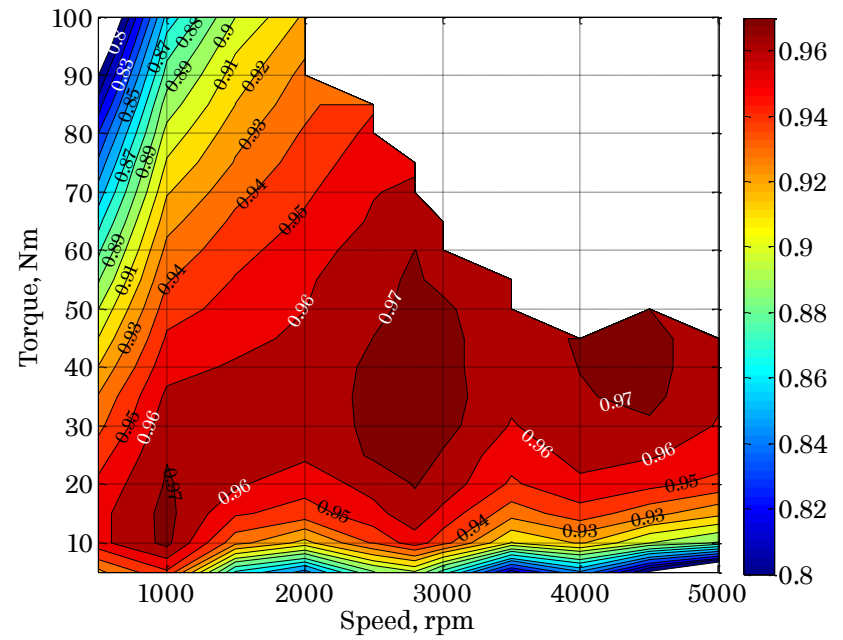
Similarly, efficiency of the motor is calculated at various torque-speed points, which is then used to plot efficiency map of the prototype machine. Figure 6.21 shows the comparison of the predicted and measured efficiency map for the torque speed envelope that was achieved during tests due to limitation of the AVL dynamometer in terms of the torque and also the inverter limitation at high torque and/or high speed operation as it was also a prototype inverter.

Compared with predicted efficiency map in Figure 6.21 (a), the measured efficiency map in Figure 6.21 (b) agrees reasonably well with the prediction for operation at lower speeds. However, at higher speed, there are differences. The main cause of the difference is the fact that the quality of the inverter current control performance deteriorates under field-weakening operation when the voltage limit is reached. In addition, the error in speed and torque measurements by the controller as well as bearing friction and windage loss, which are more likely to be significant at high speeds, may also contribute to the difference.

Based on the measured efficiency map over discrete torque-speed points, the computational model for predicting losses over the torque-speed envelope is calibrated by considering (a) the measured resistance of the phase windings (3% increase), (b) a build factor of 1.32 for iron loss derived from no-load iron loss test data, and (c) the measured friction and windage loss. Figure 6.22 shows the comparison of the predicted and the calibrated efficiency map of the prototype

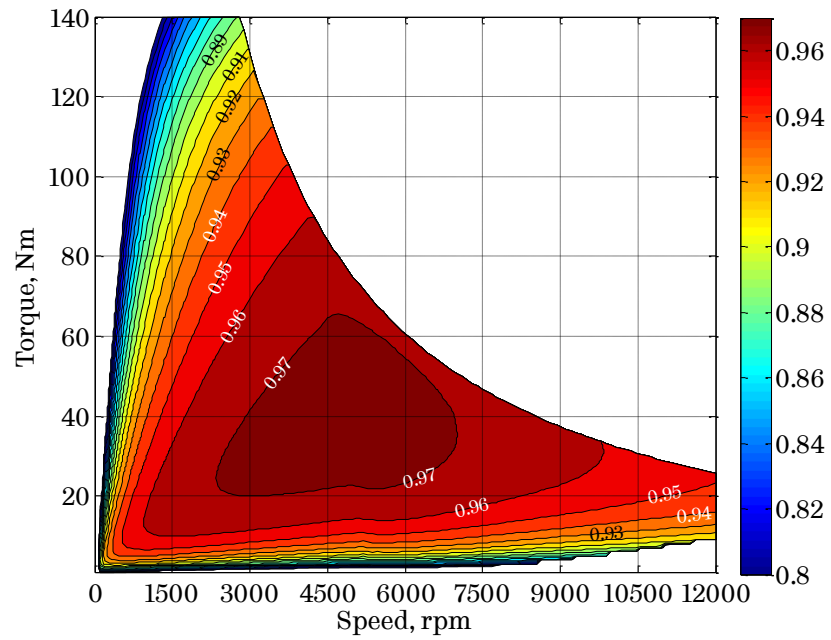


(a) Predicted efficiency map

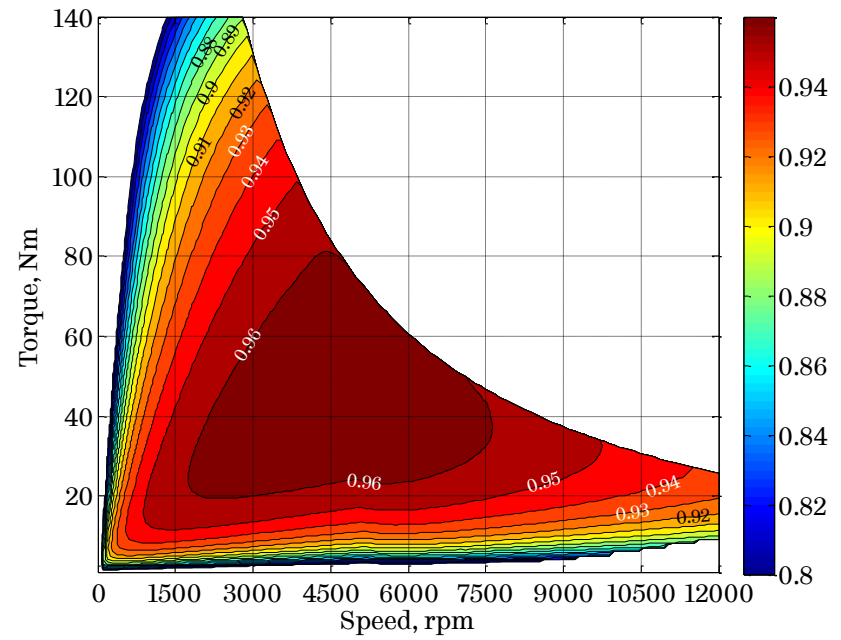


(b) Measured efficiency map

Figure 6.21. Comparison of predicted and measured efficiency map up to 5000 rpm.



(a) Predicted efficiency map



(b) Calibrated efficiency map

Figure 6.22. Comparison of predicted and calibrated efficiency map.

motor. Compared to predicted efficiency map (Figure 6.22 (a)), the efficiency is reduced by up to 1% in the calibrated efficiency map (Figure 6.22 (b)) mainly due to the above three factors. Also, at higher speeds, as the quality of current control in the field-weakening region deteriorates slightly due to voltage saturation, the reduction in efficiency is more than that at lower speeds.

6.5.4 Peak torque capability

As discussed before, the AVL dynamometer limits the range of preliminary tests as its continuous torque is only up to 100 N·m, whereas the designed and prototype machine for a segment-A EV has peak torque capability of 140 N·m. The unique design feature of the developed novel winding for 6-phase, 18-slot, 8-pole machine enables to test the peak torque capability even with limited range of the dynamometer. The 6-phase IPM motor enhances the availability of the drivetrain in the event of an inverter fault on one set of 3-phase system. Each set of 3-phase system (motor and inverter) produce almost 50% torque and power at all speeds within the torque-speed envelope. This enables to test the prototype motor for its peak torque capability having only one set of 3-phase winding excited and fed by one of the two 3-phase inverter prototyped with an independent control till peak torque capability of 70 N·m. Figure 6.23 shows the tested torque-speed envelope of the prototype motor with only one set of 3-phase system operational.

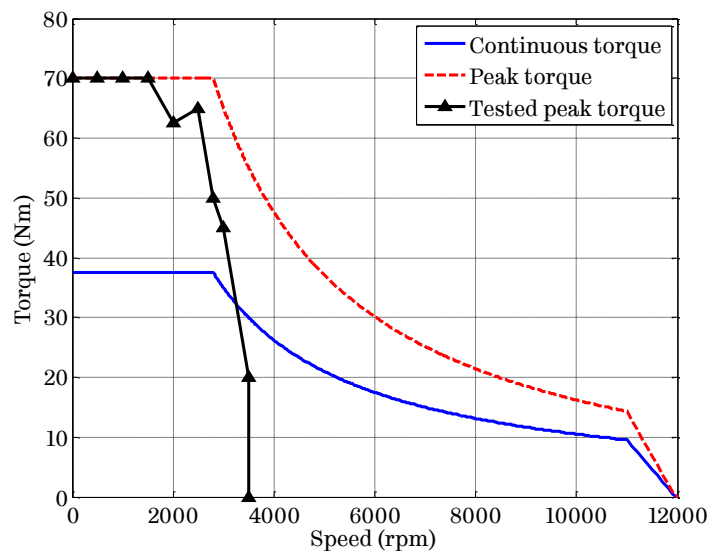


Figure 6.23. Tested torque-speed envelope of the prototype motor with only one set of 3-phase windings excited and fed by one 3-phase inverter.

As will be seen, the prototype motor is capable to provide peak torque of 70 N·m with only one set of 3-phase system operational. Therefore, it can be concluded that with all its phases in operation, the peak torque capability of 140 N·m is achievable by the prototype motor. The reduction of the peak torque limit with increasing speed (beyond 2000 rpm) is mainly due to lower DC link voltage (275V rather than 320V), limitation of the inverter in terms of quality of the current control at peak torque operation and also at high speed operation at the time of testing.

Figure 6.24 shows the comparison of the predicted and the measured efficiency of the prototype motor in 3-phase operation mode at 2800 rpm. As will be seen, similar trend of measured and predicted efficiency is observed between 6-phase operation and 3-phase operation.

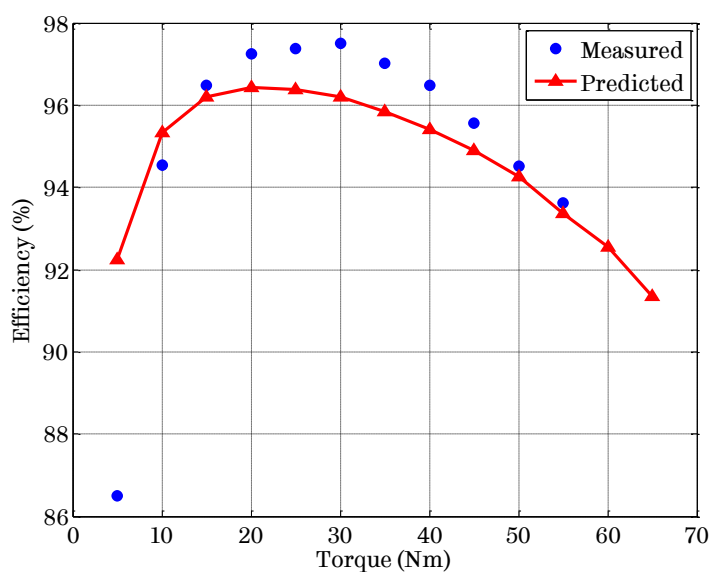


Figure 6.24. Comparison of the predicted and the measured efficiency of the prototype motor in 3-phase operation mode at 2800 rpm.

6.5.5 Thermal test at the rated torque operation

In order to validate the thermal design and thermal analysis model, thermal test is performed at the rated torque operation, as per the procedure described in Appendix D. The motor is loaded with 75 N·m torque demand at the base speed of 2800 rpm and allowed to operate continuously till the motor temperatures reach steady-state.

Figure 6.25 shows the comparison of the measured and predicted temperatures of the windings. It shows four series of measured temperatures mentioned as Test-TC1/TC2/TC3/TC4, whose location in the windings is listed in Table 6.1. Also, the predicted temperatures are shown as three series labelled as average, cool-spot and hotspot for the average, the coldest and the hottest temperatures of the coil respectively. The thermal transient is predicted using the calibrated losses of the prototype motor based on the measurements, and the environmental conditions during the thermal test. As seen, the measured temperatures of the motor windings are within the range of cool-spot and hotspot predictions by the thermal model. The measured average winding temperature at steady-state is 89°C, which matches closely with the predicted average winding temperature of 89.7°C.

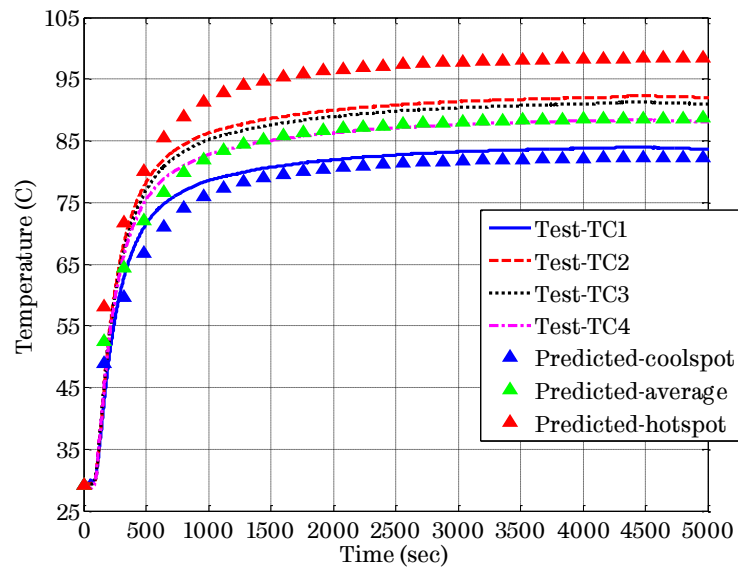


Figure 6.25. Comparison of the predicted and the measured transient temperatures of the motor windings at the rated torque operation.

Due to mechanical limitation of the test set up, the rotor temperatures are not measured. However, once the thermal model is validated, the rotor temperatures can be derived with less uncertainty to account for accuracy of air-gap thermal conduction and convection. Figure 6.26 shows the predicted transient temperatures of the motor components at the rated torque operation.

It is seen from Figure 6.26, the rotor temperatures are higher than the stator temperatures. The temperature difference between the rotor surface and the stator bore surface is $\sim 12^{\circ}\text{C}$. As explained in section 5.6.5.1 of Chapter 5, this is expected due to large thermal resistance of the air-gap through which almost all of the rotor losses are dissipated. It should be noted that the difference between the stator and the rotor temperatures will increase further with increase in speed as rotor losses have to be dissipated via higher thermal resistance compared to stator, which is directly cooled by water.

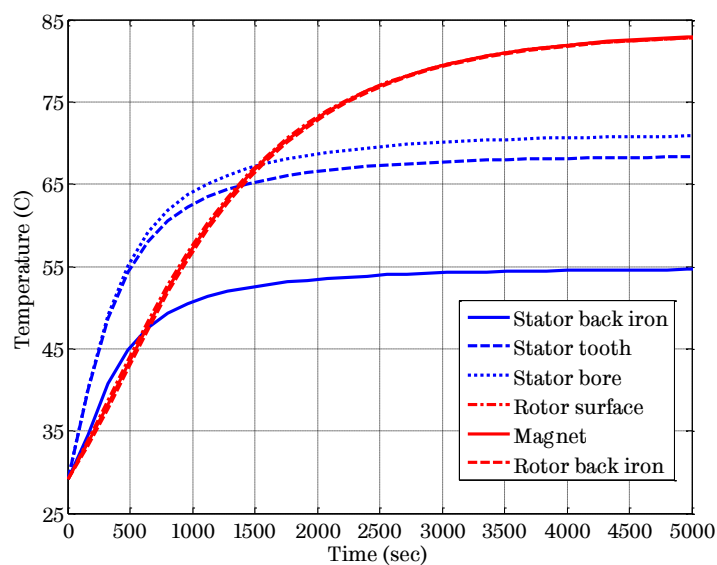


Figure 6.26. Predicted transient temperatures of the motor components at the rated torque operation based on the thermal test.

6.6 Investigation of partial demagnetization of the prototype motor during high speed testing

From the preliminary tests at The University of Sheffield, it is evident that the prototype motor could not be tested for the complete torque-speed envelope covering high speed operation (beyond 5000 rpm) because of the poor quality of the current control at high speeds in the prototype inverter. Also, as part of the FP7 CASTOR project, the motor was required to be tested at OEM's facilities (Volkswagen). Hence, the prototype motor was sent to Germany for further testing including high speed operation. The author had visited Volkswagen's facilities in

Germany to support further testing along with engineers from Infineon Technologies who have developed the prototype inverter.

The primary objective of the testing was focused on improvising the current control of the inverter at all speed and torque levels within the designed capability of the prototype motor. The current control and the calibration of the position sensor was further improved. The prototype motor was run successfully till the maximum speed of 12000 rpm with zero torque reference.

After confirming the improvement, next test was to run the motor with some torque demand till maximum speed. The test started with 30 N·m demand from lower speed. As speed increased, the torque demand was adjusted (reduced) to ensure the motor operation at 22 kW. At 10750 rpm and torque demand of 20 N·m, the motor was running under control for about 30 sec. After that, one set of 3-phase system (A-B-C) of the motor lost control and the currents increased dramatically. The sequence of the events during the incident is shown in Figure 6.27. It shows the measured six phase currents, speed, torque and vibration (accelerometer output) against time.

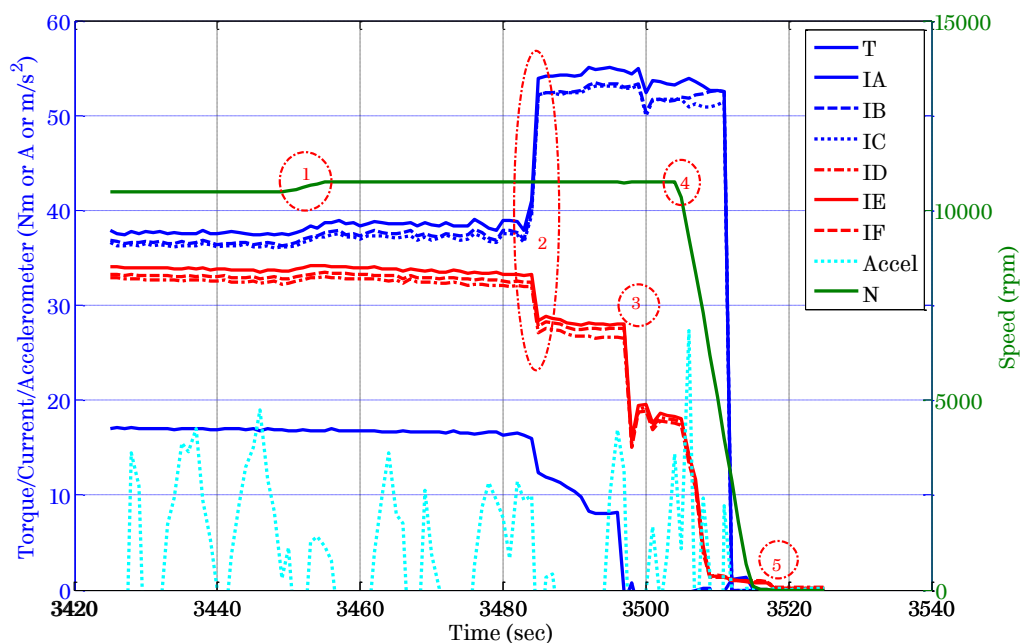


Figure 6.27. Sequence of events during the incident of partial demagnetization of the prototype motor.

6.6.1 Sequence of events

- 1) With reference torque of 20 N·m, speed of the dynamometer was increased to 10750 rpm from 10500 rpm.
- 2) The currents unexpectedly increased in A-B-C windings and reduced in D-E-F windings.
- 3) After observing sharp increase in the reference d -axis current (I_d), the torque reference was set to zero (0 N·m). The currents in D-E-F windings followed the torque command whereas the currents in A-B-C did not change. At this time, the measured torque drops to half, i.e. ~8.5 N·m.
- 4) Upon observing the abnormal behaviour, the speed of the dynamometer was reduced to zero. The currents in A-B-C windings did not reduce until the speed reached ~3000 rpm. After that, the A-B-C phase currents drop to zero instantly. This confirms that the control of A-B-C system through inverter was lost and A-B-C system of the motor was in generation mode.
- 5) It was observed that DC link voltage was set at 250 V. The motor was operating under deep field weakening at this test point as the rated voltage for the motor is 320 V.

6.6.1.1 Partial demagnetization

When the test was resumed, it was noted that the torque was reduced by about 25% and the back EMF measurement was subsequently taken. The back EMF of the motor is reduced by ~26% than the previously measured values, listed in Table 6.11. This confirms the partial demagnetization of the prototype motor reducing its capability by ~26%, i.e. 17 kW continuous instead of 22 kW.

6.6.2 Investigation of root causes

Due to space limitation, only the summary of detailed investigation into root causes of the partial demagnetization of the prototype motor is presented in the thesis, and is as follows:

6.6.2.1 Designed capability of the high power motor

The prototype motor is designed for 320 V DC link voltage with 22 kW continuous power and 32 kW peak power at maximum cruise speed of 11000 rpm. The operation at the test point (20 N·m, 10750 rpm) should be safe with 320 V.

However, the test point at which the partial demagnetization happened, the DC link voltage was 250 V. The actual DC link voltage used by the controller is 95%, i.e. 237.5 V.

With 250 V, the motor capability reduces to 17 kW continuous power and 25 kW peak power at maximum cruise speed of 8600 rpm. Therefore, the test point (20 N·m, 10750 rpm) was beyond the designed capability of the prototype motor as shown in Figure 6.28, and should not be allowed. As per IEEE standard 11-2000, the peak operation is allowed under normal cooling conditions for a short period only. The motor was operating in peak power region with 250 V from medium speed (~5850 rpm) till the timing of the incident leading to possibility of losing control, overheat and risk of demagnetization.

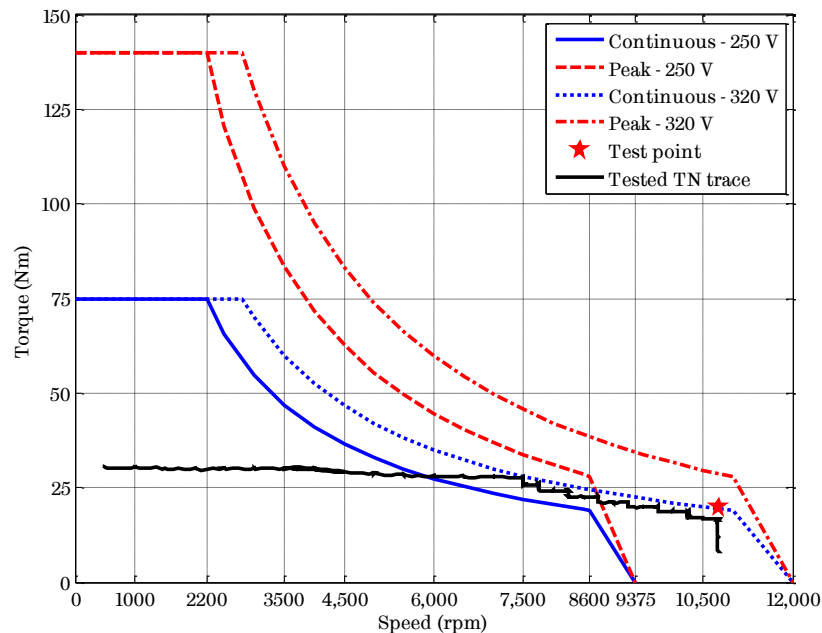


Figure 6.28. Designed capability of the prototype motor and the test point.

6.6.2.2 Controller-drive simulations to replicate the observed behaviour during the incident

The controller-drive simulations were carried out in MATLAB replicating the test behaviour at the time of incident. The diode-rectifier effect is well modelled in MATLAB to account for uncontrolled generation in the event of losing control due to inverter shut down as this was frequently experienced during the tests at The University of Sheffield as well as Volkswagen. Out of various simulation cases,

it was found that the case with A-B-C losing control followed by gradual demagnetization of the motor over 0.5 sec replicates the test behaviour in the best way.

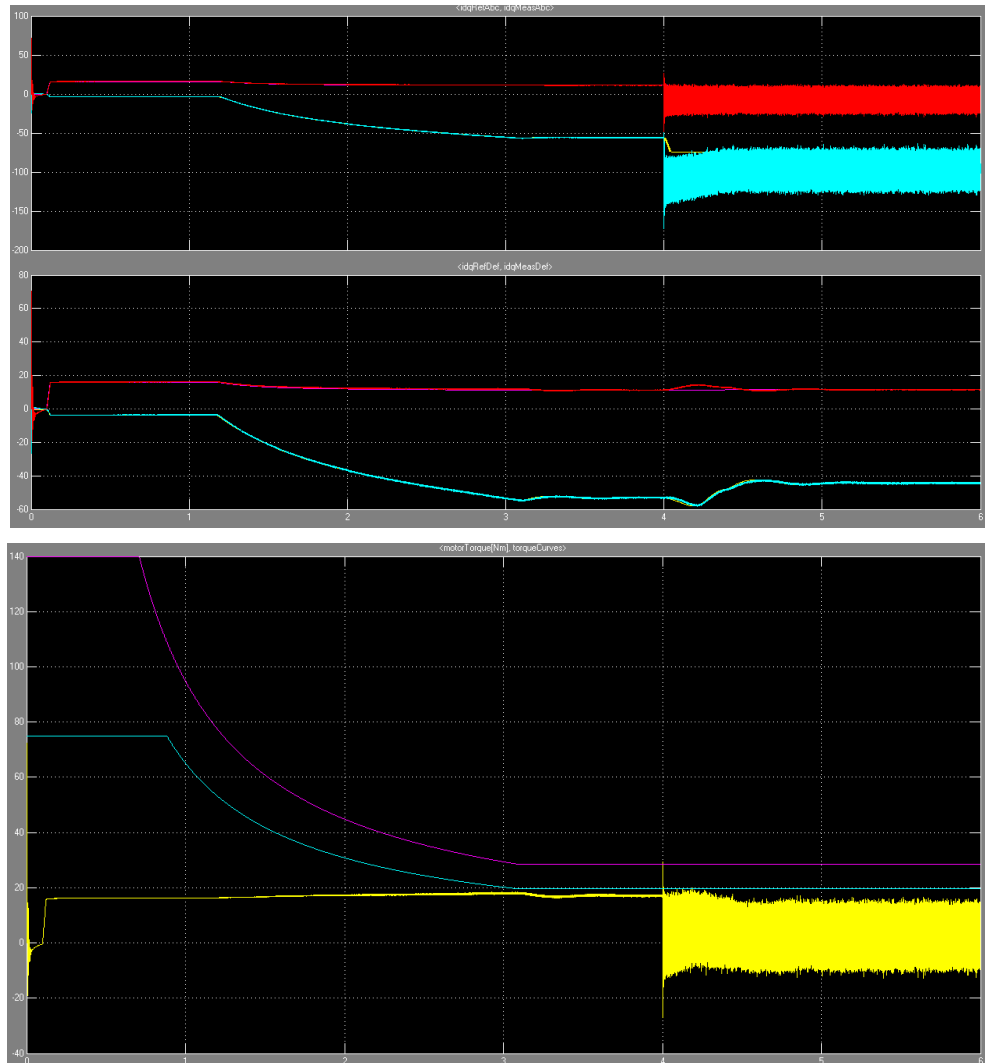


Figure 6.29. MATLAB simulation to replicate the observed behaviour during the incident, Simulation case of A-B-C losing control and demagnetization happens gradually over 0.5 sec, Top chart shows reference and actual values of I_d , I_q for A-B-C, and D-E-F respectively, whereas bottom chart shows the torque-speed envelope with torque response of the motor during the incident.

The simulated currents in A-B-C, D-E-F and generated torque matches quite well with the recorded test data as shown in Figure 6.29. It is also observed that sudden transient peak currents of about -175A and -50A have been generated in d - and q -axis of A-B-C phase system during short-circuit condition (battery

impedance is almost negligible causing virtual short circuit of motor terminals) at the time of losing control. Such high transient short circuit currents most likely led to partial demagnetization (detail analysis of partial irreversible demagnetization is presented in section 7.2 of Chapter 7) albeit these transient currents were not captured (Figure 6.27) due to high filtering of the data acquisition.

6.6.2.3 Electromagnetic FEA and thermal analysis at the incident point

During field weakening operation, d -axis current (I_d) controls the voltages, whereas q -axis current generates the required torque. In order to control the voltages, the flux is forced to concentrate towards air-gap resulting into lower flux linkage to stator windings. Higher concentration of flux towards the rotor and higher order harmonics penetrating deeply inside the rotor tend to increase the rotor losses in fractional-slot PM machines. If field weakening is employed with lower DC link voltage, then higher I_d is required to produce the same torque at a given speed resulting into much higher flux concentration & penetration in the rotor.

The effect of lower DC link voltage on the rotor losses for the same torque-speed point is analysed using electromagnetic FEA, as shown in Table 6.17. The losses obtained from electromagnetic analysis are used to carry out the thermal analysis at 20°C ambient air and water inlet temperature, and 15 litre/minute water flow as per the recorded test data. In order to account for inaccuracy of iron loss prediction, the iron losses are increased by the build factor of 1.32, whereas the bearing friction loss, and windage loss are taken from the dummy rotor tests. The analyses are carried out at 10750 rpm with 16 N·m (measured torque was 16 N·m at the time of incident) for 320 V and 250 V. The results of the thermal analyses are shown in Table 6.17. It was found that with 250 V (i.e. 237.5 V drive voltage limit), the rotor losses increases by 27% compared to those of 320 V. This results into steady-state rotor temperature of 195°C which is 30°C higher than that of 320 V. The design limit on the operating temperature of the NdFeB magnets is 180°C.

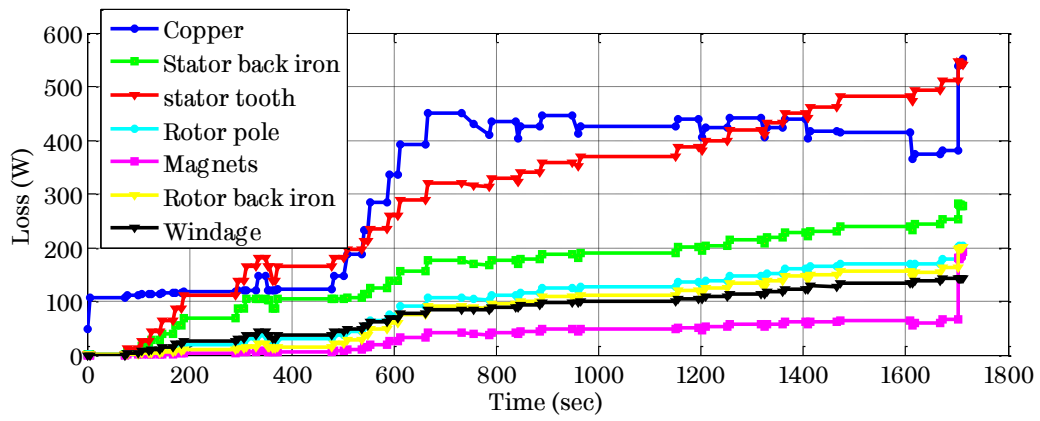
Although steady-state temperatures are 15°C higher than the design limit, it is observed that steady-state was not achieved as the recorded temperatures were still rising, and also, the test was run at this point for about 30 sec only.

Table 6.17. Steady-state thermal analyses at various DC link voltages

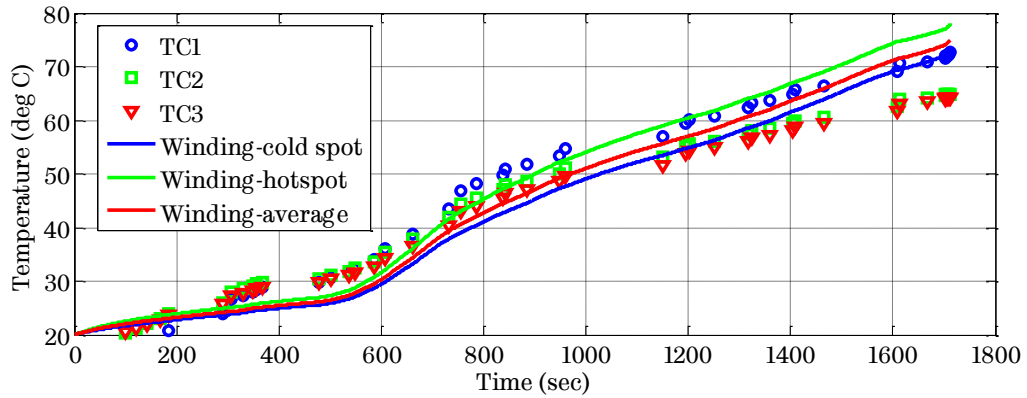
DC link voltage	250 V	320 V	320 V
Controller voltage limit (% of DC link voltage)	95%	95%	100%
Phase RMS current	42.1 A	35.7 A	34.4 A
Torque produced	15.6 N·m	15.5 N·m	15.7 N·m
Line-line voltage (fundamental)	237.8 V	301.3 V	317.6 V
Copper loss	597 W	430 W	398 W
Iron loss – stator	528 W	504 W	506 W
Iron loss – rotor	280 W	235 W	226 W
Eddy current loss in magnets	57 W	41 W	39 W
Total rotor loss to be dissipated	337 W	277 W	265 W
Rotor back iron temperature	195.4°C	165.1°C	159.6°C
Rotor magnet temperature	194.8°C	164.6°C	159.1°C
Rotor surface temperature	191.8°C	162.3°C	156.9°C
Stator surface temperature	113.4°C	98.2°C	95.7°C
Stator tooth temperature	104.0°C	90.4°C	88.2°C
Average winding temperature	116.5°C	97.9°C	94.9°C

The transient thermal analysis of the motor is performed over the test sequence (shown in Figure 6.28) to evaluate the motor temperatures. Figure 6.30 (a) shows the variation of losses in different components of the motor over the test sequence having total duration of 1713 sec. It is to be noted that the total loss to be dissipated is higher with operation at 250 V compared to 320 V, especially during the field weakening as more current is required to weaken the flux to meet the lower voltage limit. The measured winding temperatures (TC1, TC2, and TC3) match reasonably well with the predicted winding temperatures (cold-spot, hotspot, and average) as seen from Figure 6.30 (b). As will be seen from Figure 6.30 (c), the magnet temperature reaches almost 140°C at 1713 sec. It is to be noted that the predicted temperature is average temperature across the machine length.

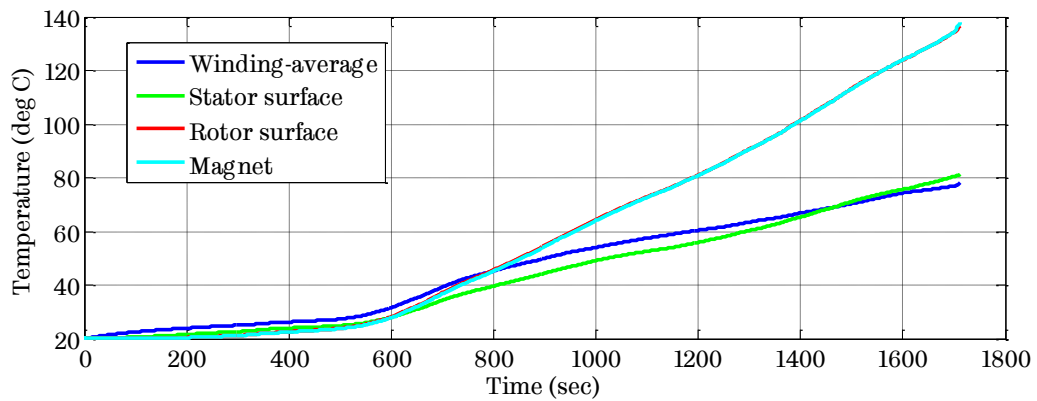
Considering the 10-15% variation in the rotor temperatures due to uncertainty in the rotor thermal model, and the fact that the middle part of the rotor (axially) has maximum temperature, the actual rotor temperature may be



(a) Loss variations over the test sequence



(b) Comparison of predicted and measured winding temperatures



(c) Predicted temperatures of the motor components

Figure 6.30. Transient response of the motor over the test sequence with DC link voltage of 250V, 15 litre/min, 20°C ambient air and water inlet temperature.

~160°C-165°C. The magnets used in the prototype motor have demagnetizing characteristics if operated beyond 150°C, as shown in Appendix G. Also, the current

measurements may be erroneous up to 10% because of high filtering in the data acquisition system. This translates to ~200 A peak demagnetizing currents in the machine at the instant of A-B-C inverter losing control (as seen from Figure 6.29). These two factors together might have resulted into the partial irreversible demagnetization of the prototype motor. It will be shown in Chapter 7 that the rotor magnets will be demagnetized up to 22% if exposed to peak demagnetizing transient currents of ~220 A. This may justify 26% reduction in back EMF post demagnetization (as discussed in 6.6.1.1), although the reduction in back EMF of the machine may not be proportional to the demagnetized volume of the rotor magnets.

It is likely that the temperature of the rotor magnets along with the peak transient demagnetizing currents at the instant of A-B-C losing control were responsible for the partial demagnetization of the prototype motor.

6.6.3 Summary of investigation

- 1) The rotor has partially been demagnetized. On an average, the back EMF of the motor is reduced by ~26%.
- 2) Test point with 250 V DC link voltage was beyond the continuous operating capability of the motor posing serious risk of overheating and demagnetization. This operation is however not sustainable for a long period as the rotor temperature will eventually be above the operating temperature (180°C) of the magnets.
- 3) Electromagnetic analysis shows that with 250V DC link voltage
 - a. Higher d -axis current (I_d) is required to produce same torque at a given speed.
 - b. Increases rotor losses leading to higher rotor temperature.
 - c. As temperature increases, the magnets are more vulnerable to demagnetization.
- 4) Controller-drive Simulations show that loss of control, most likely due to inverter shut down, on A-B-C system results into transient short-circuit through inverter diodes, forcing very high currents to flow which caused gradual partial demagnetization as the temperature continues to increase.

It follows that the partial demagnetisation is due to (1) operation beyond safe limit leading to higher rotor temperatures, and (2) A-B-C inverter shut down at the high speed.

For any reduction in DC link voltage from 320 V, the continuous power, the maximum cruise speed, and the maximum speed must be reduced accordingly.

6.6.4 Preventive measures undertaken

Since it is not possible to completely eliminate similar converter failures at the development stage, preventive measures have to be adopted to ensure the second prototype machine can survive even under overload and unexpected fault conditions. The preventive measures, taken by the author and the engineers from Infineon Technologies, are as below.

- 1) Rotor has been redesigned by the author
 - a. to reduce losses in the rotor
 - b. to prevent any risk of partial demagnetization

These measures are adopted as precautions to any unexpected incident for second prototype motor.

- 2) If the inverter cannot be operated at 320 V as specified in design specifications in the next tests, the maximum speed and power should be reduced accordingly.
- 3) It is also necessary to ensure that the inverter does not accidentally shut down as this would result into transient currents greater than the normal operation and pose risk of damage to the motor. This was taken care by the engineers from the Infineon Technologies.

6.7 Comparison of two prototypes

To reduce the losses in the rotor laminations, the author has selected 0.2 mm thick steel laminations of NO20 material, and to prevent any risk of partial demagnetization, Samarium Cobalt ($\text{Sm}_2\text{Co}_{17}$) magnets are selected. Table 6.18 compares the two prototype rotors. It is to be noted that only rotor has been built

for second prototype, whereas the stator of first prototype is used to assemble second prototype motor for the segment-A vehicle under consideration.

Table 6.19 compares the material properties of NO20 and M270-35A electrical steel. As seen, second prototype rotor will not have any mechanical stress issue as its yield strength is ~425 MPa, and the maximum stress in the rotor material is only ~392 MPa at 1.5 times the maximum operating speed, i.e. 18000 rpm (Figure 5.17).

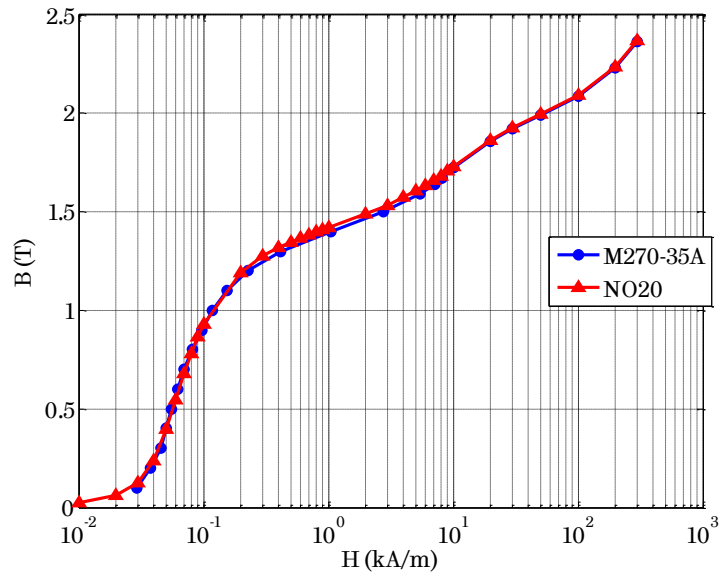
Table 6.18. Comparison of two prototype rotors

	Rotor-1	Rotor-2	Unit
Steel material	M270-35A	NO20	-
Thickness of lamination	0.35	0.2	mm
Density of rotor material	7650	7620	kg/m ³
Normalized weight of the rotor	1.000	0.996	pu
PM material – grade	N35EH	RECOMA28	-
Design limit – PM temperature	180	300	°C
Density of PM material	7500	8300	kg/m ³
Normalized weight of PM	1.000	1.107	pu
Electrical resistivity of PM	180	90	Ωμ-cm

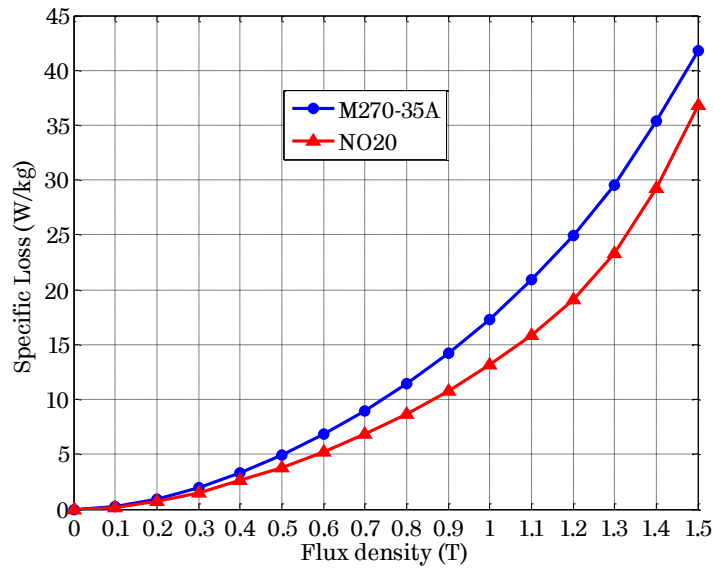
Table 6.19. Comparison of material properties of M270-35A and NO20

	M270-35A	NO20	Unit
Thickness of lamination	0.35	0.2	mm
Typical yield strength	450	424.3	MPa
Typical tensile strength	565	508.5	MPa
Electrical resistivity	0.52	0.52	μΩ-m

Figure 6.31 shows the comparison of B-H characteristics and specific loss characteristics of M270-35A and NO20 electrical steel respectively. As will be seen, NO20 electrical steel requires slightly lower magnetic field intensity compared to M270-35A to produce the same magnetic field. Also, the specific loss of NO20 is ~24% lower than M270-35A up to 1.2 T on average. Beyond it, the specific loss of NO20 is ~17% lower than M270-35A on an average. Table 6.20 compares the magnet properties for both the prototype rotors. As seen, Sm₂Co₁₇ (RECOMA 28) magnets



(a) B-H characteristics



(b) Specific loss characteristics

Figure 6.31. Comparison of characteristics of M270-35A and NO20 electrical steel.

Table 6.20. Comparison of magnet properties of NdFeB and Sm₂Co₁₇ [125, 126]

	NdFeB	Sm ₂ Co ₁₇	NdFeB	Sm ₂ Co ₁₇	Unit
Temperature	20		150		°C
B_r	1.19	1.1	1.004	1.05	T
$H_{c,B}$	899	800	716	750	kA/m
μ_r	1.053	1.094	1.116	1.114	-
BH_{max}	275	225	192	197	kJ/m ³

have ~7.5% lower residual induction (B_r) compared to NdFeB (N35EH) magnets at room temperature of 20°C, whereas at higher temperatures, RECOMA 28 magnets have ~4.6% higher B_r than N35EH magnets.

Table 6.21 shows the performance of second prototype motors at the rated and the peak torque operations at the base speed as well as at the maximum cruise speed operation. Compared to first prototype, the rotor iron loss of 2nd prototype is reduced by 28.6% and 39.4% at the rated torque and the peak torque operation respectively, whereas the PM eddy current loss is increased by 63.6% and 61.8% at the rated torque and the peak torque operation respectively. The reduction in rotor iron loss is because of lower eddy current loss in the NO20 steel due to the thinner lamination material, whereas the increase in PM eddy current loss is because of lower resistivity of Sm₂Co₁₇ magnets, which is half of NdFeB magnets. Also, for thermal behaviour of second prototype motor, the total rotor iron loss to be dissipated at the maximum cruise speed operation is 199 W, which is 34.1% lower than first prototype machine (302 W, Table 5.10). Hence, the risk of partial demagnetization will not be present in second prototype motor due to (a) lower rotor losses to be dissipated at high speed operations, (b) higher temperature withstand-ability of Samarium Cobalt magnets.

Table 6.21. Performance prediction for 2nd prototype motor

Parameter	Second prototype motor			Unit
	Rated torque	Peak torque	Max. cruise speed op.	
Torque	75.0	140.0	19.1	N·m
Speed	2800	2800	11000	rpm
Power	22.0	41.0	22.0	kW
Torque ripple	2.5	5.0	2.2	%
Peak phase current	77.0	191.0	54.7	A
Line-line voltage (V_{ll})	217.9	319.9	322.6	V
Current density	10.1	25.1	7.2	A/mm ²
Copper loss	942	5796	475	W
Iron loss – stator	158	247	534	W
Iron loss – rotor	20	28.5	113	W
PM eddy current loss	18	116.5	86	W
Power efficiency	95.1	86.9	94.8	%

For the same magnet temperature, compared to first prototype, the efficiency at both the rated and the peak torque operation has increased by 0.3% and 1.6% respectively, because of higher residual induction of second prototype motor leading to lower current requirement to generate the same torque.

The parameters of second prototype motor have been extracted using 2-D FEA as mentioned in Chapter 5, and are incorporated in the inverter controller as new machine model for the testing. The parameters of second prototype (L_d versus I_d , L_q versus I_q , λ_m versus I_q) are tabulated in Appendix F. The preliminary tests are conducted on second prototype motor at The University of Sheffield as well as Volkswagen Facilities at Germany.

6.8 Preliminary tests on 2nd prototype motor

6.8.1 Back EMF measurement

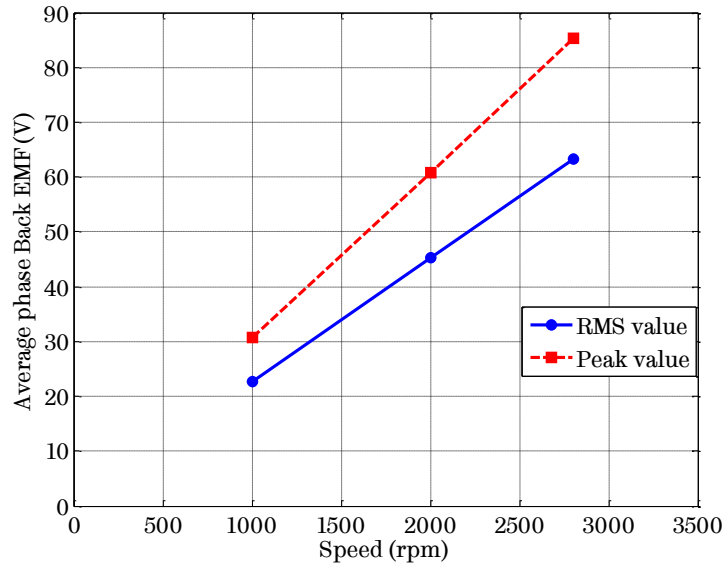
The back EMF of second prototype is measured at room temperature of 23°C at different speeds, i.e. 1000 rpm, 2000 rpm, and 2800 rpm. Figure 6.32 (a) shows the measured back EMF (peak and RMS values) with respect to speed. The back EMF constant of second prototype motor is 30.361 mV/rpm from the peak values of the measured back EMF at different speeds. This translates to open circuit peak line-line voltage at maximum speed (12000 rpm) of 631 V, which is below the limit of 650 V. From the comparison, it is found that the RMS and peak values of the measured back EMFs are 7.7% and 6.8% lower than the prediction, which is higher than the difference observed for first prototype motor. The prediction is made using the measured properties of the magnets, and at the same temperature at which the test is conducted. The difference can be attributed to lower permanent magnet width in the prototype due to grinding or tolerance requirement for inserting them inside the rotor, and the resulting air-gap between the magnets and rotor core, as well as slightly different BH characteristics of the laminations between the datasheet and the actual materials used in the prototype.

6.8.2 No-load loss measurement

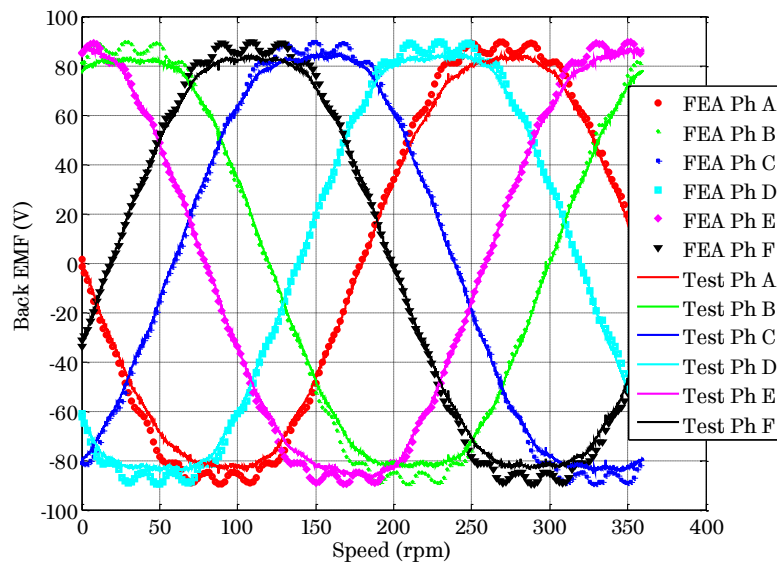
The no-load loss of second prototype motor is measured from standstill to maximum operating speed of 12000 rpm. The bearing friction and windage loss is

also measured using dummy rotor. Using the polynomial fit, the bearing friction and windage loss is expressed as a function of speed, both in per unit, as shown in Figure 6.33. The base speed of 11000 rpm, and the base loss of 150 W is used to derive per unit quantities.

$$P_{bf} + P_w = 0.1078N^3 + 0.9223N^2 - 0.155N + 0.0164 \quad (6.9)$$



(a) Measurement of back EMF constant



(b) Comparison of back EMF waveform

Figure 6.32. Measured back EMF of 2nd prototype motor at room temperature of 23°C.

For the maximum operating speed of 12000 rpm (*i.e.*, 1.043 pu), the measured bearing friction and windage loss is 147.2 W (*i.e.*, 0.981 pu). Figure 6.33 shows the comparison of no-load iron loss between the prediction and the measurement after deducting bearing friction and windage loss. It also shows the calibrated no-load iron loss after accounting for build factor of 1.24.

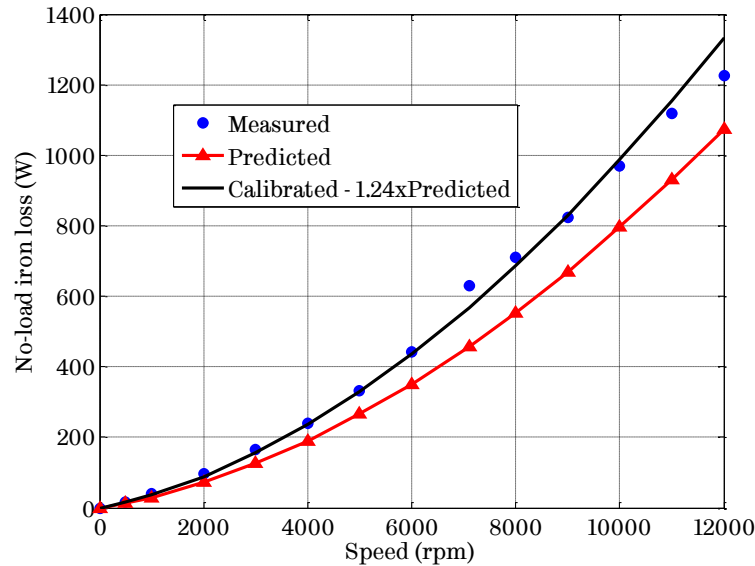


Figure 6.33. Comparison of measured and predicted no-load iron loss for 2nd prototype.

Compared to first prototype, the uncertainty in predicting iron loss is reduced from 32% to 24%. Also, at maximum cruise speed of 11000 rpm, the no-load iron loss of second prototype (1118 W) is 11.1% lower than 1st prototype (1258 W, Figure 6.14)

6.8.3 Measurement of efficiency map

Due to the requirement of the OEM project partner, the tests of efficiency map are conducted at different DC link voltage, *i.e.*, 250 V, 320 V, and 370 V.

6.8.3.1 Drive operation at 250 V

Figure 6.34 shows the comparison of the predicted and the measured efficiency map for the torque-speed envelope that was achieved during testing at The University of Sheffield due to limitation of the AVL dynamometer in terms of the torque and also the inverter limitation, with DC link voltage set at 250 V. It is worthwhile to note that with drive operation at 250 V, the maximum speed of the

motor reduces to 9375 rpm, the maximum cruise speed with continuous power reduces to 8600 rpm, and the base speed reduces to 2200 rpm. It is evident that second prototype motor too has a high efficiency over wide torque-speed range like first prototype motor.

Compared with the predicted efficiency map in Figure 6.34 (a), the measured efficiency map in Figure 6.34 (b) agrees reasonably well with the prediction for different torque levels at lower speeds. However, at higher speed, there are differences. The main cause of the difference is the fact that the quality of the inverter current control performance deteriorates under field-weakening operation when the voltage limit is reached. This results in a large d -axis current and hence greater copper loss than what can be achieved theoretically. In addition, the errors of torque and speed measurement as well as windage and frictional loss, which are likely more significant at high speeds, may also contribute to the difference.

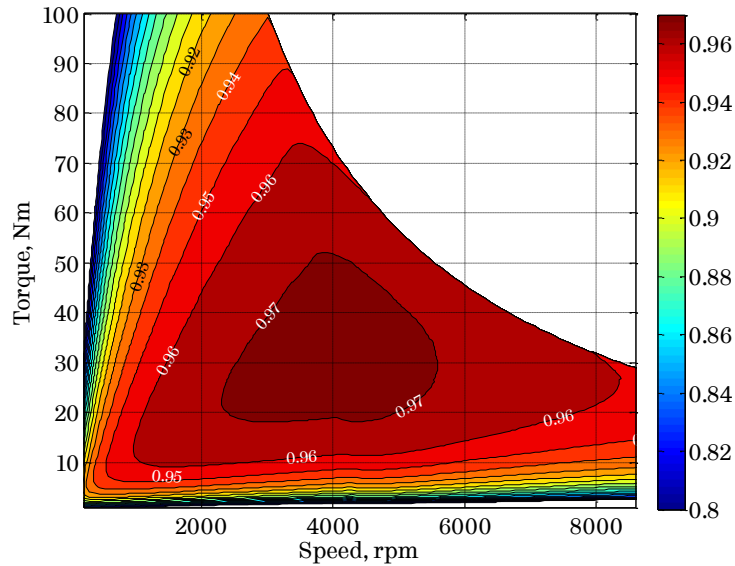
6.8.3.2 Drive operation at 320 V

Because of the time constraints, the efficiency map measurements with 320 V is not carried out at The University of Sheffield. However, the measurements with 320 V are carried out at Volkswagen's research centre located at Isenbuttel, DE. It is worthwhile to note that the test bench at Volkswagen is different than that at The University of Sheffield as both have different instrumentation employed to measure the input and the output power of the motor/inverter.

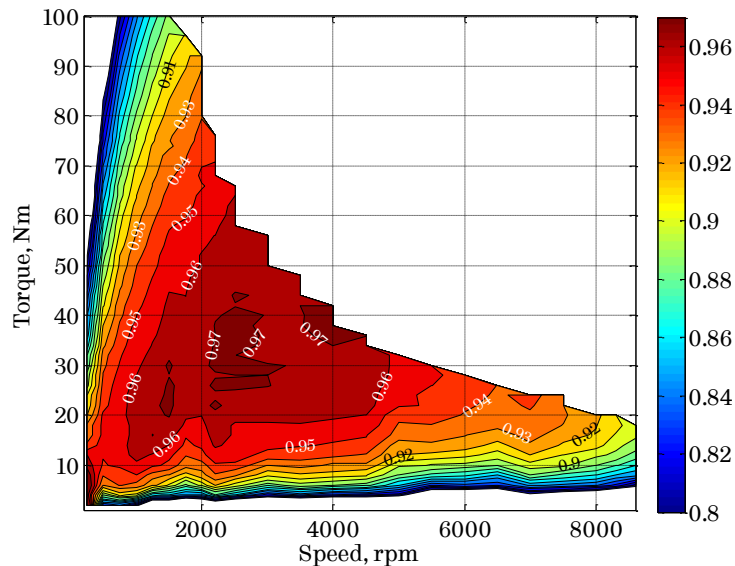
Figure 6.35 shows the comparison of the predicted and the measured efficiency map of the motor with drive operation at 320V. As seen, the measured efficiency is lower than the predicted one, and the difference is larger than what has been observed (refer Figure 6.24) for the test bench at The University of Sheffield. This was mainly due to large range torque transducer (0-1000 N·m) used by Volkswagen's test bench, which compromises the accuracy of the torque measurements at lower torques. From the comparison of efficiency maps of Figure 6.35, it can be inferred that at lower speeds, the torque transducer accuracy is compromised yielding to lower measured torque and hence lower efficiency, whereas at higher speeds, the accuracy of the torque transducer improves, resulting into very close match between the predicted and the measured efficiency.

It should be noted that the bearing friction and windage loss also influence the difference between the measured and the predicted efficiency at all speeds, as the predicted efficiency map doesn't account for them.

From comparison of Figure 6.34 and Figure 6.35, it is observed that the efficiency of the motor improves with increase in DC link voltage, as expected.

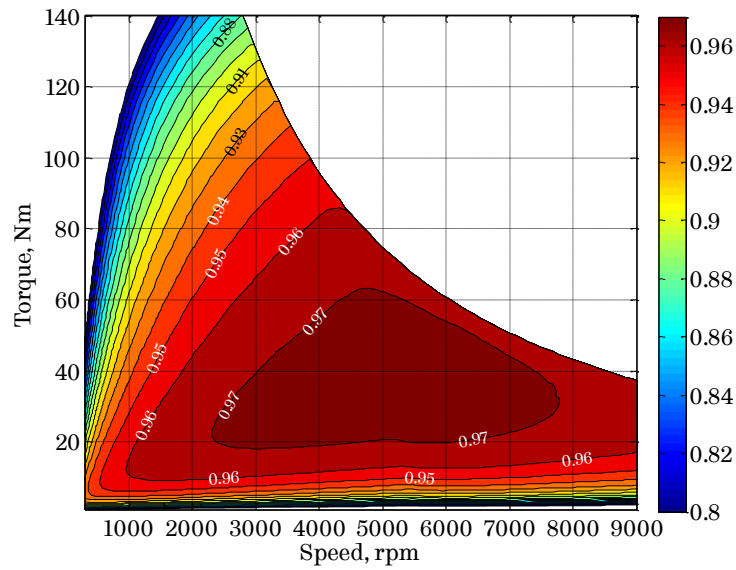


(a) Predicted efficiency map

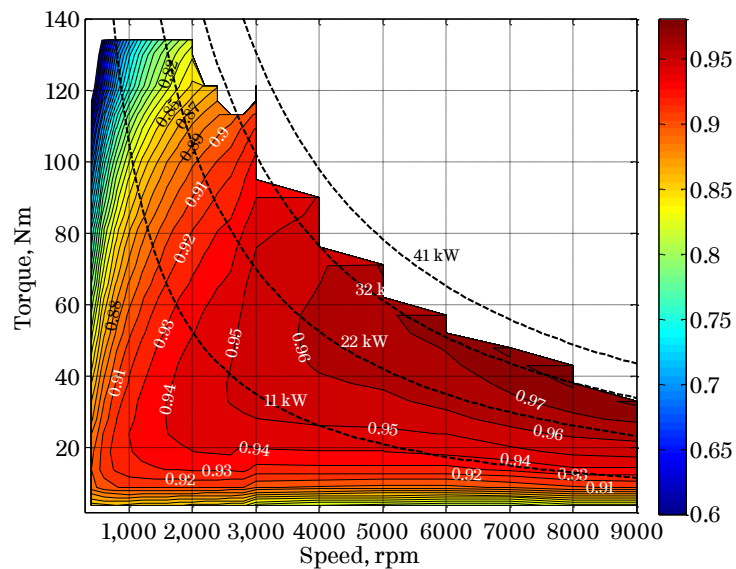


(b) Measured efficiency map

Figure 6.34. Comparison of efficiency map of 2nd prototype motor at 250 V.



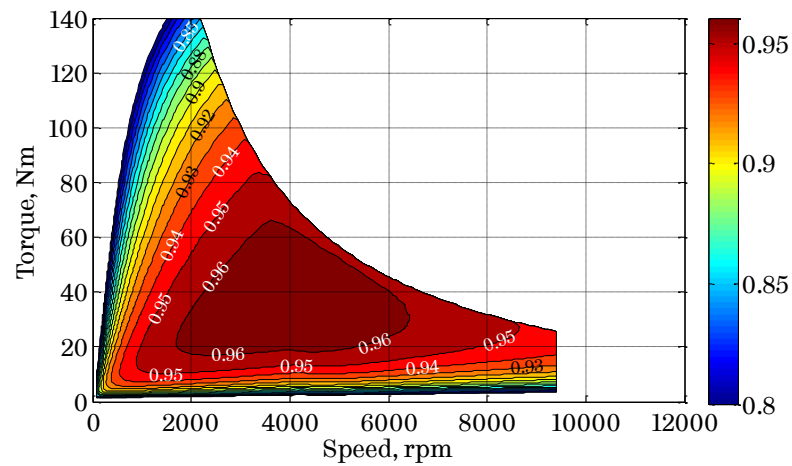
(a) Predicted efficiency map



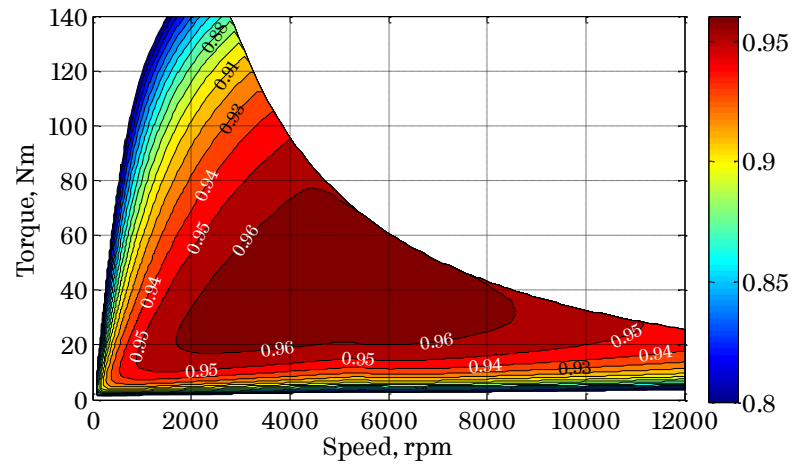
(b) Measured efficiency map

Figure 6.35. Comparison of efficiency map of 2nd prototype motor at 320 V.

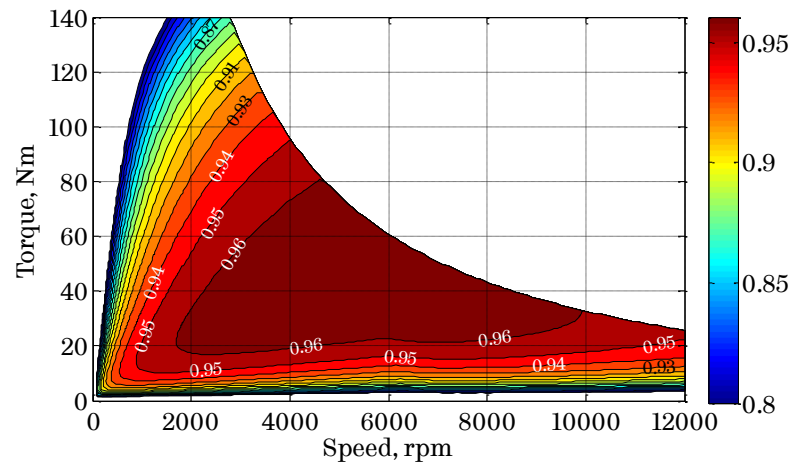
Based on the measured bearing friction and windage loss, the measured iron loss, and the measured efficiency map over discrete points with 250V DC, the computational model for predicting losses over the torque speed envelope is calibrated by adjusting the resistance of the windings, and a build factor to allow for better iron loss prediction. Figure 6.36 (a), (b), and (c) shows the calibrated



(a) Calibrated efficiency map at 250 V



(b) Calibrated efficiency map at 320 V



(c) Calibrated efficiency map at 370 V

Figure 6.36. Comparison of calibrated efficiency map of 2nd prototype motor for different DC link voltages.

efficiency maps of second prototype motor with drive operation at 250 V, 320 V and 370 V respectively. Compared to the predicted efficiency maps, the efficiency of the motor is reduced by ~1% over the torque-speed envelope due to higher losses in the prototype motor. Among these, 2.3% resistance increase accounts for higher copper losses and a build factor of 1.45 accounts for (a) any deterioration of material properties of laminations resulting in to higher iron losses, and (b) bearing friction and windage losses. Also, at higher speeds as the quality of current control in the field-weakening region deteriorates, the reduction in efficiency is more than that at lower speed.

Compared to first prototype, second prototype motor has higher efficiency especially at high speed operations due to lower rotor eddy current losses, as seen from Figure 6.36 (b) and Figure 6.22.

6.8.4 Thermal test

The thermal test on second prototype is conducted at maximum cruise speed of 8600 rpm with continuous torque of 24 N·m, for the drive operation at 250 V. Table 6.22 lists the important observed parameters during the thermal test.

Table 6.22. Important parameters observed during the thermal test

At 250V, 24 N·m, 8600 rpm	Unit	
Cooling water flow rate	10.0	litre/min
Cooling water inlet temperature	20.0	°C
d-axis current (peak)	-36.0	A
q-axis current (peak)	17.3	A
Phase current (peak)	39.9	A
Current angle	64.4	degree
Cooling water temp. at steady-state	24.0	°C
Total time of the thermal test	3:52:56	hh:mm:ss

Based on the observed parameters, the 2-D transient FEA model of second prototype motor is updated to derive the heat generating sources inside the motor. These losses are calibrated based on the measured resistance, the measured no-load iron loss and the measured bearing and friction loss before passing them to Motor-CAD software for thermal analysis. The measured current waveform which

has harmonics up to 30th order due to switching and other noise related issues during testing, is used to perform FEA. Figure 6.37 shows the comparison of the predicted and the measured transient temperatures of second prototype motor at maximum cruise speed operation with 250 V. As seen, the measured temperatures match very well with the predicted temperatures.

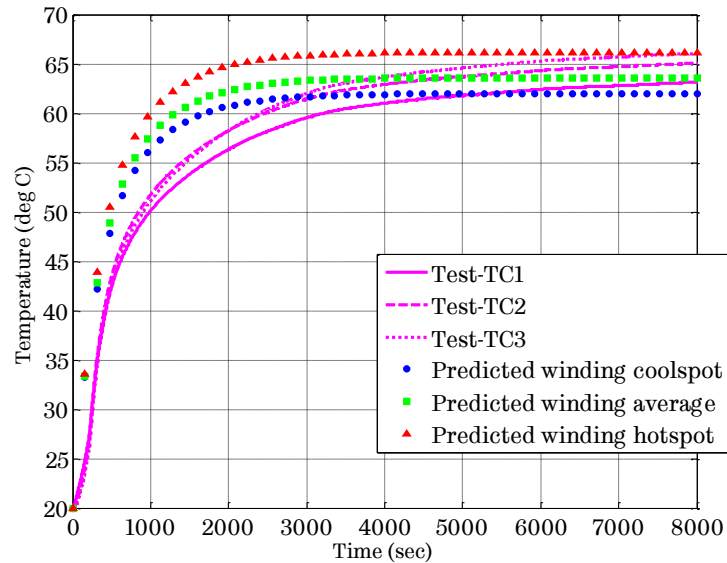


Figure 6.37. Comparison of measured and predicted transient temperatures of 2nd prototype at the maximum cruise speed operation with 250 V.

Due to mechanical limitations, the rotor temperatures are not measured. However, it is possible to estimate the temperature of the magnets at steady-state indirectly by measuring back EMF of the motor at the end of thermal steady-state. The back EMF of second prototype motor is measured after reaching thermal steady-state at the rated power and 5000 rpm by turning off the inverter. The speed is reduced to 5000 rpm in very short time (10 sec), sufficiently low, such that uncontrollable rectifier will not occur when the inverter is switched off.

Figure 6.38 shows the measured back EMF of one 3-phase windings (A-B-C) at the thermal steady-state. The temperature of the rotor or permanent magnet is estimated using (6.10).

$$T_{pm} = 100 \times \frac{\left(\frac{E_{T1}}{E_{T0}} - 1 \right)}{\alpha_{T-PM}} \quad (6.10)$$

where T_{pm} is temperature of the magnet in °C, E_{T0} and E_{T1} are back EMF of the motor at the room temperature and at the thermal steady-state at the same speed respectively in V, and α_{T-PM} is the reversible temperature co-efficient of induction in %/°C, usually described in the date-sheet. The author has used the reversible temperature co-efficient of induction of -0.03157 %/°C, derived from the measurements of the back EMF of second prototype motor at two different temperatures (20°C and 65°C), which is lower than that specified in data-sheet of RECOMA 28 (-0.035 %/°C).

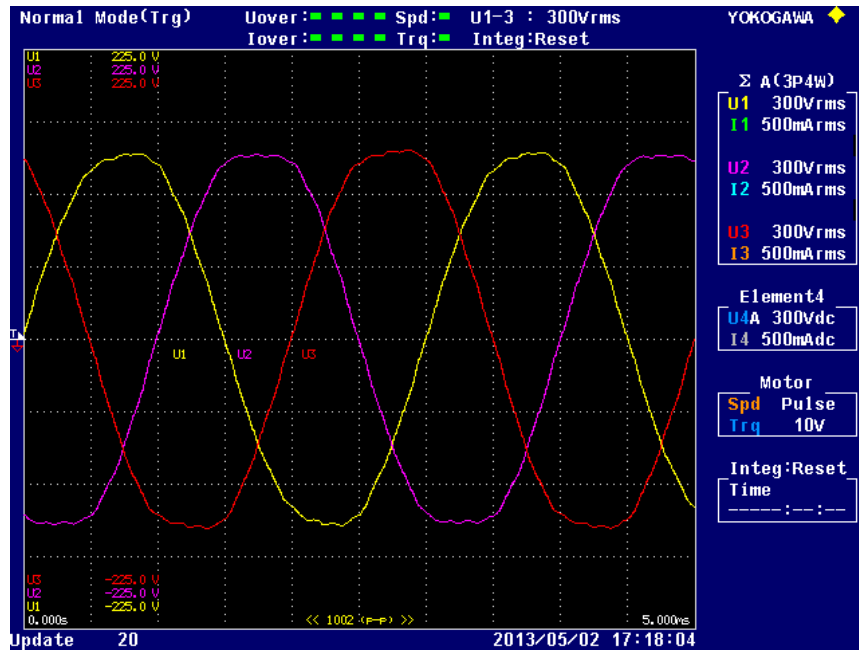


Figure 6.38. Back EMF waveform recorded at 5000 rpm after reaching thermal steady-state for operation at 24 N·m, 8600 rpm.

From the test data, the reduction of back EMF from its value at the room temperature yields the rotor magnet temperature of 81.1°C, which is slightly lower than the predicted temperature of 85.7°C from the calibrated thermal model.

Chapter 7

Design Aspects of Novel Fractional-slot per Pole per Phase (18-slot, 8-pole) Winding Configuration for EV Applications

Important design aspects of the novel fractional-slot per pole per phase winding configuration having 18-slot, 8-pole topology for electric vehicle applications are investigated. These include (a) effect of phase shifts on PM eddy current loss and unbalanced magnetic pull of the machine, (b) demagnetization assessment for fractional-slot PM machines, and (c) thermal analyses over driving cycles.

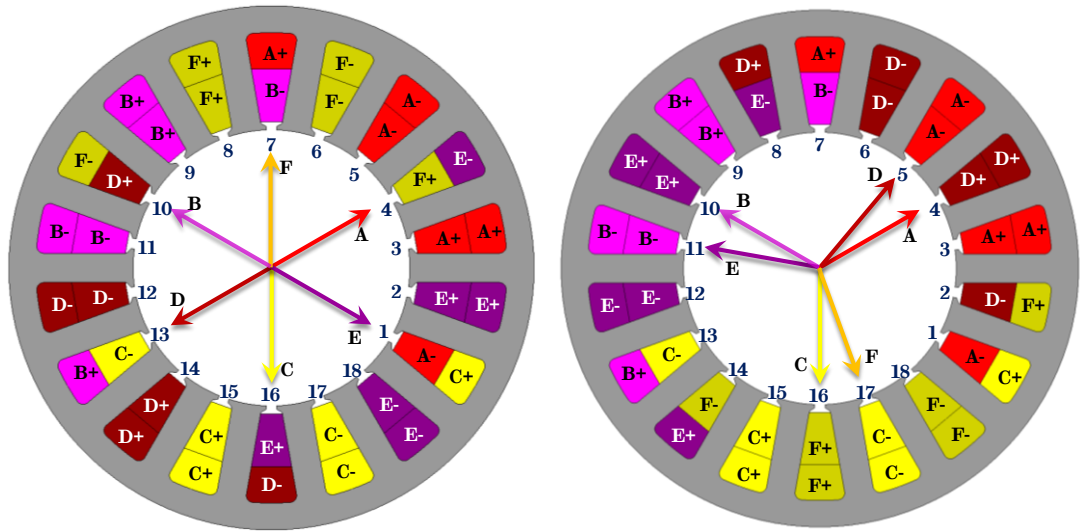
Major content of this chapter is published by the author in [127], [128], and [129].

7.1 Effect of phase shifts on PM eddy current loss and unbalanced magnetic pull

As discussed in the thesis, the author has designed a 6-phase, 18-slot, 8-pole fractional-slot per pole per phase IPM machine [92] targeting the design specifications for a segment-A electric vehicle in order to improve safety and to enhance power drivetrain availability, and to reduce/eliminate the most harmful MMF space harmonics in a simple and cost effective ways [110].

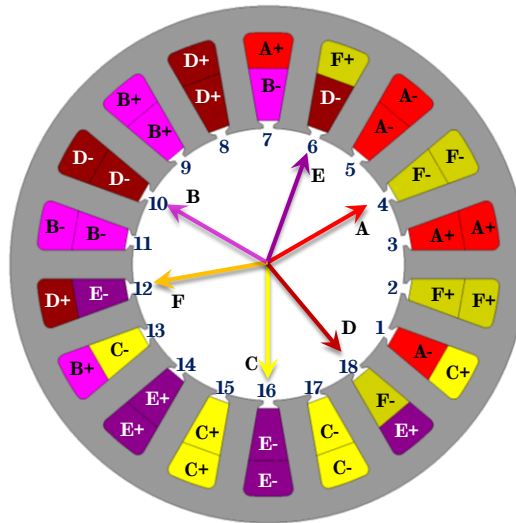
For this winding configuration, the possible phase shifts between two sets of 3-phase windings (A-B-C and D-E-F) are 0° , 20° or 40° [93]. This results into balanced windings irrespective of whether the machine is operated with 6-phases or just one set of 3-phase system. This feature enhances the capability of the winding configuration for traction application as it is fault-tolerant. In the event of fault on

one set of the drive system, the vehicle can continue to operate using the remaining healthy set of 3-phase drive system without any sudden stops or compromising vehicle stability and passenger safety. Figure 7.1 shows all the possible phase shifts for 6-phase, 18-slot, 8-pole winding configuration, which can be achieved by appropriate slot shift between A-B-C and D-E-F windings.



(a) 0° phase shift (3/9/15 slot shift)

(b) 20° phase shift (1/7/13 slot shift)



(c) 40° phase shift (5/11/17 slot shift)

Figure 7.1. Possible phase shifts in 6-phase, 18-slot, 8-pole winding configuration.

The normalized MMF space harmonics distribution for all three phase shifts are compared against one another in Figure 4.15 of Chapter 4. As seen, the 6-phase, 18-slot, 8-pole winding configuration with 0° phase shift eliminates all odd MMF

space harmonics that are present in 9-slot, 8-pole winding configuration, therefore results into much improved performance. The effect of 20° and 40° phase shift is same – both help in reducing the 2nd harmonic by ~50%, however, gives rise to other odd harmonics (1st, 7th, and 11th) that were otherwise not present with 0° phase shift. However, these odd MMF space harmonics are less significant due to their lower frequency (for 1st order), or lower magnitude (for 7th and 11th order).

Table 4.6 in Chapter 4 lists the total harmonic distortion (THD) of all three phase shifts between A-B-C and D-E-F windings. It is evident that the THD of 20° phase shift is 1.6% and 0.6% lower than that of 0° and 40° phase shifts respectively. Lower THD of 20° phase shift will result into comparatively lower rotor iron loss including PM eddy current loss.

7.1.1 2-D transient finite element model and operating conditions under consideration

To predict eddy current loss in the rotor magnets and the unbalanced magnetic force in the air-gap for various phase shifts between A-B-C and D-E-F windings of 6-phase, 18-slot, 8-pole IPM machine, time stepped 2-D transient finite element analysis (FEA) is carried out using commercially available FE package.

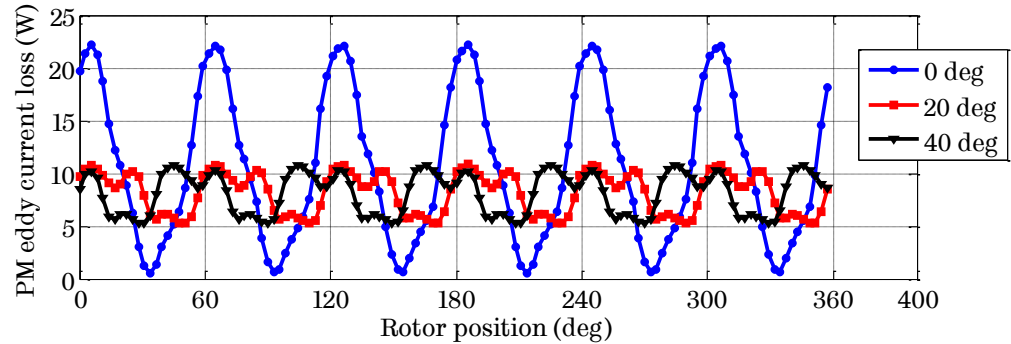
Various operating conditions are considered to evaluate the effect of phase shift on PM eddy current loss and the unbalanced magnetic pull in the air-gap, as listed in Table 7.1.

Table 7.1. Various operating conditions to evaluate the effect of phase shifts on PM eddy current loss

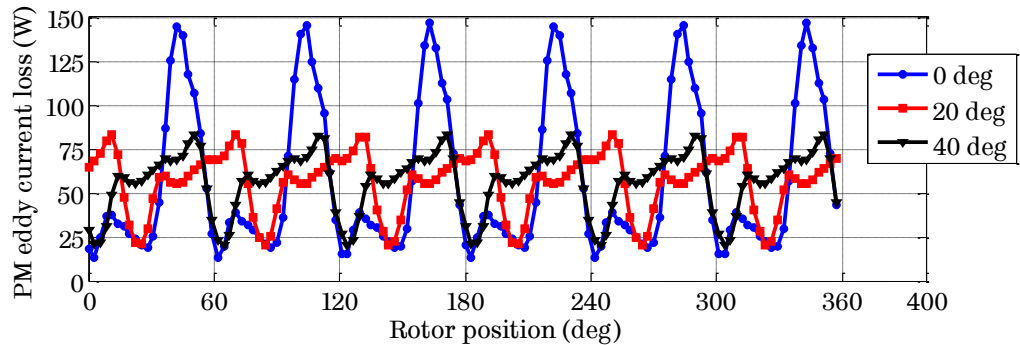
Operating condition	Power (kW)	Torque (N·m)	Speed (rpm)
Rated torque operation	22.0	75.0	2800
Peak torque operation	41.0	140.0	2800
Maximum cruise speed operation	22.0	19.1	11000

7.1.2 Effect of phase shifts on magnet eddy current loss

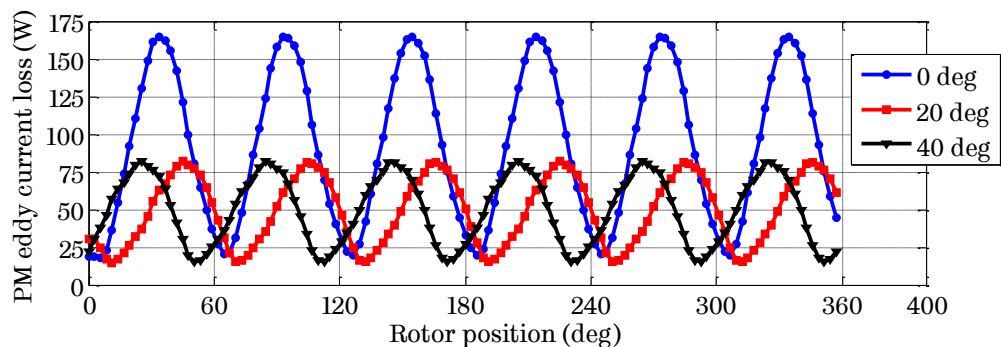
Figure 7.2 shows the variation of eddy current loss in rotor magnets over an electrical cycle at the rated torque, the peak torque, and the maximum cruise speed operations. It is evident that the magnet eddy current loss has very high ripple for 0° phase shift between A-B-C and D-E-F compared to 20° and 40° phase shifts.



(a) Rated torque operation



(b) Peak torque operation



(c) Maximum cruise speed operation

Figure 7.2. Variation of magnet eddy current loss over an electric cycle for various phase shifts between A-B-C and D-E-F windings of 6-phase, 18-slot, 8-pole IPM machine.

Compared to 0° phase shift, ~24% lower magnet eddy current loss is observed for 20° and 40° phase shifts at the rated torque operation. The magnet eddy current loss, predicted by FEA, under various operating conditions, is listed in Table 7.2.

Table 7.2. Magnet eddy current loss for various phase shifts

Phase shift	Rated torque	Peak torque	Max. cruise speed
0°	10.6 W	57.4 W	91.8 W
20°	8.1 W	56.7 W	49.6 W
40°	8.1 W	56.7 W	49.8 W

As will be seen, 20° and 40° phase shift results into ~46% lower magnet eddy current loss compared to 0° phase shift under the maximum cruise speed operation. However, for the peak torque operation, only marginal reduction (~1.2%) is observed for 20° and 40° phase shifts. This may be attributed to highly saturated magnetic circuit of the machine at the peak torque operation.

7.1.2.1 Source of eddy currents

The eddy currents in the rotor magnets are induced by the lower and higher order MMF space harmonics, which rotate at different speeds relative to the rotor. In order to understand, which MMF space harmonics are responsible for a specific magnet eddy current loss harmonic, the maximum cruise speed operation is considered to derive the frequency of eddy current loss harmonics (ECLH) and corresponding skin depth.

Table 7.3 lists the lower and higher order MMF space harmonics (seen from Figure 4.15), their rotating direction with respect to the 4th order working harmonic in this machine, the resultant order of the eddy current loss harmonic, corresponding frequency and skin depth, and its presence in the machine with various phase shifts. For example, the forward (FW) rotating harmonic 19 and the backward (BW) rotating harmonic 11, induce the 15th order eddy current loss harmonic (ECLH) in the rotor magnets at 2750 Hz, and this will only be seen for 20° and 40° phase shifts, not for 0° phase shift. Likewise, other orders of ECLH are derived. The **bold** letters indicate the significant MMF space harmonics, which

create eddy current loss in the magnets. The **red bold** letters are only for 20° and 40° phase shifts. The presence of higher order harmonics, *i.e.*, 8, 16, 17, 20, 25, 26, 28, 29, 34, ..., does not induce significant eddy current loss in the magnets as their magnitudes are much lower.

Table 7.3. Frequencies and skin depth of forward and backward rotating MMF space harmonics at maximum cruise speed operation

MMF harmonic order		Order of ECLH	Freq. of ECLH (Hz)	Skin depth (mm)	Presence in machine with phase shift of		
BW	FW				0°	20°	40°
-	1	3	550	19.3	×	✓	✓
-	7	3	550	19.3	×	✓	✓
2	10	6	1100	13.6	✓	✓	✓
8	16	12	2200	9.6	✓	✓	✓
11	19	15	2750	8.6	×	✓	✓
14	22	18	3300	7.9	✓	✓	✓
17	25	21	3850	7.3	×	✓	✓
20	28	24	4400	6.8	✓	✓	✓
26	34	30	5500	6.1	✓	✓	✓
32	40	36	6600	5.6	✓	✓	✓

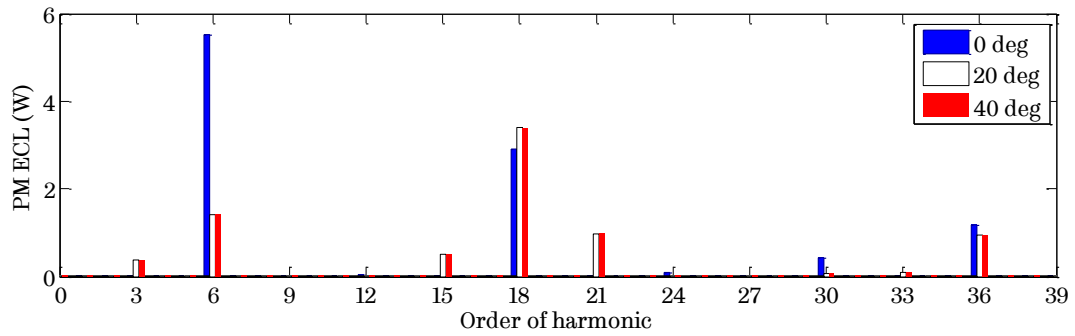
7.1.2.2 Eddy current loss harmonics distribution

In order to understand the difference in magnet eddy current loss for various phase shifts, the current density in each element of the magnet from FEA has been extracted over one mechanical cycle, and then processed in a MATLAB program to decompose the eddy current loss of all elements into the harmonic distribution of eddy current loss (ECLH) using (7.1).

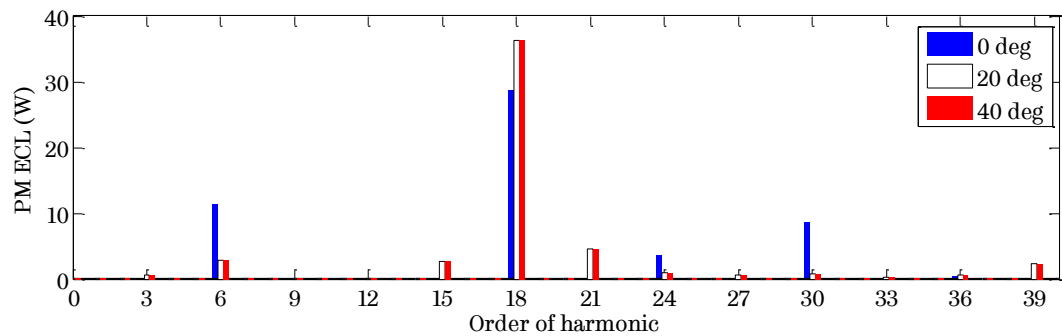
$$ECL = \sum_{i=1}^{2pN_{mp}} P_i(t) = \sum_{i=1}^{2pN_{mp}} \rho \left(\sum_{e=1}^{n_e} (J_e^2(t) A_e) \right) L \quad (7.1)$$

where ECL is total eddy current loss of the machine, p is number of pole pair, N_{mp} is number of magnets per pole, ρ is resistivity of magnet material, J_e and A_e are the current density and the area of an element e respectively, L is the stack length of

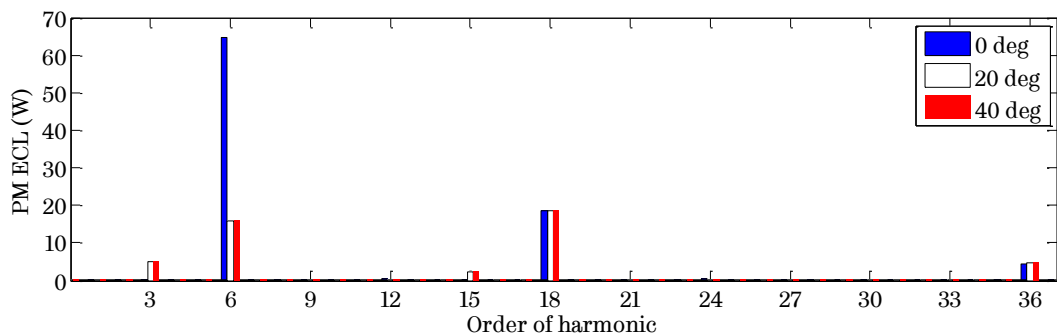
the machine, n_e is the number of elements in i^{th} magnet, and t is the time instant. The harmonic distribution of eddy current loss can then be obtained using Fast Fourier Transform (FFT) on the eddy current loss waveform obtained in (7.1). Figure 7.3 shows the harmonics distribution of magnet eddy current loss at the rated torque, the peak torque, and the maximum cruise speed operation.



(a) Rated torque operation



(b) Peak torque operation



(c) Maximum cruise speed operation

Figure 7.3. Harmonics distribution of magnet eddy current loss for various phase shifts between A-B-C and D-E-F windings of 6-phase, 18-slot, 8-pole IPM machine at different operating conditions.

As will be seen from Figure 7.3, for all the operating conditions, the dominant magnet eddy current loss harmonics are 3, 6, 15, 18, and 36. The 6th order ECLH is a result of BW rotating 2nd order MMF space harmonic and FW rotating 10th order MMF space harmonic. As 2nd order MMF space harmonic is reduced to half for 20° and 40° phase shifts, the resultant 6th order ECLH is reduced by ~75% at all the three operating conditions. However, the introduction of 1st and 7th order MMF space harmonics due to phase shifts introduces 3rd order ECLH albeit has comparatively low magnitude as the relative speed of 1st order MMF space harmonic is half (550 Hz) compared to that of 2nd order MMF space harmonic (1100 Hz). At the peak torque operation, 18th order ECLH is dominant, whereas for other continuous rated operations at all speeds, 6th order ECLH is dominant. This may be attributed to highly saturated magnetic circuit at the peak torque operation. At the peak torque operation, for 20° and 40° phase shifts, 75% reduction in 6th and 24th and ~90% reduction in 30th order eddy current loss harmonic compensates the increase in eddy current loss due to (a) additional harmonics (15th, 21st, 39th), and (b) 35.3% increase in 18th order ECLH, resulting into only marginal reduction (1.2%) in total eddy current loss at the peak torque operation. For continuous torque-speed envelope, the 18th order ECLH and integer multiple of it are unaffected as phase shifts do not affect 14th and 22nd, 32nd and 40th, 50th and 58th, ..., order MMF space harmonics, which arise due to the slot-pole combination (integer multiple of slot number \pm pole pair number).

Table 7.4 shows the comparison of magnet eddy current loss for various phase shifts in second prototype machine having M270-35A and NO20 electrical steel in the stator and the rotor respectively, and Samarium Cobalt (Sm₂Co₁₇) magnets in the rotor. As will be seen from Table 7.2 and Table 7.4, similar reduction in eddy current loss is observed for NdFeB and Sm₂Co₁₇ magnets in the rotor.

Table 7.4. Magnet eddy current loss for various phase shifts in 2nd prototype machine (NO20 electrical steel in rotor and Sm₂Co₁₇ magnets)

Phase shift	Rated torque	Peak torque	Max. cruise speed
0°	22.4 W	117.9 W	171.7 W
20°	17.7 W	116.4 W	85.6 W
40°	17.8 W	116.5 W	86.2 W

The eddy current loss in $\text{Sm}_2\text{Co}_{17}$ magnets is approximately doubled as the resistivity of $\text{Sm}_2\text{Co}_{17}$ magnets is half compared to NdFeB magnets.

7.1.3 Effect of phase shifts on unbalanced magnetic pull

Although the novel winding configuration proposed in this thesis (6-phase, 18-slot, 8-pole) with 0° phase shift between A-B-C and D-E-F completely eliminates the unbalanced magnetic pull present in 9-slot, 8-pole machine topology, as explained in Chapter 4 [92], the other two phase shift options (20° and 40°) between A-B-C and D-E-F windings give rise to odd harmonics, which may lead to unbalanced magnetic force.

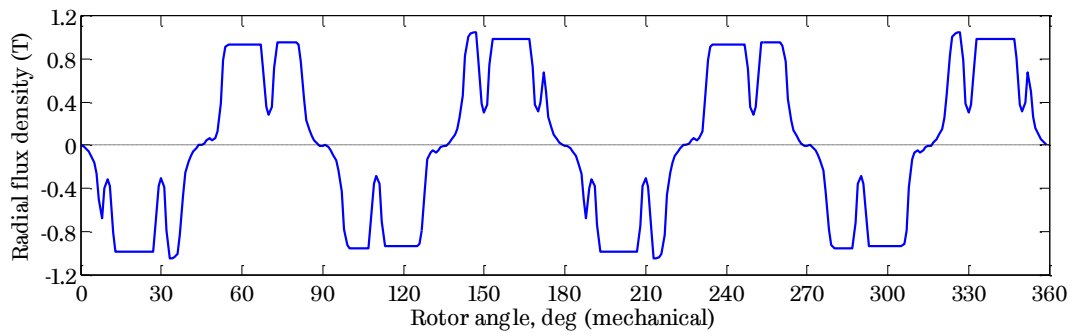
The radial force density distribution on the inner surface of the stator, i.e. stator bore, is the main cause for electromagnetically induced noise and vibrations [130]. It results from no-load as well as on-load magnetic fields in the air-gap. The radial force density can be evaluated by Maxwell stress tensor method, as shown in (7.2).

$$F_{rd}(\theta_r, t) = \frac{1}{2\mu_0} [B_r^2(\theta_r, t) - B_t^2(\theta_r, t)] \quad (7.2)$$

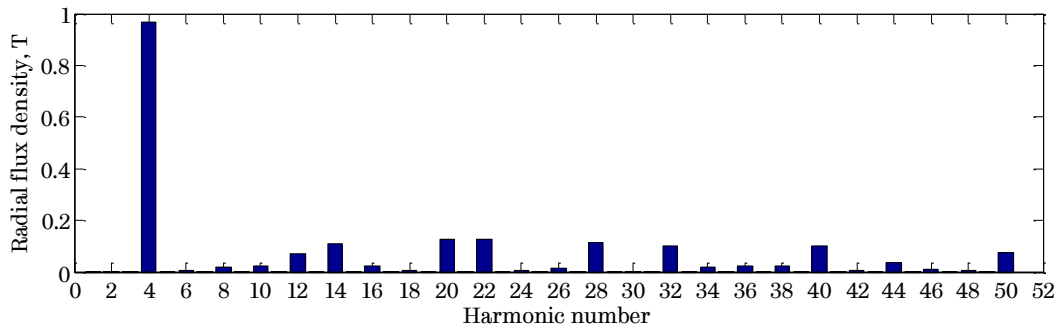
where F_{rd} is radial force density in N/m^2 , B_r and B_t are radial and tangential (or circumferential) flux density in the air-gap respectively, θ_r is the rotor position, and t is the time instant.

7.1.3.1 Radial force density distribution in the air-gap at no-load

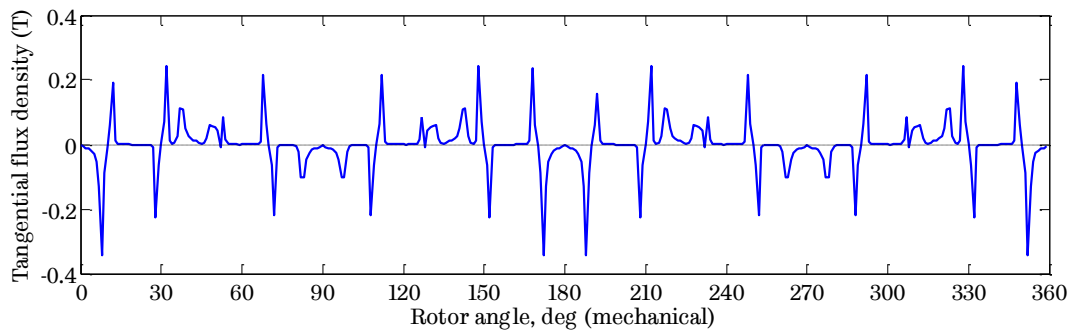
In order to evaluate the radial force density (RFD) for various phase shifts between A-B-C and D-E-F windings, the radial and tangential flux density in the air-gap of the machine at no-load and the rated torque operation, from 2-D transient FEA, are analysed. Figure 7.4 shows the radial and tangential flux density in the air-gap at no-load and corresponding harmonics distribution, at time $t = 0$. As expected, the working harmonic, i.e., 4th order, is dominant in this machine. It is to be noted that phase shifts will not affect the no-load flux density distributions. Using (7.2), the radial force density in the air-gap at no-load is evaluated and is shown in Figure 7.5.



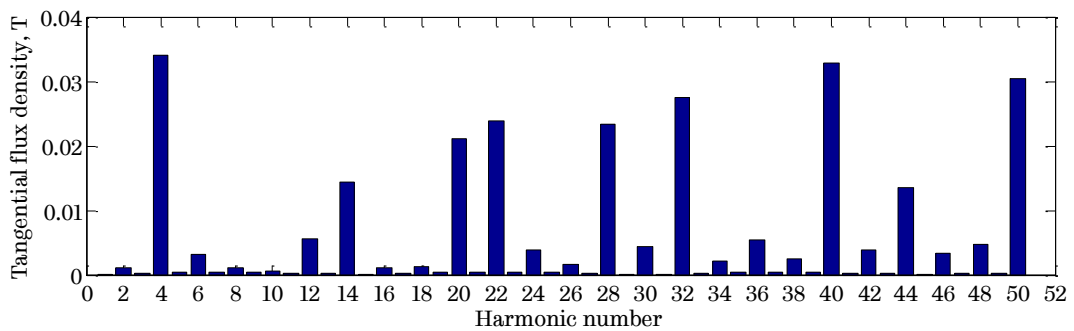
(a) Radial flux density in the air-gap, no-load



(b) Harmonics distribution of radial flux density

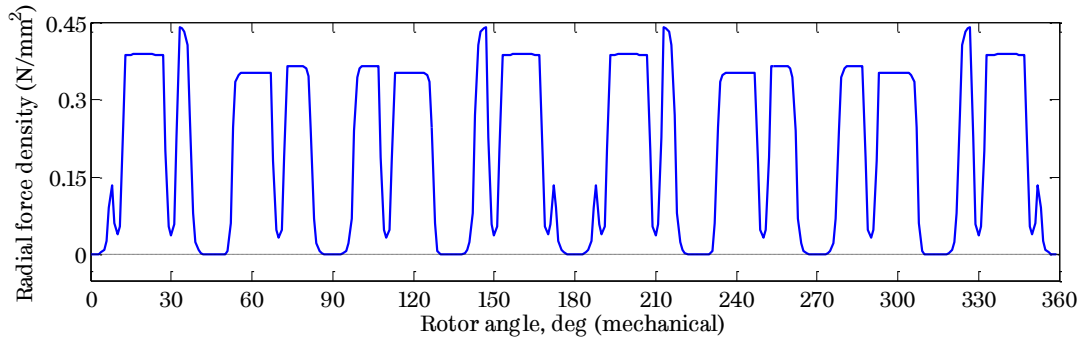
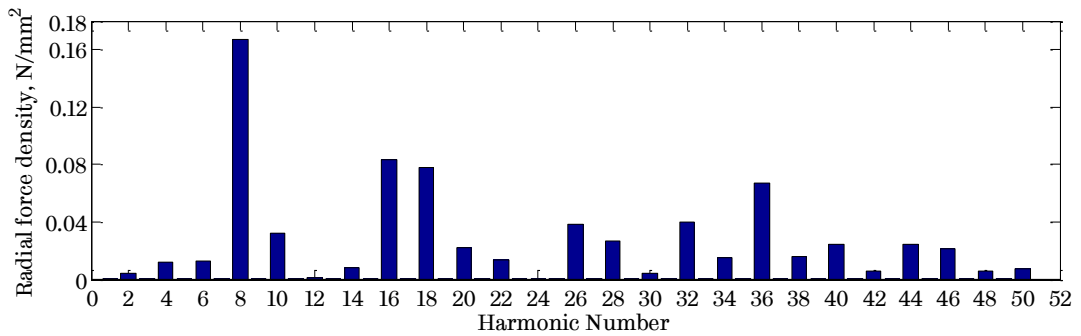


(c) Tangential flux density in the air-gap, no-load



(d) Harmonics distribution of tangential flux density

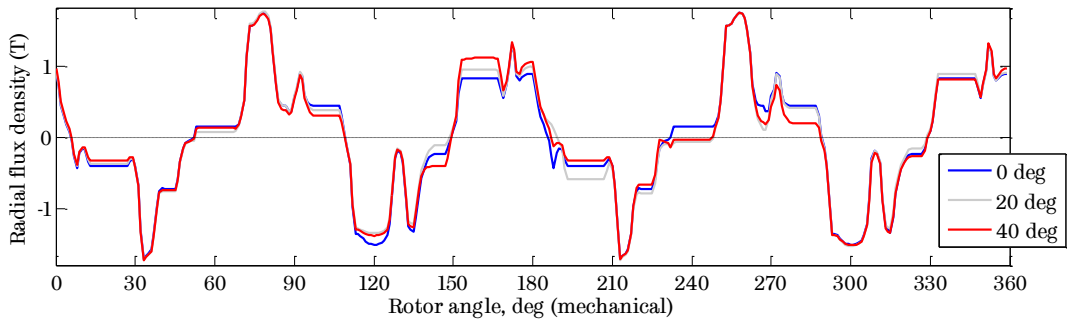
Figure 7.4. Radial and tangential flux density in the air-gap at no-load.

(a) Radial force density in the air-gap, no-load, $t = 0$ (b) Harmonics distribution of radial force density, no-load, $t = 0$ *Figure 7.5. Radial force density in the air-gap at no-load, $t = 0$.*

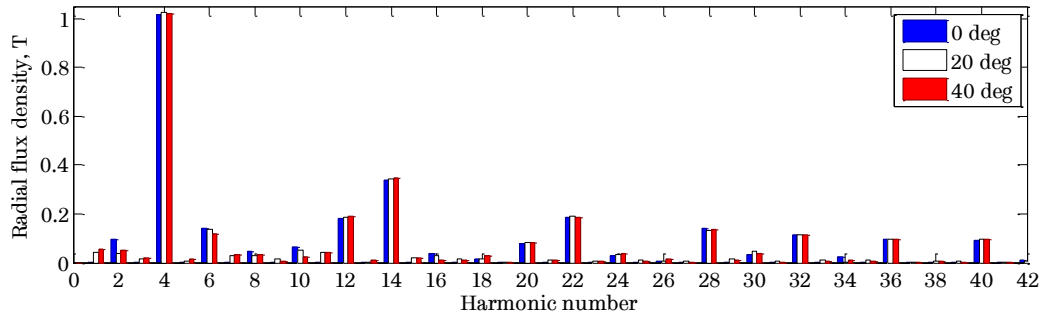
As seen from Figure 7.5, the RFD harmonics under no-load due to permanent magnet field and slotting effect contain harmonics of order that are integer multiple of 2, the dominant harmonics being integer multiple of $2p$. In addition to the harmonics due to slotting, other even order harmonics with low magnitude (2, 4, 6, 10, 20, ...) may be attributed to saturated bridges in the IPM machine.

7.1.3.2 Radial force density distribution in the air-gap at rated load

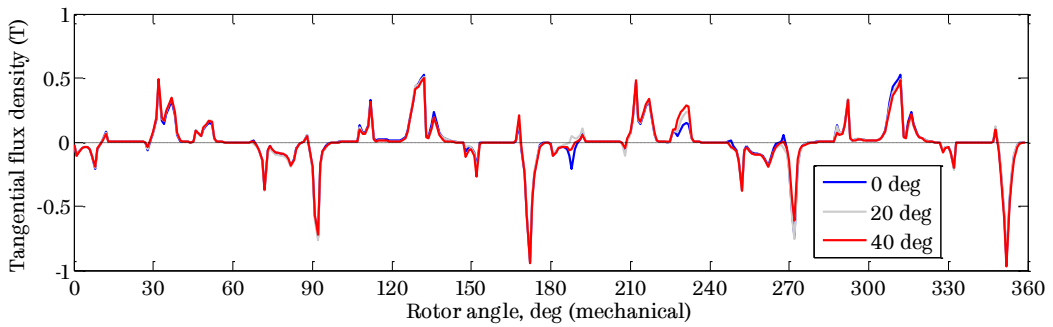
Similarly, the radial and the tangential flux density at the rated torque operation is also extracted from 2-D FEA for various phase shifts, and are shown in Figure 7.6. As will be seen, the 4th order harmonic is dominant for all the three phase shifts, as expected. At the rated torque operation, the tangential flux density is higher than that at no-load, but lower than the radial flux density for all the three phase shifts. Using (7.2), the radial force density in the air-gap at no-load is evaluated and is shown in Figure 7.7.



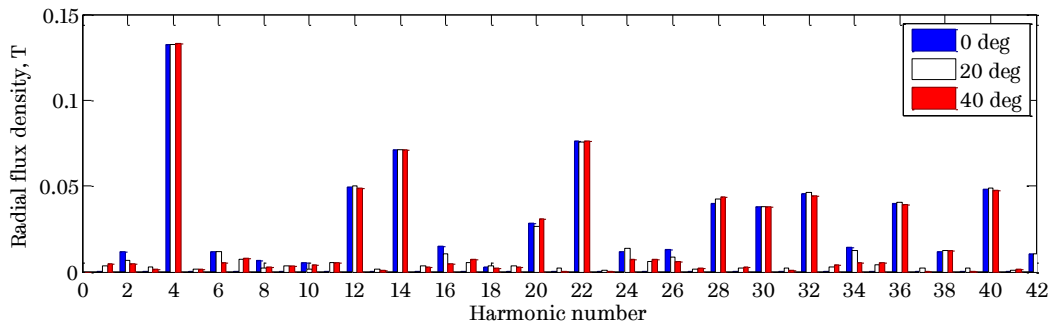
(a) Radial flux density in the air-gap, rated torque operation



(b) Harmonics distribution of radial flux density



(c) Tangential flux density in the air-gap, rated torque operation



(d) Harmonics distribution of tangential flux density

Figure 7.6. Radial and tangential flux density in the air-gap at the rated torque operation for various phase shifts between A-B-C and D-E-F windings.

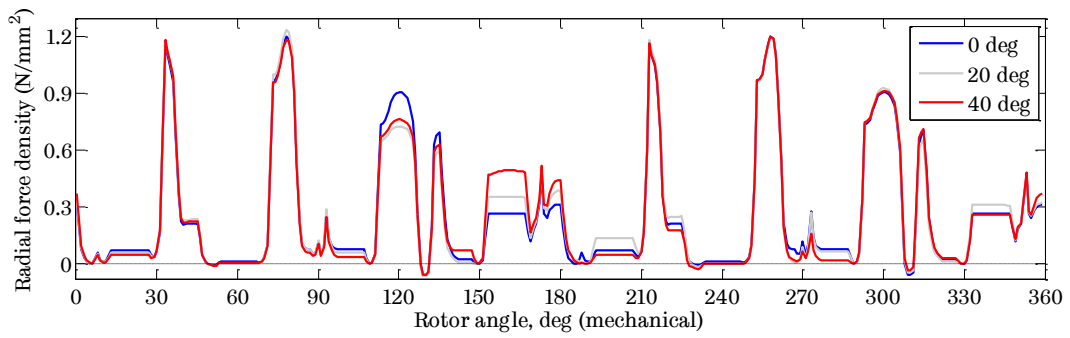
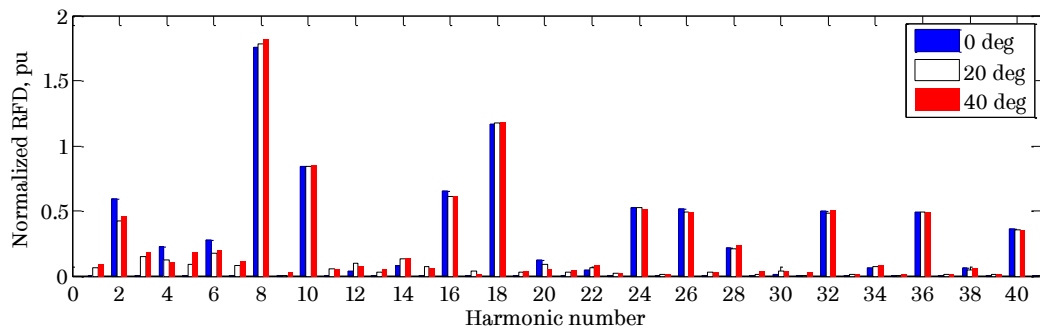
(a) Radial force density in the air-gap, rated load, $t = 0$ (b) Normalized harmonics distribution of RFD, rated load, $t = 0$ *Figure 7.7. Radial force density in the air-gap at the rated torque, $t = 0$.*

Figure 7.7 (b) shows the normalized harmonics distribution of RFD at the rated torque operation with respect to the magnitude of the 8th RFD harmonic at no-load operation. The space harmonics distribution of the radial force density at the rated torque operation for various phase shifts results from the combined effect of permanent magnet and armature reaction fields. The RFD with 0° phase shift contains only even order harmonics while those with the other two phase shifts include odd harmonics which result predominantly from the odd MMF space harmonics in the armature reaction field as shown in Figure 4.15.

It is worthwhile to note that the RFD of 6-phase, 18-slot, 8-pole machine, with all the 3 phase shifts, contains a relatively large 2nd order space harmonic, which results from the interaction of 4th order PM working harmonic field with 2nd order armature reaction harmonic. However, this 2nd order RFD harmonic is reduced by 29% and 23% for 20° and 40° phase shifts respectively, compared to that for 0° phase shift. Consequently, the amplitude of mode 2 vibrations, which is proportional to the magnitude of the 2nd order RFD harmonic, is reduced. It is very important to

note that the vibration amplitude is inversely proportional to the 4th power of the RFD harmonic order and hence the low modes of vibrations can be more critical [130].

7.1.3.3 Unbalanced magnetic pull

The presence of 1st order RFD harmonic with 20° and 40° phase shifts in 6-phase, 18-slot, 8-pole IPM machine gives rise to unbalanced magnetic pull in the machine. The resultant unbalanced magnetic pull for all 3 phase shifts, under the rated torque operation, is shown in Figure 7.8. It also shows the unbalanced magnetic pull of the 3-phase, 9-slot, 8-pole IPM machine, which is designed for the same specifications with the same volumetric and thermal constraints as the 6-phase, 18-slot, 8-pole IPM machine, which are listed in Table 5.4.

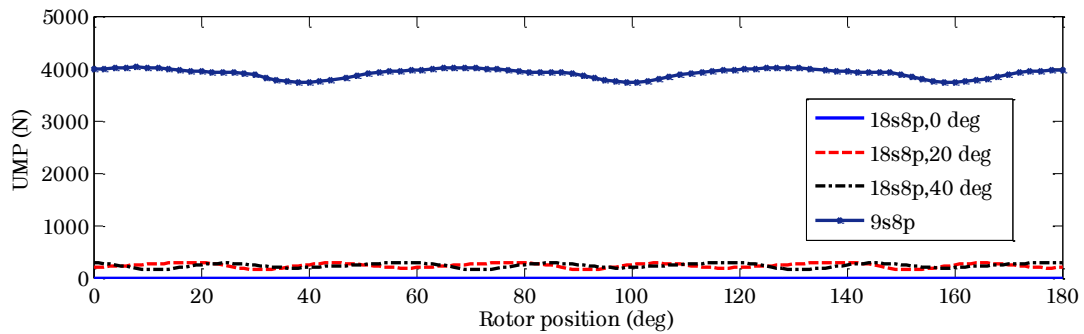


Figure 7.8. Comparison of unbalanced magnetic pull for various phase shifts in 6-phase, 18-slot, 8-pole IPM machine and 3-phase, 9-slot, 8-pole IPM machine, under the rated torque operation.

As will be seen from Figure 7.8, both 20° and 40° phase shifts result into an average unbalanced magnetic pull (UMP) of 236.8 N, which is more than an order of magnitude lower than that of 9-slot, 8-pole machine (3923 N). For 0° phase shift, the unbalanced magnetic pull is zero. This offers design engineer a trade-off between (a) improved performance with 20°/40° phase shifts having an inherent 236.8 N UMP, which may require frequent bearing replacement, and (b) 0° phase shift with no UMP but higher rotor iron loss including magnet eddy current loss.

7.1.4 Summary

The effect of the possible phase shifts, 0°/20°/40°, between two sets of 3-phase windings, on magnet eddy current loss and unbalanced magnetic pull in 6-

phase fractional-slot PM machines with low space harmonics has been analysed. It has been shown that both 20° and 40° phase shifts reduce the 2nd order MMF space harmonic in the armature reaction field. This is conducive to reduction of the rotor eddy current loss in the magnets and amplitude of mode 2 vibrations. However, they give rise to odd MMF space harmonics and consequently unbalanced magnetic pull, albeit their magnitudes are very small.

7.2 Demagnetization assessment of 6-phase fractional-slot PM machines under various fault conditions

As discussed before, fractional-slot winding produces a large number of lower and higher order MMF space harmonics [17], which penetrates deep inside the rotor and increases the risk of demagnetization.

One of the essential requirements for PM brushless machines in traction applications is their capability to operate in field-weakening regions of the torque-speed envelope [131]. Because of presence of MMF space harmonics flux deep inside the rotor and higher d -axis current to control the air-gap flux at high speeds, the magnets may be vulnerable to partial irreversible demagnetization even in Interior Permanent Magnet (IPM) machines. Hence, it is essential to have an adequate demagnetization withstand capability at the maximum operating temperature and during field weakening operation at high speeds for PM brushless machines. To ensure reliability and safety, it is required that risk of partial irreversible demagnetization of the magnets is comprehensively assessed under the worst operating conditions [103].

An analytic technique to assess the risk of partial demagnetization for tubular PM machine by superposing the fields in the magnets, which is validated by FEA, is described in [103]. Various analytical demagnetization models are employed to estimate post-demagnetization performance of an overloaded surface mounted PM (SPM) synchronous machine with distributed windings in [132]. A linear demagnetization model considering temperature dependency is used in FEA for Toyota Prius IPM motor with distributed windings in [133]. Demagnetization assessment for various IPM rotor types is carried out using average flux density

distribution in different PM segments per pole over an electric cycle in [134] at various load angles. However, the approach does not take into account the direction of flux density with respect to the direction of magnetization, hence leading to inaccurate assessment for partial demagnetization. Demagnetization analysis under short-circuit faults is reported in [135] using the quotient between minimum flux density along the PM surface and the remanence flux density of PMs. The dynamic response of distributed wound IPM machine drive under various fault conditions and resulting demagnetization effect is analysed in [136] using the remanence ratio defined as % decrease in remanent flux density using post-fault and pre-fault remanent flux density of PMs. The demagnetization characteristics of IPM machines with distributed winding configuration during fault conditions are investigated in [137] using the flux density vector plots at multiple time instants during the short circuit fault transient derived from predicted d - q axis currents through machine model.

Majority of publications in the literature deals with demagnetization assessment for PM machines with distributed windings over one pole-pair magnets. Also, almost all of them use magnet flux density in variety of concepts to assess demagnetization, which are debatable with respect to accuracy of partial irreversible demagnetization. Comprehensive demagnetization assessment of PM brushless machines employing fractional-slot per pole per phase winding configuration has not been reported. Also, for fractional-slot windings, demagnetization assessment involving only one pole-pair magnets is not sufficient due to presence of low order MMF space harmonics.

The risk of partial irreversible demagnetization for the 6-phase, 18-slot, 8-pole fractional-slot IPM machine under short circuit faults at different speeds and load conditions using 2-D transient FEA is comprehensively assessed by the author in this section. Also, the comparison of irreversible partial demagnetization between fractional-slot (6-phase, 18-slot, 8-pole) and distributed wound (6-phase, 48-slot, 8-pole) IPM machine, both designed for the same specifications under the same volumetric and thermal constraints is presented. The results provide useful insight for selecting winding configurations for applications requiring stringent demagnetization capabilities.

7.2.1 Demagnetization analysis of 6-phase, 18-slot, 8-pole IPM machine

The cross-section of 6-phase, 18-slot, 8-pole IPM machine, designed and optimized for segment-A electric vehicle, is again shown in Figure 7.9 for illustration. Each phase of stator winding consists of three series connected coils wired around adjacent teeth with the polarity as indicated by '+' and '-', and phases are denoted as A, B, C, D, E, and F. The magnets are shown in red and green as indicated by M_iP_j , where $i = 1, 2$ denotes the i^{th} magnet of the j^{th} rotor pole ($j = 1$ to 8).

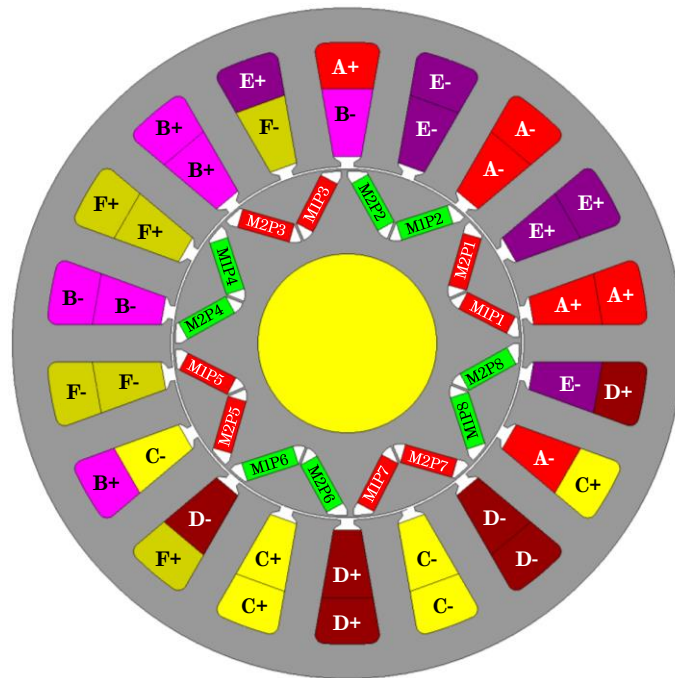


Figure 7.9. Cross-section of 6-phase, 18-slot, 8-pole IPM machine.

7.2.1.1 2-D transient FEA model

The 2-D transient FEA of the machine is carried out using the commercial FEA software, FLUX ver. 11.1.2, released by CEDRAT, France. Appendix G shows the demagnetization curves of the N35EH for various operating temperatures, provided by the magnet supplier [125]. For demagnetization analysis, the operating temperature of 180°C is considered. It is evident, if the flux density in the direction of magnetization reduces to less than ~0.3 T, partial irreversible demagnetization will result. For 2-D transient FEA, the current sources are connected in parallel

with switches, as shown in Figure 7.10, which can be turned on at a specific rotor position with regard to the line voltage at zero or at peak when a short circuit fault occurs.

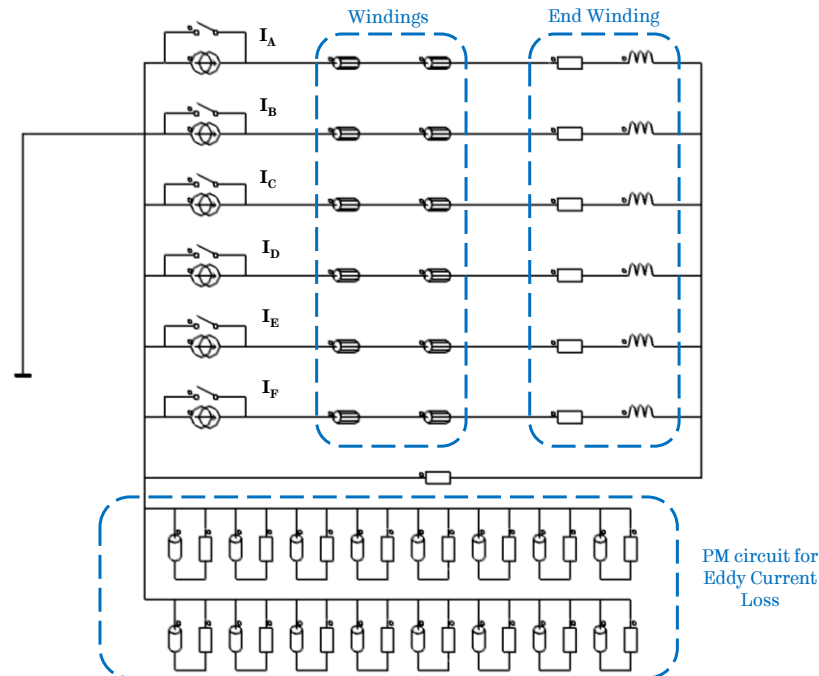


Figure 7.10. Circuit model for creating short circuit in 2-D transient FEA.

7.2.1.2 Fault conditions for demagnetization assessment

Various fault conditions can be considered for demagnetization assessment. However, the author has focused on the fault conditions, listed in Table 7.5, which are most critical with respect to partial irreversible demagnetization.

Table 7.5. Various fault conditions for demagnetization assessment

	Fault	Pre-fault operation	Torque	Speed
F1	6-phase short circuit	Rated torque	75 N·m	2800 rpm
F2	6-phase short circuit	Peak torque	140 N·m	2800 rpm
F3	3-phase short circuit	Rated torque	75 N·m	2800 rpm
F4	3-phase short circuit	Peak torque	140 N·m	2800 rpm
F5	6-phase short circuit	Rated power	19.1 N·m	11000 rpm
F6	6-phase short circuit	Peak power	27.8 N·m	11000 rpm

7.2.1.3 Proposed approach for accurate assessment of demagnetization

As discussed before, most of the published literature takes into account the magnitude of flux density in magnet (before and/or after the fault condition) to assess partial irreversible demagnetization without considering the direction of flux density. To assess partial irreversible demagnetization in PM machines more accurately, it is necessary to decompose the flux density in each node of the magnets into two components (1) along the magnetizing direction, and (2) perpendicular to the magnetizing direction. Figure 7.11 illustrates the decomposition of nodal flux density of M1P1 and M2P1 along the magnetizing direction as below:

$$\begin{aligned} B_{PXn} &= B_{Xn} \cos \theta_n + B_{Yn} \sin \theta_n \\ B_{PYn} &= -B_{Xn} \sin \theta_n + B_{Yn} \cos \theta_n \end{aligned} \quad (7.3)$$

where n is node number, B_{PXn} and B_{PYn} are nodal flux density component in the direction of magnetization defined by an angle θ_n and perpendicular to it respectively, B_{Xn} and B_{Yn} are flux density component in X- and Y-direction respectively.

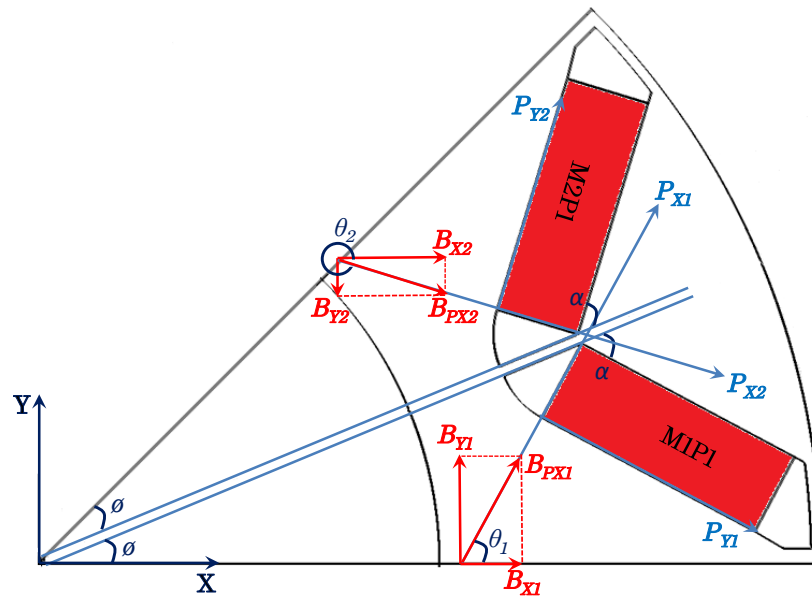


Figure 7.11. Decomposition of nodal flux density of a magnet in the direction of magnetization.

Table 7.6 lists the general formulation for θ_n , where ϕ and α are calculated from the geometry, P_j is the pole number under consideration, and P is number of poles in a machine. To prevent partial irreversible demagnetization at a given node in a magnet, the flux density in the direction of magnetization (B_{PXn}) must be greater than 0.3 T.

Table 7.6. Decomposition angle for various magnets

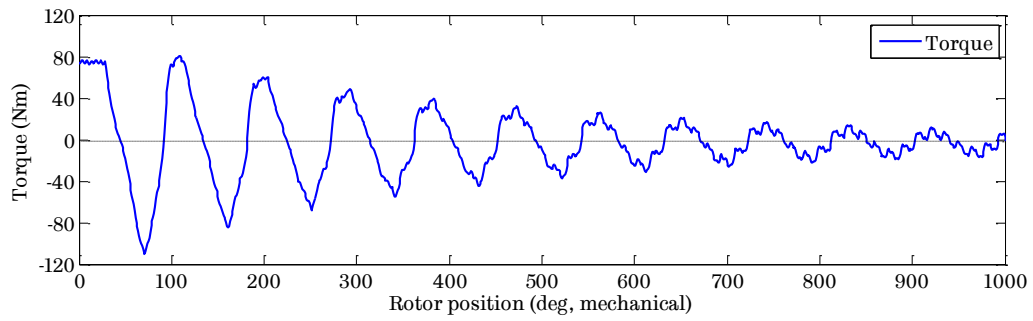
Magnet (M_i)	Pole (P_j)	Angle between XY and P_xP_y (θ_n)
1	1, 3, 5, 7	$90 + \phi - \alpha + \theta_r + (P_j - 1) * (360/P)$
2	1, 3, 5, 7	$90 + \phi - \alpha + \theta_r + (P_j - 1) * (360/P) + 180$
1	2, 4, 6, 8	$90 + \phi - \alpha + \theta_r + (P_j - 1) * (360/P) + 180$
2	2, 4, 6, 8	$90 + \phi - \alpha + \theta_r + (P_j - 1) * (360/P)$

7.2.1.4 Transient response of the motor during faults

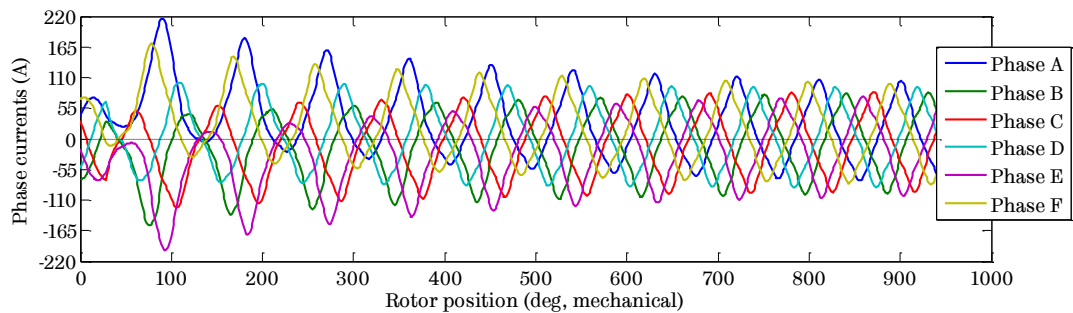
The 2-D transient FEA is carried out at the pre-fault operating conditions listed in Table 7.5 and transient behaviour of the machine is observed as shown in Figure 7.12 under fault condition F1 with pre-fault operation at the rated torque. It shows the torque, phase currents, and d - q axis currents during transient. As will be seen, the peak demagnetizing current occurs at rotor position 86° mechanical. Similar transients are observed for various fault conditions under consideration. Table 7.7 summarizes the peak demagnetizing currents (d - and q -axis current), maximum generating torque during the transient, and number of electrical cycles to reach steady-state for all the fault conditions.

Table 7.7. Comparison of peak transient torque and currents for various fault conditions

	F1	F2	F3	F4	F5	F6
Maximum generating torque (N·m)	-110.4	-132.3	-25.3	-11.0	-44.3	-46.4
Maximum phase current (A)	215.6	245.8	201.6	225.5	134.5	136.1
Maximum d -axis current (A)	-193.7	-227.3	-201.6	-254.7	-122.3	-120.3
Corresponding q -axis current (A)	-15.4	-8.7	-7.2	-56.8	-2.6	5.5
Maximum peak current (A)	194.3	227.5	201.7	261.8	122.3	120.5
No. of cycles to reach steady-state	24	24	24	24	64	64



(a) Torque during transient



(b) Phase currents during transient

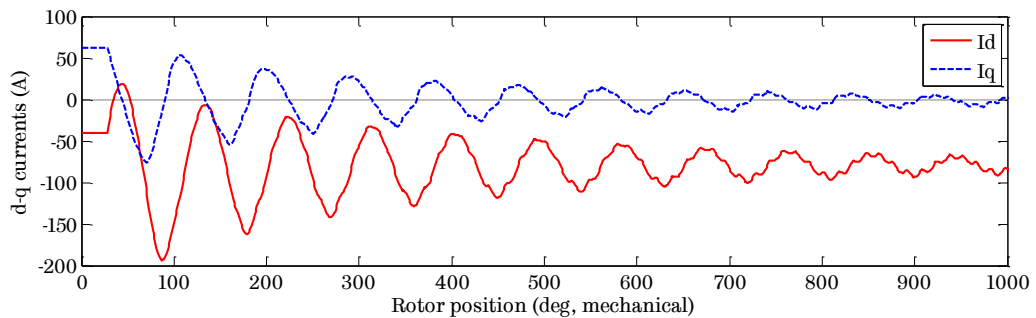
(c) d - q axis currents during transient

Figure 7.12. Transient response of 6-phase, 18-slot, 8-pole IPM machine under short circuit fault at the rated torque operation.

For better insight on the d - and q -axis current behaviour during the various faults (F1, F2, ..., F6), Figure 7.13 plots the current trajectory in the d - q axes plane for all the fault conditions mentioned in Table 7.5. As seen, the short circuit is applied at the pre-fault operating condition for all cases of motoring operation at the base speed (Figure 7.13 (a-d)) and at the maximum cruise speed operation (Figure 7.13 (e-f)). As the fault transient progresses, the trajectory of d - q axis currents pass through the peak demagnetizing current, identified by an arrow. The steady-state short circuit current is marked as star. It is observed from the FEA

that transient response of the machine does not change with respect to the instant of short circuit (*i.e.*, at $V_{line-line} = 0$ or $V_{line-line} = \text{peak value}$) since the initial condition for the post-fault transient is given by the d - and q -axis currents which are assumed to be constant prior to the fault injection, and the peak d -axis current coincides with peak demagnetizing current.

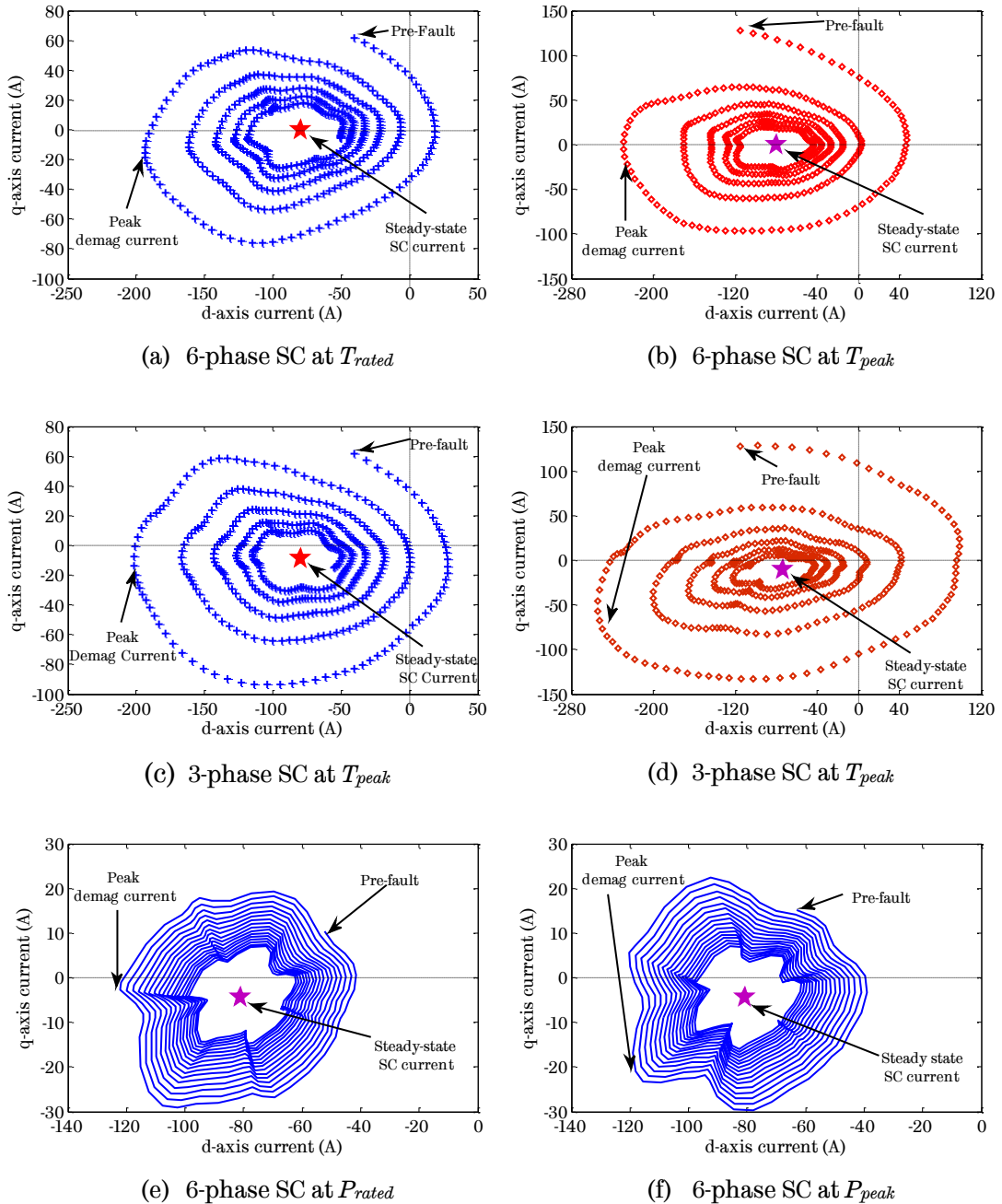


Figure 7.13. Current trajectories of 6-phase, 18-slot, 8-pole IPM machine under short circuit fault at various pre-fault operating conditions ($F1, F2, \dots, F6$).

From the summary of maximum torque, maximum motor currents, and time taken to reach steady-state in Table 7.7, and from the comparison of current trajectories of Figure 7.13, the following observations can be made:

- 1) The peak demagnetizing current of the machine coincides with the peak d -axis current for all the fault conditions.
- 2) With an increase in pre-fault operating current, the peak demagnetizing current during transient also increases.
- 3) The 3-phase short circuit fault results into higher peak demagnetizing current compared to the 6-phase symmetrical short circuit fault.
- 4) With increase in pre-fault operating speed, the fault current transient takes much longer time to reach steady-state and hence poses serious risk of partial irreversible demagnetization for the same pre-fault operating current, as it passes through higher d -axis current with relatively lower q -axis current many times.
- 5) Among all fault conditions, F2 with pre-fault operation at the peak torque and the base speed is worst with respect to demagnetization.

7.2.1.5 Demagnetization assessment using nodal flux density of PM

The results of 2-D FEA are post-processed to plot the flux density along the magnetizing direction at each node in each permanent magnet of the 6-phase, 18-slot, 8-pole IPM machine. There are 247 nodes in each magnet as shown in Figure 7.14.

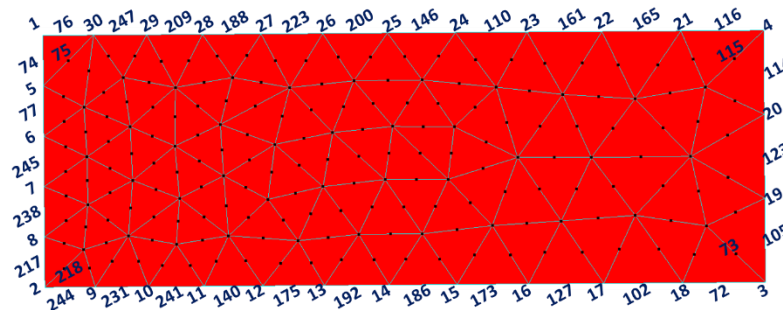


Figure 7.14. Nodes of 1st magnet of 1st pole (MPI1).

The nodes which have flux density along the magnetizing direction below 0.3 T are plotted to assess the risk of partial irreversible demagnetization. Figure 7.15 shows the flux density in the magnetizing direction in MIP1 (1st magnet of pole 1) and MIP6 (1st magnet of pole 6) during 6-phase short circuit transient at 2800 rpm and the rated torque. It is seen that different poles have different demagnetization levels (for 1st node, -0.55 T in MIP1 versus -0.75 T in MIP6). The black horizontal line is drawn at 0.3 T to determine which nodes are demagnetizing during the transient.

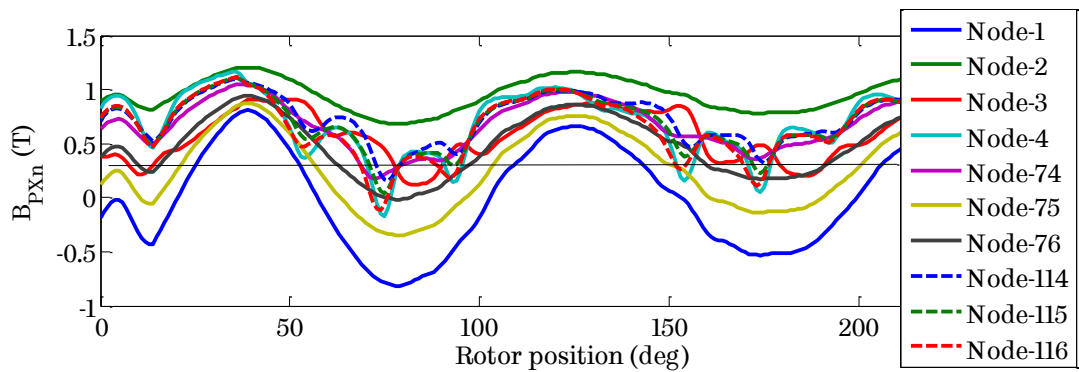
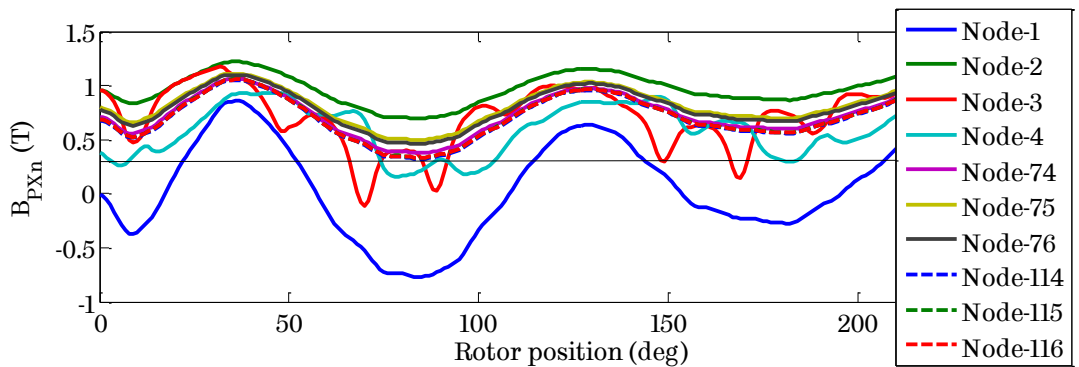
(a) Demagnetization in 1st PM of pole 1(b) Demagnetization in 1st PM of pole 6

Figure 7.15. Demagnetization in different poles during 6-phase SC at T_{rated} .

As seen from Figure 7.15, the nodes 1, 3, and 4 are affected mostly with demagnetizing currents during transient, and have negative flux density along the magnetizing direction, leading to irreversible demagnetization. It is to be noted that node 1 is demagnetized even during the normal operation as it is located at the V-bridge of the IPM rotor which is highly saturated. It is also observed that the different nodes demagnetize (when $B_{PNx} \leq 0.3$ T) at different rotor position, which may be attributed to MMF space harmonics rotating at different speeds and having

different penetration depth inside the rotor. Hence, for fractional-slot PM machines, to assess the demagnetization, one has to consider the whole transient period starting from the instant of short circuit till the machine transient currents reach steady-state as only one time instant is not sufficient.

For all the fault conditions, listed in Table 7.5, similar plots are obtained from the 2-D FEA for all the magnets of the motor and lowest flux density along the magnetizing direction of nodes are summarised in Table 7.8. It is seen that for any fault condition, different poles have different demagnetization levels. The difference may be attributed to lower order space harmonics that rotate at different speed with respect to the rotor and affect the magnet working point at different nodes. Hence, to assess the demagnetization risk for PM machines having fractional-slot per pole per phase winding configuration, consideration of one pole-pair is not enough.

Table 7.8. Comparison of lowest flux density along the magnetizing direction of all magnets during the transient under various fault conditions

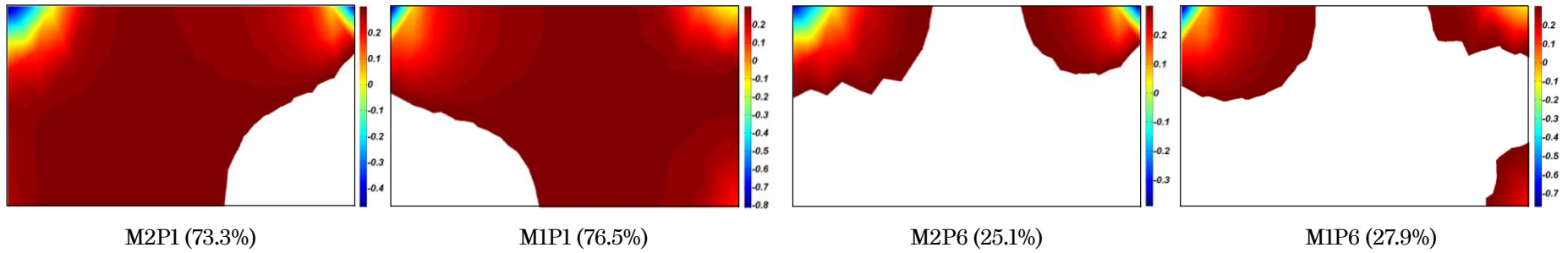
	F1	F2	F3	F4	F5	F6
M1P1	-0.55	-0.81	-0.35	-0.63	-0.17	-0.21
M2P1	-0.26	-0.46	-0.23	-0.41	-0.17	-0.21
M1P2	-0.53	-0.63	-0.27	-0.54	-0.07	-0.04
M2P2	-0.35	-0.44	-0.26	-0.41	-0.07	-0.04
M1P3	-0.72	-0.67	-0.33	-0.52	-0.15	-0.09
M2P3	-0.42	-0.39	-0.01	-0.36	-0.15	-0.09
M1P4	-0.23	-0.63	-0.36	-0.54	0.03	0.02
M2P4	-0.16	-0.36	-0.12	-0.37	0.03	0.02
M1P5	-0.38	-0.72	-0.27	-0.46	-0.02	0.02
M2P5	-0.27	-0.44	-0.17	-0.34	0.02	0.02
M1P6	-0.75	-0.77	-0.54	-0.70	-0.28	-0.26
M2P6	-0.39	-0.39	-0.31	-0.33	-0.28	-0.26
M1P7	-0.59	-0.58	-0.46	-0.58	0.05	0.01
M2P7	-0.47	-0.44	-0.33	-0.31	0.00	-0.02
M1P8	-0.56	-0.47	-0.39	-0.56	0.05	0.04
M2P8	-0.36	-0.38	-0.29	-0.30	0.04	0.04

Although the 3-phase SC faults results in to higher demagnetizing currents during the transients, the demagnetizing effect is less severe as the remaining 3-phase system operates under healthy condition. This is confirmed by the flux density of the nodes observed during the transient from Table 7.8 for 6-phase and 3-phase faults. As seen, the 6-phase faults have lower flux density compared to 3-phase faults (F1 versus F3, and F2 versus F4). Lower the flux density, higher is the demagnetizing effect.

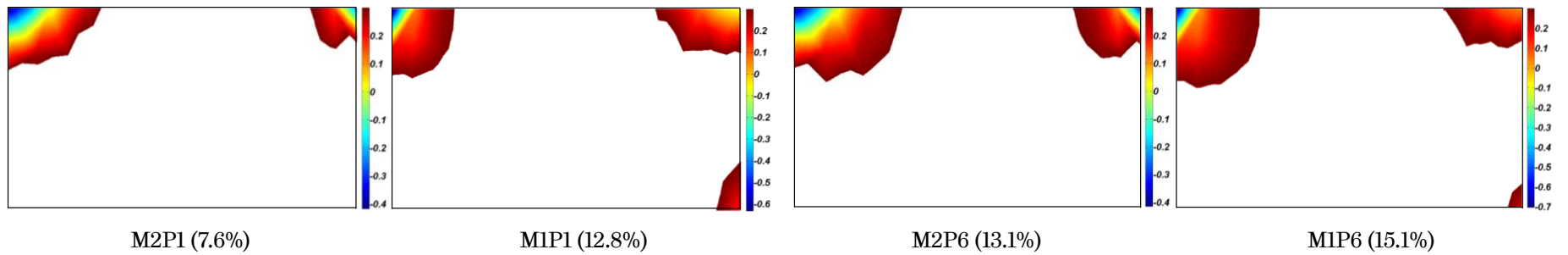
In order to have a better visual perspective of this phenomenon, Figure 7.16 shows the partially demagnetized regions of selected magnets under 6-phase and 3-phase short circuit faults at the peak torque and the base speed. It is worthwhile to note that these plots represents typical characteristics during the fault transient. The demagnetized area, shown in colour contour map, is obtained after assessing the flux density at every node of each magnet during the time period from the instant of short circuit till the machine transient currents reach the steady-state. It is the area covered by the nodes which have flux density ≤ 0.3 T in the direction of magnetization during the transient period. The demagnetized nodes are quantified as % of total nodes for each pole as shown in Figure 7.16. As seen, the 6-phase SC fault has more demagnetizing effect than the 3-phase SC fault, and the demagnetization is not uniform for every pole pair unlike distributed windings PM machines.

As observed from Table 7.8, SC faults at higher speeds do not results in to worst demagnetization as the required torque and hence currents are relatively lower due to field weakening in operation. However, the transient takes much longer to reach steady-state due to higher frequency as seen from Figure 7.13 (e) and (f).

Figure 7.17 shows the demagnetization plot of the rotor pole having the worst demagnetization during the transient for various 6-phase fault conditions.

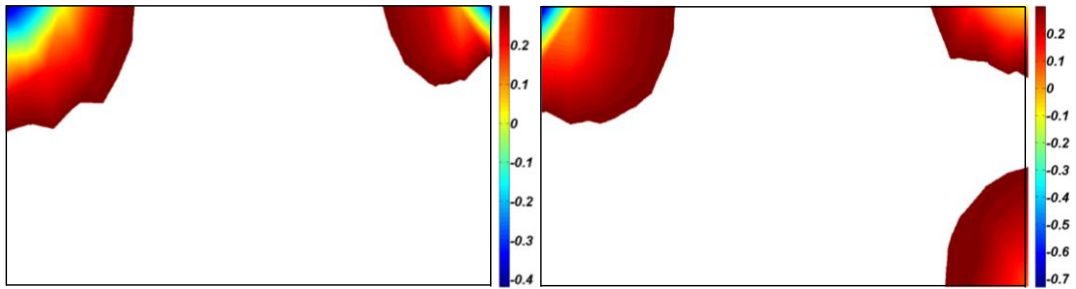


(a) 6-phase SC at T_{peak} (21.5% nodes demagnetized considering all nodes of all the magnets)

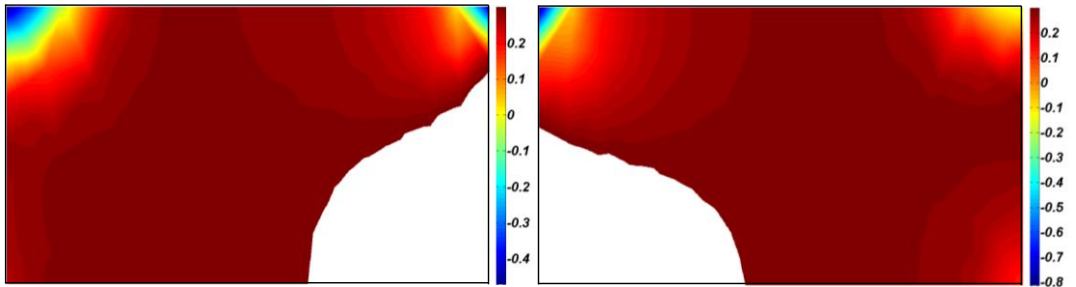


(b) 3-phase SC at T_{peak} (9.6% nodes demagnetized considering all nodes of all the magnets)

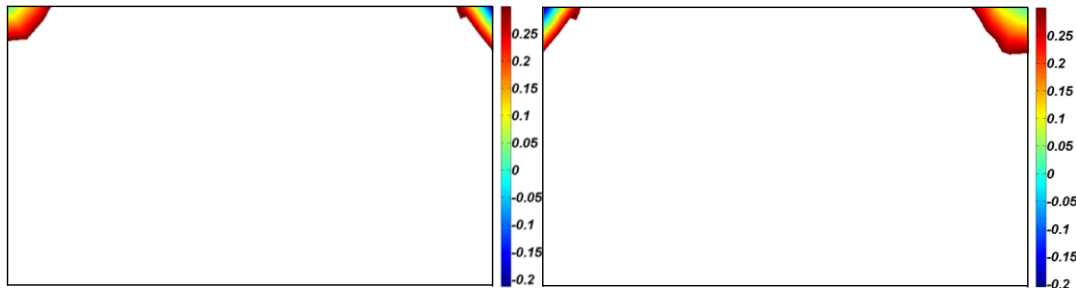
Figure 7.16. Partially demagnetized area of selected magnets during the transient (% denotes demagnetized nodes of the total nodes).



F1 : 6-phase SC at T_{rated} (Pole 3, 17.9% nodes demagnetized)



F2 : 6-phase SC at T_{peak} (Pole 1, 74.9% nodes demagnetized)

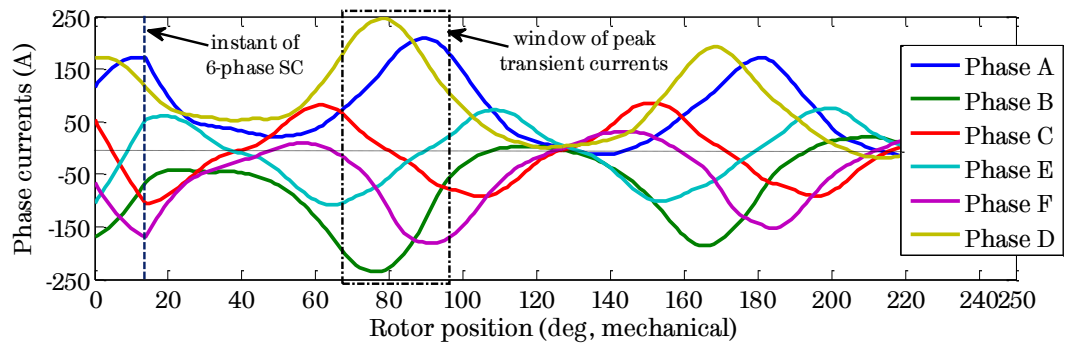


F6 : 6-phase SC at P_{peak} (Pole 1, 4.7% nodes demagnetized)

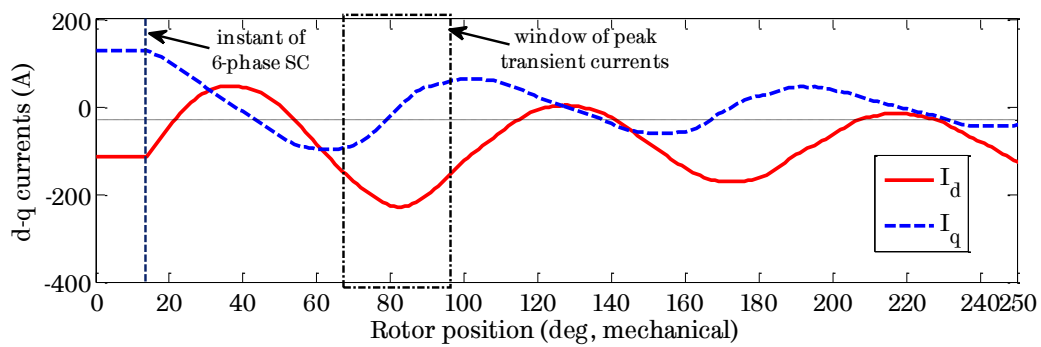
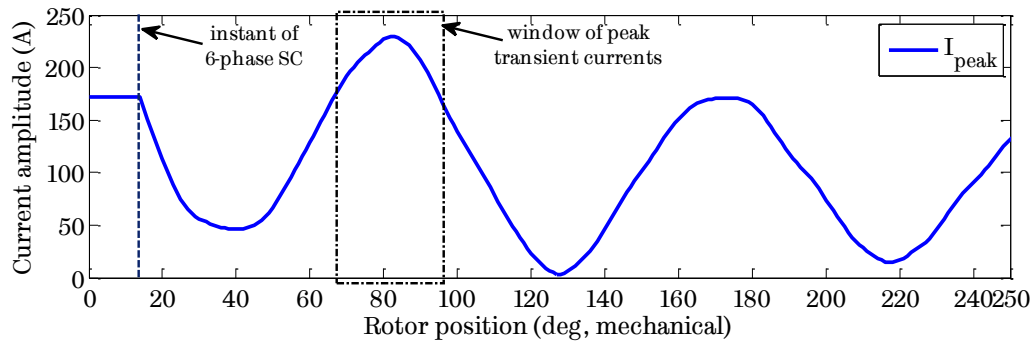
Figure 7.17. Partially demagnetized area of the rotor pole having maximum demagnetization during the transient for various 6-phase SC faults.

7.2.2 Investigation for vulnerability of first pole magnets to demagnetization than other poles

As will be seen from Figure 7.17, the worst demagnetization happens when 6-phase SC fault occurs at the peak torque operation. It is also observed that during this fault, the magnets of the first pole are affected worse than any other pole. In order to investigate the vulnerability of first pole magnets with respect to demagnetization, Figure 7.18 plots the initial transient response of the motor up to 250° mechanical after the 6-phase SC fault has been applied to the motor terminals in 2-D FEA.



(a) Phase currents during transient

(b) d - q axis currents during transient

(c) Current amplitude during the transient

Figure 7.18. Transient response of 6-phase, 18-slot, 8-pole IPM machine under short circuit fault at the peak torque operation.

As will be seen, the first peak transient in currents occurs between rotor position 70° to 90° mechanical. From the demagnetization assessment at various rotor position within the window of peak transient currents, it is found that the maximum nodes are demagnetized when the rotor reaches 80° mechanical. At that position, d - and q - axis currents are -227.3 A and -8.7 A respectively, and the

corresponding current amplitude is 227.5 A. At this rotor position, the distribution of phase current densities in the machine windings are plotted in Figure 7.19, and the amplitude of phase currents are listed in Table 7.9.

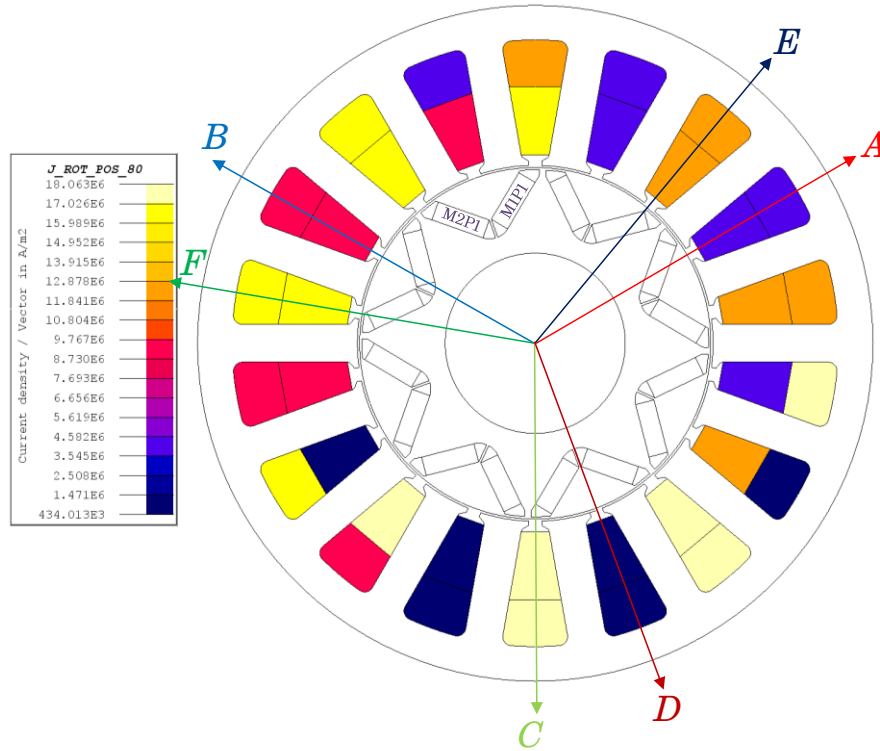


Figure 7.19. Current density distribution in phase windings at rotor position 80° during 6-phase SC fault at the peak torque operation.

Table 7.9. Amplitude of phase currents at rotor position 80° during 6-phase SC fault at the peak torque operation

θ_r	I_a	I_b	I_c	I_d	I_e	I_f
80°	163.4 A	-227.8 A	-5.9 A	243.4 A	-55.4 A	-117.8 A

As will be seen, the concentration of currents are more on the upper half of the machine (Phase A, B, E, and F) than that of the lower half (Phase C, and D). The MMF distribution of the machine can be plotted as in Figure 7.20. It also shows the position of all the magnets and rotor poles of the machine for better understanding of the phenomenon at 80° rotor position. As seen, the magnets of first pole are subjected to highest average demagnetizing MMF (2964 AT) compared to other magnets of any other pole. Also, being aligned with the middle of the slot, as seen

in Figure 7.19, which is source of the demagnetizing MMF during fault, makes the magnets of pole 1 more vulnerable to any other magnets. The magnets of pole 3 are also subjected to demagnetizing MMF albeit lower than the magnets of first pole, and they are aligned with the middle of the tooth, as seen from Figure 7.19, hence, they're not affected as worse as the magnets of first pole. Although the magnets of pole 5 are also subjected to higher demagnetizing MMF and are also aligned with the middle of the slot, the demagnetizing effect on those magnets are not worse as the peak MMF is lower and the current concentration of the machine during the peak transient is much more on the upper half of the machine than that of the lower half (Phase C has almost zero current).

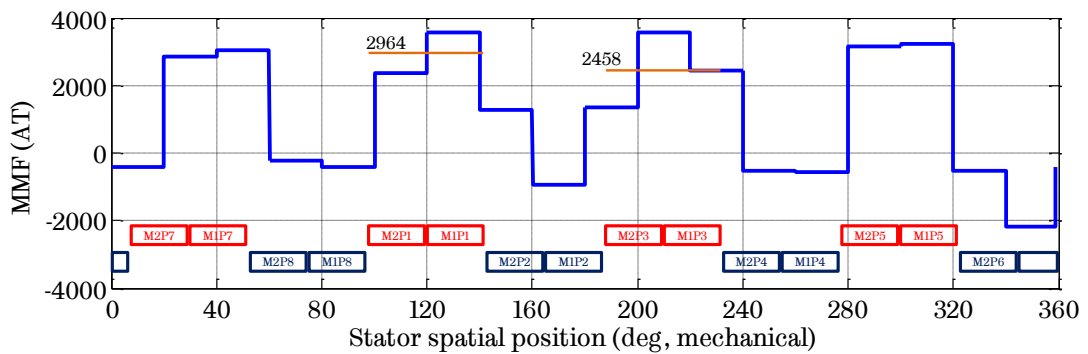


Figure 7.20. MMF distribution of the machine at rotor position 80° during 6-phase SC fault at the peak torque operation.

Among the even numbered poles, only pole 6 is subjected to highest demagnetizing MMF and its magnets are affected most with respect to demagnetization compared to other even numbered poles.

7.2.3 Comparison of distributed winding and fractional-slot winding with respect to demagnetization during faults

The operating duty cycles under wide variety of environmental conditions for PM traction motors are far more severe than most of the industrial or consumer applications. Also, the automotive industry expects the lifetime of the vehicle up to 15 years with little or almost no change in performance [138]. This calls for acute need to characterise demagnetization of the PM traction motor at any stage in their operating life cycle. The amount of demagnetization depends on variety of factors

like physical shape of the magnet, rotor geometry, grade of the magnet material, shape of its magnetic characteristics, etc. As the fractional-slot PM machines are increasingly being used for traction applications due to their numerous advantages, it is of utmost importance from design engineer's perspective to assess how fractional-slot PM machines compare with distributed wound PM machines in terms of demagnetization during fault conditions.

In order to compare the demagnetizing characteristics of the designed and optimized 6-phase, 18-slot, 8-pole IPM machine for segment-A electric vehicle application with distributed wound PM machine, the author has selected 6-phase, 48-slot, 8-pole IPM machine topology. It is also designed and optimized for the same specifications (Table 5.4) under the same volumetric, thermal and mechanical constraints (Table 5.6) as those of 6-phase, 18-slot, 8-pole IPM machine, as per the design optimization described in Chapter 5. In order to have a fair comparison, the rotor design is not changed, only the stator is optimized to achieve best energy efficiency over the NEDC. Figure 7.21 shows the cross-section of the optimized design of both the machines.

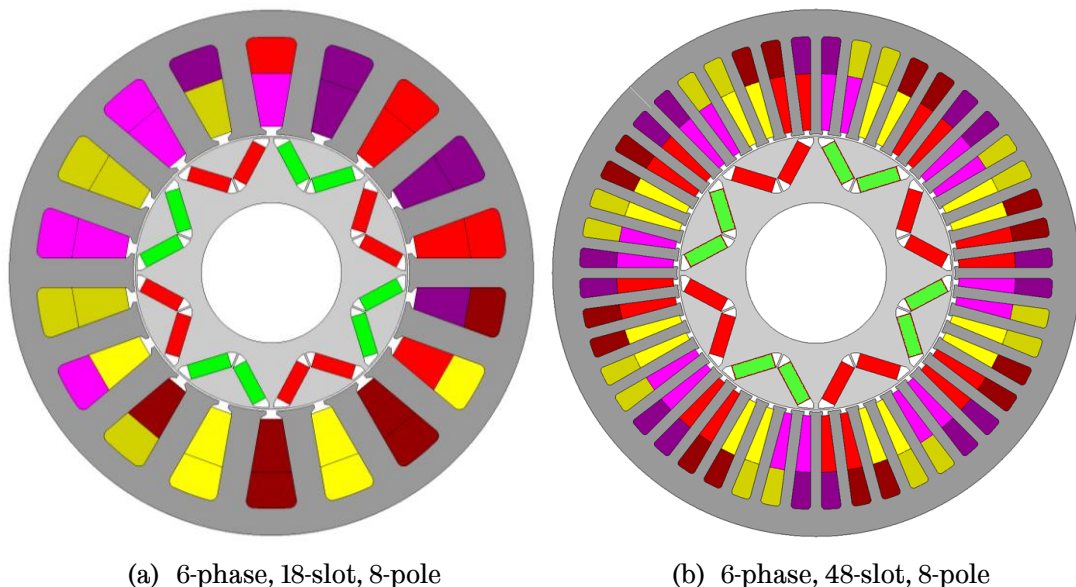


Figure 7.21. Comparison of optimized cross-section of fractional-slot (6-phase, 18-slot, 8-pole) and distributed wound (6-phase, 48-slot, 8-pole) IPM machines.

7.2.3.1 Performance comparison

Table 6.21 compares the performance of both the machines at the rated and the peak torque operations at the base speed. It is to be noted that the magnet (NdFeB, grade N35EH) properties used in the prediction are at 150°C for both the machines. The copper losses are calculated based on the calculated winding resistance at 120°C.

Table 7.10. Performance comparison of fractional-slot (6-phase, 18-slot, 8-pole) and distributed wound (6-phase, 48-slot, 8-pole) IPM machines

Parameter	Rated torque		Peak torque		Unit
	18s8p	48s8p	18s8p	48s8p	
Torque	75.0	74.9	140.0	140.0	N·m
Speed	2800	2800	2800	2800	rpm
Power	22.0	22.0	41.0	41.0	kW
Torque ripple	2.4	11.1	5.0	18.7	%
Peak phase current	79.5	70.8	205.0	158.5	A
Line-line voltage (V_{l-l})	218.0	206.0	327.0	236.5	V
Current density	10.4	9.6	26.9	21.6	A/mm ²
Copper loss	1004	917.5	6677	4605	W
Iron loss – stator	159	155	257	235	W
Iron loss – rotor	28	15	47	21	W
PM eddy current loss	11	0	72	0	W
Power efficiency	94.8	95.3	85.3	89.6	%
NEDC energy efficiency	94.9			94.0	%

As seen from the above table, the distributed windings PM machine has higher torque ripple as expected. The skew may be employed in the rotor/stator if it has to be used for electric vehicle applications, making the manufacturing comparatively costlier. Due to overlapping distributed windings, the resistance of the 6-phase, 48-slot, 8-pole IPM machine is also higher compared to that of 6-phase, 18-slot, 8-pole IPM machine. The efficiency of the distributed IPM is 0.5% and 4.3% higher at the rated torque and the peak torque operation respectively. This is mainly due to lower saturated magnetic circuit for distributed winding machine compared to fractional-slot IPM machine resulting into higher torque production

for the same current. Also, the eddy current loss in magnets are present only in fractional-slot IPM machine due to lower and higher order MMF space harmonics. However, the energy efficiency of the distributed IPM machine is 0.9% lower than that of fractional-slot IPM machine due to its lower d -axis inductance, which results into higher current required to produce the torque under the voltage limit at higher speeds.

7.2.3.2 Demagnetization assessment of 6-phase, 48-slot, 8-pole IPM

As observed from the demagnetization assessment of 6-phase, 18-slot, 8-pole IPM machine, the worst case with respect to demagnetization occurs when 6-phase SC fault happens at the peak torque operation. Hence, to compare the demagnetization levels between 6-phase, 18-slot, 8-pole IPM and 6-phase, 48-slot, 8-pole IPM machines, mainly two fault conditions have been selected: (1) 6-phase SC fault at the peak torque operation, and (2) 6-phase SC fault at the rated torque operation.

Figure 7.22 and Figure 7.23 compares the current trajectories, current transient, and torque transient of both the machines under 6-phase SC fault at the peak torque and at the rated torque operation respectively. Table 7.11 lists the peak values of torque, d - and q -axis currents, current amplitude and steady-state short circuit current for both the machines.

Table 7.11. Comparison of peak transient torque and currents for 6-phase, 18-slot, 8-pole and 6-phase, 48-slot, 8-pole IPM machines

	SC at peak torque		SC at rated torque	
	18s8p	48s8p	18s8p	48s8p
Maximum generating torque (N·m)	-132.3	-174.3	-110.4	-148.3
Maximum d -axis current (A)	-227.3	-224.3	-193.7	-218.8
Corresponding q -axis current (A)	-8.7	-21.5	-15.4	-6.1
Maximum peak fault current (A)	227.5	225.3	194.3	219.0
Steady-state short circuit current (A)	-79.5	-101.9	-79.5	-101.9

As will be seen, the steady-state short circuit current is higher in distributed wound IPM (48-slot, 8-pole) than the fractional-slot IPM (18-slot, 8-pole) as expected, which is mainly due to lower inductance of distributed wound IPM

than that of fractional-slot IPM. Also, the peak demagnetizing currents are almost same during 6-phase SC fault at the peak torque operation for both the machines.

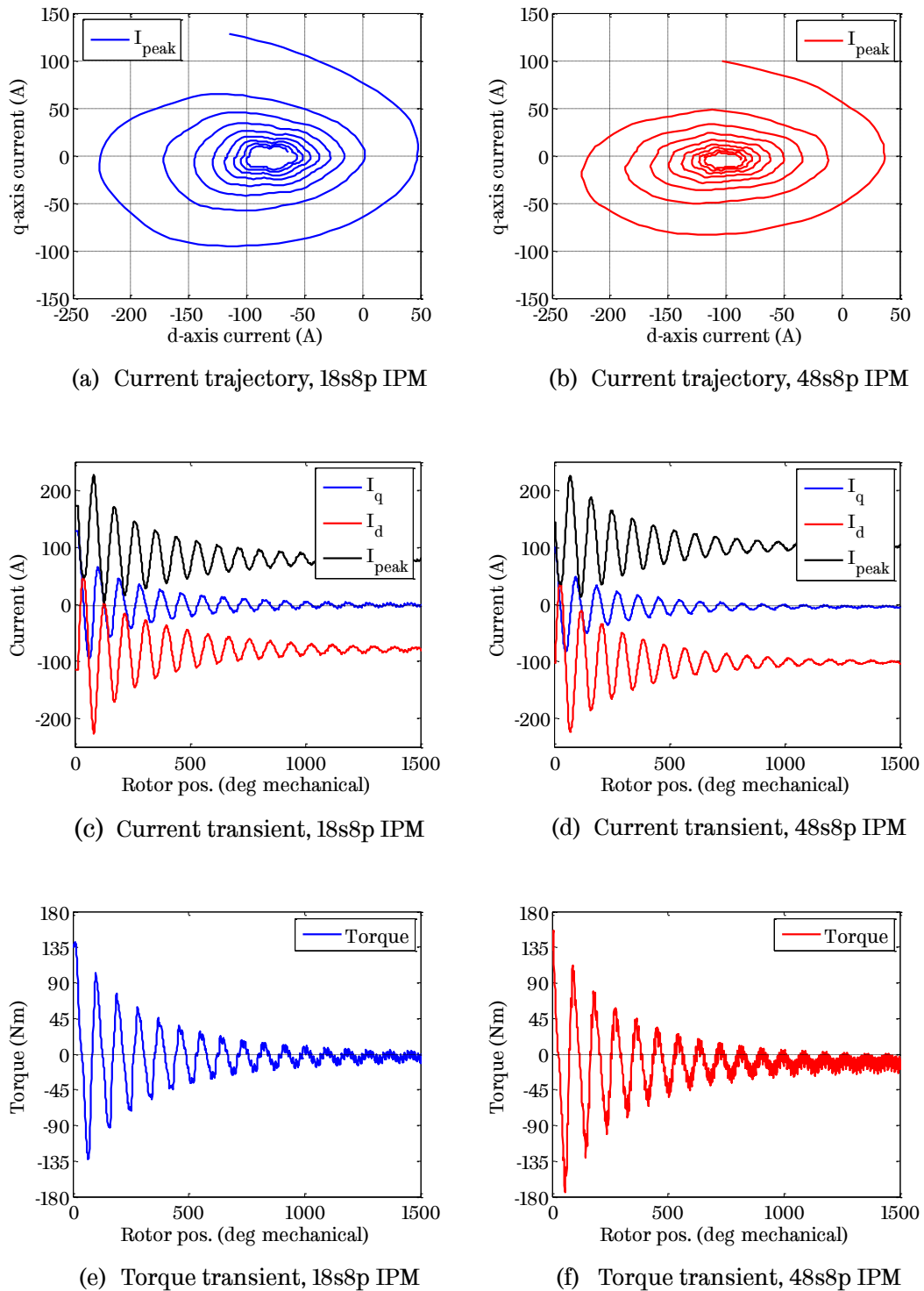
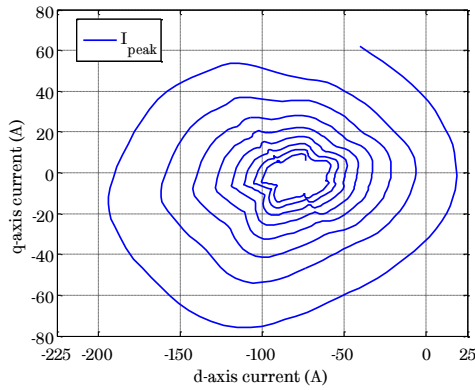
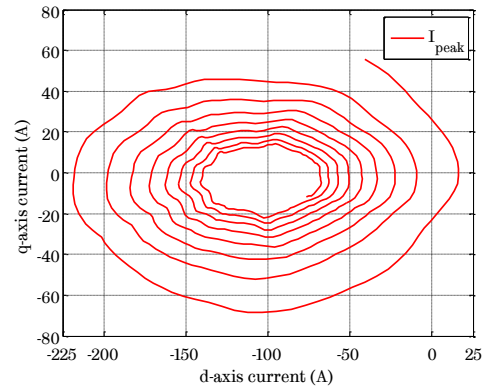


Figure 7.22. Comparison of machine behaviour under 6-phase SC fault at the peak torque operation for 6-phase, 18-slot, 8-pole and 6-phase, 48-slot, 8-pole IPM machines.

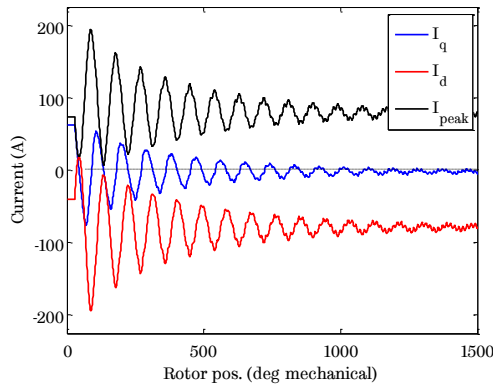
Whereas the peak demagnetizing currents are ~13% higher during 6-phase SC fault at the rated torque operation for distributed wound (48-slot, 8-pole) IPM than the fractional-slot (18-slot, 8-pole) IPM.



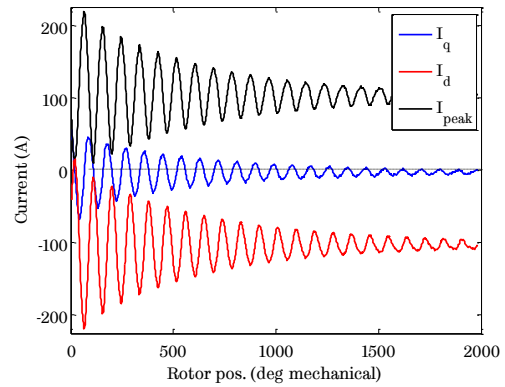
(a) Current trajectory, 18s8p IPM



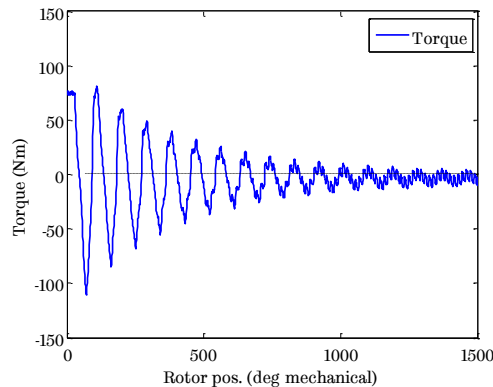
(b) Current trajectory, 48s8p IPM



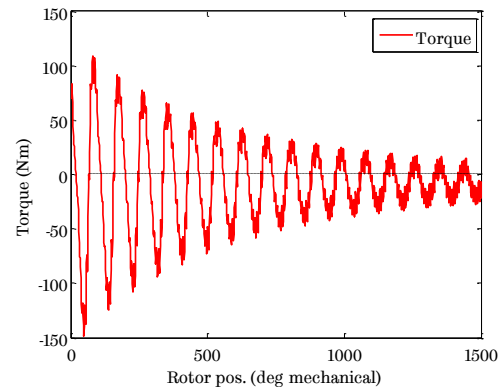
(c) Current transient, 18s8p IPM



(d) Current transient, 48s8p IPM



(e) Torque transient, 18s8p IPM



(f) Torque transient, 48s8p IPM

Figure 7.23. Comparison of machine behaviour under 6-phase SC fault at the rated torque operation for 6-phase, 18-slot, 8-pole and 6-phase, 48-slot, 8-pole IPM machines.

Using the proposed method of decomposing nodal flux density along the magnetizing direction over the transient duration, as explained in section 7.2.1.3, the demagnetized regions of the poles are compared in Figure 7.24 for 6-phase SC fault at the peak torque and at the rated torque operation respectively for both the machines. As will be seen, the first pole magnets of the fractional-slot IPM machine have ~75% nodes demagnetized compared to ~50% of the distributed wound IPM machine during 6-phase SC fault at the peak torque operation. However, during 6-phase SC fault at the rated torque operation, the demagnetization is worse in the distributed wound IPM machine (~42% demagnetized nodes) than the fractional-slot IPM machine (~9% demagnetized nodes). This is mainly due to higher demagnetizing currents in distributed wound IPM machine than the fractional-slot IPM machine during 6-phase SC fault at the rated torque operation, as observed from Figure 7.23 and Table 7.11. It is worth to note that all the magnets in various poles will have similar demagnetization for the distributed wound IPM, whereas the fractional-slot IPM has non-uniform demagnetization (as discussed in section 7.2.1.5).

Following observations can be made from the comparison of demagnetization during 6-phase SC fault at the peak torque and the rated torque operation between fractional-slot IPM and distributed wound IPM machines.

- 1) The fractional-slot PM machines have non-uniform demagnetization across the various rotor poles, whereas the distributed wound PM machines have uniform demagnetization.
- 2) Between two magnets of the same pole, the fractional-slot PM machines have asymmetric demagnetization, whereas the distributed wound PM machines have almost symmetrical demagnetization.
- 3) For same specifications and design constraints, the fractional-slot PM machines have higher d - and q -axis inductances compared to distributed wound PM machines. Hence, the steady-state short circuit current (determined by λ_m/L_d) is higher in the distributed -

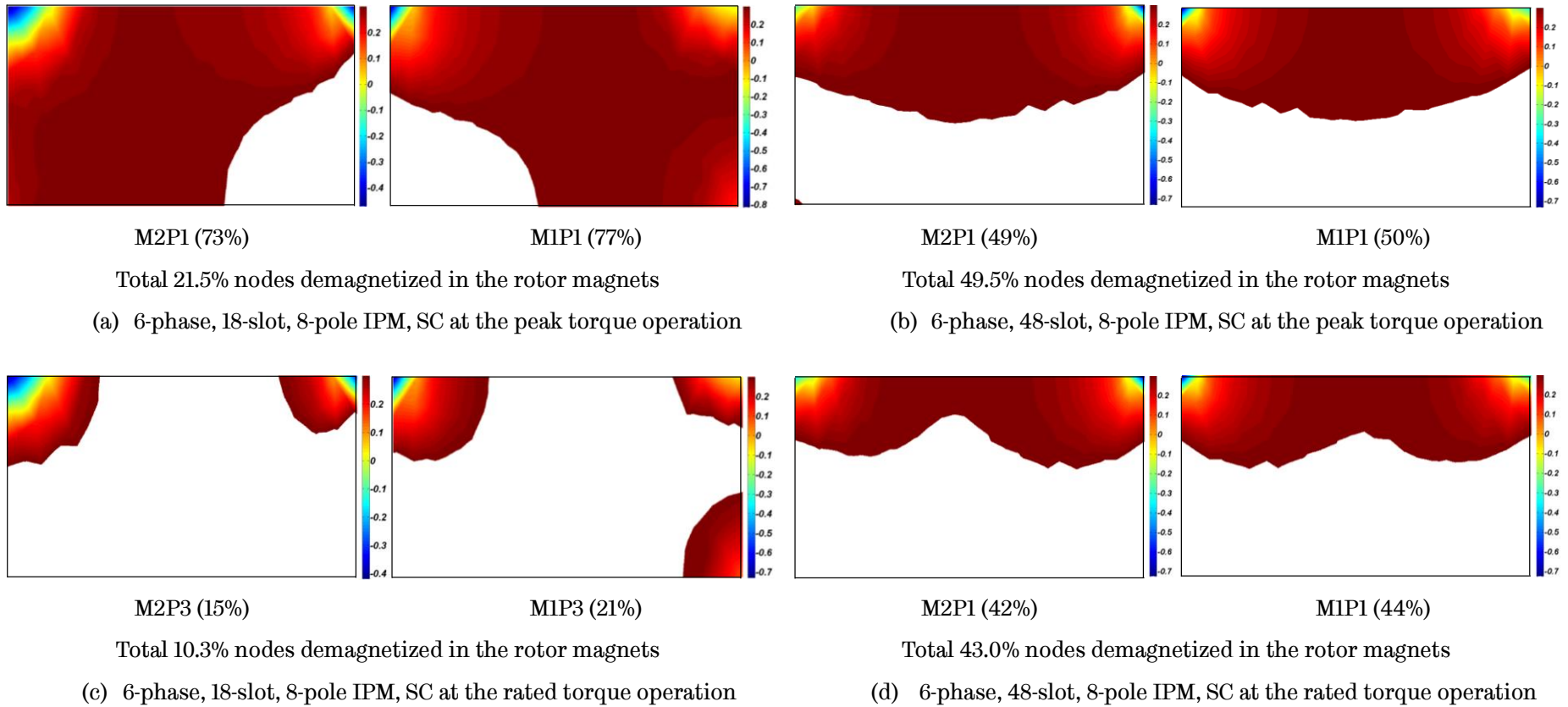


Figure 7.24. Partially demagnetized area of 1st pole magnets during the transient (% denotes demagnetized nodes of the total nodes) for 6-phase, 18-slot, 8-pole and 6-phase, 48-slot, 8-pole IPM machines for 6-phase SC faults at different operating conditions.

- wound PM machines than the fractional-slot PM machines, which may have severe implications with respect to demagnetization.
- 4) Due to presence of lower order MMF space harmonics in the fractional-slot PM machines, some of the magnets in the rotor have more demagnetization than the others. However, the overall demagnetization of the machine is less compared to distributed wound PM machines. This is confirmed from the comparison of demagnetization between 6-phase, 18-slot, 8-pole and 6-phase, 48-slot, 8-pole IPM machines, presented in Figure 7.24.
- 5) Due to non-uniform demagnetization in the fractional-slot PM machines, the resultant back EMF of the machine post demagnetization will be asymmetrical, whereas the distributed wound PM machines will have symmetrical and uniform back-EMF waveform post demagnetization.

7.2.4 Summary

The post-fault transient characteristics of PM synchronous machines with fractional-slot per pole per phase winding configuration as well as distributed winding configuration under various fault conditions are comprehensively investigated.

The results confirm that 3-phase SC faults in a 6-phase machine increases the peak demagnetizing currents; however, the risk of partial irreversible demagnetization is reduced compared to 6-phase symmetrical faults because of the remaining healthy 3-phase system. The magnitude of demagnetizing currents depends on the pre-fault operating currents of the machine, however, the demagnetization does not depend on the instant of short circuit (*i.e.*, at $V_u = 0$ or $V_u = \text{peak value}$). However, different nodes of the magnet demagnetize at different time of the transient. Among all the faults considered, 6-phase SC fault at the peak torque and the base speed is worst with respect to demagnetization.

The author has proposed a more reliable and accurate approach by decomposing the flux density in each node of the magnet along the magnetizing direction to access the partial irreversible demagnetization in PM synchronous

machines for various short circuit fault conditions. Unlike distributed winding PM synchronous machines, consideration of only one pole pair to evaluate partial irreversible demagnetization under fault conditions is not enough due to the presence of lower order MMF space harmonics that is typical of fractional-slot per pole per phase winding configurations. Hence, the demagnetization withstand capability is an important design requirement for the fractional-slot per pole per phase PM synchronous machines even for IPM rotor types. The demagnetization is neither symmetrical nor uniform in all magnets for fractional-slot per pole per phase wound PM synchronous machines.

Compared to fractional-slot PM synchronous machines, the distributed wound PM machines have symmetrical and uniform demagnetization in all magnets. Although the fractional-slot PM synchronous machines have some magnets more demagnetized compared to distributed wound PM synchronous machines, the overall demagnetization of the machine is more in distributed wound PM synchronous machines. The resultant back EMF post demagnetization will be symmetrical in distributed wound PM synchronous machines.

7.3 Thermal analyses over the driving cycles

The EV traction requires machines to be capable of providing high starting torque at lower speeds for fast acceleration and constant power operation over a wide speed range. It has been shown that a machine design optimized against the rated torque at the base speed does not necessarily lead to an optimal design over a given driving cycle [86]. Hence, the design of 6-phase, 18-slot, 8-pole IPM is optimized against the specifications under the volumetric and the thermal constraints to maximum energy efficiency over the NEDC using 2-D FEA in Chapter 5. Because the rotor loss in fractional-slot per pole per phase PM synchronous machines is significant and is highly dependent on the speed and the current, the design process must account for thermal limits under worst scenarios imposed by various materials over the complete torque speed operating range as well as over the desired driving cycles.

While thermal modelling and analysis of PM machines have been extensively reported in literature [139-146], thermal behaviours of *fractional-slot permanent*

magnet machines over driving cycles such as the New European Driving Cycle (NEDC) and Artemis Urban Driving Cycle (AUDC) have not been documented and their implications on machine design have not been well understood. The author has evaluated the thermal behaviour of the IPM machine with novel fractional-slot per pole per phase winding configuration (6-phase, 18-slot, 8-pole) over driving cycles (NEDC and AUDC), by combining 2-D transient electromagnetic FEA with a lumped parameters transient thermal model using commercially available software package.

7.3.1 Thermal analyses over the driving cycles

The thermal model of 6-phase, 18-slot, 8-pole is validated using the experimental test data as discussed in Chapter 6. After the calibration of the thermal model, thermal analyses of the machine over the driving cycles are performed. The transient thermal model takes the losses in motor components which are derived from the calibrated loss models using the torque and speed requirements from the driving cycle at each second as inputs. The duty cycle (NEDC or AUDC) is repeated 9 times in the analysis to ensure the motor temperatures reach the steady-state.

7.3.1.1 Thermal analysis over the NEDC

The NEDC consists of four recurring ECE-15 city driving cycles along with an extra urban driving cycle with a maximum speed of 120 km/h, as shown in Figure 7.25 (a). It covers ~11 km with an average speed of 33.6 km/h. Figure 7.25 (b) shows the torque requirements over the NEDC for the motor.

The transient temperature response of the motor winding and the rotor magnets is shown in Figure 7.26. As will be seen, there is about 35°C temperature difference between the stator winding and rotor magnets mainly due to the rotor loss.

The maximum temperature occurs when the vehicle/motor operates at the maximum speed of the cycle (120 km/h), and the resulting loss is relatively high.

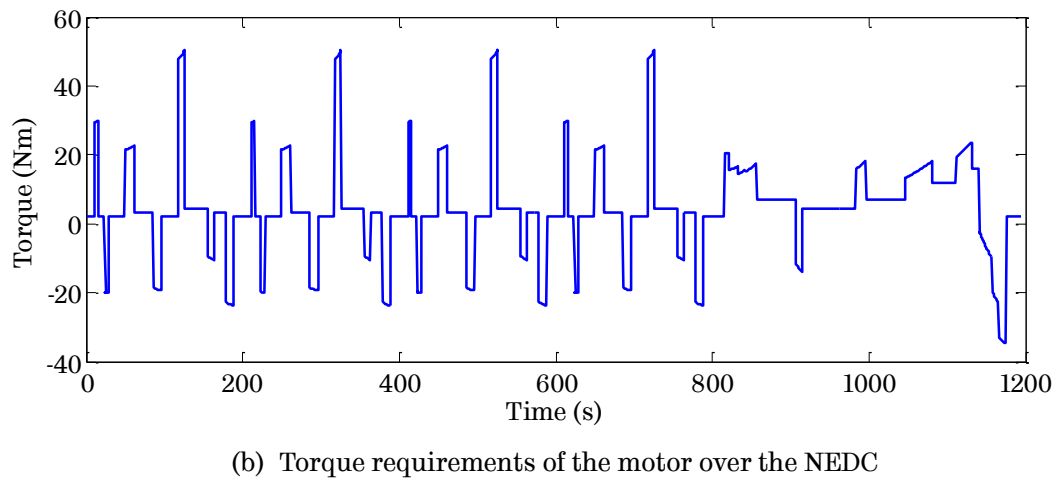
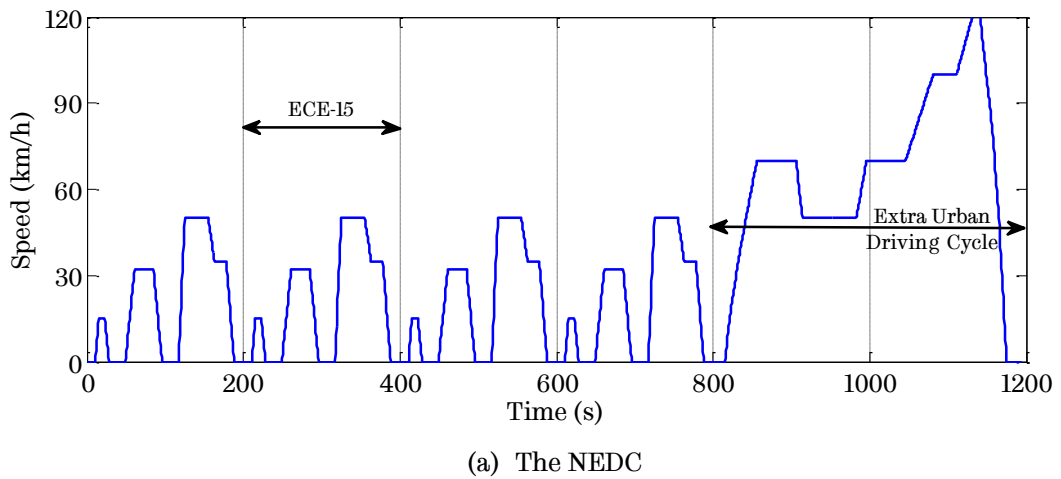


Figure 7.25. The New European Driving Cycle and corresponding torque requirements of the motor.

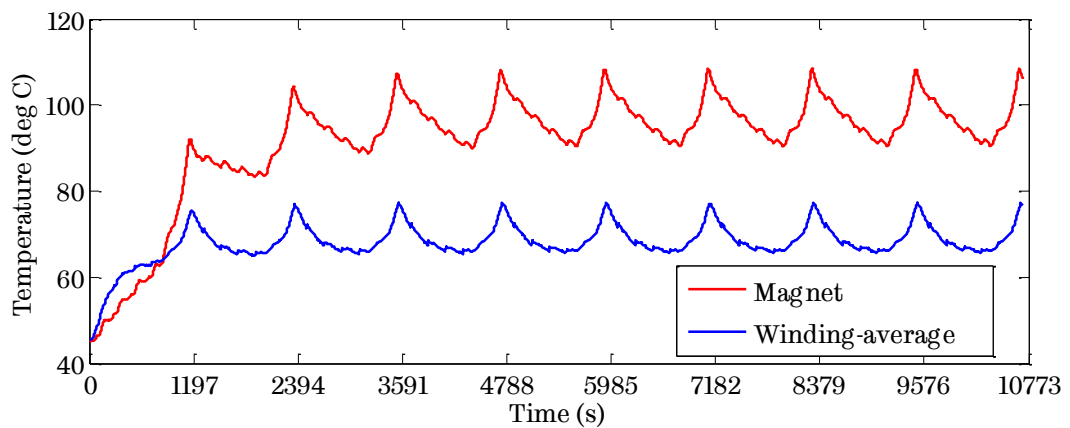


Figure 7.26. Transient temperature response of the motor winding and the rotor magnets of 6-phase, 18-slot, 8-pole IPM machine over repeated NEDC cycle.

7.3.1.2 Thermal analysis over the AUDC

As shown in Figure 7.27 (a), the AUDC consists of five cycles, one each of urban dense, free-flow urban, congested stops, congested low speeds, and flowing stable with a maximum speed of 57.7 km/h. It covers ~4.9 km with an average speed of 17.7 km/h. The corresponding torque requirements over the AUDC is shown in Figure 7.27 (b). As will be seen, the AUDC demands peak torque more often than the NEDC from the motor. The transient temperature response of the motor windings and the magnets is shown in Figure 7.28. As seen, the temperature difference between stator windings and the rotor magnets is only 10°C over the AUDC compared to 35°C over the NEDC.

7.3.1.3 Discussion on thermal behaviours over the NEDC and the AUDC

Higher temperature difference between the stator winding and the rotor magnets over the NEDC than that over AUDC is because of more rotor losses at high speeds and the concentration of the stator iron loss at the stator bore due to longer field weakening operations than the AUDC, which makes the rotor loss dissipation difficult through air-gap.

The peak temperatures over the driving cycle are dependent on the characteristics of the driving cycles. The NEDC requires vehicle/motor to operate over wide speed range within the rated torque envelope (Figure 5.5), whereas the AUDC requires vehicle/motor to operate at lower speeds but with peak torque demands (Figure 5.8) as it is mainly an urban city driving cycle involving high acceleration and frequent start and stop. Thus, the AUDC puts high torque demands on the motor resulting into higher motor current, which may be thermally demanding for the stator windings. However, the stator copper loss can be dissipated effectively by the water cooling jacket while the high torque demands are only for short duration, making the motor winding temperatures not as worse as they could be with peak torque demands for longer durations. On contrary, the NEDC impacts the iron loss in the machine as the speed range is quite wide imposing thermal challenge for the rotor magnets for PM machines. Rotor cooling is more challenging in fractional-slot PM synchronous machines as the rotor losses are higher than the distributed wound PM synchronous machines due to presence of MMF space harmonics. This is confirmed from the transient temperature

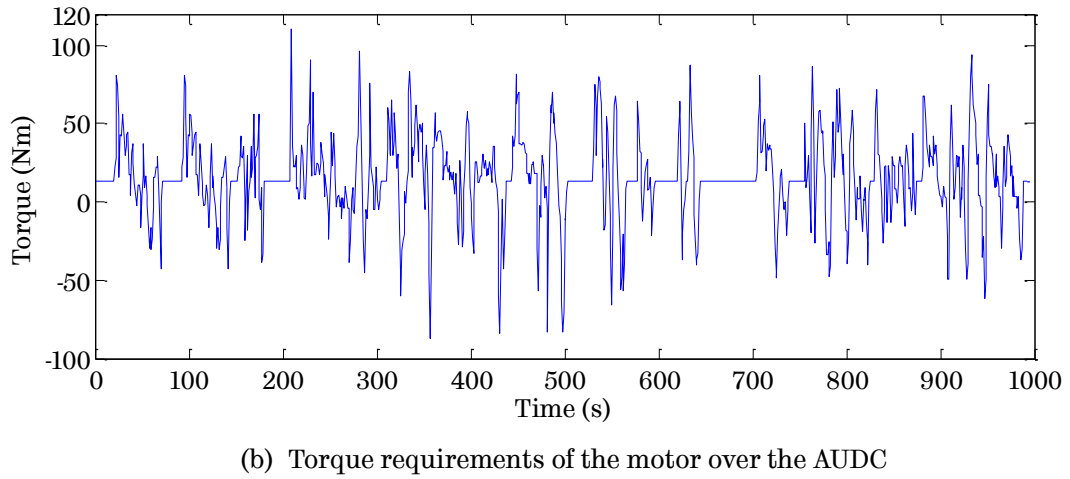
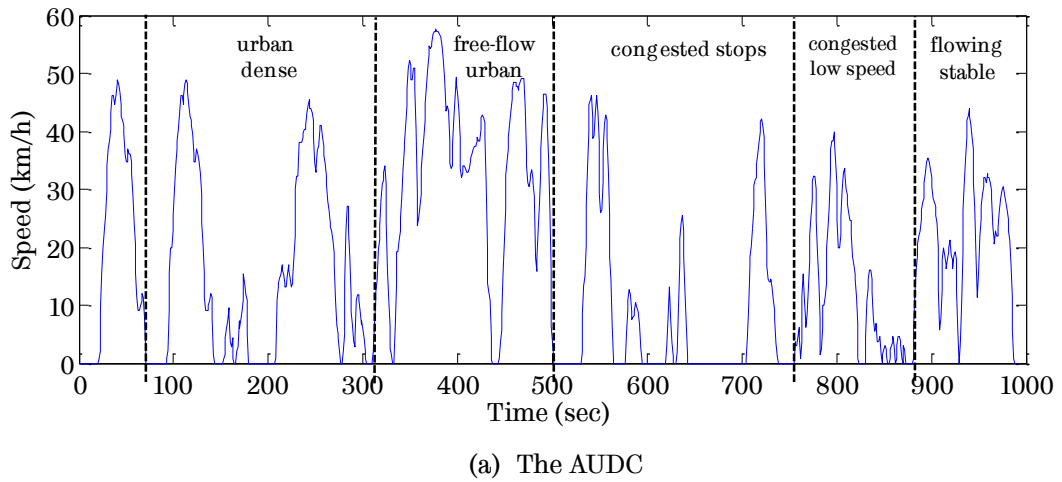


Figure 7.27. The Artemis Urban Driving Cycle and corresponding torque requirements of the motor.

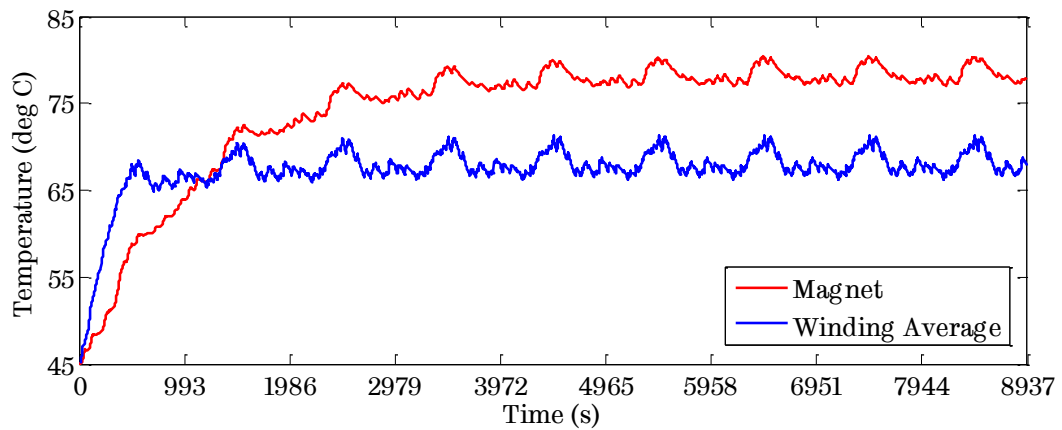


Figure 7.28. Transient temperature response of the motor winding and the rotor magnets of 6-phase, 18-slot, 8-pole IPM machine over repeated AUDC cycle.

response over the NEDC and the AUCD as the rotor magnets have the maximum temperature compared to stator iron or copper temperatures. Hence, it is necessary to check the thermal behaviour of the motor under driving cycles for electric vehicle applications.

7.3.2 Summary

For fractional-slot PM synchronous machines, the rotor cooling is more challenging than that of distributed wound PM synchronous machines because of higher rotor losses including PM eddy current losses due to MMF space harmonics. The thermal analyses confirm that the temperatures of various motor components are well within the thermal limits over the driving cycles. Among the NEDC and the AUCD, the NEDC poses more difficulty for the rotor heat dissipation due to high-speed rotor losses and concentration of stator iron loss at the stator bore surface because of longer field weakening operations than the AUCD.

Chapter 8

Conclusions & Future Scope of Work

The research work undertaken by the author over the course of his PhD is concluded in this chapter. The future scope of work in the relevant technical field is also presented.

8.1 Conclusions

The electric vehicles with advanced technology and reduced cost are the key to meet international energy security goals, and to contain the global warming by reducing the CO₂ footprint. Achieving these goals requires power-dense, high efficient electric traction machines, which pave the way for the development and swift realization of EVs.

From comprehensive literature survey on state-of-the-art technologies for electric traction machines, it is inferred that PM synchronous machines with fractional-slot per pole per phase winding configurations is better suited for traction applications due to their numerous advantages. However, the induction machines are continuing to be considered by transportation industry due to their simple construction, absence of rare-earth PM materials, lower cost and ease of control with advanced power electronics.

Through preliminary design study for micro-sized EV application, it is shown that the benefits of variable field excitation in hybrid excited PM flux switching machines are outweighed by their drawbacks in terms of lower torque density, more complex structure, and higher iron loss owing to saturated stator (as the stator windings, field windings and magnets are competing for space for given volumetric and thermal constraints) compared to competing PM machine

technologies (SPM and/or IPM) with fractional-slot per pole per phase winding configurations. For EV applications, high torque requirement at low speed conflicts with low back EMF requirement at high speed, making SPM machine less attractive than IPM machine even though SPM has better controllability than IPM due to low saturation level and less operation-dependent parameter variations.

The novel winding configurations for fractional-slot PM machines with low space harmonics have been devised and analysed. It has been shown that compared with a class of the conventional fractional-slot PM machines in which the number of slots is equal to the number of poles plus or minus one, the proposed winding configurations with the associated slot-pole combinations can eliminate the dominant undesirable MMF space harmonics and all odd or even harmonics as well as unbalanced radial force in a simple and cost-effective way. It has been shown that the availability of power drivetrain in EV applications is enhanced by designing 6-phase machine using the proposed winding configurations as two independent 3-phase windings, which are controlled by two independent inverters. All the possible combinations of the phase shift between two sets of 3-phase windings in 6-phase, 18-slot, 8-pole machines are explored. It is concluded that instead of usual 60° phase shift between two sets of 3-phase windings in a 6-phase, 18-slot, 8-pole machine, 20° and/or 40° phase shift results into improved harmonics distribution in the stator MMF, which in turn improves the performance of the machine.

The proposed winding configuration has been applied to design a 6-phase, 18-slot, 8-pole IPM machine for a segment-A EV application having a peak power capability of 41 kW. The detailed approach to derive electric traction machine specifications from the driving cycle (New European Driving Cycle in this case) in terms of continuous power and torque ratings using the vehicle data from the OEM is described. It has been shown that the peak torque capability of the traction machine are dictated by the acceleration targets and drive-away performance requirements. The 12 points representation of the NEDC using the *energy centre of gravity* principle is obtained for the target design specifications, which significantly reduces the number of calculations to perform design optimization in a reasonable time frame with a systematic approach. The design optimization,

aimed to achieve minimum energy consumption over the representative driving cycle (NEDC in this case) against the target specifications under the volumetric, thermal, mechanical, and electrical constraints, and having the iterative design process between electromagnetic, thermal, and mechanical designs, is explained in detail. The cooling system for the machine is designed using simple heat dissipation calculation and the final dimensions are obtained by an iterative thermal design at the maximum cruise speed operation. The sensitivity study on the thermal performance of the optimized machine with various sources of uncertainty is also performed. It has been shown that the optimized design of the IPM machine with the proposed winding configuration exhibits high efficiency at the rated torque operation as well as over a wide speed range and enhanced availability for EV applications. It has also been shown that the steady state terminal short-circuit current of one 3-phase winding is 1.05 times the rated current. This indicates that the machine can accommodate continuous terminal short-circuit without much overheating.

The designed machine is demonstrated by constructing a prototype machine and is validated by a series of preliminary tests on a highly precise and accurate test bench. The measurement results show that the prototype machine has a high efficiency over a wide operating speed range as desired. The causes behind slight mismatch between the predicted and the measured values are identified and explained. Various design models including loss models, and performance prediction models are calibrated using the experimental data. The root cause analysis is performed to investigate the partial demagnetization of the first prototype due to overloading over excessive period and converter failure at high speed. Since it is not possible to completely eliminate similar converter failures at the development stage, preventive measures have to be adopted to ensure the second prototype machine can survive even under overload and unexpected fault conditions. They are incorporated in building second prototype having thinner (0.2 mm) rotor laminations and high temperature Samarium Cobalt magnets. Further, the series of preliminary tests have validated second prototype machine with a reasonable match between the prediction and the measurements.

Finally, important design aspects of the novel 6-phase, 18-slot, 8-pole IPM machine are investigated in detail. It has been shown that both 20° and 40° phase shifts between two sets of 3-phase windings reduce the 2nd order MMF space harmonic in the armature reaction field, which is conducive to reduction of the rotor eddy current loss in the magnets and amplitude of mode 2 vibrations. However, they give rise to odd MMF space harmonics and consequently unbalanced magnetic pull, albeit their magnitudes are very small.

For assessment of partial irreversible demagnetization, more reliable and accurate approach is proposed by decomposing the nodal flux density in all magnets along the magnetizing direction during various short circuit fault conditions. It is inferred that unlike distributed winding PM synchronous machines, consideration of only one pole pair to evaluate partial irreversible demagnetization in fractional-slot PM synchronous machines is not enough due to presence of low order MMF space harmonics. It is concluded that demagnetization is neither symmetrical nor uniform in all magnets of fractional-slot PM synchronous machines. The demagnetization of distributed wound and fractional-slot PM synchronous machines are compared for various fault conditions, which are designed for the same design specifications under the same volumetric and thermal constraints. It is shown that although the fractional-slot PM machines have some magnets more demagnetized than the others, the overall demagnetization of the machine is more in distributed wound PM machines. However, the resultant back EMF post demagnetization is symmetrical in distributed wound PM machines unlike fractional-slot PM machines.

It is shown that for fractional-slot PM synchronous machines, the rotor cooling is more challenging than that of distributed wound PM machines because of higher rotor losses including PM eddy current loss due to MMF harmonics. The thermal analyses confirm that the temperatures of various motor components are well within the thermal limits (a) over the driving cycles, (b) at the maximum cruise speed operation, and (c) at the rated torque operation. From these analyses, the worst operating condition occurs at (b) when more loss incurs at high speeds. Among the NEDC and the AUDC, the NEDC poses more difficulty for the rotor heat

dissipation due to high-speed rotor losses and concentration of stator iron loss at the stator bore because of longer field weakening operations than the AUDC.

8.2 Future scope of work

The research work described by the author in this thesis indicates various directions to pursue further research work in this domain as outlined below.

- A. Assessment of wound field synchronous machines for electric vehicle applications as they have variable field controllability. For micro-sized EV, the research outcomes presented in this thesis in terms of comparison of machine technologies combined with the assessment of wound field synchronous machines will provide a complete know-how for the automotive industry and academia with respect to comparative merits and demerits of all machine technologies for EV applications.
- B. Assessment of the proposed novel winding configuration for other applications. By way of example, for domestic appliances, the detailed comparison of the proposed winding configuration with state-of-the-art machine technologies will provide know-how on performance of the proposed winding for another set of design specifications and performance requirements.
- C. Extension of multiplicity concept to eliminate MMF space harmonics further by way of multiple 3-phase windings in PM machines [147]. By selecting appropriate space and time phase shifts, specific order MMF space harmonics can be cancelled out.
- D. Investigation of mismatch between measured and predicted q -axis inductances at lower q -axis current levels.
- E. Analysis of fault-tolerant behaviour, e.g., comparison of short-circuit current in a single and a few short-circuited turns with terminal short-circuit current, remedy actions by imposing terminal short circuit current through inverter control if the short-circuit current in a single or a few turns is higher than the terminal short circuit

current, the resultant torque production capability and thermal behaviour over the short-circuit transients, etc.

References

- [1] "World Population Prospects: The 2012 Revision - Highlights and Advance Tables," ESA/P/WP.228, 13 June 2013.
- [2] "BP Statistical Review of World Energy," 2013.
- [3] "Redrawing the Energy-Climate Map - Executive Summary," International Energy Agency, June 2013.
- [4] "Global EV Outlook - Understanding the Electric Vehicle Landscape to 2020," International Energy Agency, April 2013.
- [5] *Timeline: History of the Electric Car.* Available: www.pbs.org/now/shows/223/electric-car-timeline
- [6] C. D. Anderson, *Electric and Hybrid Cars : A History.* North Carolina: McFarland & Company, 2010.
- [7] *US Department of Energy : Energy Efficiency and Renewable Energy.* Available: <http://www.eere.energy.gov/>
- [8] *REGULATION (EEC) No 4064/89 - MERGER PROCEDURE,* 1999.
- [9] "European Vehicle Market Statistics," International Council on Clean Transportation, 2012.
- [10] M. Duoba, "Test procedures and benchmarking."
- [11] *EV Everywhere Grand Challenge: DOE's 10-Year Vision for Plug-in Electric Vehicles.* Available: <http://www1.eere.energy.gov/vehiclesandfuels>
- [12] S. Kozawa, "Trends and Problems in Research of Permanent Magnet Motors - Addressing Scarcity Problem of Rare Earth Elements," *Science and Technology Trends*, vol. No. 38, pp. 40-54, Jan. 2011 2011.
- [13] J. Gieras and M. Wing, *Permanent magnet motor technology: design and applications:* Marcel Dekker, 2002.
- [14] *A historical overview of permanent magnet motors.* Available: <http://www.ohioelectricmotors.com/a-historical-overview-of-permanent-magnet-motors-1704>
- [15] M. T. Abolhassani and H. A. Toliyat, "Fault tolerant permanent magnet motor drives for electric vehicles," in *IEEE International Electric Machines and Drives Conference (IEMDC)*, pp. 1146-1152, 2009.
- [16] J. Wang, X. Z. Ping, and D. Howe, "Three-phase modular permanent magnet brushless Machine for torque boosting on a downsized ICE vehicle," *Vehicular Technology, IEEE Transactions on*, vol. 54, pp. 809-816, 2005.

-
- [17] J. Wang, K. Atallah, Z. Q. Zhu, and D. Howe, "Modular Three-Phase Permanent-Magnet Brushless Machines for In-Wheel Applications," *Vehicular Technology, IEEE Transactions on*, vol. 57, pp. 2714-2720, 2008.
- [18] V. I. Patel, J. Wang, C. Gould, D. Nugraha, R. Vuletic, J. Tousen, and J. Klenner. (2013). *6-phase Fault-Tolerant Permanent Magnet Traction Drive for Electric Vehicles*. Available: http://www.artemis-ioe.eu/events/presentations/26.09.2013_NESEM_2013_Toulouse_C.Gould_University_of_Sheffield_6-Phase_Fault-tolerant_Permanent_Magnet_Traction_Drive_for_EVs_Final.pdf
- [19] C. C. Chan, "The State of the Art of Electric, Hybrid, and Fuel Cell Vehicles," *Proceedings of the IEEE*, vol. 95, pp. 704-718, 2007.
- [20] Y. Honda, T. Nakamura, T. Higaki, and Y. Takeda, "Motor design considerations and test results of an interior permanent magnet synchronous motor for electric vehicles," in *Proc. IEEE Industry Applications Society Annual Meeting*, pp. 75-82 vol.1, 1997.
- [21] Z. Q. Zhu and C. C. Chan, "Electrical machine topologies and technologies for electric, hybrid, and fuel cell vehicles," in *Vehicle Power and Propulsion Conference, 2008. VPPC '08. IEEE*, pp. 1-6, 2008.
- [22] J. F. Eastham, T. Cox, and J. Proverbs, "Application of planar modular windings to linear induction motors by harmonic cancellation," *Electric Power Applications, IET*, vol. 4, pp. 140-148, 2010.
- [23] L. Alberti and N. Bianchi, "Design and tests on a fractional-slot induction machine," in *Energy Conversion Congress and Exposition (ECCE), 2012 IEEE*, pp. 166-172, 2012.
- [24] A. M. El-Refaie and M. R. Shah, "Comparison of Induction Machine Performance with Distributed and Fractional-Slot Concentrated Windings," in *Industry Applications Society Annual Meeting, 2008. IAS '08. IEEE*, pp. 1-8, 2008.
- [25] H. Neudorfer, N. Wicker, and A. Binder, "Comparison of three different electric powertrains for the use in hybrid electric vehicles," in *Power Electronics, Machines and Drives, 2008. PEMD 2008. 4th IET Conference on*, pp. 510-514, 2008.
- [26] H. Neudorfer, "Comparison of three different electric powertrains for the use in high performance Electric Go-Kart," in *Electrical Machines and Power Electronics, 2007. ACEMP '07. International Aegean Conference on*, pp. 21-26, 2007.
- [27] X. Wei, Z. Jianguo, G. Youguang, W. Shuhong, W. Yi, and S. Zhanghai, "Survey on electrical machines in electrical vehicles," in *Applied Superconductivity and Electromagnetic Devices, 2009. ASEMD 2009. International Conference on*, pp. 167-170, 2009.

-
- [28] G. Nanda and N. C. Kar, "A Survey and Comparison of Characteristics of Motor Drives Used in Electric Vehicles," in *Electrical and Computer Engineering, 2006. CCECE '06. Canadian Conference on*, pp. 811-814, 2006.
- [29] X. D. Xue, K. W. E. Cheng, and N. C. Cheung, "Selection of electric motor drives for electric vehicles," in *Power Engineering Conference, 2008. AUPEC '08. Australasian Universities*, pp. 1-6, 2008.
- [30] *Toyota Prius*. Available: http://en.wikipedia.org/wiki/Toyota_Prius
- [31] *Chevrolet Volt*. Available: http://en.wikipedia.org/wiki/Chevrolet_Volt
- [32] *Nissan Leaf*. Available: http://en.wikipedia.org/wiki/Nissan_Leaf
- [33] *Tesla Model S*. Available: http://en.wikipedia.org/wiki/Tesla_Model_S
- [34] *Mitsubishi i-MiEV*. Available: http://en.wikipedia.org/wiki/Mitsubishi_i-MiEV
- [35] *Honda Civic*. Available: http://en.wikipedia.org/wiki/Honda_Civic_Hybrid
- [36] E. Levi, R. Bojoi, F. Profumo, H. A. Toliyat, and S. Williamson, "Multiphase induction motor drives - a technology status review," *Electric Power Applications, IET*, vol. 1, pp. 489-516, 2007.
- [37] S. Williamson and S. Smith, "Pulsating torque and losses in multiphase induction machines," *Industry Applications, IEEE Transactions on*, vol. 39, pp. 986-993, 2003.
- [38] A. Matyas, G. Aroquiadassou, C. Martis, A. Mpanda-Mabwe, and K. Biro, "Design of six-phase synchronous and induction machines for EPS," in *Electrical Machines (ICEM), 2010 XIX International Conference on*, pp. 1-6, 2010.
- [39] D. G. Dorrell, M. Popescu, L. Evans, D. A. Staton, and A. M. Knight, "Comparison of permanent magnet drive motor with a cage induction motor design for a hybrid electric vehicle," in *Power Electronics Conference (IPEC), 2010 International*, pp. 1807-1813, 2010.
- [40] Y. Ozoglu, M. Garip, and E. Mese, "New pole tip shapes mitigating torque ripple in short pitched and fully pitched switched reluctance motors," in *Industry Applications Conference, 2002. 37th IAS Annual Meeting. Conference Record of the*, pp. 43-50 vol.1, 2002.
- [41] T. Higuchi, T. Ueda, and T. Abe, "Torque ripple reduction control of a novel segment type SRM with 2-steps slide rotor," in *Power Electronics Conference (IPEC), 2010 International*, pp. 2175-2180, 2010.
- [42] M. Divandari and A. Dadpour, "Radial force and torque ripple optimization for acoustic noise reduction of SRM drives via fuzzy logic control," in *Industry Applications (INDUSCON), 2010 9th IEEE/IAS International Conference on*, pp. 1-6, 2010.

- [43] Z. Zhang, C. Cai, and W. Liu, "Study on reduction of running noise from a switched reluctance motor," in *Computer Science and Education (ICCSE), 2010 5th International Conference on*, pp. 1204-1027, 2010.
- [44] H. Ishikawa, W. Daohong, and H. Naitoh, "A new switched reluctance motor drive circuit for torque ripple reduction," in *Power Conversion Conference, 2002. PCC-Osaka 2002. Proceedings of the*, pp. 683-688 vol.2, 2002.
- [45] (3-May-2011). *Synchronous reluctance motors offer a choice of high outputs or IE4 efficiency*. Available: <http://www.drivesncontrols.com/news/archivestory.php/aid/3180/>
- [46] (21-Jun-2011). *Pilot user of synchronous reluctance drive reports 10% saving*. Available: <http://www.drivesncontrols.com/news/archivestory.php/aid/3251/>
- [47] (10-May-2012). *Pump-maker's synchronous reluctance motors meet IE4*. Available: <http://www.drivesncontrols.com/news/fullstory.php/aid/3502/>
- [48] (10-Dec-2012). *First trial of IE4 synchronous reluctance drive delivers 6% energy saving*. Available: <http://www.drivesncontrols.com/news/fullstory.php/aid/3689/>
- [49] V. Ostovic, "Memory motors-a new class of controllable flux PM machines for a true wide speed operation," in *Industry Applications Conference, 2001. Thirty-Sixth IAS Annual Meeting. Conference Record of the 2001 IEEE*, pp. 2577-2584 vol.4, 2001.
- [50] Y. Chuang, K. T. Chau, L. Xinhua, and J. Z. Jiang, "A flux-mnemonic permanent magnet brushless motor for electric vehicles," *Journal of Applied Physics*, vol. 103, pp. 07F103-07F103-3, 2008.
- [51] Y. Chuang, Z. Xiaodong, G. Shuang, and W. Diyun, "Comparison of permanent magnet brushless motors for electric vehicles," in *Vehicle Power and Propulsion Conference (VPPC), 2010 IEEE*, pp. 1-5, 2010.
- [52] D. Fodorean, A. Djerdir, I. A. Viorel, and A. Miraoui, "A Double Excited Synchronous Machine for Direct Drive Application—Design and Prototype Tests," *Energy Conversion, IEEE Transactions on*, vol. 22, pp. 656-665, 2007.
- [53] L. Yuefeng, F. Liang, and T. A. Lipo, "A novel permanent magnet motor with doubly salient structure," *Industry Applications, IEEE Transactions on*, vol. 31, pp. 1069-1078, 1995.
- [54] T. Kosaka, Y. Kano, N. Matsui, and C. Pollock, "A novel multi-pole permanent magnet synchronous machine with SMC bypass core for magnet flux and SMC field-pole core with toroidal coil for independent field strengthening/weakening," in *Power Electronics and Applications, 2005 European Conference on*, pp. 10 pp.-P.10, 2005.

- [55] M. Aydin, H. Surong, and T. A. Lipo, "Performance evaluation of an axial flux consequent pole PM motor using finite element analysis," in *Electric Machines and Drives Conference, 2003. IEMDC'03. IEEE International*, pp. 1682-1687 vol.3, 2003.
- [56] J. A. Tapia, F. Leonardi, and T. A. Lipo, "Consequent-pole permanent-magnet machine with extended field-weakening capability," *Industry Applications, IEEE Transactions on*, vol. 39, pp. 1704-1709, 2003.
- [57] E. H. Y. Amara, M. Gabsi, M. Lecrivain, A. H. B. Almed, and S. Derou, "Measured Performances of a New Hybrid Synchronous Machine," *EPE Journal*, vol. 12, pp. 42-50, 2002.
- [58] L. Vido, M. Gabsi, M. Lecrivain, Y. Amara, and F. Chabot, "Homopolar and bipolar hybrid excitation synchronous machines," in *Electric Machines and Drives, 2005 IEEE International Conference on*, pp. 1212-1218, 2005.
- [59] Y. Amara, J. Lucidarme, M. Gabsi, M. Lecrivain, A. H. B. Almed, and A. D. Akemakou, "A new topology of hybrid synchronous machine," *Industry Applications, IEEE Transactions on*, vol. 37, pp. 1273-1281, 2001.
- [60] C. C. Chan, K. T. Chau, J. Z. Jiang, W. Xia, M. Zhu, and R. Zhang, "Novel permanent magnet motor drives for electric vehicles," *Industrial Electronics, IEEE Transactions on*, vol. 43, pp. 331-339, 1996.
- [61] J. S. Hsu, L. Seong-Taek, and L. M. Tolbert, "High-Strength Undiffused Brushless (HSUB) Machine," in *Industry Applications Society Annual Meeting, 2008. IAS '08. IEEE*, pp. 1-8, 2008.
- [62] L. Xiaogang and T. A. Lipo, "A synchronous/permanent magnet hybrid AC machine," *Energy Conversion, IEEE Transactions on*, vol. 15, pp. 203-210, 2000.
- [63] T. Finken and K. Hameyer, "Study of Hybrid Excited Synchronous Alternators for Automotive Applications Using Coupled FE and Circuit Simulations," *Magnetics, IEEE Transactions on*, vol. 44, pp. 1598-1601, 2008.
- [64] N. Naoe and T. Fukami, "Trial production of a hybrid excitation type synchronous machine," in *Electric Machines and Drives Conference, 2001. IEMDC 2001. IEEE International*, pp. 545-547, 2001.
- [65] K. T. Chau, J. Z. Jiang, and W. Yong, "A novel stator doubly fed doubly salient permanent magnet brushless machine," *Magnetics, IEEE Transactions on*, vol. 39, pp. 3001-3003, 2003.
- [66] C. Ming, K. T. Chau, and C. C. Chan, "New split-winding doubly salient permanent magnet motor drive," *Aerospace and Electronic Systems, IEEE Transactions on*, vol. 39, pp. 202-210, 2003.

- [67] F. Ying and K. T. Chau, "Design, Modeling, and Analysis of a Brushless Doubly Fed Doubly Salient Machine for Electric Vehicles," *Industry Applications, IEEE Transactions on*, vol. 44, pp. 727-734, 2008.
- [68] E. Hoang, M. Lecrivain, and M. Gabsi, "A new structure of a switching flux synchronous polyphased machine with hybrid excitation," in *Power Electronics and Applications, 2007 European Conference on*, pp. 1-8, 2007.
- [69] L. Chunhua, K. T. Chau, J. Z. Jiang, L. Xinhua, and W. Zheng, "Design and Control of a Doubly-Excited Permanent-Magnet Brushless Integrated-Starter-Generator for Hybrid Electric Vehicles," in *Industry Applications Conference, 2007. 42nd IAS Annual Meeting. Conference Record of the 2007 IEEE*, pp. 1702-1709, 2007.
- [70] G. Dajaku and D. Gerling, "A Novel 24-Slots/10-Poles Winding Topology for Electric Machines," in *IEEE International Electric Machines & Drives Conference (IEMDC)*, pp. 65-70, 2011.
- [71] C. Yu, Z. Q. Zhu, and D. Howe, "Three-Dimensional Lumped-Parameter Magnetic Circuit Analysis of Single-Phase Flux-Switching Permanent-Magnet Motor," *Industry Applications, IEEE Transactions on*, vol. 44, pp. 1701-1710, 2008.
- [72] Z. Q. Zhu, Y. Pang, D. Howe, S. Iwasaki, R. Deodhar, and A. Pride, "Analysis of electromagnetic performance of flux-switching permanent-magnet Machines by nonlinear adaptive lumped parameter magnetic circuit model," *Magnetics, IEEE Transactions on*, vol. 41, pp. 4277-4287, 2005.
- [73] E. Hoang, A. H. Ben-Ahmed, and J. Lucidarme, "Switching flux permanent magnet polyphased synchronous machines," in *Proc. of 7th European Conference on Power Electronics and Applications*, pp. 903-908, 1997.
- [74] E. Hoang, M. Gabsi, M. Lecrivain, and B. Multon, "Influence of magnetic losses on maximum power limits of synchronous permanent magnet drives in flux-weakening mode," in *Industry Applications Conference, 2000. Conference Record of the 2000 IEEE*, pp. 299-303 vol.1, 2000.
- [75] E. Hoang, S. Hlioui, M. Lecrivain, and M. Gabsi, "Experimental comparison of lamination material case of switching flux synchronous machine with hybrid excitation," in *Power Electronics and Applications, 2009. EPE '09. 13th European Conference on*, pp. 1-7, 2009.
- [76] Y. Amara, L. Vido, M. Gabsi, E. Hoang, A. Hamid Ben Ahmed, and M. Lecrivain, "Hybrid Excitation Synchronous Machines: Energy-Efficient Solution for Vehicles Propulsion," *Vehicular Technology, IEEE Transactions on*, vol. 58, pp. 2137-2149, 2009.

- [77] E. Sulaiman, T. Kosaka, and N. Matsui, "Design and performance of 6-slot 5-pole PMFSM with hybrid excitation for hybrid electric vehicle applications," in *Power Electronics Conference (IPEC), 2010 International*, pp. 1962-1968, 2010.
- [78] E. Sulaiman, T. Kosaka, and N. Matsui, "FEA-based design and parameter optimization study of 6-slot 5-pole PMFSM with field excitation for Hybrid Electric Vehicle," in *Power and Energy (PECon), 2010 IEEE International Conference on*, pp. 206-211, 2010.
- [79] V. I. Patel and J. Wang, "Assessment of 12-slot, 14-pole permanent magnet flux switching machine with hybrid excitation for electric vehicle application," in *Energy Conversion Congress and Exposition (ECCE), 2013 IEEE*, pp. 5092-5099, 2013.
- [80] A. M. El-Refaie and T. M. Jahns, "Optimal flux weakening in surface PM machines using fractional-slot concentrated windings," *Industry Applications, IEEE Transactions on*, vol. 41, pp. 790-800, 2005.
- [81] N. Bianchi, S. Bolognani, M. D. Pr e, and G. Grezzani, "Design considerations for fractional-slot winding configurations of synchronous machines," *Industry Applications, IEEE Transactions on*, vol. 42, pp. 997-1006, 2006.
- [82] Z. Q. Zhu, D. Ishak, D. Howe, and C. Jintao, "Unbalanced Magnetic Forces in Permanent-Magnet Brushless Machines With Diametrically Asymmetric Phase Windings," *Industry Applications, IEEE Transactions on*, vol. 43, pp. 1544-1553, 2007.
- [83] A. M. El-Refaie, T. M. Jahns, and D. W. Novotny, "Analysis of surface permanent magnet machines with fractional-slot concentrated windings," *Energy Conversion, IEEE Transactions on*, vol. 21, pp. 34-43, 2006.
- [84] J. K. Tangudu, T. M. Jahns, and A. El-Refaie, "Unsaturated and saturated saliency trends in fractional-slot concentrated-winding interior permanent magnet machines," in *IEEE Energy Conversion Congress and Exposition (ECCE)*, pp. 1082-1089, 2010.
- [85] E. Sulaiman, T. Kosaka, Y. Tsujimori, and N. Matsui, "Design of 12-slot 10-pole Permanent Magnet Flux-Switching Machine with hybrid excitation for hybrid electric vehicle," in *Power Electronics, Machines and Drives (PEMD 2010), 5th IET International Conference on*, pp. 1-5, 2010.
- [86] J. Wang, X. Yuan, and K. Atallah, "Design Optimization of a Surface-Mounted Permanent-Magnet Motor With Concentrated Windings for Electric Vehicle Applications," *Vehicular Technology, IEEE Transactions on*, vol. 62, pp. 1053-1064, 2013.

-
- [87] P. Morrison, A. Binder, B. Funieru, and C. Sabirin, "Drive train design for medium-sized zero emission electric vehicles," in *Power Electronics and Applications, 2009. EPE '09. 13th European Conference on*, pp. 1-10, 2009.
- [88] K. Atallah, W. Jiabin, and D. Howe, "Torque-ripple minimization in modular permanent-magnet brushless machines," *Industry Applications, IEEE Transactions on*, vol. 39, pp. 1689-1695, 2003.
- [89] E. Hoang, M. Lecrivain, S. Hlioui, and M. Gabsi, "Hybrid excitation synchronous permanent magnets synchronous machines optimally designed for hybrid and full electrical vehicle," in *Power Electronics and ECCE Asia (ICPE & ECCE), 2011 IEEE 8th International Conference on*, pp. 153-160, 2011.
- [90] P. Lazari, J. Wang, and L. Chen, "A computationally efficient design technique for electric vehicle traction machines," in *Electrical Machines (ICEM), 2012 XXth International Conference on*, pp. 2596-2602, 2012.
- [91] A. G. Jack, B. C. Mecrow, P. G. Dickinson, D. Stephenson, J. S. Burdess, N. Fawcett, and J. T. Evans, "Permanent-magnet machines with powdered iron cores and prepressed windings," *Industry Applications, IEEE Transactions on*, vol. 36, pp. 1077-1084, 2000.
- [92] J. Wang, V. I. Patel, and W. Wang, "Fractional-Slot Permanent Magnet Brushless Machines with Low Space Harmonic Contents," *Magnetics, IEEE Transactions on*, vol. 50, pp. 1-9, 2014.
- [93] V. I. Patel, J. Wang, W. Wang, and X. Chen, "Analysis and design of 6-phase fractional slot per pole per phase permanent magnet machines with low space harmonics," in *IEEE International Electric Machines & Drives Conference (IEMDC)*, pp. 386-393, 2013.
- [94] E. M. Tingley, "Two-phase and three-phase lap windings in unequal groups," *Elec. Rev. and Western Electric*, vol. 66, pp. 166-168, 1915.
- [95] M. G. Malti and F. Herzog, "Fractional-Slot and Dead-Coil Windings," *American Institute of Electrical Engineers, Transactions of the*, vol. 59, pp. 782-794, 1940.
- [96] C. Shi-Uk, K. Jong-Moo, K. Dae-Hyun, W. Byung-Chul, H. Do-Kwan, and L. Ji-Young, "Fractional Slot Concentrated Winding Permanent Magnet Synchronous Machine With Consequent Pole Rotor for Low Speed Direct Drive," *Magnetics, IEEE Transactions on*, vol. 48, pp. 2965-2968, 2012.
- [97] T. T. T. Oikawa, K. Masumoto, H. Akita, H. Kawaguchi, and H. Kometani, "Development of high efficiency brushless DC motor with new manufacturing method of stator for compressors," presented at the International Compressor Engineering Conference, 2002.

-
- [98] Z. Q. Zhu and D. Howe, "Influence of design parameters on cogging torque in permanent magnet machines," *Energy Conversion, IEEE Transactions on*, vol. 15, pp. 407-412, 2000.
- [99] L. Sun-Kwon, K. Gyu-Hong, and H. Jin, "Finite Element Computation of Magnetic Vibration Sources in 100 kW Two Fractional-Slot Interior Permanent Magnet Machines for Ship," *Magnetics, IEEE Transactions on*, vol. 48, pp. 867-870, 2012.
- [100] W. Jiabin, K. Atallah, R. Chin, W. M. Arshad, and H. Lendenmann, "Rotor Eddy-Current Loss in Permanent-Magnet Brushless AC Machines," *Magnetics, IEEE Transactions on*, vol. 46, pp. 2701-2707, 2010.
- [101] L. Jian, C. Da-Woon, S. Dong-Hyeok, and C. Yun-Hyun, "Effects of MMF Harmonics on Rotor Eddy-Current Losses for Inner-Rotor Fractional Slot Axial Flux Permanent Magnet Synchronous Machines," *Magnetics, IEEE Transactions on*, vol. 48, pp. 839-842, 2012.
- [102] J. D. Ede, K. Atallah, G. W. Jewell, J. B. Wang, and D. Howe, "Effect of Axial Segmentation of Permanent Magnets on Rotor Loss in Modular Permanent-Magnet Brushless Machines," *Industry Applications, IEEE Transactions on*, vol. 43, pp. 1207-1213, 2007.
- [103] J. Wang, W. Wang, K. Atallah, and D. Howe, "Demagnetization Assessment for Three-Phase Tubular Brushless Permanent-Magnet Machines," *Magnetics, IEEE Transactions on*, vol. 44, pp. 2195-2203, 2008.
- [104] G. Dajaku, "Elektrische Maschine," DE 102008 057 349 B3, July 15, 2010.
- [105] G. Dajaku and D. Gerling, "A novel tooth concentrated winding with low space harmonic contents," in *Electric Machines & Drives Conference (IEMDC), 2013 IEEE International*, pp. 755-760, 2013.
- [106] P. B. Reddy, H. Kum-Kang, and A. El-Refaie, "Effect of stator shifting on harmonic cancellation and flux weakening performance of interior PM machines equipped with fractional-slot concentrated windings for hybrid traction applications," in *IEEE Energy Conversion Congress and Exposition (ECCE)*, pp. 525-533, 2012.
- [107] J. Wang, Z. P. Xia, and D. Howe, "Analysis of three-phase surface-mounted magnet modular permanent magnet machines," in *Power Electronics, Machines and Drives, 2004. (PEMD 2004). Second International Conference on (Conf. Publ. No. 498)*, pp. 27-32, 2004.
- [108] L. J. Wu, Z. Q. Zhu, J. T. Chen, and Z. P. Xia, "An Analytical Model of Unbalanced Magnetic Force in Fractional-Slot Surface-Mounted Permanent Magnet Machines," *Magnetics, IEEE Transactions on*, vol. 46, pp. 2686-2700, 2010.

- [109] C. Xiao, W. Jiabin, P. Lazari, and C. Liang, "Permanent Magnet Assisted Synchronous Reluctance Machine with fractional-slot winding configurations," in *Electric Machines & Drives Conference (IEMDC), 2013 IEEE International*, pp. 374-381, 2013.
- [110] V. Patel, J. Wang, W. Wang, and X. Chen, "6-phase Fractional Slot per Pole per Phase Permanent Magnet Machines with Low Space Harmonics for Electric Vehicle Application," *Industry Applications, IEEE Transactions on*, vol. PP, pp. 1-1, 2014.
- [111] V. Patel, J. Wang, J. Tousen, X. Motger, T. Hoffmann, R. Vuletic, . . . R. Bahr, "Subsystems specification report," FP7 - CASTOR Project Deliverable D1.4, 2011.
- [112] M. ANDRÉ, "Real-world driving cycles for measuring cars pollutant emissions – Part A: The ARTEMIS European driving cycles," Institut National De Recherche Sur Les Transports Et Leur Securite, 2004.
- [113] *SKF Bearings*. Available: <http://www.skf.com/uk/products/bearings-units-housings/ball-bearings>
- [114] K. Ressler, K. Brucker, and M. Nagurka, "A thermal time-constant experiment," *International Journal of Engineering Education*, vol. 19, pp. 603-609, 2003.
- [115] J. Goss, P. H. Mellor, R. Wrobel, D. A. Staton, and M. Popescu, "The design of AC permanent magnet motors for electric vehicles: A computationally efficient model of the operational envelope," in *Power Electronics, Machines and Drives (PEMD 2012), 6th IET International Conference on*, pp. 1-6, 2012.
- [116] KTY84 series: silicon temperature sensors [Online]. Available: http://www.nxp.com/documents/data_sheet/KTY84_SER.pdf
- [117] RM44 Encoder Base Unit [Online]. Available: <http://rls.si/en/rm44-up-to-13-bit-encoder-base-unit--15897>
- [118] R. Vuletic, D. Nugraha, T. Roewe, O. Vermesan, and J. Ostby, "Main Inverter Design Report," 2012.
- [119] (2010-2013). *Car Multi-Propulsion Integrated Power Train*. Available: <http://www.egvi.eu/projectslist/8/37/CASTOR>
- [120] *SKF Bearing Calculator*. Available: <http://www.skf.com/uk/knowledge-centre/engineering-tools/skfbearingcalculator.html>
- [121] J. E. Vrancik, "Prediction of windage power loss in alternators," NASA-Langley TND-4849, 1968.
- [122] C. Huynh, L. Zheng, and D. Acharya, "Losses in High Speed Permanent Magnet Machines Used in Microturbine Applications," *Journal of Engineering for Gas Turbines and Power*, vol. 131, pp. 022301:1-6, 2009.

- [123] K. M. Rahman and S. Hiti, "Identification of machine parameters of a synchronous motor," *Industry Applications, IEEE Transactions on*, vol. 41, pp. 557-565, 2005.
- [124] P. H. Mellor, R. Wrobel, and D. Holliday, "A computationally efficient iron loss model for brushless AC machines that caters for rated flux and field weakened operation," in *Electric Machines and Drives Conference, 2009. IEMDC '09. IEEE International*, pp. 490-494, 2009.
- [125] A. M. Technologies. *Neodymium-Iron-Boron Magnet Catalogs*. Available: http://www.arnoldmagnetics.com/Neodymium_Literature.aspx
- [126] A. M. Technologies. *RECOMA Samarium Cobalt Magnet Catalogs*. Available: http://www.arnoldmagnetics.com/Samarium_Cobalt_Literature.aspx
- [127] V. I. Patel and J. Wang, "Effect of phase shifts on PM eddy current loss and unbalanced magnetic force in 6-phase fractional slot PM machines with low space harmonics content," *IEEE Transactions on Magnetics*, vol. Submitted for review on 1 Mar. 2014, 2014.
- [128] V. I. Patel and J. Wang, "Demagnetization assessment of 6-phase fractional slot per pole per phase permanent magnet machines with low space harmonics for various fault conditions at different speeds," in *IET International Power Electronics, Machines and Drives Conference (PEMD)*, Manchester, 2014.
- [129] V. I. Patel, J. Wang, W. Wang, and X. Chen, "Thermal design and analysis of 6-phase fractional slot permanent magnet machines considering driving cycles," in *IET International Power Electronics, Machines and Drives Conference (PEMD)*, Manchester, 2014.
- [130] J. Wang, Z. P. Xia, S. A. Long, and D. Howe, "Radial force density and vibration characteristics of modular permanent magnet brushless ac machine," *IEE Proceedings on Electric Power Applications*, vol. 153, pp. 793-801, 2006.
- [131] Z. Q. Zhu and D. Howe, "Electrical Machines and Drives for Electric, Hybrid, and Fuel Cell Vehicles," *Proceedings of the IEEE*, vol. 95, pp. 746-765, 2007.
- [132] S. Ruoho, E. Dlala, and A. Arkkio, "Comparison of Demagnetization Models for Finite-Element Analysis of Permanent-Magnet Synchronous Machines," *Magnetics, IEEE Transactions on*, vol. 43, pp. 3964-3968, 2007.
- [133] P. Zhou, D. Lin, Y. Xiao, N. Lambert, and M. A. Rahman, "Temperature-Dependent Demagnetization Model of Permanent Magnets for Finite Element Analysis," *Magnetics, IEEE Transactions on*, vol. 48, pp. 1031-1034, 2012.
- [134] K. Ki-Chan, K. Kwangsoo, K. Hee-jun, and L. Ju, "Demagnetization Analysis of Permanent Magnets According to Rotor Types of Interior Permanent Magnet Synchronous Motor," *Magnetics, IEEE Transactions on*, vol. 45, pp. 2799-2802, 2009.

-
- [135] Z. Guoxin, T. Lijian, S. Qiping, and T. Renyuan, "Demagnetization Analysis of Permanent Magnet Synchronous Machines under Short Circuit Fault," in *Power and Energy Engineering Conference (APPEEC), 2010 Asia-Pacific*, pp. 1-4, 2010.
- [136] C. Gilsu and T. M. Jahns, "Interior permanent magnet synchronous machine rotor demagnetization characteristics under fault conditions," in *Energy Conversion Congress and Exposition (ECCE), 2013 IEEE*, pp. 2500-2507, 2013.
- [137] J. McFarland and T. Jahns, "Investigation of the Rotor Demagnetization Characteristics of Interior PM Synchronous Machines during Fault Conditions," *Industry Applications, IEEE Transactions on*, vol. PP, pp. 1-1, 2013.
- [138] COBHAM. *Characterising lifecycle behaviour of permanent magnets is critical to emergent electrical machine applications*. Available: http://motor-design-software.com/brushless-machines/characterising-lifecycle-behaviour-permanent-magnets-critical-emergent-electrical-machine-applications/?utm_source=Vectorfields-Email-List&utm_campaign=ae42907320-DeMag_PRII_21_2013&utm_medium=email&utm_term=0_83240751eb-ae42907320-35735569
- [139] A. Boglietti, A. Cavagnino, M. Popescu, and D. Staton, "Thermal Model and Analysis of Wound Rotor Induction Machine," *Industry Applications, IEEE Transactions on*, vol. PP, pp. 1-1, 2013.
- [140] G. D. Demetriades, H. Z. de la Parra, E. Andersson, and H. Olsson, "A Real-Time Thermal Model of a Permanent-Magnet Synchronous Motor," *Power Electronics, IEEE Transactions on*, vol. 25, pp. 463-474, 2010.
- [141] F. JinXin, Z. Chengning, W. Zhifu, A. R. Tariq, C. E. Nino, and E. G. Strangas, "Design and thermal analysis of traction motor for electric vehicle based on driving duty cycle," in *Electromagnetic Field Computation (CEFC), 2010 14th Biennial IEEE Conference on*, pp. 1-1, 2010.
- [142] F. Marignetti and V. Delli Colli, "Thermal Analysis of an Axial Flux Permanent-Magnet Synchronous Machine," *Magnetics, IEEE Transactions on*, vol. 45, pp. 2970-2975, 2009.
- [143] D. Staton, A. Boglietti, and A. Cavagnino, "Solving the More Difficult Aspects of Electric Motor Thermal Analysis in Small and Medium Size Industrial Induction Motors," *Energy Conversion, IEEE Transactions on*, vol. 20, pp. 620-628, 2005.
- [144] P. K. Vong and D. Rodger, "Coupled electromagnetic-thermal modeling of electrical machines," *Magnetics, IEEE Transactions on*, vol. 39, pp. 1614-1617, 2003.

- [145] T. Wenming, T. Renyun, A. Zhongliang, and S. Qiping, "Water cooling system design and thermal analysis for low speed permanent magnet machines," in *Electrical Machines and Systems (ICEMS), 2011 International Conference on*, pp. 1-4, 2011.
- [146] R. Wrobel, J. Goss, A. Mlot, and P. Mellor, "Design Considerations of a Brushless Open-Slot Radial-Flux PM Hub Motor," *Industry Applications, IEEE Transactions on*, vol. PP, pp. 1-1, 2013.
- [147] X. Chen, J. Wang, and V. Patel, "A generic approach to reduction of magneto-motive-force harmonics in permanent magnet machines with concentrated, multiple 3-phase windings," *IEEE Transactions on Magnetics*, vol. Submitted for review in March 2014, pp. 1-4, 2014.

Table of Figures

Figure 1.1. Primary energy demand of the world in past two decades	2
Figure 1.2. New registrations of vehicles in the world ²	2
Figure 1.3. Timeline of Electric Vehicles [4-6]	4
Figure 1.4. Sales of HEV in United States.....	5
Figure 1.5. Sales of PEV in United States	5
Figure 1.6. Architecture of HEVs	9
Figure 1.7. Architecture of BEVs.....	11
Figure 1.8. Centralized power drivetrain for a small BEV	12
Figure 2.1. Typical torque-speed characteristics of EV traction motor	26
Figure 2.2. Cross-section of conventional electrical machine technologies	27
Figure 2.3 Cross-section of synchronous reluctance machine	36
Figure 2.4 Classification of permanent magnet machines.....	38
Figure 2.5 Cross-section of IPM and SPM machines	39
Figure 2.6 Cross-section of different types of variable flux machines	42
Figure 2.7 Cross-section of mechanically adjusted DSPM machines	43
Figure 2.8 Cross-section of different types of hybrid excited PM machines.....	44
Figure 2.9 Classification of parallel flux path hybrid excited PM machines.....	45
Figure 2.10 Radial flux CPMM machine and Claw pole machine (shown without PMs).....	46
Figure 2.11 Typical SynRM machine and dual-rotors machine.....	47
Figure 2.12 Cross-section of parallel flux hybrid excited PM machines having PM and field coils on the stator.....	48

Figure 3.1. Cross-section of a 12-slot, 14-pole, SPM machine.....	53
Figure 3.2. Cross-section of a 24-slot, 14-pole, IPM machine.....	55
Figure 3.3. Cross-section of a 12-slot, 14-pole HE-PMFSM.....	56
Figure 3.4. Principle of flux switching and flux concentration.....	57
Figure 3.5. Architecture of distributed power drivetrain for preliminary design study.....	59
Figure 3.6. The New European Driving Cycle (NEDC).....	60
Figure 3.7. Target torque-speed characteristics for the preliminary design study	60
Figure 3.8. Cross-section of FSCW 24-slot, 14-pole IPM with influential geometrical parameters.....	62
Figure 3.9. Design optimization trends for FSCW 24-slot, 14-pole IPM.....	63
Figure 3.10. Cross-section of the optimized design for FSCW 24-slot, 14-pole IPM	64
Figure 3.11. Influential geometrical parameters of 12-slot, 14-pole HE-PMFSM.....	65
Figure 3.12. Design optimization trends for 12-slot, 14-pole HE-PMFSM.....	67
Figure 3.13. Cross-section of the optimized design for 12-slot, 14-pole HE-PMFSM (armature windings are not shown for clarity).....	68
Figure 3.14. Per unit flux linkage, back EMF and EMF harmonics of the promising machine technologies at the base speed of 1350 rpm.....	70
Figure 3.15. Torque waveforms of the promising machine technologies at the base speed of 1350 rpm.....	71
Figure 3.16. Torque-speed characteristics of the machine with 12 NEDC points ...	76
Figure 4.1. Schematic of 3-phase, 9-slot, 8-pole winding configuration as per prior art.....	85
Figure 4.2. Schematic of proposed 3-phase, 18-slot, 8-pole winding configuration	86
Figure 4.3. Stator MMF profiles of 9-slot, 8-pole and the proposed 18-slot, 8-pole winding configurations.....	88

Figure 4.4. Normalized stator MMF space harmonics distribution	89
Figure 4.5. Schematic of 9-slot, 10-pole and proposed 18-slot, 10-pole winding configuration.....	90
Figure 4.6. Normalized stator MMF space harmonics distribution for the proposed 3-phase, 18-slot, 10-pole winding configuration	91
Figure 4.7. Schematic of the proposed 3-phase, 36-slot, 8-pole winding configuration	93
Figure 4.8. Normalized stator MMF space harmonics distribution of the proposed 3-phase, 36-slot, 8-pole winding configuration	94
Figure 4.9. Application of proposed winding configurations to various machine technologies.....	95
Figure 4.10. Schematic of the proposed 6-phase, 16-slot, 8-pole winding configuration.....	97
Figure 4.11. Stator MMF profile of 6-phase, 18-slot, 8-pole winding configuration.	98
Figure 4.12. Comparison of normalized stator MMF space harmonics distribution	99
Figure 4.13. Phase shift between two sets of 3-phase windings in a 6-phase machine	100
Figure 4.14. Reduction technique by analysing phase space vectors in 6-phase machine	102
Figure 4.15. Comparison of normalized stator MMF space harmonics distribution for various phase shifts between A-B-C and D-E-F in 6-phase, 18-slot, 8-pole winding configuration.....	103
Figure 5.1. Centralized power drivetrain configuration for a segment-A vehicle.	106
Figure 5.2. Required wheel torque, wheel power for the segment-A vehicle over the NEDC.....	109
Figure 5.3. MATLAB Simulink model to check acceleration performance targets	110

Figure 5.4. Torque-speed characteristics of the segment-A vehicle	112
Figure 5.5. Torque-speed characteristics for the drive motor of the segment-A vehicle along with the NEDC envelope.....	113
Figure 5.6. The Artemis Urban Driving Cycle (AUDC)	113
Figure 5.7. Torque and power requirements over the AUDC	114
Figure 5.8. Torque-speed characteristics for the drive motor of the segment-A vehicle along with the Artemis Urban Driving Cycle envelope	115
Figure 5.9. Energy distribution of the EV under consideration over the NEDC....	118
Figure 5.10. Energy distribution of the EV under consideration over the NEDC, excluding the six operating points having maximum energy.....	118
Figure 5.11. Variation of minimum and maximum d-axis inductance with number of pole pairs for 6-phase IPM machine	123
Figure 5.12. Cross-section of 18-slot, 8-pole IPM machine with influential geometrical parameters, phase windings are not shown for clarity.	125
Figure 5.13. Flow-chart for the design of 6-phase, 18-slot, 8-pole IPM machine.....	126
Figure 5.14. Design optimization trends during one of the design iteration.....	128
Figure 5.15. Cross-section of optimized 6-pase, 18-slot, 8-pole IPM machine.....	129
Figure 5.16. Geometry of the optimized rotor pole for mechanical stress analysis.	131
Figure 5.17. Von Mises stress plot of the optimized rotor lamination at 18000 rpm.	131
Figure 5.18. Rotor geometry for the rotor dynamics study and first order bending modes.	132
Figure 5.19. Cambell diagram of the optimized 18-slot, 8-pole IPM rotor.	133
Figure 5.20. Machine enclosure designed for thermal cooling (a) cooling chamber, (b) cooling sleeve, (c) cooling jacket.	134

Figure 5.21. Representative cross-section of the cooling chamber.....	136
Figure 5.22. Radial and axial cross-section of the machine model in Motor-CAD.	137
Figure 5.23. Transient temperature response of the machine components at maximum cruise speed operation (19.1 N·m, 22 kW, 11000 rpm).....	139
Figure 5.24. Optimized cross-section of 6-phase, 18-slot, 8-pole IPM machine.....	149
Figure 5.25. Torque profile of the optimized machine over an electrical cycle.....	150
Figure 5.26. Flux plots from 2-D FEA at the rated torque operation (74.0 N·m, 22 kW, 2800 rpm).....	152
Figure 5.27. Predicted efficiency map of 6-phase, 18-slot, 8-pole IPM machine.....	153
Figure 5.28. Predicted efficiency map of 6-phase, 18-slot, 8-pole IPM machine under 3-phase operation (A-B-C in operation, D-E-F open circuited).....	154
Figure 5.29. Inductance map of 6-phase, 18-slot, 8-pole IPM machine.....	157
Figure 5.30. Flux-linkage map of 6-phase, 18-slot, 8-pole IPM machine.	158
Figure 5.31. PM flux-linkage map of 6-phase, 18-slot, 8-pole IPM machine.	159
Figure 6.1. Components and sub-assembly of the stator.....	161
Figure 6.2. Developed winding diagram of the novel fractional-slot 6-phase, 18-slot, 8-pole topology.	162
Figure 6.3. Components and sub-assembly of the rotor.	163
Figure 6.4. Assembly of the prototype motor.	163
Figure 6.5. Configuration of signal connector.	164
Figure 6.6. Schematic of test set-up with data acquisition system.	167
Figure 6.7. Prototype motor mounted on test bench with in-line torque transducer.	168
Figure 6.8. Development of a phase coil in the prototype machine.....	172

Figure 6.9. Measured back EMF at different speeds to determine back EMF constant.....	176
Figure 6.10. Measured and predicted back EMF waveform at 2800 rpm.	177
Figure 6.11. Speed versus time curve during the mechanical integrity check on the prototype motor.	178
Figure 6.12. Measured no-load loss of the prototype motor.....	180
Figure 6.13. Measured bearing friction and windage loss using dummy rotor.	180
Figure 6.14. Comparison of measured and predicted no-load iron loss of the motor.	181
Figure 6.15. Measured phase current, phase voltage, and position signal	187
Figure 6.16. Comparison of measured and predicted d-axis inductance with $I_q = 10$ A.....	188
Figure 6.17. Comparison of measured and predicted q-axis inductance with $I_d = 0$ A.	188
Figure 6.18. d-q axis circuit representation involving iron loss.....	190
Figure 6.19. Comparison of permanent magnet flux linkage when $I_d = 0$ A.....	193
Figure 6.20. Comparison of measured and predicted efficiency of prototype IPM machine at base speed of 2800 rpm with DC link voltage of 275V.	193
Figure 6.21. Comparison of predicted and measured efficiency map up to 5000 rpm.	195
Figure 6.22. Comparison of predicted and calibrated efficiency map.....	196
Figure 6.23. Tested torque-speed envelope of the prototype motor with only one set of 3-phase windings excited and fed by one 3-phase inverter.....	197
Figure 6.24. Comparison of the predicted and the measured efficiency of the prototype motor in 3-phase operation mode at 2800 rpm.	198
Figure 6.25. Comparison of the predicted and the measured transient temperatures of the motor windings at the rated torque operation.....	199

Figure 6.26. Predicted transient temperatures of the motor components at the rated torque operation based on the thermal test.	200
Figure 6.27. Sequence of events during the incident of partial demagnetization of the prototype motor.	201
Figure 6.28. Designed capability of the prototype motor and the test point.	203
Figure 6.29. MATLAB simulation to replicate the observed behaviour during the incident, Simulation case of A-B-C losing control and demagnetization happens gradually over 0.5 sec, Top chart shows reference and actual values of I_d , I_q for A-B-C, and D-E-F respectively, whereas bottom chart shows the torque-speed envelope with torque response of the motor during the incident.	204
Figure 6.30. Transient response of the motor over the test sequence with DC link voltage of 250V, 15 litre/min, 20°C ambient air and water inlet temperature.	207
Figure 6.31. Comparison of characteristics of M270-35A and NO20 electrical steel.	211
Figure 6.32. Measured back EMF of 2 nd prototype motor at room temperature of 23°C.	214
Figure 6.33. Comparison of measured and predicted no-load iron loss for 2 nd prototype.	215
Figure 6.34. Comparison of efficiency map of 2 nd prototype motor at 250 V.	217
Figure 6.35. Comparison of efficiency map of 2 nd prototype motor at 320 V.	218
Figure 6.36. Comparison of calibrated efficiency map of 2 nd prototype motor for different DC link voltages.	219
Figure 6.37. Comparison of measured and predicted transient temperatures of 2 nd prototype at the maximum cruise speed operation with 250 V.	221
Figure 6.38. Back EMF waveform recorded at 5000 rpm after reaching thermal steady-state for operation at 24 N·m, 8600 rpm.	222
Figure 7.1. Possible phase shifts in 6-phase, 18-slot, 8-pole winding configuration.	224

Figure 7.2. Variation of magnet eddy current loss over an electric cycle for various phase shifts between A-B-C and D-E-F windings of 6-phase, 18-slot, 8-pole IPM machine.....	226
Figure 7.3. Harmonics distribution of magnet eddy current loss for various phase shifts between A-B-C and D-E-F windings of 6-phase, 18-slot, 8-pole IPM machine at different operating conditions.	229
Figure 7.4. Radial and tangential flux density in the air-gap at no-load.....	232
Figure 7.5. Radial force density in the air-gap at no-load, $t = 0$	233
Figure 7.6. Radial and tangential flux density in the air-gap at the rated torque operation for various phase shifts between A-B-C and D-E-F windings.	234
Figure 7.7. Radial force density in the air-gap at the rated torque, $t = 0$	235
Figure 7.8. Comparison of unbalanced magnetic pull for various phase shifts in 6-phase, 18-slot, 8-pole IPM machine and 3-phase, 9-slot, 8-pole IPM machine, under the rated torque operation.	236
Figure 7.9. Cross-section of 6-phase, 18-slot, 8-pole IPM machine.	239
Figure 7.10. Circuit model for creating short circuit in 2-D transient FEA.....	240
Figure 7.11. Decomposition of nodal flux density of a magnet in the direction of magnetization.	241
Figure 7.12. Transient response of 6-phase, 18-slot, 8-pole IPM machine under short circuit fault at the rated torque operation.....	243
Figure 7.13. Current trajectories of 6-phase, 18-slot, 8-pole IPM machine under short circuit fault at various pre-fault operating conditions (F1, F2, ..., F6).....	244
Figure 7.14. Nodes of 1 st magnet of 1 st pole (M1P1).	245
Figure 7.15. Demagnetization in different poles during 6-phase SC at T_{rated}	246
Figure 7.16. Partially demagnetized area of selected magnets during the transient (% denotes demagnetized nodes of the total nodes).	249

Figure 7.17. Partially demagnetized area of the rotor pole having maximum demagnetization during the transient for various 6-phase SC faults.	250
Figure 7.18. Transient response of 6-phase, 18-slot, 8-pole IPM machine under short circuit fault at the peak torque operation.....	251
Figure 7.19. Current density distribution in phase windings at rotor position 80° during 6-phase SC fault at the peak torque operation.	252
Figure 7.20. MMF distribution of the machine at rotor position 80° during 6-phase SC fault at the peak torque operation.....	253
Figure 7.21. Comparison of optimized cross-section of fractional-slot (6-phase, 18-slot, 8-pole) and distributed wound (6-phase, 48-slot, 8-pole) IPM machines.	254
Figure 7.22. Comparison of machine behaviour under 6-phase SC fault at the peak torque operation for 6-phase, 18-slot, 8-pole and 6-phase, 48-slot, 8-pole IPM machines.	257
Figure 7.23. Comparison of machine behaviour under 6-phase SC fault at the rated torque operation for 6-phase, 18-slot, 8-pole and 6-phase, 48-slot, 8-pole IPM machines.	258
Figure 7.24. Partially demagnetized area of 1 st pole magnets during the transient (% denotes demagnetized nodes of the total nodes) for 6-phase, 18-slot, 8-pole and 6-phase, 48-slot, 8-pole IPM machines for 6-phase SC faults at different operating conditions.	260
Figure 7.25. The New European Driving Cycle and corresponding torque requirements of the motor.....	264
Figure 7.26. Transient temperature response of the motor winding and the rotor magnets of 6-phase, 18-slot, 8-pole IPM machine over repeated NEDC cycle.	264
Figure 7.27. The Artemis Urban Driving Cycle and corresponding torque requirements of the motor.....	266
Figure 7.28. Transient temperature response of the motor winding and the rotor magnets of 6-phase, 18-slot, 8-pole IPM machine over repeated AUDC cycle.	266

List of Tables

Table 1.1. Classification of cars [8, 9]	13
Table 1.2. Classification of EVs [7]	13
Table 1.3. Most popular electric cars across the world	14
Table 1.4. New EV announcements in recent past and the near future	15
Table 1.5. Target goals for traction drive system in future EVs [11]	16
Table 2.1. Performance comparison of IM, PM and SRM [25]	31
Table 2.2. Qualitative comparison of conventional machine technologies	32
Table 2.3. Qualitative comparison of SPM and IPM with different winding configurations	40
Table 3.1. Design constraints for the preliminary design study	61
Table 3.2. Optimized geometrical parameters of FSCW 24-slot, 14-pole IPM	64
Table 3.3. Optimized geometrical parameters of 12-slot, 14-pole HE-PMFSM	68
Table 3.4. Performance comparison of the promising machine technologies for EV traction	72
Table 3.5. Performance comparison of the promising machine technologies for EV traction	72
Table 4.1. Comparison of working harmonic, most dominant higher and lower order space harmonics, and total harmonic distortion for various slot-pole combinations	81
Table 4.2. Slot-pole combinations of prior art	84
Table 4.3. Proposed slot-pole combinations having low space harmonics in stator MMF	92
Table 4.4. Possible phase shifts in 6-phase, 18-slot, 8-pole winding configuration	101

Table 4.5. Reduced phase shifts in 6-phase, 18-slot, 8-pole winding configuration	102
Table 4.6. Total harmonic distortion for various phase shifts.....	104
Table 5.1. Typical vehicle data of a segment-A vehicle	106
Table 5.2. Acceleration performance requirements for a segment-A vehicle	107
Table 5.3. Comparison of acceleration and drive-away performance for the segment-A vehicle for two different peak torque ratings	111
Table 5.4. Design specifications of the traction motor for a centralized power drivetrain in the segment-A electric vehicle	116
Table 5.5. Representative points of the NEDC for the EV under consideration	119
Table 5.6. Volumetric, electrical, mechanical and thermal constraints	123
Table 5.7. Geometrical parameters of the machine.	130
Table 5.8. Sensitivity study for rotor dynamics	133
Table 5.9. Design calculation for the cooling chamber.....	136
Table 5.10. Input data to Motor-CAD model for thermal analysis.	137
Table 5.11. Steady-state temperatures of the machine components at maximum cruise speed operation (19.1 N·m, 22 kW, 11000 rpm).....	140
Table 5.12. Comparison of losses in machine at two different operating conditions.	140
Table 5.13. Comparison of machine temperatures at two different operating conditions.	141
Table 5.14. Sensitivity of machine temperatures with losses.	142
Table 5.15. Losses in machine components with steel lamination thickness.	143
Table 5.16. Influence of lamination thickness on machine temperatures.....	143
Table 5.17. Machine temperatures with 0.2 mm thick rotor lamination with 115% copper loss and 150% iron loss.	144

Table 5.18. Influence of vent holes on machine temperatures.....	145
Table 5.19. Machine temperatures with open vent holes ($4 \times \text{Ø}25$ mm) in end plates with 115% copper loss and 150% iron loss.....	145
Table 5.20. Influence of water flow rate on machine temperatures.....	146
Table 5.21. Sensitivity of the machine temperatures with rotor radial fins.	147
Table 5.22. Important design parameters of the optimized machine.	148
Table 5.23. Performance of the optimized machine at the rated and the peak torque operation at the base speed.....	149
Table 5.24. Performance of the optimized machine over 12 representative points for the NEDC.....	151
Table 6.1. Instrumentation and feedback device.....	164
Table 6.2. Signal connector terminal identification	165
Table 6.3. List of instruments and equipment used in the test set-up.....	166
Table 6.4. List of files acquiring real-time data during the tests	170
Table 6.5. Environmental conditions during the preliminary tests	170
Table 6.6. List of preliminary tests.....	170
Table 6.7. Resistance measurement before making neutral points at 28°C	173
Table 6.8. Resistance measurement after cable connections at 17°C	174
Table 6.9. Comparison of measured resistance with calculated one at 17°C	175
Table 6.10. Summary of measured per phase resistance at 17°C	175
Table 6.11. Comparison of measured and predicted back EMF at room temperature	177
Table 6.12. Validation of torque control mode at different speeds	184
Table 6.13. Validation of current control mode at different speeds & currents	184

Table 6.14. Comparison of measured and the reference currents in current control mode.....	185
Table 6.15. Comparison of measured and predicted torque under current control mode.....	191
Table 6.16. Comparison of measured torque with reference torque at 1500 rpm..	192
Table 6.17. Steady-state thermal analyses at various DC link voltages.....	206
Table 6.18. Comparison of two prototype rotors.....	210
Table 6.19. Comparison of material properties of M270-35A and NO20.....	210
Table 6.20. Comparison of magnet properties of NdFeB and Sm ₂ Co ₁₇ [125, 126]....	211
Table 6.21. Performance prediction for 2 nd prototype motor.....	212
Table 6.22. Important parameters observed during the thermal test.....	220
Table 7.1. Various operating conditions to evaluate the effect of phase shifts on PM eddy current loss.....	225
Table 7.2. Magnet eddy current loss for various phase shifts.....	227
Table 7.3. Frequencies and skin depth of forward and backward rotating MMF space harmonics at maximum cruise speed operation.....	228
Table 7.4. Magnet eddy current loss for various phase shifts in 2 nd prototype machine (NO20 electrical steel in rotor and Sm ₂ Co ₁₇ magnets.....	230
Table 7.5. Various fault conditions for demagnetization assessment.....	240
Table 7.6. Decomposition angle for various magnets.....	242
Table 7.7. Comparison of peak transient torque and currents for various fault conditions.....	242
Table 7.8. Comparison of lowest flux density along the magnetizing direction of all magnets during the transient under various fault conditions.....	247
Table 7.9. Amplitude of phase currents at rotor position 80° during 6-phase SC fault at the peak torque operation.....	252

Table 7.10. Performance comparison of fractional-slot (6-phase, 18-slot, 8-pole) and distributed wound (6-phase, 48-slot, 8-pole) IPM machines 255

Table 7.11. Comparison of peak transient torque and currents for 6-phase, 18-slot, 8-pole and 6-phase, 48-slot, 8-pole IPM machines 256

List of Symbols and Acronyms

Symbols

<i>Symbol</i>	<i>Description</i>
η_{NEDC}	Energy efficiency over the NEDC, %
μ_0	Permeability of free space, H/m ²
λ_d	<i>d</i> -axis flux linkage, Wb
η_g	Efficiency of the differential, %
λ_m	Permanent magnet flux linkage, Wb
λ_q	<i>q</i> -axis flux linkage, Wb
μ_r	Relative permeability
α_s	Number of slot shifts
ΔT	Temperature difference, °C
α_{T-PM}	Reversible temperature co-efficient of induction, %/ °C
A	Surface area required for heat dissipation, m ²
a_e	Open circuit eddy current loss of the machine, W
A_e	Area of an element, mm ²
A_{gc}	Surface area per groove, m ²
a_h	Open circuit hysteresis loss of the machine, W
a_x	Open circuit excess loss of the machine, W
B	Viscous friction coefficient, N·m·s
b_1	Width of the groove, mm
b_2	Width of the cooling channel wall, mm
b_e	Short circuit eddy current loss of the machine, W
b_h	Short circuit hysteresis loss of the machine, W
BI	Stator back iron thickness, mm

<i>Symbol</i>	<i>Description</i>
B_{Pxn}	Nodal flux density in the direction of magnetization, T
B_r	Residual induction in a magnet, T
B_r	Radial flux density in the air-gap, T
<i>BRIDGE</i>	Rotor bridge thickness, mm
B_t	Tangential flux density in the air-gap, T
b_x	Short circuit excess loss of the machine, W
B_{Xn}	Nodal flux density in x -direction, T
B_{Yn}	Nodal flux density in y -direction, T
C	Calculated or predicted value of a quantity
c_dA	Product of drag coefficient and frontal area, m ²
D	Stator outer diameter, mm
d_p	Rotor pole depth, mm
d_s	Stator slot depth, mm
dt	Time duration, s
E	Induced back EMF, V
E_m	Maximum permissible line-line voltage, V
E_{T0}	Back EMF of the machine at room temperature, V
E_{Tl}	Back EMF of the machine at temperature T_l , V
F	Net force required by the vehicle, N
F_a	Force required to overcome the air drag resistance, N
F_i	Force required to overcome the inertia of the vehicle, N
f_{offset}	Offset parameter to control the area of field windings, mm
F_r	Force required to overcome the rolling resistance, N
f_r	Reference frequency, Hz
F_{rd}	Radial force density, N/m ²
g	Gravitational constant, m/s ²

<i>Symbol</i>	<i>Description</i>
G_r	Differential gear ratio
h	Height of the groove or the cooling channel wall, mm
h_a	Height of armature slot, mm
h_c	Convection heat transfer coefficient, W/m ² /°C
h_{pm}	Height of permanent magnet, mm
h_q	Magnet cap depth, mm
i_d	d -axis current, A
i_{da}	d -axis current influenced by the iron loss of the machine, A
i_{db}	d -axis current for the peak torque at the base speed, A
i_{dm}	d -axis current for the peak torque at the maximum cruise speed, A
I_m	Maximum machine current, A
$IPMHQ$	Magnet cap depth, mm
i_q	q -axis current, A
i_{qa}	q -axis current influenced by the iron loss of the machine, A
i_{qb}	q -axis current for the peak torque at the base speed, A
i_{qm}	q -axis current for the peak torque at the maximum cruise speed, A
J	Moment of inertia of the system, kg·m ²
J_c	Continuous current density, A/mm ²
J_e	Current density of an element, A/mm ²
k	Integer
K_e	Back EMF constant, V/rpm
k_r	Rolling resistance coefficient
k_s	The saliency ratio
L	Stack length of the machine, mm
L_d	d -axis inductance, H
L_{d-max}	Maximum d -axis inductance, H

<i>Symbol</i>	<i>Description</i>
$L_{d\text{-min}}$	Minimum d -axis inductance, H
l_g	Length of air-gap, mm
LM	Length of magnet, mm
l_m	Length of magnet, mm
L_q	q -axis inductance, H
m	Number of phases
$MAGWID$	Width of magnet per pole, mm
m_{pm}	Mass of magnet material, kg
m_v	Mass of the vehicle, kg
N	Rotational speed, rpm
n	Harmonic number
n	Magnet node number
N_c	Number of coils per phase
n_e	Number of elements in a magnet
N_g	Number of grooves
N_s	Number of stator slots
p	Number of pole pairs
P	Number of poles
P	Heat to be dissipated, W
P_{bf}	Bearing friction loss of the machine, W
P_c	Continuous rated power, kW
P_{cu}	Copper loss, W
P_{fe}	Iron loss, W
P_{fe-OC}	Open circuit iron loss of the machine, W
P_{fe-SC}	Short circuit iron loss of the machine, W
P_{nl}	No-load loss of the machine, W

<i>Symbol</i>	<i>Description</i>
P_{nl-fe}	No-load iron loss of the machine, W
P_{pb}	Peak power at base speed, kW
P_{pc}	Peak power at maximum cruise speed, kW
P_{pm}	Peak power at maximum speed, kW
P_w	Windage loss of the machine, W
q	Ratio of the number of slots per phase to the number of poles
R	Resistance of the phase windings, Ω
$RADI$	Rotor radius, mm
R_{fe-d}	d -axis resistance to represent iron loss, Ω
R_{fe-q}	q -axis resistance to represent iron loss, Ω
R_{gb}	Groove bottom radius, mm
r_r	Rotor radius, mm
r_s	Stator outer radius, mm
r_{sh}	Rotor shaft radius, mm
r_w	Radius of the wheel, mm
SD	Stator slot depth, mm
S_o	Stator slot opening, mm
S_{od}	Stator slot opening depth, mm
T	Test or measured value of a quantity
t	Time instant, s
T_a	Ambient air temperature, $^{\circ}\text{C}$
T_c	Rated torque below and at base speed, N·m
TC	Thermocouple
T_{cc}	Continuous torque at maximum cruise speed, N·m
T_{cu}	Copper winding temperature, $^{\circ}\text{C}$
T_e	Electromagnetic torque of the machine, N·m

<i>Symbol</i>	<i>Description</i>
T_{fe}	Steel lamination temperature, °C
TH	Thermistor
T_L	Load torque, N·m
T_m	Torque of the machine, N·m
t_n	Number of turns per coil
T_p	Peak torque below and at base speed, N·m
T_{pc}	Peak torque at maximum cruise speed, N·m
T_{pm}	Permanent magnet temperature, °C
T_w	Torque of the wheel, N·m
T_{wi}	Water inlet temperature, °C
TWS	Stator tooth width, mm
v	Velocity of the vehicle, km/h
V_d	d -axis voltage, V
V_{da}	Voltage drop due to d -axis current, V
V_{dc}	DC link voltage, V
V_{dr}	Reference d -axis voltage, V
V_{m-l}	Line-line voltage of the machine, V
V_q	q -axis voltage, V
w_a	Width of armature slot, mm
w_{bi}	Width of stator back iron, mm
WEB	Rotor web thickness, mm
w_m	Width of magnet per pole, mm
w_p	Rotor pole width, mm
w_{pm}	Width of permanent magnet, mm
w_t	Stator tooth width, mm
β_m	Magnet pole arc, °electrical

<i>Symbol</i>	<i>Description</i>
θ	Phase shift between two sets of 3-phase windings, °
θ_r	Rotor position, °electrical/mechanical
θ_s	Slot pitch angle, °
ρ	Air density, kg/m ³
ρ	Resistivity of the magnet material, Ω·m
ω	Angular speed, rad/s
ω_b	Base speed of the machine, rpm
ω_c	Maximum cruise speed of the machine, rpm
ω_e	Electrical speed of the machine, rad/s
ω_m	Maximum speed, rpm
ω_m	Angular speed of the machine, rad/s
ω_{ms}	Cruise speed, rpm
ω_w	Angular speed of the wheel, rad/s

Acronyms

<i>Acronym</i>	<i>Description</i>
2DS	2°C Scenario
AC	Alternating Current
AlNiCo	Aluminium Nickel Cobalt magnets
AUDC	Artemis Urban Driving Cycle
BEV	Battery operated Electric Vehicle
BLAC	Brushless Alternating Current
BLDC	Brushless Direct Current
BP	British Petroleum
BW	Backward

<i>Acronym</i>	<i>Description</i>
CPPM	Consequent Pole Permanent Magnet machines
DC	Direct Current
DCM	Direct Current Machines
DEDSM	Double-Excited Dual-Stator Permanent Magnet machines
DESM	Doubly Excited Synchronous Machines
DSPM	Doubly Salient Permanent Magnet machines
DTC	Direct Torque Control
ECL	Eddy Current Loss in magnets
ECLH	Eddy Current Loss Harmonics
EMD	Electrical Machines and Drives
EMF	Electro-Motive-Force
EV	Electric Vehicles
EVI	Electric Vehicles Initiative
FE	Finite Element
FEA	Finite Element Analysis
FFT	Fast Fourier Transform
FM-PMBL	Flux-Mnemonic Permanent Magnet Brushless machines
FoM	Figure of Merit
FSCW	Fractional-slot Concentrated Winding
FW	Forward
GPIB	General Purpose Interface Bus
HE-PMFSM	Hybrid Excited Permanent Magnet Flux Switching Machines
HEV	Hybrid Electric Vehicles
HF-DSPM	Hybrid Field Doubly Salient Permanent Magnet machines
HF-DSPM	Hybrid Field Doubly Salient Permanent Magnet machines
HSUB	High Strength Un-diffused Brushless machines

<i>Acronym</i>	<i>Description</i>
ICE	Internal Combustion Engine
IEA	International Energy Agency
IEEE	Institute of Electrical and Electronics Engineers
IM	Induction Machines
IPM	Interior mounted Permanent Magnet Machines
LCM	Lowest Common Multiple
MMF	Magneto-Motive-Force
MPPA	Maximum Power Per Ampere
MTPA	Maximum Torque Per Ampere
MTPV	Maximum Torque Per Voltage
NdFeB	Neodymium Iron Boron magnets
NEDC	New European Driving Cycle
OECD	Organization for Economic Co-operation and Development
OEM	Original Equipment Manufacturer
PEV	Plug-in Electric Vehicles
PHEV	Plug-in Hybrid Electric Vehicle
PM	Permanent Magnet
PMFS	Permanent Magnet Flux Switching machines
PMSM	Permanent Magnet Synchronous Machines
PWM	Pulse Width Modulation
RFD	Radial Force Density
RMS	Root Mean Square value of a waveform
SC	Short Circuit
SM	Synchronous Machines
SMC	Soft Magnetic Composites
SmCo	Samarium Cobalt magnets

SPM	Surface mounted Permanent Magnet Machines
SRM	Switched Reluctance Machines
SynPM	Synchronous Permanent Magnet machines
SynRM	Synchronous Reluctance Machines
THD	Total Harmonic Distortion
UMP	Unbalanced Magnetic Pull
USB	Universal Serial Bus
VA	Volt-Ampere

Appendices

Appendix A Winding functions for 3-phase, 9-slot, 8-pole, and 3-phase, 18-slot, 8-/10-pole machine

In order to simplify the derivation, following assumptions are made:

- (a) Stator and rotor cores are infinitely permeable.
- (b) Effect of stator slotting is neglected (assuming slot-less stator).
- (c) The current distribution in the slotted stator is represented by an equivalent current sheet with a surface current density.

The surface current density is given by

$$J_s(\theta, t) = \frac{q}{2} \left[\sum_{\substack{n=qk+1 \\ k=0,1,2,\dots}}^{\infty} J_n \cos(n\theta - p_r \omega_r t) - \sum_{\substack{n=qk-1 \\ k=1,2,3,\dots}}^{\infty} J_n \cos(n\theta + p_r \omega_r t) \right] \quad (1)$$

where q is number of phases, p_r is number of pole-pairs of the rotor permanent magnets, θ is the angular displacement on the stator bore, and ω_r is the angular speed of the rotor. J_n is the amplitude of the n th space harmonic given by (2).

$$J_n = \frac{2N_s I_p}{\pi R_s} K_{wn} \quad (2)$$

where N_s and I_p are number of turns in series per phase, and the peak current respectively, R_s is the stator bore radius, and K_{wn} is the winding factor associated with the n th harmonic. For machines with concentrated windings, it is given by (3).

$$K_{wn} = \sin\left(\frac{n\pi}{N_{ss}}\right) \frac{\sin(n\beta_0)}{n\beta_0} \quad (3)$$

where N_{ss} is number of stator slots and β_o is the width of the slot opening in radian.

Equation (1) can be further expressed in rotor reference frame as (4).

$$J_s(\theta_r, t) = \frac{q}{2} \left[\sum_{\substack{n=qk+1 \\ k=0,1,2,\dots}}^{\infty} J_n \cos(n\theta_r + (n - p_r)\omega_r t) - \sum_{\substack{n=qk-1 \\ k=1,2,3,\dots}}^{\infty} J_n \cos(n\theta_r + (n + p_r)\omega_r t) \right] \quad (4)$$

where θ_r is the angular position at the stator bore referred to the rotor reference frame.

I. 3-phase, 9-slot, 8-pole winding function

For 3-phase, 9-slot, 8-pole machine, the winding function in terms of the surface current density at the stator bore is expressed by (5).

$$J_s(\theta_r, t) = \frac{3}{2} \left[\sum_{\substack{n=3k+1 \\ k=0,1,2,\dots}}^{\infty} J_n \cos(n\theta_r + (n - 4)\omega_r t) - \sum_{\substack{n=3k-1 \\ k=1,2,3,\dots}}^{\infty} J_n \cos(n\theta_r + (n + 4)\omega_r t) \right] \quad (5)$$

where $n = 3k+1$, $k = 0, 1, 2, 3, \dots$ represents the forward rotating harmonics, and $n = 3k-1$, $k = 1, 2, 3, \dots$ represents the backward rotating harmonics. Table I lists the backward and forward rotating harmonics in 3-phase, 9-slot, 8-pole machine.

Table I. Forward and backward rotating harmonics in 3-phase, 9-slot, 8-pole machine

k	Forward rotating harmonic (3k + 1)	Backward rotating harmonic (3k - 1)
0	1	-
1	4	2
2	7	5
3	10	8
4	13	11
5	16	14

6	19	17
---	----	----

II. 3-phase, 18-slot, 8-pole winding function

For 3-phase, 18-slot, 8-pole machine, the winding function in terms of the surface current density at the stator bore is expressed by (6).

$$J_s(\theta_r, t) = \frac{3}{2} \left[\sum_{\substack{n=6k-2 \\ k=1,2,3,\dots}}^{\infty} J_n \cos(n\theta_r + (n-4)\omega_r t) - \sum_{\substack{n=6k+2 \\ k=0,1,2,\dots}}^{\infty} J_n \cos(n\theta_r + (n+4)\omega_r t) \right] \quad (6)$$

where $n = 6k-2$, $k = 0, 1, 2, 3, \dots$ represents the forward rotating harmonics, and $n = 6k+2$, $k = 1, 2, 3, \dots$ represents the backward rotating harmonics. Table II lists the backward and forward rotating harmonics in 3-phase, 18-slot, 8-pole machine.

Table II. Forward and backward rotating harmonics in 3-phase, 18-slot, 8-pole machine

k	Forward rotating harmonic (6k - 2)	Backward rotating harmonic (6k + 2)
0	-	2
1	4	8
2	10	14
3	16	20
4	22	26
5	28	32
6	34	38

III. 3-phase, 18-slot, 10-pole winding function

For 3-phase, 18-slot, 10-pole machine, the winding function in terms of the surface current density at the stator bore is expressed by (7).

$$J_s(\theta_r, t) = \frac{3}{2} \left[\sum_{\substack{n=6k-1 \\ k=1,2,3,\dots}}^{\infty} J_n \cos(n\theta_r + (n-5)\omega_r t) - \sum_{\substack{n=6k+1 \\ k=0,1,2,\dots}}^{\infty} J_n \cos(n\theta_r + (n+5)\omega_r t) \right] \quad (7)$$

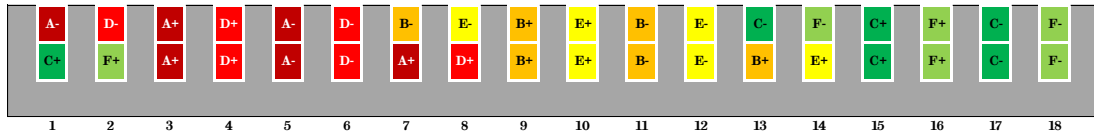
where $n = 6k-1, k = 0, 1, 2, 3, \dots$ represents the forward rotating harmonics, and $n = 6k+1, k = 1, 2, 3, \dots$ represents the backward rotating harmonics. Table III lists the backward and forward rotating harmonics in 3-phase, 18-slot, 10-pole machine.

Table III. Forward and backward rotating harmonics in 3-phase, 18-slot, 10-pole machine

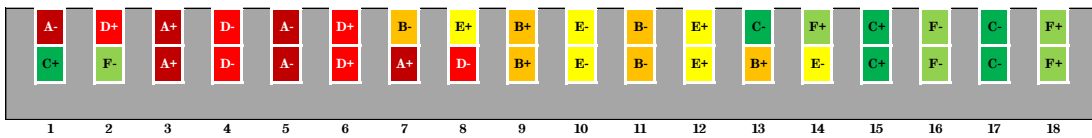
k	Forward rotating harmonic (6k - 1)	Backward rotating harmonic (6k + 1)
0	-	1
1	5	7
2	11	13
3	17	19
4	23	25
5	29	31
6	35	37

Appendix B Winding configurations for each of the phase shifts between A-B-C and D-E-F windings of 6-phase, 18-slot, 8-pole Machine

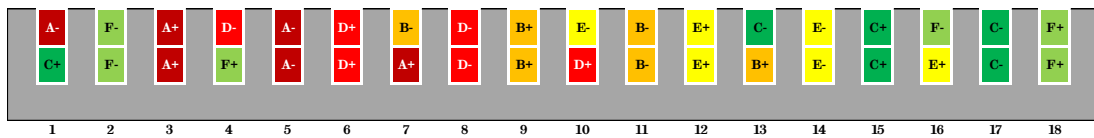
I. 6-phase, 18-slot, 8-pole winding configurations



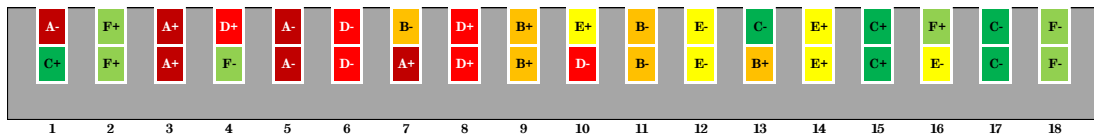
(g) Slot-shift = 1, Similar polarity, Phase shift between A-B-C and D-E-F = 80°



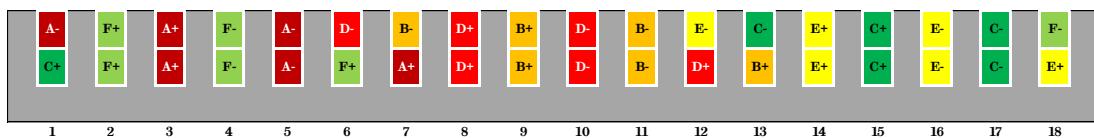
(h) Slot-shift = 1, Opposite polarity, Phase shift between A-B-C and D-E-F = 260°



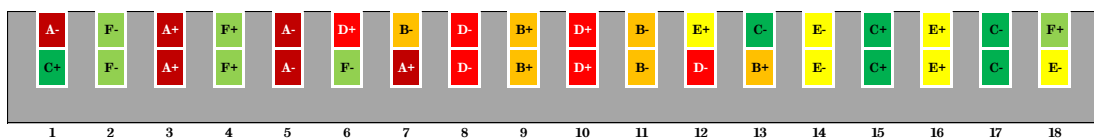
(i) Slot-shift = 3, Similar polarity, Phase shift between A-B-C and D-E-F = 240°



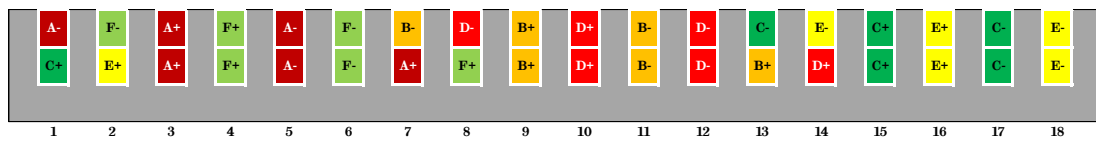
(j) Slot-shift = 3, Opposite polarity, Phase shift between A-B-C and D-E-F = 60°



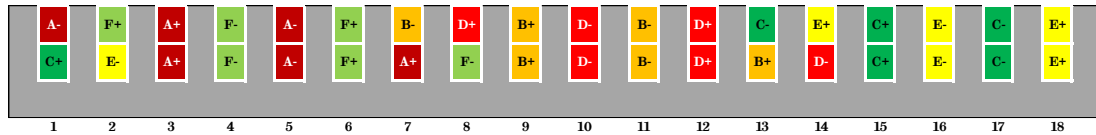
(k) Slot-shift = 5, Similar polarity, Phase shift between A-B-C and D-E-F = 40°



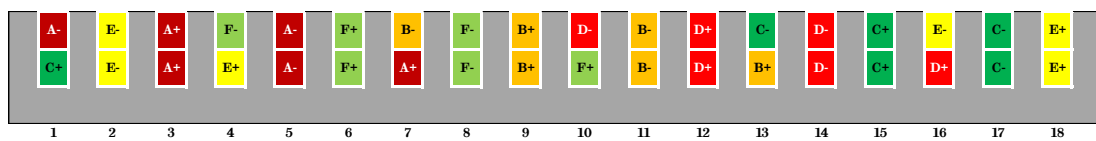
(l) Slot-shift = 5, Opposite polarity, Phase shift between A-B-C and D-E-F = 220°



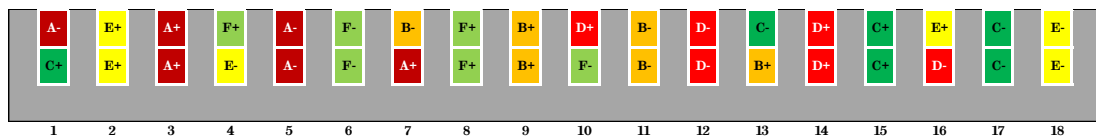
(m) Slot-shift = 7, Similar polarity, Phase shift between A-B-C and D-E-F = 200°



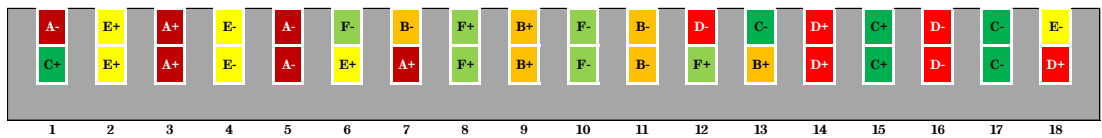
(n) Slot-shift = 7, Opposite polarity, Phase shift between A-B-C and D-E-F = 20°



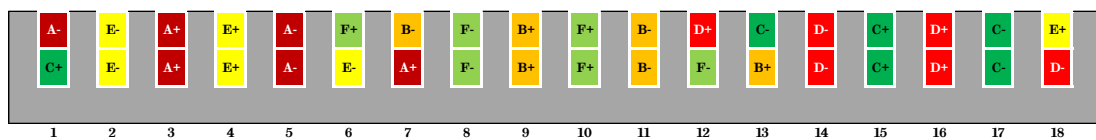
(o) Slot-shift = 9, Similar polarity, Phase shift between A-B-C and D-E-F = 0°



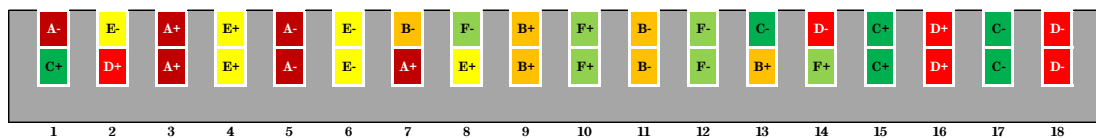
(p) Slot-shift = 9, Opposite polarity, Phase shift between A-B-C and D-E-F = 180°



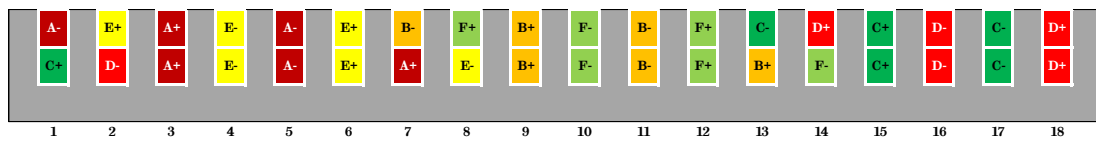
(q) Slot-shift = 11, Similar polarity, Phase shift between A-B-C and D-E-F = 160°



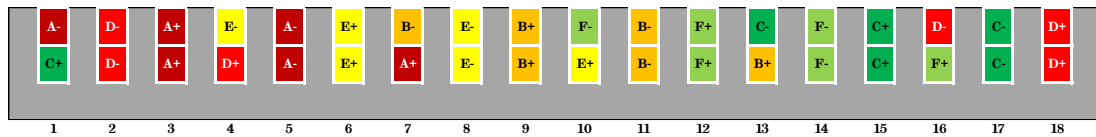
(r) Slot-shift = 11, Opposite polarity, Phase shift between A-B-C and D-E-F = 340°



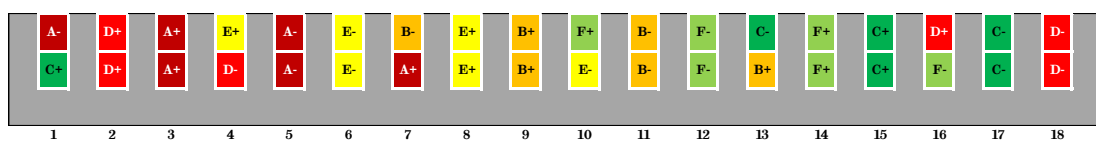
(s) Slot-shift = 13, Similar polarity, Phase shift between A-B-C and D-E-F = 320°



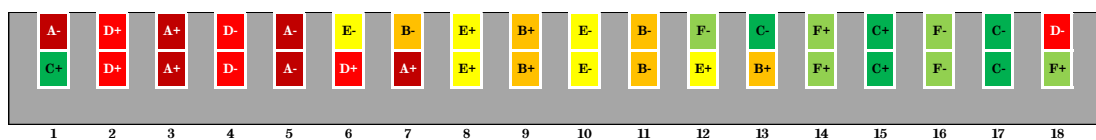
(t) Slot-shift = 13, Opposite polarity, Phase shift between A-B-C and D-E-F = 140°



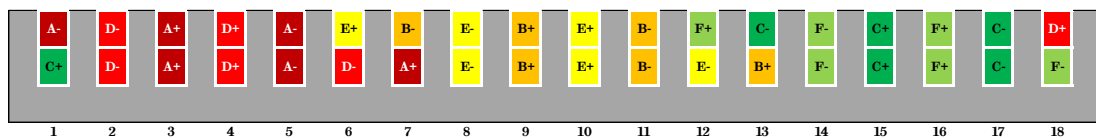
(u) Slot-shift = 15, Similar polarity, Phase shift between A-B-C and D-E-F = 120°



(v) Slot-shift = 15, Opposite polarity, Phase shift between A-B-C and D-E-F = 300°

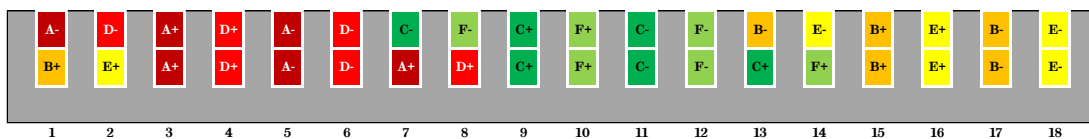


(w) Slot-shift = 17, Similar polarity, Phase shift between A-B-C and D-E-F = 280°

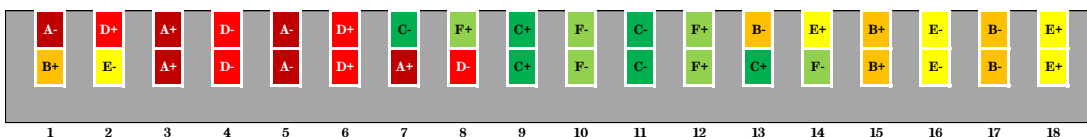


(x) Slot-shift = 17, Opposite polarity, Phase shift between A-B-C and D-E-F = 100°

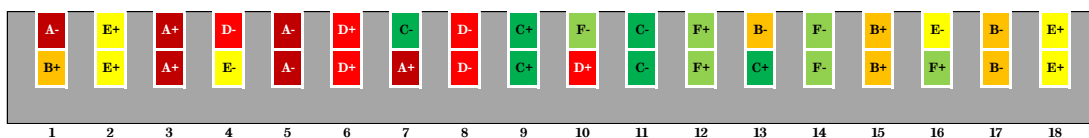
II. 6-phase, 18-slot, 10-pole winding configurations



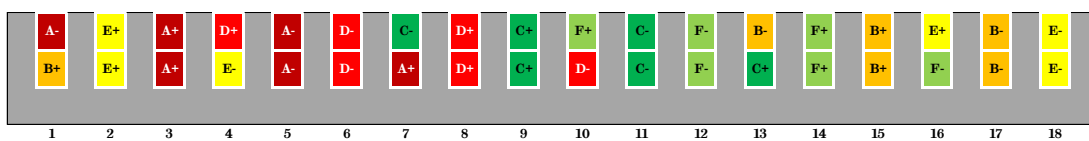
(a) Slot-shift = 1, Similar polarity, Phase shift between A-B-C and D-E-F = 100°



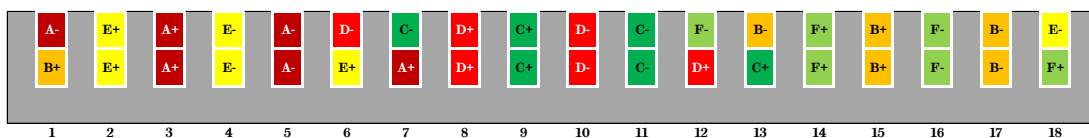
(b) Slot-shift = 1, Opposite polarity, Phase shift between A-B-C and D-E-F = 280°



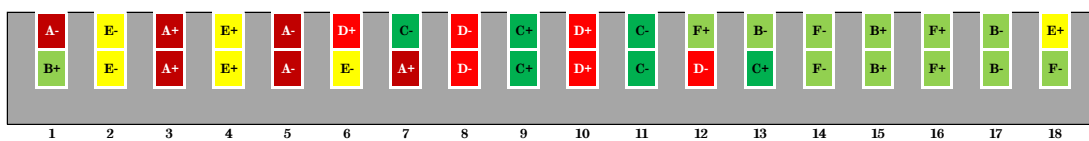
(c) Slot-shift = 3, Similar polarity, Phase shift between A-B-C and D-E-F = 300°



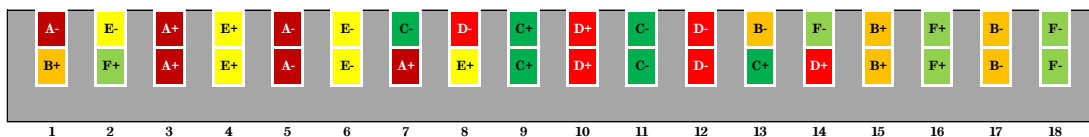
(d) Slot-shift = 3, Opposite polarity, Phase shift between A-B-C and D-E-F = 120°



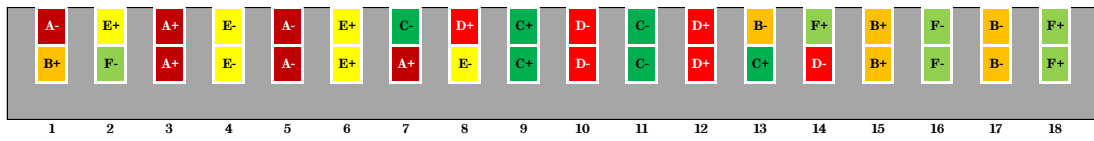
(e) Slot-shift = 5, Similar polarity, Phase shift between A-B-C and D-E-F = 140°



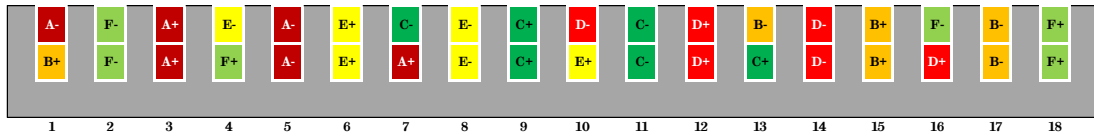
(f) Slot-shift = 5, Opposite polarity, Phase shift between A-B-C and D-E-F = 320°



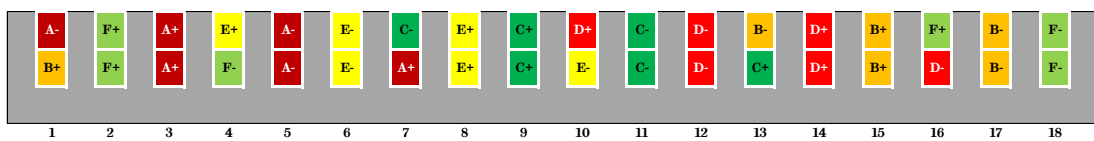
(g) Slot-shift = 7, Similar polarity, Phase shift between A-B-C and D-E-F = 340°



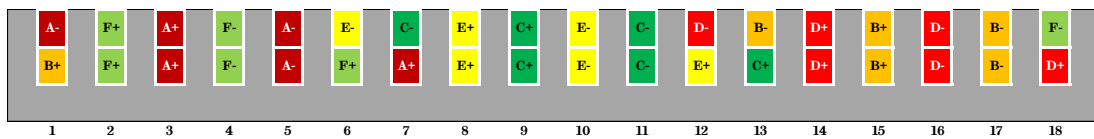
(h) Slot-shift = 7, Opposite polarity, Phase shift between A-B-C and D-E-F = 160°



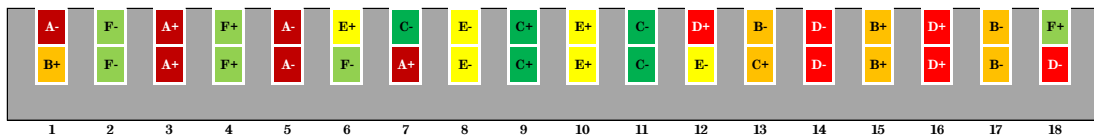
(i) Slot-shift = 9, Similar polarity, Phase shift between A-B-C and D-E-F = 180°



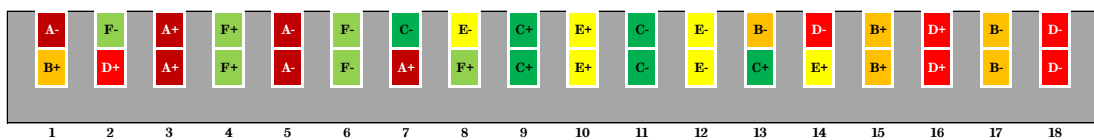
(j) Slot-shift = 9, Opposite polarity, Phase shift between A-B-C and D-E-F = 0°



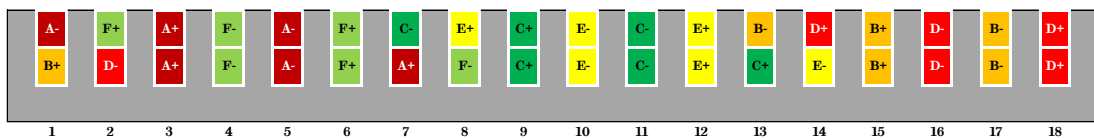
(k) Slot-shift = 11, Similar polarity, Phase shift between A-B-C and D-E-F = 20°



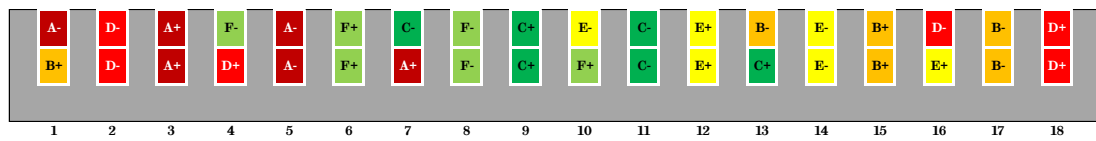
(l) Slot-shift = 11, Opposite polarity, Phase shift between A-B-C and D-E-F = 200°



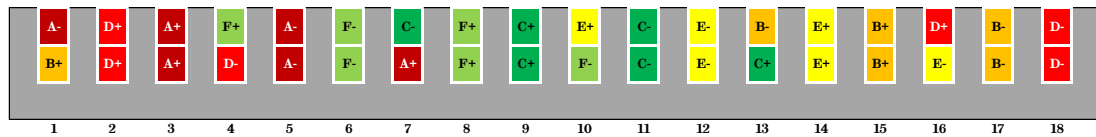
(m) Slot-shift = 13, Similar polarity, Phase shift between A-B-C and D-E-F = 220°



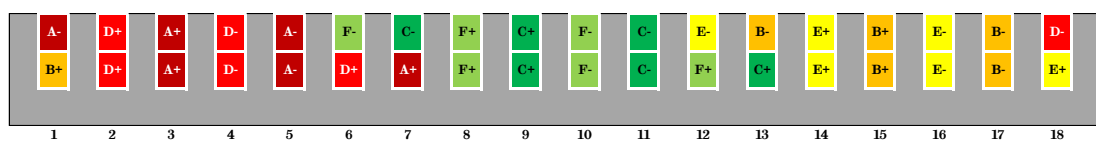
(n) Slot-shift = 13, Opposite polarity, Phase shift between A-B-C and D-E-F = 40°



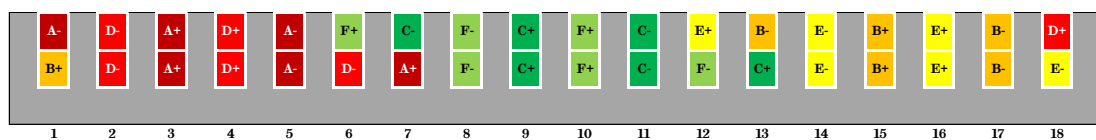
(o) Slot-shift = 15, Similar polarity, Phase shift between A-B-C and D-E-F = 60°



(p) Slot-shift = 15, Opposite polarity, Phase shift between A-B-C and D-E-F = 240°



(q) Slot-shift = 17, Similar polarity, Phase shift between A-B-C and D-E-F = 260°



(r) Slot-shift = 17, Opposite polarity, Phase shift between A-B-C and D-E-F = 80°

Appendix C Inductance and flux-linkage map of the designed 6-phase, 18-slot, 8-pole IPM machine (or 1st prototype machine)

I_d (A)	I_q (A)	L_d (mH)	L_q (mH)	λ_d (mWb)	λ_q (mWb)	T (N·m)
0	0	-	-	85.2	0.0	0.0
0	25	-	1.853	82.6	46.3	24.8
0	50	-	1.453	77.0	72.6	46.2
0	75	-	1.202	71.0	90.2	63.9
0	100	-	1.019	65.2	101.9	78.3
0	125	-	0.882	60.1	110.2	90.1
0	150	-	0.776	55.6	116.4	100.1
0	175	-	0.694	51.7	121.4	108.7
0	200	-	0.628	48.4	125.6	116.3
-25	0	1.070	-	58.5	0.0	0.0
-25	25	0.919	1.951	59.7	48.8	32.5
-25	50	0.772	1.552	57.7	77.6	57.9
-25	75	0.692	1.272	53.7	95.4	76.9
-25	100	0.632	1.068	49.4	106.8	91.4
-25	125	0.581	0.916	45.6	114.5	102.7
-25	150	0.537	0.801	42.2	120.1	111.9
-25	175	0.499	0.712	39.3	124.6	119.8
-25	200	0.466	0.641	36.8	128.3	126.8
-50	0	1.088	-	30.8	0.0	0.0
-50	25	0.992	1.866	33.0	46.6	37.9
-50	50	0.842	1.585	34.9	79.3	68.5
-50	75	0.742	1.313	33.9	98.5	89.6
-50	100	0.668	1.099	31.8	109.9	104.1
-50	125	0.608	0.939	29.7	117.4	114.9
-50	150	0.557	0.817	27.7	122.6	123.5
-50	175	0.514	0.724	26.0	126.7	130.7
-50	200	0.478	0.650	24.5	130.1	137.0
-75	0	1.074	-	4.7	0.0	0.0
-75	25	1.013	1.730	6.6	43.2	40.9

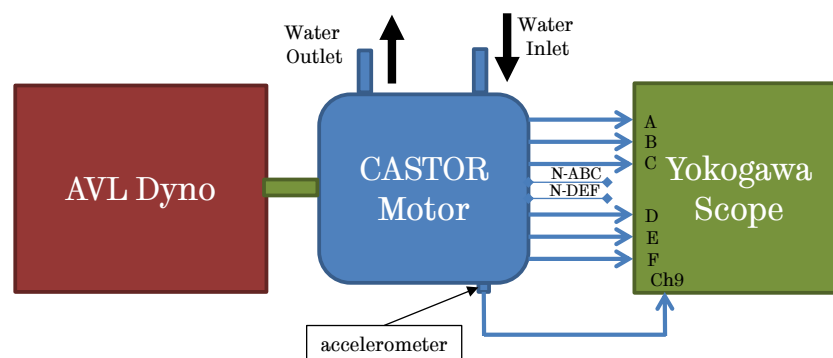
-75	50	0.891	1.550	10.2	77.5	75.9
-75	75	0.782	1.318	12.3	98.9	100.1
-75	100	0.698	1.110	12.9	111.0	115.4
-75	125	0.630	0.948	12.8	118.5	125.9
-75	150	0.573	0.825	12.6	123.7	134.0
-75	175	0.526	0.729	12.3	127.7	140.6
-75	200	0.487	0.655	11.9	130.9	146.5
-100	0	1.056	-	-20.4	0.0	0.0
-100	25	1.012	1.594	-18.6	39.8	42.2
-100	50	0.914	1.469	-14.4	73.5	79.5
-100	75	0.808	1.283	-9.8	96.2	106.6
-100	100	0.717	1.096	-6.5	109.6	123.7
-100	125	0.644	0.942	-4.3	117.7	134.8
-100	150	0.584	0.821	-2.8	123.2	142.8
-100	175	0.534	0.728	-1.7	127.3	149.3
-100	200	0.493	0.654	-0.9	130.7	154.8
-125	0	1.034	-	-44.0	0.0	0.0
-125	25	0.997	1.454	-41.9	36.3	41.9
-125	50	0.913	1.362	-37.0	68.1	79.9
-125	75	0.815	1.214	-30.8	91.1	108.8
-125	100	0.725	1.058	-25.3	105.8	128.3
-125	125	0.650	0.920	-21.2	115.0	140.7
-125	150	0.588	0.808	-18.0	121.1	149.4
-125	175	0.538	0.719	-15.5	125.8	156.1
-125	200	0.496	0.647	-13.5	129.5	161.8
-150	0	0.989	-	-63.1	-0.1	0.0
-150	25	0.959	1.305	-61.2	32.6	40.4
-150	50	0.888	1.237	-56.1	61.9	77.7
-150	75	0.802	1.126	-49.2	84.5	107.8
-150	100	0.719	1.002	-42.6	100.2	129.2
-150	125	0.647	0.885	-36.9	110.6	143.6
-150	150	0.587	0.785	-32.4	117.7	153.5
-150	175	0.537	0.703	-28.8	123.0	161.0
-150	200	0.495	0.636	-25.8	127.3	167.1
-175	0	0.929	-	-77.4	-0.2	0.0
-175	25	0.905	1.165	-75.7	29.1	38.4

-175	50	0.846	1.115	-71.0	55.8	74.5
-175	75	0.774	1.033	-64.5	77.5	104.6
-175	100	0.702	0.936	-57.6	93.6	127.5
-175	125	0.636	0.840	-51.2	105.0	143.7
-175	150	0.579	0.754	-45.8	113.2	155.2
-175	175	0.532	0.682	-41.3	119.3	163.8
-175	200	0.491	0.621	-37.6	124.2	170.7
-200	0	0.868	-	-88.4	-0.3	0.0
-200	25	0.848	1.040	-86.9	26.0	36.4
-200	50	0.799	1.006	-82.8	50.3	71.0
-200	75	0.740	0.944	-77.0	70.8	100.6
-200	100	0.678	0.869	-70.3	86.9	124.1
-200	125	0.619	0.791	-63.8	98.9	141.7
-200	150	0.568	0.720	-58.0	107.9	154.7
-200	175	0.523	0.656	-52.9	114.9	164.6
-200	200	0.485	0.602	-48.6	120.5	172.5

Appendix D Procedures for various preliminary functional tests on the prototype machine

I. Procedure for measurement of back EMF

During this test, the motor operates in open-circuit and is driven by the dynamometer. Hence, the inverter is disconnected from the motor terminals. The schematic of the test set-up is shown below. For simplicity, the coupling is not shown.



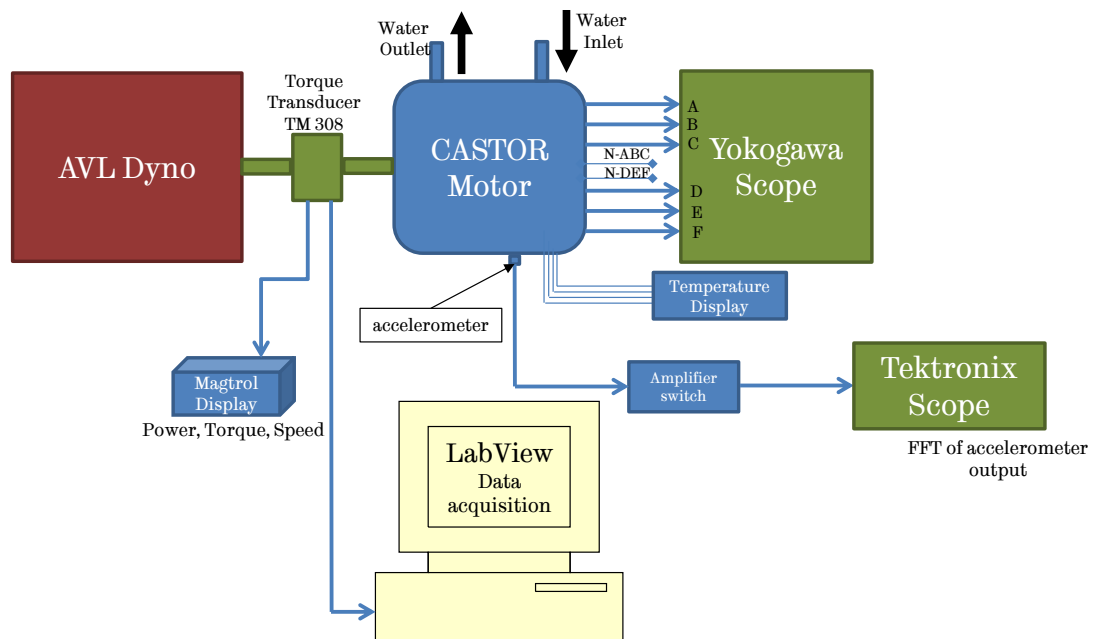
Schematic of test set-up for measurement of back EMF

The test is performed as per the following procedure:

- 1) Set the AVL dynamometer to operate in speed control mode.
- 2) Turn on the cooling water supply to the motor using tool-temp machine.
- 3) Slowly increase the dynamometer speed to 1000 rpm.
- 4) Let the motor run at constant speed set by the dynamometer.
- 5) Record the phase voltages V_a , V_b , V_c , V_d , V_e , V_f in the Yokogawa Scope. Save the waveform data file.
- 6) Increase the speed of the dynamometer to the next speed level. Monitor the accelerometer output on the Yokogawa scope while increasing the speed.
- 7) Repeat the steps 4 to 6 for various speeds (i.e., 2000 rpm, 2800 rpm, 3000 rpm, 4000 rpm, 5000 rpm, 6000 rpm, and 7000 rpm).

II. Procedure for measurement of no-load loss

During this test, the motor driven by the Dynamometer operates in open-circuit and the inverter is disconnected from the motor terminals. The schematic of the test set-up is shown below. The couplings are not shown for simplicity. The motor vibrations are observed on Tektronics Scope through the accelerometer. The temperatures are displayed and recorded through Pico temperature logger.



Schematic of test set-up for measurement of no-load losses

The test is performed as per the following procedure:

- 1) Set the AVL dynamometer to operate in speed control mode.
- 2) Turn on the cooling water supply to the motor using tool-temp machine.
- 3) Slowly increase the dynamometer speed to 500 rpm.
- 4) Let the motor run at constant speed set by the dynamometer.
- 5) Measure the generated torque, the shaft speed and hence power through Magtrol display and record the data in PC. The no-load losses of the motor comprise of no-load iron losses, friction losses in bearings, and windage losses.
- 6) Increase the speed of the dynamometer to the next speed level. Monitor the accelerometer output on the scope while increasing the speed gradually.
- 7) Repeat the steps 4 to 6 for various speeds till maximum speed of 11000 rpm.

III. Procedure for characterizing the motor parameters

In order to characterise the motor parameters, namely the d - and q -axis inductances, the test is performed as per the following procedure. The schematic of this test set-up is shown in Figure 6.6.

- 1) Set the AVL dynamometer to operate in speed control mode.
- 2) Turn on the cooling water supply to the motor using tool-temp machine. Also, turn on the cooling water supply to the inverter.
- 3) Gradually increase the speed of the dynamometer to 1500 rpm.
- 4) The motor is fed with 6-phase sinusoidal currents by the inverter. The motor operates under current control mode during this test.
- 5) Let the motor run at constant speed set by the dynamometer, i.e. 1500 rpm for this test.
- 6) Apply the d -axis and q -axis current demand through inverter control.
- 7) Record the position signals, phase A voltage, and phase A current on the Yokogawa Scope.
- 8) Change the d -axis and q -axis current demands to the next level.
- 9) Repeat the steps 7 to 9 till all desired range of d - and q -axis currents are achieved.
- 10) Use the recorded signals and values to calculate the motor inductances (L_d , and L_q).

IV. Procedure for measurement of efficiency map

In order to measure the efficiency of the motor and the inverter, the motor is controlled by the inverter, and efficiency of the motor and the inverter is measured. The schematic of this test set-up is shown in Figure 6.6. The test is performed as per the following procedure:

- 1) Set the AVL dynamometer to operate in speed control mode.
- 2) Turn on the cooling water supply to the motor using tool-temp machine. Also, turn on the cooling water supply to the inverter.

- 3) The motor is fed with 6-phase sinusoidal currents by the inverter. During this test, the motor operates under torque control mode.
- 4) Slowly increase the speed of the dynamometer to 500 rpm.
- 5) Let the motor run at constant speed set by the dynamometer.
- 6) Slowly increase the torque demand on the motor from 0 N·m to peak torque in steps of 5 N·m through inverter control. Record all data from power analyser, Magtrol display and temperature logger.
- 7) Reduce the torque demand to zero in discrete steps after reaching peak torque level before increasing the speed.
- 8) Increase the speed of the dynamometer to the next speed level. Monitor the accelerometer output on the scope while increasing the speed gradually.
- 9) Repeat the steps 6 to 9 for various speeds till maximum speed of 11000 rpm.

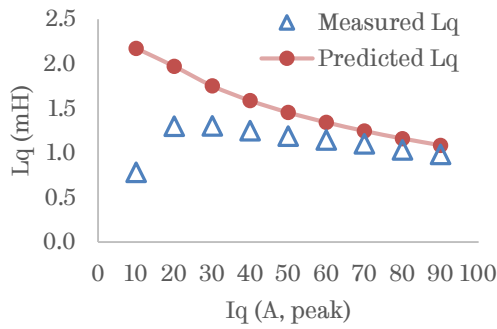
V. Procedure for thermal test

In order to evaluate thermal behaviour of the motor, the test is performed as per the following procedure. The schematic of this test set-up is shown in Figure 6.6.

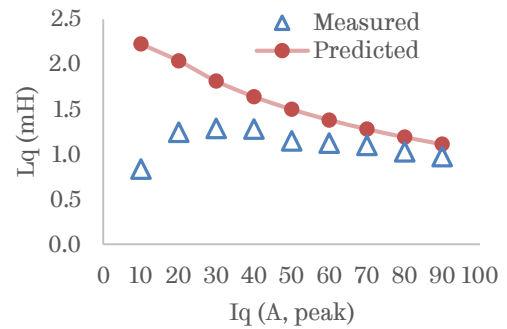
- 1) Set the AVL dynamometer to operate in speed control mode.
- 2) Turn on the cooling water supply to the motor using tool-temp machine. Set the flow rate of the cooling water to 15 litre/min. The cooling water temperature for inlet is set at 20°C. Also, turn on the cooling water supply to the inverter.
- 3) The motor is fed with 6-phase sinusoidal currents by the inverter. The motor operates under torque control mode during this test.
- 4) Gradually increase the speed of the dynamometer to 2800 rpm.
- 5) Let the motor run at constant speed set by the dynamometer.
- 6) The torque demand on the motor is increased from 0 N·m to the rated torque (i.e. 75 N·m) in steps of 5 Nm through inverter control.

- 7) Let the motor run at this condition until temperatures reach steady-state.
- 8) Record all the data from power analyser, Magtrol display, and temperature logger.
- 9) Repeat the steps (1) to (8) for thermal test at continuous torque at high speed operation (for example, 8600 rpm, 22 kW).

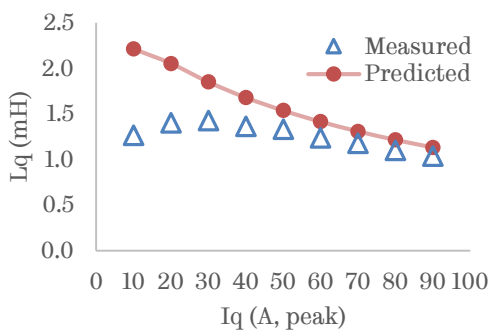
Appendix E Comparison of predicted and measured d - and q -axis inductances



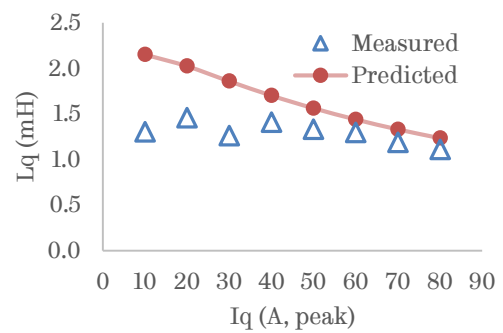
(a) $I_d = 0$ A



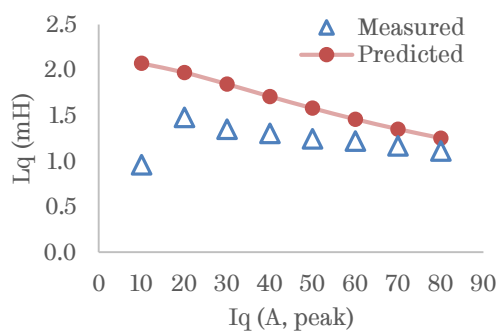
(b) $I_d = -10$ A



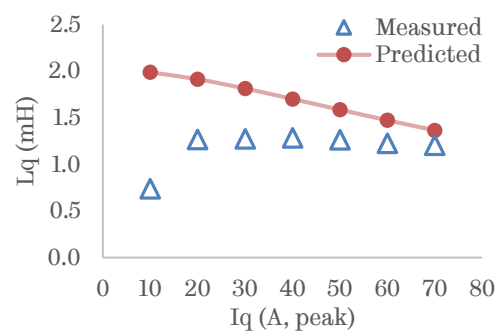
(c) $I_d = -20$ A



(d) $I_d = -30$ A

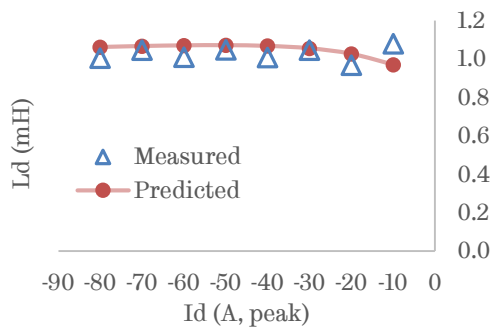


(e) $I_d = -40$ A

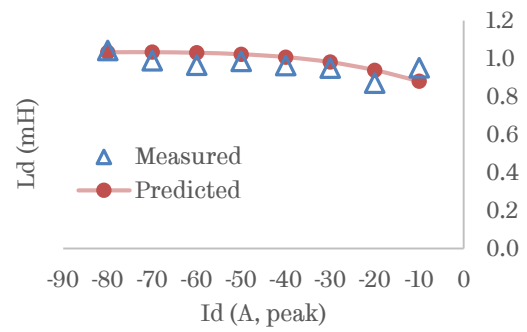


(f) $I_d = -50$ A

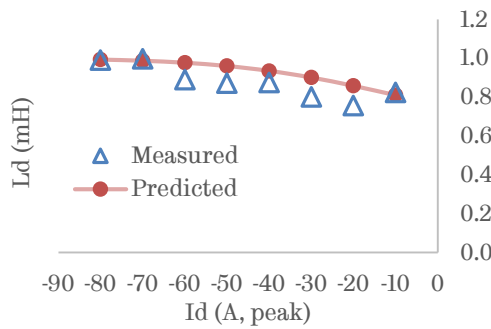
Comparison of measured and predicted q -axis inductance with q -axis current at various d -axis currents



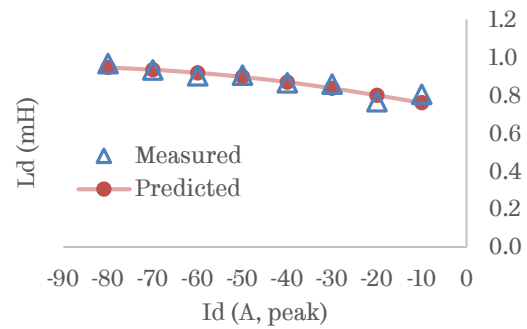
(a) $I_q = 10$ A



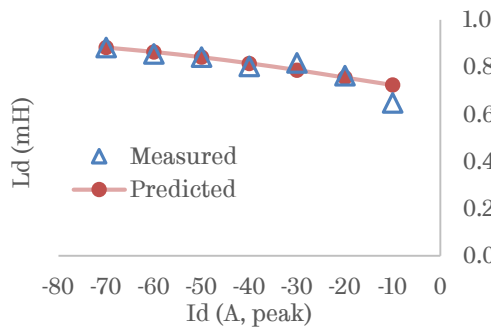
(b) $I_q = 20$ A



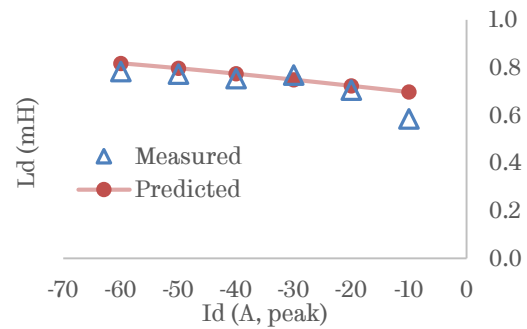
(c) $I_q = 30$ A



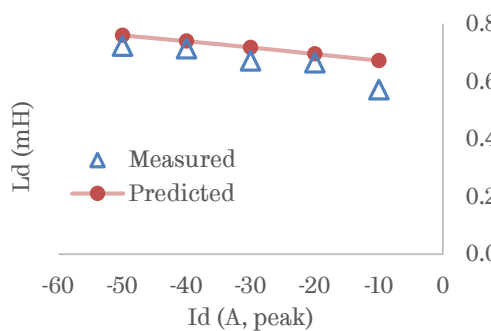
(d) $I_q = 40$ A



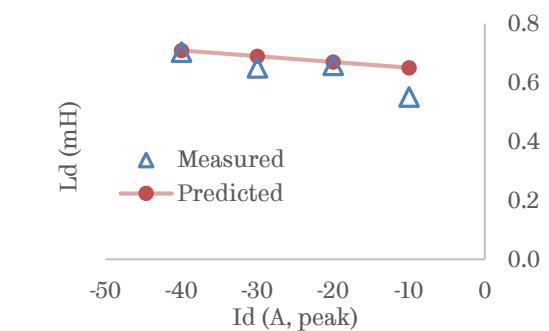
(e) $I_q = 50$ A



(f) $I_q = 60$ A



(g) $I_q = 70$ A



(h) $I_q = 80$ A

Comparison of measured and predicted d -axis inductance with d -axis current at various q -axis currents

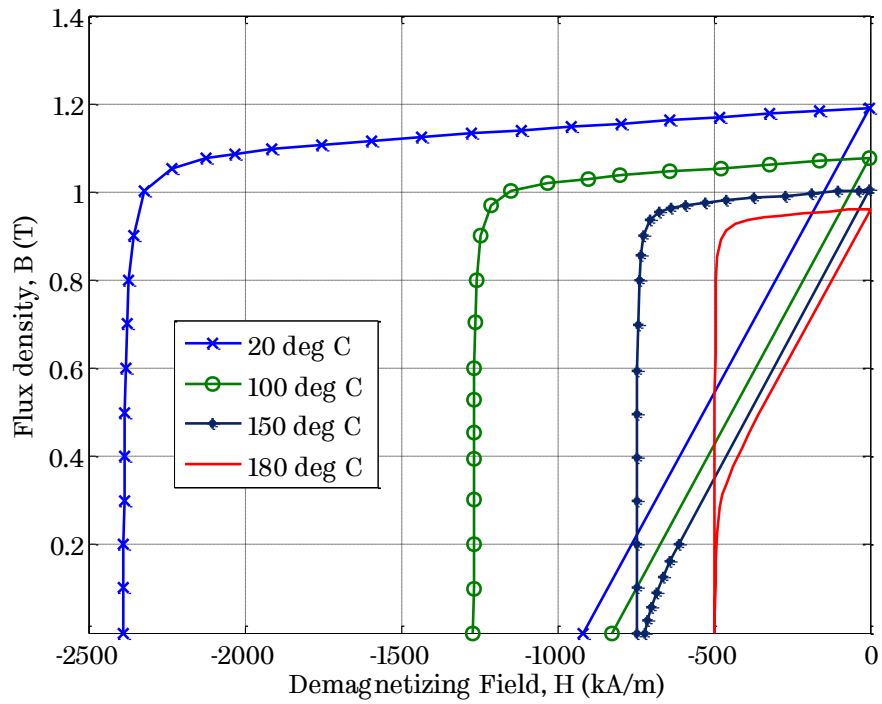
Appendix F Inductance and flux-linkage map of the 2nd prototype of 6-phase, 18-slot, 8-pole IPM machine

I_d (A)	I_q (A)	L_d (mH)	L_q (mH)	λ_d (mWb)	λ_q (mWb)	T (N·m)
0	0	-	-	81.0	0.0	0.0
0	20	-	2.078	79.6	41.6	19.1
0	40	-	1.654	75.5	66.2	36.2
0	60	-	1.390	70.7	83.4	50.9
0	80	-	1.194	65.9	95.5	63.3
0	100	-	1.043	61.4	104.3	73.8
0	120	-	0.924	57.3	110.8	82.6
0	140	-	0.828	53.7	116.0	90.3
0	160	-	0.751	50.4	120.2	97.1
0	180	-	0.688	47.6	123.8	103.1
-20	0	1.133	-	58.4	0.0	0.0
-20	20	1.011	2.136	59.3	42.7	24.5
-20	40	0.852	1.743	58.4	69.7	44.8
-20	60	0.767	1.460	55.4	87.6	60.9
-20	80	0.705	1.246	51.8	99.7	73.7
-20	100	0.654	1.081	48.4	108.1	84.1
-20	120	0.608	0.953	45.2	114.3	92.6
-20	140	0.569	0.851	42.3	119.1	99.9
-20	160	0.534	0.768	39.8	122.9	106.1
-20	180	0.503	0.701	37.6	126.2	111.8
-40	0	1.141	-	35.4	0.0	0.0
-40	20	1.064	2.034	37.0	40.7	28.4
-40	40	0.918	1.765	38.8	70.6	52.5
-40	60	0.815	1.502	38.1	90.1	70.7
-40	80	0.743	1.282	36.2	102.5	84.0
-40	100	0.682	1.109	34.1	110.9	94.3
-40	120	0.631	0.974	32.1	116.8	102.4
-40	140	0.587	0.867	30.2	121.3	109.2
-40	160	0.548	0.781	28.5	124.9	115.0

-40	180	0.515	0.711	27.0	127.9	120.2
-60	0	1.128	-	13.4	0.0	0.0
-60	20	1.078	1.901	14.9	38.0	31.0
-60	40	0.961	1.724	17.8	69.0	58.2
-60	60	0.855	1.509	19.4	90.5	79.1
-60	80	0.774	1.297	19.5	103.8	93.4
-60	100	0.707	1.123	19.0	112.3	103.7
-60	120	0.650	0.985	18.3	118.2	111.6
-60	140	0.602	0.876	17.6	122.6	118.0
-60	160	0.560	0.788	16.8	126.1	123.4
-60	180	0.524	0.716	16.2	129.0	128.2
-80	0	1.110	-	-7.8	0.1	0.0
-80	20	1.075	1.770	-6.4	35.4	32.5
-80	40	0.984	1.647	-3.3	65.9	61.7
-80	60	0.885	1.480	-0.1	88.8	85.1
-80	80	0.797	1.289	2.2	103.1	101.0
-80	100	0.725	1.121	3.4	112.1	111.7
-80	120	0.664	0.986	4.2	118.3	119.6
-80	140	0.612	0.877	4.7	122.8	125.8
-80	160	0.568	0.789	5.0	126.3	131.0
-80	180	0.530	0.718	5.2	129.2	135.5
-100	0	1.092	-	-28.2	0.1	0.0
-100	20	1.064	1.644	-26.9	32.9	33.0
-100	40	0.990	1.554	-23.5	62.1	63.3
-100	60	0.899	1.419	-19.2	85.2	88.3
-100	80	0.811	1.255	-15.1	100.4	105.8
-100	100	0.735	1.103	-12.1	110.3	117.7
-100	120	0.672	0.975	-9.8	117.0	126.1
-100	140	0.618	0.870	-8.1	121.8	132.4
-100	160	0.572	0.785	-6.7	125.5	137.5
-100	180	0.533	0.715	-5.6	128.6	142.0
-120	0	1.069	-	-47.2	0.1	0.0
-120	20	1.044	1.512	-45.7	30.2	32.6
-120	40	0.979	1.445	-42.0	57.8	63.2
-120	60	0.896	1.337	-36.8	80.2	88.9
-120	80	0.813	1.201	-31.6	96.1	107.9

-120	100	0.738	1.070	-27.1	107.0	121.3
-120	120	0.674	0.954	-23.5	114.4	130.6
-120	140	0.619	0.855	-20.6	119.7	137.4
-120	160	0.573	0.774	-18.3	123.9	142.8
-120	180	0.533	0.707	-16.4	127.2	147.4
-130	0	1.050	-	-55.5	0.0	-0.1
-130	20	1.027	1.443	-54.0	28.9	32.1
-130	40	0.967	1.387	-50.2	55.5	62.5
-130	60	0.889	1.290	-44.8	77.4	88.4
-130	80	0.809	1.169	-39.3	93.5	108.1
-130	100	0.736	1.049	-34.3	104.9	122.3
-130	120	0.673	0.939	-30.1	112.7	132.1
-130	140	0.619	0.845	-26.8	118.3	139.3
-130	160	0.572	0.767	-24.0	122.7	144.9
-130	180	0.533	0.702	-21.7	126.3	149.6

Appendix G Demagnetization characteristics of a typical NdFeB magnet of grade N35EH



Demagnetization characteristics of N35EH [125].